UNIVERSITY OF CALIFORNIA SAN DIEGO

Methods in Predictive Oncology

A Dissertation submitted in partial satisfaction of the requirements
for the degree Doctor of Philosophy

in

Computer Science

by

Akshat Singhal

Committee in charge:

Professor Trey Ideker, Chair
Professor Vineet Bafna
Professor Melissa Gymrek
Professor Aritro Nath
Professor Barbara Parker

2025

The Dissertation of Akshat Singhal is approved, and it is acceptable in quality and form for publication on microfilm and electronically.

University of California San Diego

2025

DEDICATION

To my parents, for their endless sacrifice and unconditional support.

To my sister, for comic relief.

TABLE OF CONTENTS

LIST OF FIGURES

LIST OF TABLES

LIST OF ABBREVIATIONS

AI	Artificial intelligence
AUC	Area under the dose response curve
CDAPS	Community detection application and service
CDK4/6i	Cyclin dependent kinase 4 and 6 inhibitor
CESC	Cervical squamous cell carcinoma and endocervical adenocarcinoma
CNA	Copy number amplifications
CND	Copy number deletions
HER2	Human epidermal growth factor receptor 2
HR	Hormone receptor
JAK	Janus kinase
KAT6A	K(lysine) acetyltransferase 6A
LUSC	Lung squamous cell carcinoma
NeST	Nested systems in tumors
PDX	Patient derived xenograft
PFS	Progression free survival
RB1	Retinoblastoma transcriptional repressor 1
RECIST	Response evaluation criteria in solid tumors
RSi	Replication stress inducing
RTK	Receptor tyrosine kinase
RUNX1	Runt-related transcription factor 1
SHAP	Shapley additive explanations
STAT	Signal transducer and activator of transcription
TBL1XR1	Transducin beta-like 1 X-linked receptor 1
VNN	Visible neural network

ACKNOWLEDGEMENTS

I would like to thank my advisor, Trey Ideker. His enthusiasm for science is contagious and his work ethic is inspiring. But I would especially like to thank him for his mentorship: being patient (most of the time) and somehow always available.

I would like to thank the members of my thesis committee, Vineet Bafna, Melissa Gymrek, Aritro Nath, and Barbara Parker, for their guidance, feedback, and mentorship. I would also like to thank all the mentors and advisors I have worked with over the years, especially Kay Yeung, Benjamin Haibe-Kains, Rob Patro, Carl Kingsford, and Rezaul Chowdhury.

I would like to thank all the past and present members of the lab, with special thanks to Xiaoyu Zhao, Erica Silva, Sungjoon Park, Fan Zheng, Dexter Pratt, Anton Kratz, Mark Kelly, and Chris Churas for their advice, assistance, collaboration, and all our discussions. I would especially like to thank Charlotte Marquez, Patrick Wall, Leah Schaffer, Clara Hu, Ingoo Lee, Nicole Mattson, Jillian Parker, JungHo Kong, and Stephanie Harchenko for their friendship and support.

Chapter 1, in full, is a reformatted reprint of the material as it appears as “The Hallmarks of Predictive Oncology” in Cancer Discovery, 2025 by Singhal, Akshat; Zhao, Xiaoyu; Wall, Patrick; So, Emily; Calderini, Guido; Partin, Alexander; Koussa, Natasha; Vasanthakumari, Priyanka; Narykov, Oleksandr; Zhu, Yitan; Jones, Sara E.; Abbas-Aghababazadeh, Farnoosh; Nair, Sisira Kadambat; Bélisle-Pipon, Jean-Christophe; Jayaram, Athmeya; Parker, Barbara A.; Yeung, Kay T.; Griffiths, Jason I.; Weil, Ryan; Nath, Aritro; Haibe-Kains, Benjamin; Ideker, Trey. The dissertation author was a primary investigator and author of this paper.

Chapter 2, in full, is a reformatted reprint of the material as it appears as “Multiscale community detection in Cytoscape” in PLOS Computational Biology, 2020 by Singhal, Akshat; Cao, Song; Churas, Chris; Pratt, Dexter; Fortunato, Santo; Zheng, Fan; Ideker, Trey. The dissertation author was a primary investigator and author of this paper.

Chapter 3, in full, is a reformatted reprint of the material as it appears as “A deep learning model of tumor cell architecture elucidates response and resistance to CDK4/6 inhibitors” in Nature Cancer, 2024 by Park, Sungjoon; Silva, Erica; Singhal, Akshat; Kelly, Marcus R.; Licon, Kate; Panagiotou, Isabella; Fogg, Catalina; Fong, Samson; Lee, John J. Y.; Zhao, Xiaoyu; Bachelder, Robin; Parker, Barbara A.; Yeung, Kay T.; Ideker, Trey. The dissertation author was a primary investigator and author of this paper.

Chapter 4, in full, is a reformatted reprint of the material as it appears as “Cancer Mutations Converge on a Collection of Protein Assemblies to Predict Resistance to Replication Stress” in Cancer Discovery, 2024 by Zhao, Xiaoyu; Singhal, Akshat; Park, Sungjoon; Kong, JungHo; Bachelder, Robin; Ideker, Trey. The dissertation author was a primary investigator and author of this paper.

Chapter 5 contains unpublished material co-authored with Zhang, Xiaojie; Hassan, Saifa; Gu, Kelly; Yeung, Kay T.; Ideker, Trey. The dissertation author was a primary investigator and author of this chapter.

VITA

EDUCATION

2013 Bachelor of Science, National Institute of Technology Allahabad
Computer Science and Engineering

2018 Master of Science, Stony Brook University
Computer Science

2025 Doctor of Philosophy, University of California San Diego
Computer Science

PUBLICATIONS

Singhal, Akshat; Zhao, Xiaoyu; Wall, Patrick; So, Emily; Calderini, Guido; Partin, Alexander; Koussa, Natasha; Vasanthakumari, Priyanka; Narykov, Oleksandr; Zhu, Yitan; Jones, Sara E.; Abbas-Aghababazadeh, Farnoosh; Nair, Sisira Kadambat; Bélisle-Pipon, Jean-Christophe; Jayaram, Athmeya; Parker, Barbara A.; Yeung, Kay T.; Griffiths, Jason I.; Weil, Ryan; Nath, Aritro; Haibe-Kains, Benjamin; Ideker, Trey. "The hallmarks of predictive oncology." Cancer Discovery 1 February 2025; 15 (2): 271–285.

Singhal, Akshat*; Zhang, Xiaojie*; Hassan, Safia; Gu, Kelly; Yeung, Kay T.; Ideker, Trey. "Real-world analysis of a deep learning model for prediction of palbociclib response in patients with ER+ HER2− advanced breast cancer." (in preparation)

Wang, Xin*; Nguyen, Julia*; Nader, Kristen; Miihkinen, Mitro; Wall, Patrick; **Singhal, Akshat**; Ideker, Trey; Aittokallio, Tero; Haibe-Kains, Benjamin. "Unlocking predictive biomarkers in cancer therapy through computational approaches." Nature Reviews Clinical Oncology. (under review)

Park, Sungjoon*; Silva, Erica*; **Singhal, Akshat***; Kelly, Marcus R.; Licon, Kate; Panagiotou, Isabella; Fogg, Catalina; Fong, Samson; Lee, John J. Y.; Zhao, Xiaoyu; Bachelder, Robin; Parker, Barbara A.; Yeung, Kay T.; Ideker, Trey. "A deep learning model of tumor cell architecture elucidates response and resistance to CDK4/6 inhibitors." Nature Cancer 5, 996–1009 (2024).

Zhao, Xiaoyu*; **Singhal, Akshat***; Park, Sungjoon; Kong, JungHo; Bachelder, Robin; Ideker, Trey. "Cancer mutations converge on a collection of protein assemblies to predict resistance to replication stress." Cancer Discovery 1 March 2024; 14 (3): 508–523.

Bailey, Regan L.; MacFarlane, Amanda J.; Field, Martha S.; Tagkopoulos, Ilias; Baranzini, Sergio E.; Edwards, Kristen M.; Rose, Christopher J.; Schork, Nicholas J.; **Singhal, Akshat**; Wallace, Byron C.; Fisher, Kelly P.; Markakis, Konstantinos; Stover, Patrick J. "Artificial intelligence in food and nutrition evidence: The challenges and opportunities." PNAS Nexus, Volume 3, Issue 12, December 2024, pgae461.

Kong, JungHo; Zhao, Xiaoyu; **Singhal, Akshat**; Park, Sungjoon; Bachelder, Robin; Shen, Jeanne; Zhang, Haiyu; Moon, Jimin; Ahn, Changho; Ock, Chan-Young; Carter, Hannah; Ideker, Trey. “Prediction of immunotherapy response using mutations to cancer protein assemblies.” Science Advance 10,eado9746(2024).

Singhal, Akshat*; Cao, Song*; Churas, Chris*; Pratt, Dexter; Fortunato, Santo; Zheng, Fan; Ideker, Trey. “Multiscale community detection in Cytoscape.” PLOS Computational Biology 16(10): e1008239.

Sauerwald, Natalie; **Singhal, Akshat**; Kingsford, Carl. “Analysis of the structural variability of topologically associated domains as revealed by Hi-C.” NAR Genomics and Bioinformatics, Volume 2, Issue 1, March 2020, lqz008.

*co-first authors

ABSTRACT OF THE DISSERTATION

Methods in Predictive Oncology

by

Akshat Singhal

Doctor of Philosophy in Computer Science

University of California San Diego, 2025

Professor Trey Ideker, Chair

Artificial intelligence (AI) is primed for revolutionizing cancer treatment. Predictive oncology leverages AI to forecast cancer treatment outcomes for each patient using all available information: genetic, molecular, cellular, and clinical. These methods have evolved into powerful tools for understanding the effects of genetic alterations on treatments. However, the integration of predictive oncology models into routine clinical practice faces significant challenges. This dissertation addresses these challenges.

Chapter 1 proposes seven hallmarks for the development, evaluation, and clinical adoption of predictive oncology models. Considerations for each hallmark are discussed, along with an example model scorecard. Subsequent chapters detail several methods that directly address these hallmarks to advance predictive oncology.

Chapter 2 introduces a framework to organize protein-protein interaction networks into hierarchical knowledge maps. These maps are highly effective in gaining insights into biological mechanisms, such as treatment response.

Chapters 3 and 4 present interpretable or “visible” neural networks (VNNs) to predict response to cancer therapies. To elucidate the underlying mechanisms, VNNs incorporate a hierarchical knowledge map of multi-protein assemblies in cancer, which integrates rare and common alterations across hundreds of clinical panel genes. VNNs for palbociclib and cisplatin identify multiple assemblies that accurately stratify patients as responders or non-responders.

Finally, chapter 5 conducts a retrospective evaluation of the palbociclib VNN model to identify patients with durable palbociclib response. Patients with predicted sensitivity to palbociclib had significantly better progression-free survival and overall survival than patients with predicted resistance. Model prediction and biomarker interpretation were integrated to create a personalized report for each patient.

Chapter 1 The hallmarks of predictive oncology

1.1 Abstract

The rapid evolution of machine learning has led to a proliferation of sophisticated models for predicting therapeutic responses in cancer. While many of these show promise in research, standards for clinical evaluation and adoption are lacking. Here, we propose seven hallmarks by which predictive oncology models can be assessed and compared. These are Data Relevance and Actionability, Expressive Architecture, Standardized Benchmarking, Generalizability, Interpretability, Accessibility and Reproducibility, and Fairness. Considerations for each hallmark are discussed along with an example model scorecard. We encourage the broader community, including researchers, clinicians, and regulators, to engage in shaping these guidelines toward a concise set of standards.

1.2 Introduction

Predictive oncology aims to improve cancer treatment outcomes by customizing therapeutic decisions for each patient based on all available information – genetic, molecular, cellular, and clinical[1–3]. This strategy stands in contrast to a conventional one-size-fits-all approach, in which all patients with the same tumor type and stage receive the same standard of care therapy. Current examples of predictive oncology that are well-established in the clinic include BCR-ABL gene fusions in chronic myeloid leukemia, which are targeted by imatinib[4,5]; BRCA gene mutations in ovarian, breast, and other cancers, which are targeted by PARP inhibitors[6–8]; and activating mutations in BRAF in melanoma and non-small cell lung tumors, which are targeted by BRAF or MEK inhibitors[9,10].

While such targeted therapeutics have been transformative, many patients lack the required biomarkers, and those with the right biomarkers may fail to respond[11] or develop resistance[12]. This challenge of distinguishing responders from non-responders extends to non-targeted chemotherapeutics, where standard molecular indications are often lacking despite the

many patients with innate or acquired chemotherapy resistance[13]. For these reasons, the last few years have seen a surge of interest in predictive oncology models that use extensive molecular profiling and machine learning to integrate information from not just one biomarker or gene, but from dozens to thousands[14–16] (Figures 1.1A,B). Modern molecular profiling enables the large-scale identification of genetic mutations and copy number alterations from tumor tissue samples and/or whole blood, profiled for the numerous genes included on clinical cancer gene panels[17,18] or, alternatively, ascertained by whole-exome or whole-genome sequencing in cancer research studies[19–21]. Molecular profiling may also include omics layers such as DNA methylation, mRNA expression, or protein abundance and phosphorylation. These data have enabled greatly expanded precision oncology models that consider modulators of drug response not only in the targeted mechanism(s), but also in proteins that physically or functionally interact with the target in related molecular pathways. A growing number of multi-genic models have been commercialized[22–28], some of which, such as MammaPrint[22], OncoTypeDX[23], and microsatellite instability (MSI)[24,25] are in active clinical use.

Despite this progress, the vast majority of advanced predictive oncology models have not yet achieved widespread clinical impact[29,30], for several reasons. One key challenge lies in generalizability; models trained on preclinical datasets often fail to translate to patient data. This limitation primarily arises from limited access to data and disparities between preclinical training and real-world contexts, compounded by the heterogeneity of patient populations and the dynamic nature of disease status. Another major challenge relates to model transparency and interpretability – the ability to scrutinize the inner workings of a model and explain the biomolecular factors that underlie each of its predictions. The lack of model interpretation has been recognized as one of the most important barriers to building trustworthy AI systems in high-stakes clinical applications[31]. In addition to challenges in model development, the successful clinical application of predictive oncology models also faces infrastructure and regulatory hurdles. The financial, computational, and regulatory resources needed to run both retrospective and prospective studies

are rarely available outside major biomedical research campuses, especially in low-income regions. Such issues are exacerbated by the absence of a standardized predictive modeling "checklist", such as the highly useful guidelines that have been developed for vetting prognostic biomarkers [32] or reporting clinical trials[33]. These challenges, among others, highlight the need for a set of structured recommendations for model development, which clearly enumerate the methodological and clinical utility risks.

To gather a comprehensive perspective on these fundamental challenges, we engaged the community through a series of workshops involving a broad panel of cancer biologists, clinicians, ethicists, and machine learning specialists (including all of the authors on this Review). A major outcome of these meetings was to formulate key characteristics, or "modeling hallmarks", which all predictive oncology models should strive to address (Figure 1.2). The resulting recommended hallmarks are: 1) Data Relevance and Actionability, ensuring the model's input is both pertinent and actionable; 2) Expressive Architecture, denoting the model's ability to capture complex biological interactions; 3) Standardized Benchmarking, for consistent model evaluation; 4) Demonstrated Generalizability, to ensure model performance across diverse settings; 5) Mechanistic Interpretability, for understanding the biological basis of model predictions; 6) Accessibility and Reproducibility, guaranteeing user-friendly model use; and 7) Fairness, to promote equitable model application across different patient demographics and resource-constrained communities. In addition, we considered the ethical principles that apply to each of the seven hallmarks and are important to maximize the societal benefits of therapy response models. Notably, these hallmarks are not meant to replace, but to complement, the more general established guidelines in the fields of AI and clinical practice including considerations of security, privacy, or energy[34,35] (arXiv:2104.10350). In what follows, we describe each hallmark and its implications for best practices in model research, development, and ultimate deployment.

1.3 Hallmark 1: Data Relevance and Actionability

Data *relevance* refers to how closely the data used to train and evaluate a model conforms to the intended clinical settings, i.e., predicting patient responses to therapy and related clinical outcome(s) of interest. In contrast, data *actionability* refers to the practical utility of the model inputs in influencing treatment decisions, i.e., whether the acquisition of that type of data facilitates meaningful interventions to improve patient outcomes.

Data relevant to training predictive oncology models have typically been derived from one of several sources. To provide large numbers of samples for training, a major avenue has been high-throughput drug response screens conducted in preclinical cancer models such as immortalized cancer cell lines[21,36–42], patient-derived tumor cells (PDTC)[43–45], patient-derived organoids (PDO)[46–48], and patient-derived xenografts in mice (PDX)[49,50]. Similar drug response datasets gathered in the clinic, such as those provided by clinical trials[51–56] and large clinical research consortia[19,20,57], currently have fewer samples than are provided by high-throughput screens in tumor models but nonetheless are rapidly growing to sizes useful either for validation or direct model training. With this landscape in mind, clinical relevance increases progressively as one moves from data collected in 2D cell cultures to 3D organoid or sphere-culture systems to patient xenografts and (ultimately) to patients, while scalability and data completeness decrease. Cell cultures have the advantage of scalability and cost-effectiveness but do not recapitulate the tumor microenvironment, and they are susceptible to genetic drift[58,59], limiting their translational accuracy in predicting clinical outcomes[60]. PDO and PDX attempt to mitigate these issues in several ways: first, by using cancer cells derived from primary patient tumors rather than from immortalized lines[61–63], and second, by co-culture of tumor cells with various other cell types to mimic aspects of the tumor microenvironment. Relative to cell lines, such additional features come at the expense of lower screening throughput and higher cost[64]. On the other hand, training predictive models based on PDO and PDX platforms is potentially more scalable than using patient data directly; while inherently relevant, the collection of patient data faces practical

challenges such as the lengthy and resource-intensive process of clinical data acquisition and management, the impossibility of screening a wide range of drugs per tumor, and the additional complexities introduced by patient heterogeneity and evolving health status[65].

In terms of data *actionability*, the data types most often used in predictive modeling include molecular profiles, such as the genome, epigenome, transcriptome, proteome, and metabolome[16,66], as well as histology images[67] and radiomics[68,69]. Among these types, genetic alteration profiles are commonly used in predictive oncology models[16] and are also available clinically via cancer gene panels[17,18], making them highly actionable. Other 'omics profiles are considerably less common in both pre-clinical and clinical datasets and thus have limited actionability. Actionability is an evolving concept, however, as new data types emerge with interest in clinical use. For example, circulating tumor DNA has become a promising clinical data modality based on its ease of measurement from blood over successive follow-up visits, allowing longitudinal tracking of therapy resistance[70,71]. Another issue concerning data actionability relates to standardization. For example, a common practice is to normalize mRNA or protein levels so that all tumor samples have the same mean and standard deviation (z-scoring). These models do not easily work for an isolated sample, making them less clinically actionable. Overall, data across different modalities and sources requires careful preprocessing to harmonize measurements and avoid data leakage between the data used to train and test the models.

1.3.1: Ethical Considerations for Data Relevance and Actionability

Collecting and sharing data derived from patients and tumor materials is not a trivial task, as it involves protecting patient privacy and must be done responsibly[35]. If data can be de-identified with minimal risk of re-identification, the resulting data can be shared publicly through a data access committee or a binding data usage agreement.

1.4 Hallmark 2: Expressive Architecture

The *architecture* of a computational model refers to the structural layout of its components. It is a key consideration, as model architecture strongly governs the ability to integrate and extract information from input data to make predictions. In this context, architectural *expressivity* can be defined as the number and types of unique functions or patterns an architecture can capture (arXiv:1611.03530v2, arXiv:1606.05336v6). For example, deep neural networks tend to be highly expressive because successive layers within the network describe increasingly complex non-linear patterns as information moves from one layer to the next[72]. The number and size of these neural network layers can make the model more or less expressive[73]. Since the number of factors regulating therapy response can range from individual genetic mutations to multi-genic pathways to complex medical imaging[74–76], it is likely that predictive oncology models will ultimately require highly expressive architectures.

Expressivity affects how closely a model fits the training data, in a sliding scale referred to as the *bias-variance tradeoff*[77]. Insufficiently expressive architectures tend to learn marginal associations between input features and outcomes with few interacting combinations of features, and thus only "loosely" fit the data. The resulting models have high bias, as predictions are insufficiently sensitive to the feature values of individual patients. Such models perform relatively poorly on both training and test data. Conversely, overly expressive models make predictions that closely follow the training data, leading to a high variance of predictions across patients and therapies. These models perform well on the training data but not when analyzing new "out-of-distribution" datasets. Given that most big biomedical datasets contain many irrelevant features unlikely to reappear in future samples, it is important to ensure that a complex model architecture does not create undue dependencies on spurious features at the expense of identifying predictive underlying relationships. Such high-variance models are overfit to the training data, whereas high-bias models, which do not fully capture the patterns present in the training data, are underfit. A major goal of model development is therefore to balance these opposing forces, selecting a "best-

fit" architecture sufficiently expressive to model complex input patterns but simple enough to keep the model generalizable[78].

Open-source libraries like PyTorch, TensorFlow, and Scikit-Learn provide access to a wide range of learning algorithms, making it relatively easy to create models with highly expressive architectures. This situation thus enables model developers to select a highly complex architecture by default. However, given the bias-variance tradeoff mentioned above, complex models are especially susceptible to overfitting. In considering architectural choices, a useful guideline is the principle of parsimony or "Occam's Razor", i.e. seeking predictive oncology models that are as simple as possible but as complex as necessary. Developing the simplest model that achieves adequate performance may be more favorable in terms of generalizability (Hallmark 4) and interpretability (Hallmark 5), facilitating clinical translation. Techniques such as meta-learning[79], inductive bias[80,81], regularization[82,83], pruning[84], and feature selection are all of interest in building parsimonious architectures. When trade-offs between simple and complex models are unclear, a practical approach may be to present results from different architectures in a transparent and unbiased manner.

1.4.1: Ethical Considerations for Expressive Architecture

Complex architectures often require larger computational resources, which may have a substantial ecological footprint and may not be readily available to a broad user base. Down-sized models can democratize their accessibility[85] (arXiv:2301.07014v3) and minimize the environmental impact[86] (arXiv:2104.10350).

1.5 Hallmark 3: Standardized Benchmarking

Evaluating a predictive oncology model nearly always involves *benchmarking*, that is, the comparison of model performance against baseline models. However, the surge of published predictive oncology methods and the lack of agreed-upon benchmarking protocols within the community have made it challenging to carry out comparisons among the many available models[16]. Currently, bespoke performance evaluations are devised for each new modeling publication, typically invoking simple baselines, varied compositions of datasets, inconsistent data splits, arbitrary scoring metrics, and with varying protocols for hyperparameter optimization (or none at all).

To enable rigorous comparative analysis of model strengths, weaknesses, and key factors contributing to predictive performance, it is crucial for the community to adopt standard procedures of evaluation against reference baseline models (i.e. against which future models should be evaluated). Three types of baseline models are typically seen in predictive modeling applications[16]. A first straightforward option is to use standard out-of-the-box models from open-source libraries. In this case, priority should be given to libraries known for their training efficiency and accurate predictions. For example, regularized linear regression[83] and boosting algorithms[87] have been often (but not always) used for benchmarking in predictive oncology publications[76,88,89], and these might constitute a starting standard. Here the complexities of the chosen baseline models may be progressively increased to justify the need for a proposed model. A second option is ablation analysis, which can be performed at the level of the model or data. Model ablation involves substituting model attributes with simpler alternatives (e.g., replacing convolutional layers with dense layers)[90–92], while data ablation can involve removing proposed data representations or replacing them with more conventional ones (e.g., replacing molecular graph structures representing drug compounds with Morgan fingerprints)[93,94]. Regardless, conducting ablation studies that systematically analyze the progressive removal or addition of complexity is essential. Lastly, a new model can be compared with other complex state-of-the-art models that

have been recently released by the scientific community. While this option is perhaps the most laborious, benchmarking performance against advanced community models boosts credibility and opens important connections to ongoing complementary efforts in the field.

Another key consideration for developing standard benchmarks relates to the datasets used for model training, validation, and testing. Cross-validation is often used in the development of predictive oncology models to ensure these models have the ability to make accurate predictions on previously unseen data[95]. To achieve standardized benchmarking across a broad collection of models, however, all of these models should be trained and evaluated on the same cross-validation dataset(s). If these specific datasets are not available, models should be evaluated on other, better-established benchmarking datasets that are open to the community.

A final standard to consider relates to the evaluation of model accuracy, where the ideal approach is to evaluate and present multiple performance metrics. For example, correlation and mean squared error might be used for evaluating regression models; AUPRC and odds ratio might be used for evaluating binary classification models; and hazard ratio and concordance index might be used for scoring survival analysis. Furthermore, providing complete information on true and predicted outcomes for each tumor drug response, for example in a supplemental table, is necessary to enable other investigators to evaluate model performance with their methods of choice. Multiple metrics paint a fuller picture of a model, especially when outcome labels are imbalanced (e.g., if drug-resistant outcomes are far more frequent than drug-responsive ones).

1.5.1: Ethical Considerations for Standardized Benchmarking

Rigorously evaluating model performance using robust benchmarks and assessing added value compared to baseline and state-of-the-art models can justify future investment and increase the likelihood of clinical benefit. Additionally, whenever possible, model performance from both training and test data should be presented, including true labels and predictions of individual samples.

1.6 Hallmark 4: Demonstrated Generalizability

Translating predictive oncology models into clinical practice poses a variety of challenges, reflecting the complexity of models as well as the stringent standards required for clinical application. The challenge of *generalizability* in predictive oncology revolves around the ability of models to perform accurately and reliably across different application scenarios, sites of care, clinical workflows, patient populations, or data distributions that may not have been part of the initial training data. Other problems with generalizability may arise if a new group fails to implement the model correctly due to insufficient documentation (see Hallmark 6).

Predictive models can fail to generalize for at least two reasons:

Disparity between preclinical and clinical contexts: A model trained from preclinical drug response data (e.g. tumor cell lines, PDX, PDO) may fail to translate to clinical predictions in specific patient contexts. For example, models trained on preclinical drug screens are designed to predict change in cell fitness given a particular drug treatment[16]. However, the intended clinical application may require predicting a patient's overall or recurrence-free survival, or estimating other measurements included in clinical guidelines, e.g., RECIST response rate (Response Evaluation Criteria in Solid Tumors)[96]. Disparities may also occur when a subset of input features are not present in the patient data or when they are measured differently due to batch effects or the use of different technologies, requiring data harmonization to ensure efficient application of the predictive oncology models.

Heterogeneity in patient populations: Extensive biological differences across patient populations such as age, sex, race or ethnicity, and genetic background are inherently difficult to generalize. A model trained on one population may not perform well when applied to a population with differing characteristics. Such problems are exacerbated by "drift in procedures" [97], whereby clinical practices evolve or the composition of the target population changes, leading to batch effects and degradation in model performance.

Strategies to ensure generalizability of predictive oncology models, and maximize the likelihood of successful clinical translation, are as follows. First, models should be rigorously assessed using external datasets that best reflect the intended clinical application. This assessment ensures that models can make sensible predictions for previously unseen patient data. Second, models should be continually tested against clinical confounders, including age, sex, and ethnicity. Ideally, the assessment should be conducted on a cancer-specific, representative cross-section of patients[98] selected under the same standards as for clinical trials, verifying that demographic and clinical distributions of selected test sets match those observed in practice (arXiv:2001.09765). Evaluating the model from this perspective is closely related to fairness (Hallmark 7). Third, techniques such as domain adaptation and transfer learning[90] can bridge the gap between *in-vitro* and *in-vivo* data[99,100] while ascertaining a model's robustness. Finally, generalizability can be evaluated on retrospective data, but ultimately a prospective clinical study is needed to validate the real-world utility of a model.

1.6.1: Ethical Considerations for Demonstrated Generalizability

A valuable exercise is to evaluate a predictive oncology model on diverse settings within its intended scope. For instance, does a model trained on adult tumors accurately predict response to pediatric tumors? Is a model trained predominantly using data from one ethnicity applicable to make drug response predictions in a new ethnically diverse population? Reporting such outcomes define the extent of the model's generalizability and can help clinicians make informed decisions.

1.7 Hallmark 5: Mechanistic Interpretability

The concept of model *interpretability* refers to the ability to understand the inner workings of a model and the logic by which it uses input features to make predictions. In the context of predictive oncology, interpretable models elucidate the underlying biological factors leading to this response, such as genetic mutations, drug mechanisms of action, and molecular pathways relevant to cancer. Such interpretation is often accomplished by the use of a clear and simple

model structure, such as that provided by decision trees[87,101] or linear regression models[83]. In contrast, complex models such as neural networks tend to be more difficult to interpret, creating some degree of tension between this hallmark (Mechanistic Interpretability) and Hallmark 2 (Expressive Architecture). Nonetheless, a range of complex interpretable models have been recently developed by integrating prior biological knowledge, such as defined molecular pathways or tissue types, directly into the input data or the internal architecture of the model[74–76,102–106].

A closely related concept to interpretability is model *explainability*, which aims to provide meaningful justifications for a model's decisions by highlighting the most influential features or factors considered by the model for that specific instance. Explainability is typically implemented using post-hoc analysis algorithms such as SHAP, LIME, and DeepLIFT, among others[107] (arXiv:1705.07874v2, arXiv:1704.02685v2, arXiv:1610.02391v4).

Understanding the reasons why a model predicts specific treatment outcomes promotes trust by all parties involved, including patients, healthcare providers, and regulatory bodies[108,109]. After all, cancer clinicians and biomedical scientists must routinely explain to each other the reasons behind their opinions, and such discussion can inform therapy selection and is a cornerstone of continued scientific progress. Should a predictive model be held any less accountable? On the other hand, model interpretability need not be a strict requirement provided strong trust has already been established. In this respect, we see two acceptable scenarios. The first scenario is a fully interpretable model which is able to explain its predictions by prediction rules that are in line with medical evidence or can be verified experimentally. The second scenario is a model that is not readily interpretable but has a significant track record of accuracy, robustness, and generalizability.

Beyond trust, the ability to readily interpret model decisions facilitates numerous aspects of predictive oncology. Examining the inner workings of a model can help detect biases, batch effects, errors in data collection or processing, and spurious features[110–112]. Insights into feature relevance can improve model performance by highlighting which features should be included or

excluded. Identifying relevant tumor features is also crucial to ensure that the most informative clinical data are available (Hallmark 1). Lastly, by fully understanding the limitations of the model, one can work to ensure that models are equally accurate across all populations (Hallmark 7).

1.7.1: Ethical Considerations for Mechanistic Interpretability

A mechanistically interpretable model lends important insight into the treatment choice recommended to the patient. Even if the complexity of the information precludes complete comprehension by the physician or patient, providing an explanation adds legitimacy to the model's prediction. Equally important, an interpretable model facilitates further research into the molecular pathways involved in response and resistance.

1.8 Hallmark 6: Accessibility and Reproducibility

Given the complexity of developing a therapeutic response model, access to the model and its key components is necessary to ensure reproducibility, critical evaluation, and wide adoption. Here, *accessibility* refers to the availability of all materials related to a model of interest, including the data required to train and validate the model, the computer code, and the fully specified model itself including architecture, weights, parameters, and detailed documentation describing the model inputs and outputs. *Reproducibility* refers to the faithful recapitulation of published model results, including the full software environment and computational resources that implement the model software and train/test/validation datasets[113] (arXiv:2012.09932).

This hallmark is closely related to the so-called "FAIR" principles – Findability, Accessibility, Interoperability, and Reusability[114]. To address the imperative of findability, training data and relevant fitted models should be easily discoverable across diverse use cases, employing standardized metadata and data formats (e.g., using programmatic pre-defined data structures or saved checkpoint states of data structures and trained models in PyTorch). Accessibility is achieved through the availability of original frameworks and components, adopting open-source practices, and ensuring the configuration of the correct software environment.

Interoperability is fostered by the use of common data types, standardized formats for model inputs (features) and outputs (predictions), and centralized repositories that facilitate exchange of models[115,116], data, and metadata[117]. Reusability is heightened through configurations ready for execution, open-source model practices, and adherence to standardized protocols. When these principles are put into action, models can be reproduced and reused “out of the box”, and their results can be understood as they relate to model development[118,119].

Without such considerations, models can become too complex to reproduce and reuse, with the consequence that they may not be considered for future endeavors even if preliminary results are promising. Managing model complexity involves promoting transparency (through detailed documentation of model structure and parameters) coupled with open science practices. In turn, lack of reproducibility can be partially mitigated by comprehensive documentation, and limitations in computational infrastructure can be alleviated by embracing standardized data formats, open-source methodologies, and efficient training pipelines. In these respects, open-source training frameworks and execution methods are ideal for minimizing issues encountered during testing and reuse. Nonetheless, there are many published models that do not share data, computer code, or fitted models, calling for more transparency in AI research[119]. Even when the original authors fully adhere to FAIR principles during model development, issues can arise as future investigators attempt to execute the model. Indications and limitations of published models should be clearly documented to ensure the model is used as intended.

1.8.1: Ethical Considerations for Accessibility and Reproducibility

A fully specified predictive oncology model must be shared responsibly. Especially when it is trained or fine-tuned on clinical data, model sharing should not disclose private information from the original patient datasets. This issue can be prevented by enforcing differential privacy during model training or establishing a proper sharing mechanism (as is routinely done for sharing the data themselves) (arXiv:1412.7584). Regardless, access to the datasets used to train a model is

highly preferred. Without knowledge of the training data, the only way to reliably assess a model is to carry out a prospective study, since any retrospective study could unwittingly include datasets used for training.

1.9 Hallmark 7: Fairness

Fairness is an oft neglected aspect of predictive oncology models and other medical technologies. In the growing literature on AI ethics[120,121], fairness is described in terms of parity, i.e., ensuring the model is beneficial to diverse patient populations. A first step is to characterize patient populations by the attributes for which equity is a key concern. Attributes of interest include, but are not limited to, race/ethnicity; sex; age; social determinants of health (SDH) such as levels of education and income[122]; and relevant codes defined in the International Classification of Diseases (ICD)[123,124].

Because some of these patient attributes do not currently have sufficient coverage in the available cancer treatment data, therapy response models risk being unfair to the corresponding patient populations. BRAF mutations, for example, were first identified in melanoma patients of Caucasian descent leading to the development of BRAF inhibitors like vemurafenib[10,125]. The prevalence of these mutations has turned out to be lower in other ethnic groups, potentially influencing treatment strategies[126,127]. On the other hand, the essence of precision medicine is to tailor predictive models to specific individuals and subpopulations. To balance personalized recommendations with fairness to all patients, we should encourage the continual development of models relevant to underrepresented individuals such as those who have rare cancers, live in less developed countries and regions, or come from minority ethnic backgrounds. Collecting such representative data should be an early step in the development of precision oncology models, whether these models are intended to be universal or specialized (Figure 1.3A). For models developed from preclinical data such as immortalized cancer cell lines, attention should be paid to the biases that exist in the current portfolio of preclinical models[128,129].

Regardless of whether a model has been fairly balanced during training, a subsequent step is to perform rigorous “fair-aware” model validation and testing. The goal is to identify potential predictive bias within particular patient populations, which can prompt further model optimization in an attempt to explicitly rectify the model to reduce or eliminate such bias (Figure 1.3B). For models with high mechanistic interpretability (Hallmark 5), the model can also be analyzed to reveal whether particular patient populations are associated with distinct molecular or cellular pathways used to make accurate predictions (Figure 1.3C). Such pathway interpretations may be very helpful in illuminating key differences by which different race/SDH/ICD groups respond to a therapy.

Performance in machine learning is typically assessed by the four types of predictive outcomes – true positives, true negatives, false positives, and false negatives. Different combinations of these outcomes can result in different definitions of fairness[130]. For instance, if a model mistakenly predicts a positive response to a drug for a particular population (false positive), and that drug has adverse health consequences, then the cost of a false positive prediction is high and one should consider more stringent model prediction thresholds. This design decision might be made even at the expense of increasing false negatives for that or another subpopulation. On the other hand, if the health consequences and opportunity costs of a drug are modest, then one might afford a more ambitious approach that maximizes true positives instead. One also has to consider inter-population trade-offs. If augmenting fairness can only be achieved by sacrificing accuracy for the largest population, then one may be forced to choose between prioritizing accuracy versus parity for less represented populations. There is no easy formula for optimizing accuracy/fairness trade-offs, although different moral theories[131,132] such as prioritarianism[133] may favor some choices over others. Ultimately, model developers should make design choices in consultation with clinicians, ethicists, and, ideally, with feedback from the various patient populations that will be affected (Figure 1.3D).

1.9.1: Ethical Considerations for Fairness

Beyond the above considerations, models can promote fairness through a variety of approaches to reduce health disparities. For example, predictive oncology models can focus attention on conditions that disproportionately affect underserved groups. Alternatively, developers can prioritize modeling of drugs that are highly accessible and affordable, as opposed to the many drugs that are unaffordable by underserved populations.

1.10 Invoking the hallmarks: A practical example

To explore how these seven hallmarks might be implemented practically, we considered a particular precision oncology model known as TCRP (Translation of Cellular Response Prediction). TCRP was originally published by Ma et al.[134] and independently evaluated in a reusability report by So et al.[135], both of which involved present authors of this Perspective (Figure 1.4A). This model uses techniques from transfer learning, specifically few-shot learning, to promote the construction of predictive models poised to readily generalize to new contexts, for example to new patient populations, patient-derived xenografts or tumor cells. To assess this model against each of the defined hallmarks, we implemented a general hallmarks checklist (HARMONY, Table 1.1) along with a scoring criterion on a scale of 5 to 0, where 5 indicates the highest alignment with the hallmark, and 0 signifies the lowest, as follows:

5: Model implements the hallmark with no identifiable limitations.

4: Model implements the hallmark with very few limitations.

3: Model implements the hallmark with several major limitations.

2: Model implements the hallmark but fails the evaluation.

1: Model has the necessary foundation but does not implement the hallmark.

0: Model does not consider the hallmark at all, or claims to incorporate it with no available foundation (such as a codebase) for evaluation.

Below, we score the TCRP model against each hallmark and discuss its relative strengths and weaknesses (Figure 1.4B).

Hallmark 1. Data relevance and actionability [Score = 5]. The datasets used to construct TCRP are accessible via public repositories[38,43,49,136]. The model was trained to predict tumor cellular response to drugs, based on dose-response curves also available in the same repositories. Two data types, somatic mutations, and mRNA expression profiles were used as input. At least one of the data types is mandatory for the model to run inference on a new tumor sample, with the presence of both mutation and expression data enabling better performance. For incorporating clinically relevant and actionable data types, we give it a score of 5.

Hallmark 2. Expressive architecture [Score = 4]. The few-shot deep learning algorithm used in TCRP allows a model pre-trained on one set of tumor samples to be fine-tuned on a small number of examples from a new context (e.g. new tumor type). By using a deep neural network architecture, TCRP has the ability to capture both linear and non-linear relationships between input features and drug responses, while allowing developers to tune the overall complexity of the model (by adjusting the number of hidden layers for instance). However, optimization of the model hyperparameters is computationally intensive and may have a strong impact on its performance and translational capabilities. For its “fit-for-purpose” but computationally demanding architecture, we assign it a score of 4.

Hallmark 3. Standardized benchmarking [Score = 3]. The predictive performance of the TCRP model was benchmarked using multiple independent preclinical datasets, covering tumor cell lines, PDTC, and PDX models. This variety of contexts was selected with the intent of showing the model’s flexibility and robustness. Pearson correlation between predicted and actual drug responses was used to quantify performance, which has been frequently used as a standard metric in preclinical biomarker discovery[137]. Using this metric, TCRP was benchmarked against a panel of standard statistical and machine learning strategies, including regularized linear regression, random forests, and a simplified (1-layer) artificial neural network. Although these

models represent a good baseline, they did not include some state-of-the-art drug response models such as MERIDA[138], ENLIGHT[139], logic models[106,140], and OncoTreat/OncoTarget[28]. We thus give TCRP a score of 3 for its good, but still incomplete, benchmarking.

Hallmark 4. Demonstrated generalizability [Score = 3]. The goal of the few-shot learning framework is to increase model generalization, resulting in superior performance than other benchmarks in transfer across domains including new tumor cell lines, patient-derived xenografts, and clinical data from cancer patients. The original TCRP publication trained on drug responses in tumor cell lines and validated on PDTC and PDX datasets[134] was extended to two patient clinical trial datasets in the reusability report[135]. Notably, TCRP outputs a drug response as an "Area Under Dose Response Curve", since this was the unit of measurement in the tumor cell-line training data. In contrast, clinical drug response outcomes are measured by RECIST criteria, progression-free survival, or overall survival. As the TCRP framework does not provide any explicit method or algorithm to translate its predictions to clinical units, ad-hoc procedures had to be used[135]. Additionally, implementing the few-shot algorithm in a prospective clinical trial can be difficult, as some clinical data must be used to fine-tune the model, potentially preventing the first patients enrolled in the trial from benefiting from the model's prediction. For its good performance but limited evaluation in clinical trials and an incomplete end-to-end pipeline for clinical application, we give it a score of 3.

Hallmark 5. Mechanistic interpretability [Score = 3]. The TCRP architecture is a deep neural network optimized for predictive performance. The model architecture did not facilitate interpretation. However, LIME[107] was used to explain important predictive features for both mutation and expression data types. Although, in the future, TCRP can be adapted to leverage model architectural designs that prioritize biological interpretability[75,76], at present we give it a score of 3.

Hallmark 6. Accessibility and reproducibility [Score = 5]. From a computational standpoint, the TCRP framework is implemented with a compact and concise file setup, with

easily accessible methods and processes. The training and testing modules can be debugged or modified easily, and the results from the TCRP framework can be interpreted by raw prediction values or benchmark correlation metrics. The entire codebase was released by the original authors, along with the data designed to reproduce the results from the original paper. However, the reusability report found inconsistency in hyperparameter configuration and training reference files. Consequently, So et al.[135] made improvements to the documentation and codebase and created a fully specified software environment hosted on Code Ocean [https://codeocean.com/capsule/8411716/tree/v2]. This more recent release increases the reusability and accessibility of TCRP and, as a result, we assign a score of 5.

Hallmark 7. Fairness [Score = 0]. TCRP was not originally designed or assessed with attention to principles of fairness. Clinical confounding factors such as age, sex, and race or ethnicity were not reported for training and validation datasets. Model predictions did not have bias or uncertainty measures. These shortcomings are frequent limitations of predictive modeling methods; regardless, it is imperative to ensure that the clinical deployment of these models benefits the larger population of patients, and that their indications and limitations are clearly considered and discussed. We assign TCRP a score of 0 for no explicit efforts in this category.

1.11 Discussion

Here, we have covered a set of seven hallmarks to serve as guidelines for the predictive modeling field, covering Data Relevance and Actionability, Expressive Architecture, Standardized Benchmarking, Demonstrated Generalizability, Mechanistic Interpretability, Accessibility and Reproducibility, and Fairness. Notably, these hallmarks are not intended as prescriptive, detailed instructions for building models: such particular implementation details are in fact expected to evolve rapidly, as they did even in the course of writing this article. Rather, the hallmarks are intended to capture fundamental, complementary concepts that are likely to remain relevant for

many generations of model / biomarker development along the foreseeable trajectory of precision oncology.

With this article as the first step, we have aimed to establish the hallmarks to lay the foundation for reaching consensus and standards within the relevant research and clinical communities. Once the hallmarks have been established, a valuable direction, for instance, would be to apply the scoring criteria to rate the broad collection of contemporary models. The scientific community would identify a panel of reviewers based on the intended scope of the model, with expertise in machine learning, medicine, or biology. Model scores from the reviewer panel could be calibrated by converting them to percentile ranks, or by using scores to cluster models into a small number of categories with similar hallmark characteristics. Such a platform would enable the scientific community to better assess the state-of-the-art and identify gaps, and accordingly, make recommendations.

Several hallmarks might be addressed in large part by following relevant best practices that have gained maturity in other fields of research. For example, Hallmarks 3 (Standardized Benchmarking) and 6 (Accessibility and Reproducibility) are at least partially addressed by following common practices developed in software engineering over the past several decades. Software best-practice examples include Open-Source licensing, which facilitates the use, modification, and distribution of models in ways that proprietary licenses do not; unit testing, which detects and corrects errors early in the development cycle using both manual and automated approaches; and clear user interface, application programming interface, and code documentation, which facilitates adoption by new users and developers.

As of this writing, the potential of AI to impact numerous fields has been widely recognized, but the ultimate ramifications and implications are still very much evolving. We expect the field will continue to progress rapidly, creating and coping with problems as they arise rather than waiting for regulatory guidelines to be implemented or governing bodies to take action. To this point, the AI-directed legislation currently under consideration around the world[108,109,141] advances

rather cautiously in comparison to the pace that new models and capabilities are being developed. Especially as relates to model transparency and interpretability (Hallmarks 5 and 6), steps toward regulatory compliance will help to foster trust among users of predictive oncology models. While these regulatory requirements are still under development, AI developers must nonetheless spearhead guidelines for model transparency (such as the HARMONY checklist, Table 1.1) and collaborate with stakeholders with diverse levels of AI literacy to improve transparency in terms they understand[142]. Beyond initial regulatory requirements, deploying models in the electronic health record system requires close collaboration with the Information Technology (IT) teams and staff at the healthcare centers, with notable concerns for the care staff such as alert fatigue, lack of training, and increased workload[143]. In addition, it is crucial to continuously monitor the performance of the deployed models across the whole patient population to account for changes in profiling technologies and the baseline characteristics of the patients[144,145] (arXiv:2305.02474). By working with stakeholders such as healthcare providers, IT teams, and regulators, AI developers can help mitigate these challenges and perceived risks[146] and potentially increase the adoption of models in a clinical setting.

Finally, we would be remiss to not also mention the impact of AI technologies on society more broadly. AI is a swiftly developing field, and we expect that the predictive oncology hallmarks developed herein can serve as a springboard for evolving discussions in responsible AI moving forward. By suggesting these standards and principles, we hope that the broader community, not just model developers but regulators, clinicians, and lawmakers will help refine and amend them to allow for a broad positive impact of predictive oncology and allied efforts. We call on these communities to be active participants in the discussion and to ensure that the discourse moves the field forward to realize the promise of technologies like AI for patient care.

1.12 Figures

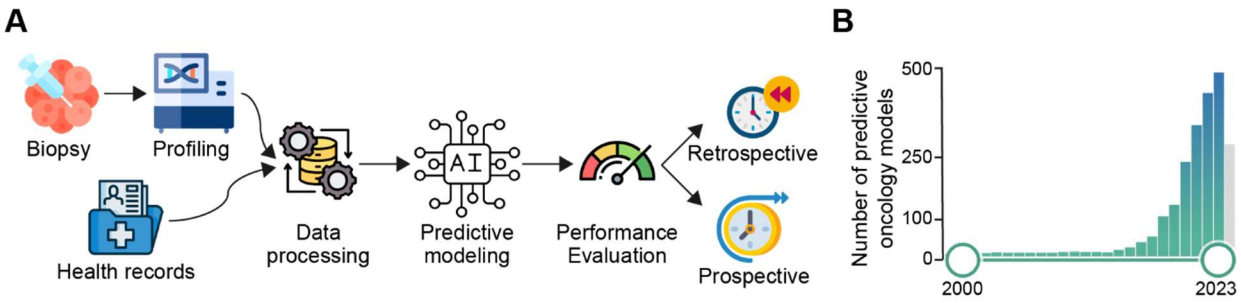

Figure 1.1: Predictive modeling workflow and development timeline.

A, High-level schematic of the standard pipeline for formulating a modern predictive oncology model. **B**, Approximate number of predictive oncology models published per year over the time period 2000 - 2023. PubMed query using search string ‘predictive oncology AND ("machine learning" OR "artificial intelligence")’ with filter: ‘from 2000 - 2023’.

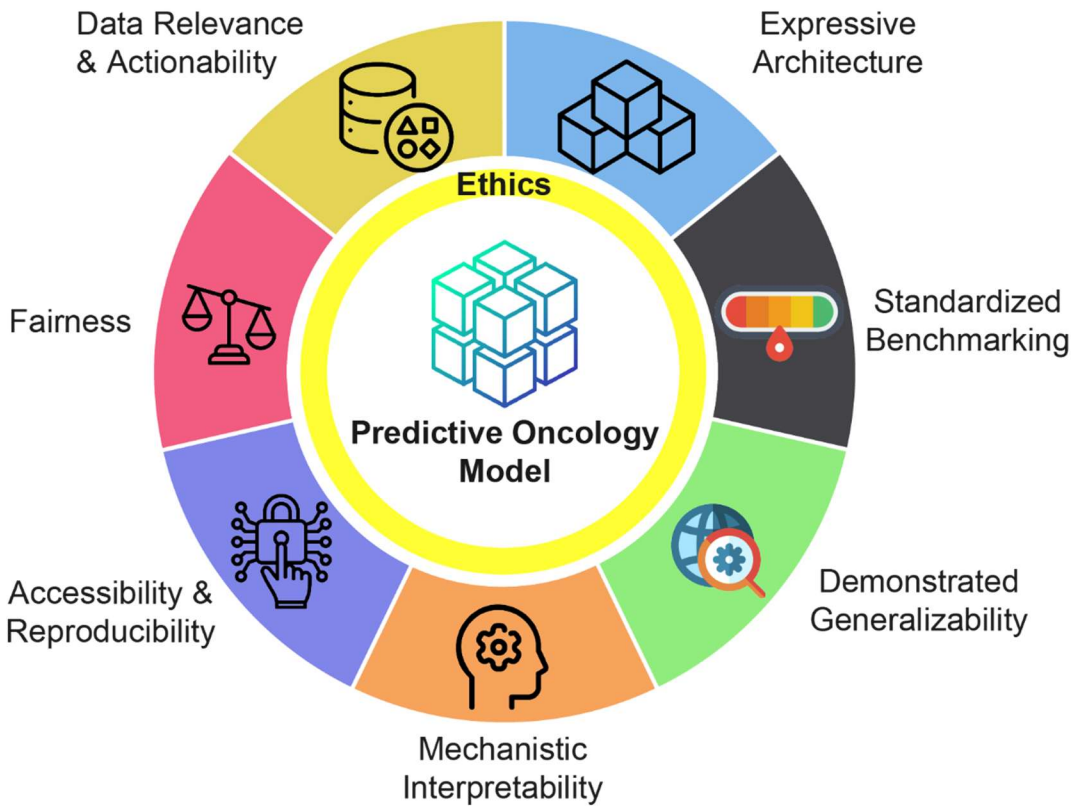

Figure 1.2: The seven hallmarks of predictive oncology.

Starting from the top left, in clockwise order the proposed hallmarks are: Data Relevance and Actionability (yellow), Expressive Architecture (blue), Standardized Benchmarking (black), Demonstrated Generalizability (green), Mechanistic Interpretability (orange), Accessibility and Reproducibility (purple) and Fairness (pink), with Ethics underlying each of these hallmarks (yellow ring).

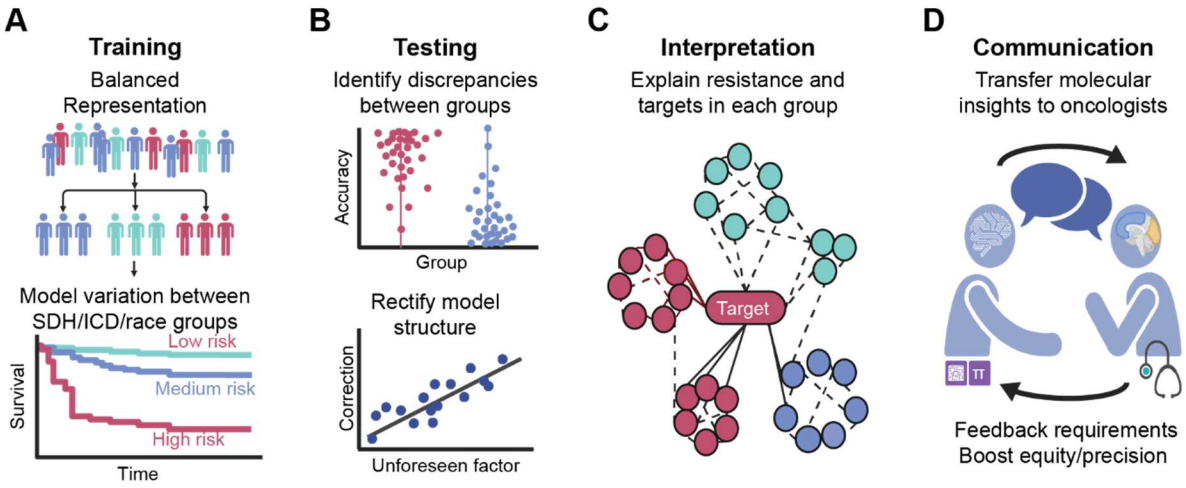

Figure 1.3: Framework for ensuring fairness of a predictive oncology model.

From left to right are depicted four key aspects of fairness, related to **A,** training, **B,** testing, **C,** interpretation, and **D,** communication. SDH, Social Determinants of Health; ICD, International Classification of Diseases. Created in BioRender.

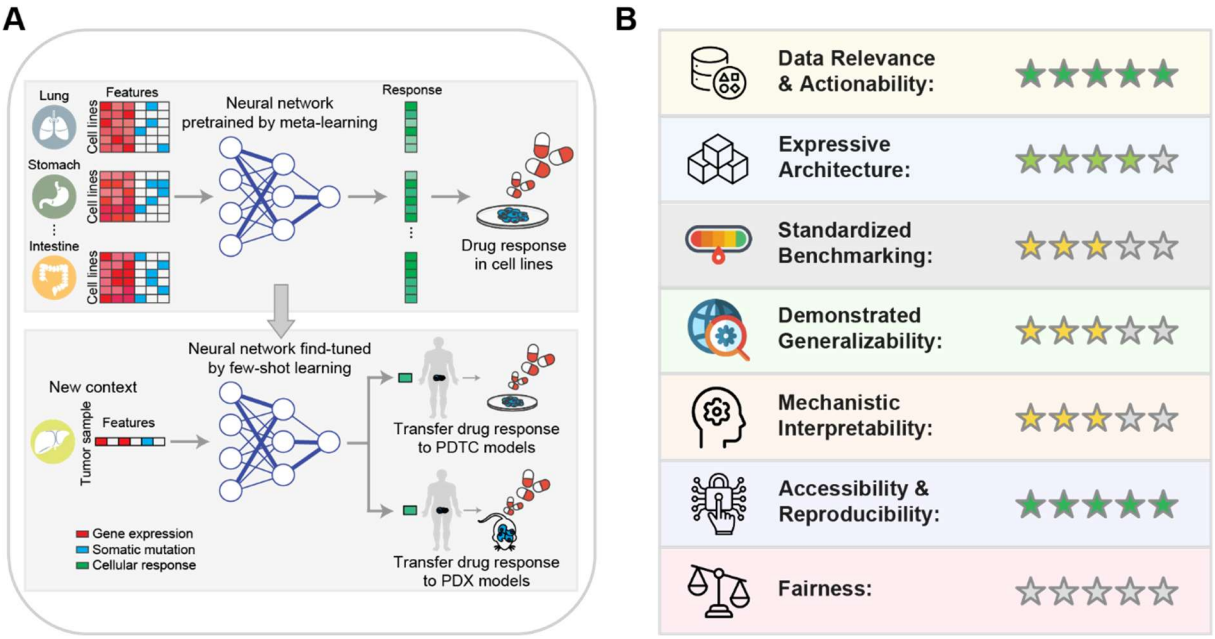

Figure 1.4: Sample model rating and comparison, with self-critique of authors' own model.

A, Overview of the TCRP model (Transfer of Cellular Response Prediction) approach. Adapted with permission from Ma et al.[134]. **B,** Scorecard for the TCRP model based on the criteria defined for scoring each hallmark.

1.13 Tables

Table 1.1: HARMONY Checklist.

RATIONALE		
1	☐	State the model objective and prior works.
ETHICAL CONSIDERATIONS		
2	☐	Discuss ethical considerations in model development and deployment.
3	☐	Outline protocols for patient data privacy.
HALLMARKS		
Data Relevance and Actionability		
4	☐	Specify data sources and criteria for data selection.
5	☐	Define actionability in the context of model objectives.
Expressive Architecture		
6	☐	Describe the model structure and capability to represent biological complexity.
7	☐	Detail the computational methods and algorithms used.
Standardized Benchmarking		
8	☐	Outline benchmark methods and metrics for evaluation.
9	☐	Describe the procedure for model validation (e.g. cross validation).
Demonstrated Generalizability		
10	☐	Outline validation datasets, methods, and metrics for evaluation.
11	☐	Present model performance across various datasets.
Mechanistic Interpretability		
12	☐	Explain how the model elucidates molecular pathways or mechanisms.
13	☐	Detail the explainability techniques used.
Accessibility and Reproducibility		
14	☐	Specify code repository and data format (input and output).
15	☐	Describe the training and evaluation procedures including dependencies.
Fairness		
16	☐	Outline approaches to ensure equitable model performance across populations.
17	☐	Describe measures to prevent bias in model predictions.
APPLICATION		
18	☐	Interpret results in the context of the hallmarks, discussing the model's limitations and implications for future research.

HARMONY: Hallmark-Adhering Recommendations for Models in predictive ONcologY

1.14 Acknowledgments

This study was supported by grants from the National Institutes of Health (NIH) including the National Cancer Institute (NCI U54 CA274502 and P30 CA023100) and National Institute for General Medical Sciences (NIGMS P41 GM103504). Additional support was provided from the Eric and Wendy Schmidt AI in Science Postdoctoral Fellowship; Cancer Moonshot Task Order No. 75N91019F00134; Frederick National Laboratory for Cancer Research Contract 75N91019D00024; U.S. Department of Energy support to Argonne National Laboratory under Contract DE-AC02-06-CH11357; the American Cancer Society grant # IRG-19-230-48.

Chapter 1, in full, is a reformatted reprint of the material as it appears as “The Hallmarks of Predictive Oncology” in Cancer Discovery, 2025 by Singhal, Akshat; Zhao, Xiaoyu; Wall, Patrick; So, Emily; Calderini, Guido; Partin, Alexander; Koussa, Natasha; Vasanthakumari, Priyanka; Narykov, Oleksandr; Zhu, Yitan; Jones, Sara E.; Abbas-Aghababazadeh, Farnoosh; Nair, Sisira Kadambat; Bélisle-Pipon, Jean-Christophe; Jayaram, Athmeya; Parker, Barbara A.; Yeung, Kay T.; Griffiths, Jason I.; Weil, Ryan; Nath, Aritro; Haibe-Kains, Benjamin; Ideker, Trey. The dissertation author was a primary investigator and author of this paper.

1.15 References

(1) National Research Council; Division on Earth and Life Studies; Board on Life Sciences; Committee on A Framework for Developing a New Taxonomy of Disease. *Toward Precision Medicine: Building a Knowledge Network for Biomedical Research and a New Taxonomy of Disease*; National Academies Press, 2012.

(2) Ashley, E. A. Towards Precision Medicine. *Nat. Rev. Genet.* 2016, *17* (9), 507–522.

(3) Nelson, M. R.; Tipney, H.; Painter, J. L.; Shen, J.; Nicoletti, P.; Shen, Y.; Floratos, A.; Sham, P. C.; Li, M. J.; Wang, J.; Cardon, L. R.; Whittaker, J. C.; Sanseau, P. The Support of Human Genetic Evidence for Approved Drug Indications. *Nat. Genet.* 2015, *47* (8), 856–860.

(4) Faderl, S.; Talpaz, M.; Estrov, Z.; O’Brien, S.; Kurzrock, R.; Kantarjian, H. M. The Biology of Chronic Myeloid Leukemia. *N. Engl. J. Med.* 1999, *341* (3), 164–172.

(5) Druker, B. J.; Sawyers, C. L.; Kantarjian, H.; Resta, D. J.; Reese, S. F.; Ford, J. M.; Capdeville, R.; Talpaz, M. Activity of a Specific Inhibitor of the BCR-ABL Tyrosine Kinase in the Blast Crisis of Chronic Myeloid Leukemia and Acute Lymphoblastic Leukemia with the

Philadelphia Chromosome. *N. Engl. J. Med.* 2001, *344* (14), 1038–1042.

(6) Bryant, H. E.; Schultz, N.; Thomas, H. D.; Parker, K. M.; Flower, D.; Lopez, E.; Kyle, S.; Meuth, M.; Curtin, N. J.; Helleday, T. Specific Killing of BRCA2-Deficient Tumours with Inhibitors of Poly(ADP-Ribose) Polymerase. *Nature* 2005, *434* (7035), 913–917.

(7) Farmer, H.; McCabe, N.; Lord, C. J.; Tutt, A. N. J.; Johnson, D. A.; Richardson, T. B.; Santarosa, M.; Dillon, K. J.; Hickson, I.; Knights, C.; Martin, N. M. B.; Jackson, S. P.; Smith, G. C. M.; Ashworth, A. Targeting the DNA Repair Defect in BRCA Mutant Cells as a Therapeutic Strategy. *Nature* 2005, *434* (7035), 917–921.

(8) Moore, K.; Colombo, N.; Scambia, G.; Kim, B.-G.; Oaknin, A.; Friedlander, M.; Lisyanskaya, A.; Floquet, A.; Leary, A.; Sonke, G. S.; Gourley, C.; Banerjee, S.; Oza, A.; González-Martín, A.; Aghajanian, C.; Bradley, W.; Mathews, C.; Liu, J.; Lowe, E. S.; Bloomfield, R.; DiSilvestro, P. Maintenance Olaparib in Patients with Newly Diagnosed Advanced Ovarian Cancer. *N. Engl. J. Med.* 2018, *379* (26), 2495–2505.

(9) Planchard, D.; Besse, B.; Groen, H. J. M.; Souquet, P.-J.; Quoix, E.; Baik, C. S.; Barlesi, F.; Kim, T. M.; Mazieres, J.; Novello, S.; Rigas, J. R.; Upalawanna, A.; D'Amelio, A. M., Jr; Zhang, P.; Mookerjee, B.; Johnson, B. E. Dabrafenib plus Trametinib in Patients with Previously Treated BRAF(V600E)-Mutant Metastatic Non-Small Cell Lung Cancer: An Open-Label, Multicentre Phase 2 Trial. *Lancet Oncol.* 2016, *17* (7), 984–993.

(10) Chapman Paul B.; Hauschild Axel; Robert Caroline; Haanen John B.; Ascierto Paolo; Larkin James; Dummer Reinhard; Garbe Claus; Testori Alessandro; Maio Michele; Hogg David; Lorigan Paul; Lebbe Celeste; Jouary Thomas; Schadendorf Dirk; Ribas Antoni; O'Day Steven J.; Sosman Jeffrey A.; Kirkwood John M.; Eggermont Alexander M.M.; Dreno Brigitte; Nolop Keith; Li Jiang; Nelson Betty; Hou Jeannie; Lee Richard J.; Flaherty Keith T.; McArthur Grant A. Improved Survival with Vemurafenib in Melanoma with BRAF V600E Mutation. *N. Engl. J. Med. 364* (26), 2507–2516.

(11) Hu, C.; Dignam, J. J. Biomarker-Driven Oncology Clinical Trials: Key Design Elements, Types, Features, and Practical Considerations. *JCO Precis Oncol* 2019, *3*.

(12) Nahta, R.; Esteva, F. J. Herceptin: Mechanisms of Action and Resistance. *Cancer Lett.* 2006, *232* (2), 123–138.

(13) Malviya, R.; Singh, A. K.; Yadav, D. *Multi-Drug Resistance in Cancer: Mechanism and Treatment Strategies*; John Wiley & Sons, 2023.

(14) Liang, G.; Fan, W.; Luo, H.; Zhu, X. The Emerging Roles of Artificial Intelligence in Cancer Drug Development and Precision Therapy. *Biomed. Pharmacother.* 2020, *128*, 110255.

(15) Ballester, P. J.; Stevens, R.; Haibe-Kains, B.; Huang, R. S.; Aittokallio, T. Artificial Intelligence for Drug Response Prediction in Disease Models. *Brief. Bioinform.* 2022, *23* (1).

(16) Partin, A.; Brettin, T. S.; Zhu, Y.; Narykov, O.; Clyde, A.; Overbeek, J.; Stevens, R. L. Deep Learning Methods for Drug Response Prediction in Cancer: Predominant and Emerging Trends. *Front. Med.* 2023, *10*, 1086097.

(17) Frampton, G. M.; Fichtenholtz, A.; Otto, G. A.; Wang, K.; Downing, S. R.; He, J.; Schnall-

Levin, M.; White, J.; Sanford, E. M.; An, P.; Sun, J.; Juhn, F.; Brennan, K.; Iwanik, K.; Maillet, A.; Buell, J.; White, E.; Zhao, M.; Balasubramanian, S.; Terzic, S.; Richards, T.; Banning, V.; Garcia, L.; Mahoney, K.; Zwirko, Z.; Donahue, A.; Beltran, H.; Mosquera, J. M.; Rubin, M. A.; Dogan, S.; Hedvat, C. V.; Berger, M. F.; Pusztai, L.; Lechner, M.; Boshoff, C.; Jarosz, M.; Vietz, C.; Parker, A.; Miller, V. A.; Ross, J. S.; Curran, J.; Cronin, M. T.; Stephens, P. J.; Lipson, D.; Yelensky, R. Development and Validation of a Clinical Cancer Genomic Profiling Test Based on Massively Parallel DNA Sequencing. *Nat. Biotechnol.* 2013, *31* (11), 1023–1031.

(18) Beaubier, N.; Tell, R.; Lau, D.; Parsons, J. R.; Bush, S.; Perera, J.; Sorrells, S.; Baker, T.; Chang, A.; Michuda, J.; Iguartua, C.; MacNeil, S.; Shah, K.; Ellis, P.; Yeatts, K.; Mahon, B.; Taxter, T.; Bontrager, M.; Khan, A.; Huether, R.; Lefkofsky, E.; White, K. P. Clinical Validation of the Tempus XT Next-Generation Targeted Oncology Sequencing Assay. *Oncotarget* 2019, *10* (24), 2384–2396.

(19) Hoadley, K. A.; Yau, C.; Hinoue, T.; Wolf, D. M.; Lazar, A. J.; Drill, E.; Shen, R.; Taylor, A. M.; Cherniack, A. D.; Thorsson, V.; Akbani, R.; Bowlby, R.; Wong, C. K.; Wiznerowicz, M.; Sanchez-Vega, F.; Robertson, A. G.; Schneider, B. G.; Lawrence, M. S.; Noushmehr, H.; Malta, T. M.; Cancer Genome Atlas Network; Stuart, J. M.; Benz, C. C.; Laird, P. W. Cell-of-Origin Patterns Dominate the Molecular Classification of 10,000 Tumors from 33 Types of Cancer. *Cell* 2018, *173* (2), 291-304.e6.

(20) AACR Project GENIE Consortium. AACR Project GENIE: Powering Precision Medicine through an International Consortium. *Cancer Discov.* 2017, *7* (8), 818–831.

(21) Barretina, J.; Caponigro, G.; Stransky, N.; Venkatesan, K.; Margolin, A. A.; Kim, S.; Wilson, C. J.; Lehár, J.; Kryukov, G. V.; Sonkin, D.; Reddy, A.; Liu, M.; Murray, L.; Berger, M. F.; Monahan, J. E.; Morais, P.; Meltzer, J.; Korejwa, A.; Jané-Valbuena, J.; Mapa, F. A.; Thibault, J.; Bric-Furlong, E.; Raman, P.; Shipway, A.; Engels, I. H.; Cheng, J.; Yu, G. K.; Yu, J.; Aspesi, P., Jr; de Silva, M.; Jagtap, K.; Jones, M. D.; Wang, L.; Hatton, C.; Palescandolo, E.; Gupta, S.; Mahan, S.; Sougnez, C.; Onofrio, R. C.; Liefeld, T.; MacConaill, L.; Winckler, W.; Reich, M.; Li, N.; Mesirov, J. P.; Gabriel, S. B.; Getz, G.; Ardlie, K.; Chan, V.; Myer, V. E.; Weber, B. L.; Porter, J.; Warmuth, M.; Finan, P.; Harris, J. L.; Meyerson, M.; Golub, T. R.; Morrissey, M. P.; Sellers, W. R.; Schlegel, R.; Garraway, L. A. The Cancer Cell Line Encyclopedia Enables Predictive Modelling of Anticancer Drug Sensitivity. *Nature* 2012, *483* (7391), 603–607.

(22) van de Vijver Marc J.; He Yudong D.; van ’t Veer Laura J.; Dai Hongyue; Hart Augustinus A.M.; Voskuil Dorien W.; Schreiber George J.; Peterse Johannes L.; Roberts Chris; Marton Matthew J.; Parrish Mark; Atsma Douwe; Witteveen Anke; Glas Annuska; Delahaye Leonie; van der Velde Tony; Bartelink Harry; Rodenhuis Sjoerd; Rutgers Emiel T.; Friend Stephen H.; Bernards René. A Gene-Expression Signature as a Predictor of Survival in Breast Cancer. *N. Engl. J. Med. 347* (25), 1999–2009.

(23) Paik, S.; Tang, G.; Shak, S.; Kim, C.; Baker, J.; Kim, W.; Cronin, M.; Baehner, F. L.; Watson, D.; Bryant, J.; Costantino, J. P.; Geyer, C. E., Jr; Wickerham, D. L.; Wolmark, N. Gene Expression and Benefit of Chemotherapy in Women with Node-Negative, Estrogen Receptor-Positive Breast Cancer. *J. Clin. Oncol.* 2006, *24* (23), 3726–3734.

(24) Tian, S.; Roepman, P.; Popovici, V.; Michaut, M.; Majewski, I.; Salazar, R.; Santos, C.; Rosenberg, R.; Nitsche, U.; Mesker, W. E.; Bruin, S.; Tejpar, S.; Delorenzi, M.; Bernards,

R.; Simon, I. A Robust Genomic Signature for the Detection of Colorectal Cancer Patients with Microsatellite Instability Phenotype and High Mutation Frequency. *J. Pathol.* 2012, *228* (4), 586–595.

(25) Boland, C. R.; Goel, A. Microsatellite Instability in Colorectal Cancer. *Gastroenterology* 2010, *138* (6), 2073-2087.e3.

(26) Dinstag, G.; Shulman, E. D.; Elis, E.; Ben-Zvi, D. S.; Tirosh, O.; Maimon, E.; Meilijson, I.; Elalouf, E.; Temkin, B.; Vitkovsky, P.; Schiff, E.; Hoang, D.-T.; Sinha, S.; Nair, N. U.; Lee, J. S.; Schäffer, A. A.; Ronai, Z.; Juric, D.; Apolo, A. B.; Dahut, W. L.; Lipkowitz, S.; Berger, R.; Kurzrock, R.; Papanicolau-Sengos, A.; Karzai, F.; Gilbert, M. R.; Aldape, K.; Rajagopal, P. S.; Beker, T.; Ruppin, E.; Aharonov, R. Clinically Oriented Prediction of Patient Response to Targeted and Immunotherapies from the Tumor Transcriptome. *Med* 2023, *4* (1), 15-30.e8.

(27) Alvarez, M. J.; Subramaniam, P. S.; Tang, L. H.; Grunn, A.; Aburi, M.; Rieckhof, G.; Komissarova, E. V.; Hagan, E. A.; Bodei, L.; Clemons, P. A.; Dela Cruz, F. S.; Dhall, D.; Diolaiti, D.; Fraker, D. A.; Ghavami, A.; Kaemmerer, D.; Karan, C.; Kidd, M.; Kim, K. M.; Kim, H. C.; Kunju, L. P.; Langel, Ü.; Li, Z.; Lee, J.; Li, H.; LiVolsi, V.; Pfragner, R.; Rainey, A. R.; Realubit, R. B.; Remotti, H.; Regberg, J.; Roses, R.; Rustgi, A.; Sepulveda, A. R.; Serra, S.; Shi, C.; Yuan, X.; Barberis, M.; Bergamaschi, R.; Chinnaiyan, A. M.; Detre, T.; Ezzat, S.; Frilling, A.; Hommann, M.; Jaeger, D.; Kim, M. K.; Knudsen, B. S.; Kung, A. L.; Leahy, E.; Metz, D. C.; Milsom, J. W.; Park, Y. S.; Reidy-Lagunes, D.; Schreiber, S.; Washington, K.; Wiedenmann, B.; Modlin, I.; Califano, A. A Precision Oncology Approach to the Pharmacological Targeting of Mechanistic Dependencies in Neuroendocrine Tumors. *Nat. Genet.* 2018, *50* (7), 979–989.

(28) Mundi, P. S.; Dela Cruz, F. S.; Grunn, A.; Diolaiti, D.; Mauguen, A.; Rainey, A. R.; Guillan, K.; Siddiquee, A.; You, D.; Realubit, R.; Karan, C.; Ortiz, M. V.; Douglass, E. F.; Accordino, M.; Mistretta, S.; Brogan, F.; Bruce, J. N.; Caescu, C. I.; Carvajal, R. D.; Crew, K. D.; Decastro, G.; Heaney, M.; Henick, B. S.; Hershman, D. L.; Hou, J. Y.; Iwamoto, F. M.; Jurcic, J. G.; Kiran, R. P.; Kluger, M. D.; Kreisl, T.; Lamanna, N.; Lassman, A. B.; Lim, E. A.; Manji, G. A.; McKhann, G. M.; McKiernan, J. M.; Neugut, A. I.; Olive, K. P.; Rosenblat, T.; Schwartz, G. K.; Shu, C. A.; Sisti, M. B.; Tergas, A.; Vattakalam, R. M.; Welch, M.; Wenske, S.; Wright, J. D.; Canoll, P.; Hibshoosh, H.; Kalinsky, K.; Aburi, M.; Sims, P. A.; Alvarez, M. J.; Kung, A. L.; Califano, A. A Transcriptome-Based Precision Oncology Platform for Patient-Therapy Alignment in a Diverse Set of Treatment-Resistant Malignancies. *Cancer Discov.* 2023, *13* (6), 1386–1407.

(29) Markowetz, F. All Models Are Wrong and Yours Are Useless: Making Clinical Prediction Models Impactful for Patients. *NPJ Precis Oncol* 2024, *8* (1), 54.

(30) Spencer, K. L.; Absolom, K. L.; Allsop, M. J.; Relton, S. D.; Pearce, J.; Liao, K.; Naseer, S.; Salako, O.; Howdon, D.; Hewison, J.; Velikova, G.; Faivre-Finn, C.; Bekker, H. L.; van der Veer, S. N. Fixing the Leaky Pipe: How to Improve the Uptake of Patient-Reported Outcomes-Based Prognostic and Predictive Models in Cancer Clinical Practice. *JCO Clin Cancer Inform* 2023, *7*, e2300070.

(31) Rudin, C. Stop Explaining Black Box Machine Learning Models for High Stakes Decisions and Use Interpretable Models Instead. *Nat Mach Intell* 2019, *1* (5), 206–215.

(32) McShane, L. M.; Altman, D. G.; Sauerbrei, W.; Taube, S. E.; Gion, M.; Clark, G. M.; Statistics Subcommittee of the NCI-EORTC Working Group on Cancer Diagnostics. REporting Recommendations for Tumour MARKer Prognostic Studies (REMARK). *Br. J. Cancer* 2005, *93* (4), 387–391.

(33) ICH Official web site : ICH https://www.ich.org/page/efficacy-guidelines (accessed Apr 9, 2024).

(34) 45 CFR part 170 subpart B -- standards and implementation specifications for health information technology https://www.ecfr.gov/current/title-45/subtitle-A/subchapter-D/part-170/subpart-B (accessed Apr 9, 2024).

(35) 45 CFR 164.514 -- Other requirements relating to uses and disclosures of protected health information https://www.ecfr.gov/current/title-45/section-164.514 (accessed Apr 9, 2024).

(36) Seashore-Ludlow, B.; Rees, M. G.; Cheah, J. H.; Cokol, M.; Price, E. V.; Coletti, M. E.; Jones, V.; Bodycombe, N. E.; Soule, C. K.; Gould, J.; Alexander, B.; Li, A.; Montgomery, P.; Wawer, M. J.; Kuru, N.; Kotz, J. D.; Hon, C. S.-Y.; Munoz, B.; Liefeld, T.; Dančík, V.; Bittker, J. A.; Palmer, M.; Bradner, J. E.; Shamji, A. F.; Clemons, P. A.; Schreiber, S. L. Harnessing Connectivity in a Large-Scale Small-Molecule Sensitivity Dataset. *Cancer Discov.* 2015, *5* (11), 1210–1223.

(37) Shoemaker, R. H. The NCI60 Human Tumour Cell Line Anticancer Drug Screen. *Nat. Rev. Cancer* 2006, *6* (10), 813–823.

(38) Iorio, F.; Knijnenburg, T. A.; Vis, D. J.; Bignell, G. R.; Menden, M. P.; Schubert, M.; Aben, N.; Gonçalves, E.; Barthorpe, S.; Lightfoot, H.; Cokelaer, T.; Greninger, P.; van Dyk, E.; Chang, H.; de Silva, H.; Heyn, H.; Deng, X.; Egan, R. K.; Liu, Q.; Mironenko, T.; Mitropoulos, X.; Richardson, L.; Wang, J.; Zhang, T.; Moran, S.; Sayols, S.; Soleimani, M.; Tamborero, D.; Lopez-Bigas, N.; Ross-Macdonald, P.; Esteller, M.; Gray, N. S.; Haber, D. A.; Stratton, M. R.; Benes, C. H.; Wessels, L. F. A.; Saez-Rodriguez, J.; McDermott, U.; Garnett, M. J. A Landscape of Pharmacogenomic Interactions in Cancer. *Cell* 2016, *166* (3), 740–754.

(39) Garnett, M. J.; Edelman, E. J.; Heidorn, S. J.; Greenman, C. D.; Dastur, A.; Lau, K. W.; Greninger, P.; Thompson, I. R.; Luo, X.; Soares, J.; Liu, Q.; Iorio, F.; Surdez, D.; Chen, L.; Milano, R. J.; Bignell, G. R.; Tam, A. T.; Davies, H.; Stevenson, J. A.; Barthorpe, S.; Lutz, S. R.; Kogera, F.; Lawrence, K.; McLaren-Douglas, A.; Mitropoulos, X.; Mironenko, T.; Thi, H.; Richardson, L.; Zhou, W.; Jewitt, F.; Zhang, T.; O'Brien, P.; Boisvert, J. L.; Price, S.; Hur, W.; Yang, W.; Deng, X.; Butler, A.; Choi, H. G.; Chang, J. W.; Baselga, J.; Stamenkovic, I.; Engelman, J. A.; Sharma, S. V.; Delattre, O.; Saez-Rodriguez, J.; Gray, N. S.; Settleman, J.; Futreal, P. A.; Haber, D. A.; Stratton, M. R.; Ramaswamy, S.; McDermott, U.; Benes, C. H. Systematic Identification of Genomic Markers of Drug Sensitivity in Cancer Cells. *Nature* 2012, *483* (7391), 570–575.

(40) Pemovska, T.; Kontro, M.; Yadav, B.; Edgren, H.; Eldfors, S.; Szwajda, A.; Almusa, H.; Bespalov, M. M.; Ellonen, P.; Elonen, E.; Gjertsen, B. T.; Karjalainen, R.; Kulesskiy, E.; Lagström, S.; Lehto, A.; Lepistö, M.; Lundán, T.; Majumder, M. M.; Marti, J. M. L.; Mattila, P.; Murumägi, A.; Mustjoki, S.; Palva, A.; Parsons, A.; Pirttinen, T.; Rämet, M. E.; Suvela, M.; Turunen, L.; Västrik, I.; Wolf, M.; Knowles, J.; Aittokallio, T.; Heckman, C. A.; Porkka, K.; Kallioniemi, O.; Wennerberg, K. Individualized Systems Medicine Strategy to Tailor

Treatments for Patients with Chemorefractory Acute Myeloid Leukemia. *Cancer Discov.* 2013, *3* (12), 1416–1429.

(41) Haverty, P. M.; Lin, E.; Tan, J.; Yu, Y.; Lam, B.; Lianoglou, S.; Neve, R. M.; Martin, S.; Settleman, J.; Yauch, R. L.; Bourgon, R. Reproducible Pharmacogenomic Profiling of Cancer Cell Line Panels. *Nature* 2016, *533* (7603), 333–337.

(42) McMillan, E. A.; Ryu, M.-J.; Diep, C. H.; Mendiratta, S.; Clemenceau, J. R.; Vaden, R. M.; Kim, J.-H.; Motoyaji, T.; Covington, K. R.; Peyton, M.; Huffman, K.; Wu, X.; Girard, L.; Sung, Y.; Chen, P.-H.; Mallipeddi, P. L.; Lee, J. Y.; Hanson, J.; Voruganti, S.; Yu, Y.; Park, S.; Sudderth, J.; DeSevo, C.; Muzny, D. M.; Doddapaneni, H.; Gazdar, A.; Gibbs, R. A.; Hwang, T.-H.; Heymach, J. V.; Wistuba, I.; Coombes, K. R.; Williams, N. S.; Wheeler, D. A.; MacMillan, J. B.; Deberardinis, R. J.; Roth, M. G.; Posner, B. A.; Minna, J. D.; Kim, H. S.; White, M. A. Chemistry-First Approach for Nomination of Personalized Treatment in Lung Cancer. *Cell* 2018, *173* (4), 864-878.e29.

(43) Bruna, A.; Rueda, O. M.; Greenwood, W.; Batra, A. S.; Callari, M.; Batra, R. N.; Pogrebniak, K.; Sandoval, J.; Cassidy, J. W.; Tufegdzic-Vidakovic, A.; Sammut, S.-J.; Jones, L.; Provenzano, E.; Baird, R.; Eirew, P.; Hadfield, J.; Eldridge, M.; McLaren-Douglas, A.; Barthorpe, A.; Lightfoot, H.; O'Connor, M. J.; Gray, J.; Cortes, J.; Baselga, J.; Marangoni, E.; Welm, A. L.; Aparicio, S.; Serra, V.; Garnett, M. J.; Caldas, C. A Biobank of Breast Cancer Explants with Preserved Intra-Tumor Heterogeneity to Screen Anticancer Compounds. *Cell* 2016, *167* (1), 260-274.e22.

(44) Yu, N.; Hwang, M.; Lee, Y.; Song, B. R.; Kang, E. H.; Sim, H.; Ahn, B.-C.; Hwang, K. H.; Kim, J.; Hong, S.; Kim, S.; Park, C.; Han, J.-Y. Patient-Derived Cell-Based Pharmacogenomic Assessment to Unveil Underlying Resistance Mechanisms and Novel Therapeutics for Advanced Lung Cancer. *J. Exp. Clin. Cancer Res.* 2023, *42* (1), 37.

(45) Bennett, A. V.; Tan, X.; Foster, M. C.; Richardson, D. R.; Bryant, A. L.; Wood, W. A.; Yocum, A. O.; Mims, A. S.; Borate, U.; Burd, A. Is Disease Response a Patient-Centered Clinical Trial Endpoint in Acute Myeloid Leukemia: Differences in Symptom Burden and Physical Function By Response Status in the Beat-AML Master Trial. *Blood* 2022, *140* (Supplement 1), 3367–3368.

(46) Lee, S. H.; Hu, W.; Matulay, J. T.; Silva, M. V.; Owczarek, T. B.; Kim, K.; Chua, C. W.; Barlow, L. J.; Kandoth, C.; Williams, A. B.; Bergren, S. K.; Pietzak, E. J.; Anderson, C. B.; Benson, M. C.; Coleman, J. A.; Taylor, B. S.; Abate-Shen, C.; McKiernan, J. M.; Al-Ahmadie, H.; Solit, D. B.; Shen, M. M. Tumor Evolution and Drug Response in Patient-Derived Organoid Models of Bladder Cancer. *Cell* 2018, *173* (2), 515-528.e17.

(47) van de Wetering, M.; Francies, H. E.; Francis, J. M.; Bounova, G.; Iorio, F.; Pronk, A.; van Houdt, W.; van Gorp, J.; Taylor-Weiner, A.; Kester, L.; McLaren-Douglas, A.; Blokker, J.; Jaksani, S.; Bartfeld, S.; Volckman, R.; van Sluis, P.; Li, V. S. W.; Seepo, S.; Sekhar Pedamallu, C.; Cibulskis, K.; Carter, S. L.; McKenna, A.; Lawrence, M. S.; Lichtenstein, L.; Stewart, C.; Koster, J.; Versteeg, R.; van Oudenaarden, A.; Saez-Rodriguez, J.; Vries, R. G. J.; Getz, G.; Wessels, L.; Stratton, M. R.; McDermott, U.; Meyerson, M.; Garnett, M. J.; Clevers, H. Prospective Derivation of a Living Organoid Biobank of Colorectal Cancer Patients. *Cell* 2015, *161* (4), 933–945.

(48) Driehuis, E.; Kretzschmar, K.; Clevers, H. Establishment of Patient-Derived Cancer

Organoids for Drug-Screening Applications. *Nat. Protoc.* 2020, *15* (10), 3380–3409.

(49) Gao, H.; Korn, J. M.; Ferretti, S.; Monahan, J. E.; Wang, Y.; Singh, M.; Zhang, C.; Schnell, C.; Yang, G.; Zhang, Y.; Balbin, O. A.; Barbe, S.; Cai, H.; Casey, F.; Chatterjee, S.; Chiang, D. Y.; Chuai, S.; Cogan, S. M.; Collins, S. D.; Dammassa, E.; Ebel, N.; Embry, M.; Green, J.; Kauffmann, A.; Kowal, C.; Leary, R. J.; Lehar, J.; Liang, Y.; Loo, A.; Lorenzana, E.; Robert McDonald, E., 3rd; McLaughlin, M. E.; Merkin, J.; Meyer, R.; Naylor, T. L.; Patawaran, M.; Reddy, A.; Röelli, C.; Ruddy, D. A.; Salangsang, F.; Santacroce, F.; Singh, A. P.; Tang, Y.; Tinetto, W.; Tobler, S.; Velazquez, R.; Venkatesan, K.; Von Arx, F.; Wang, H. Q.; Wang, Z.; Wiesmann, M.; Wyss, D.; Xu, F.; Bitter, H.; Atadja, P.; Lees, E.; Hofmann, F.; Li, E.; Keen, N.; Cozens, R.; Jensen, M. R.; Pryer, N. K.; Williams, J. A.; Sellers, W. R. High-Throughput Screening Using Patient-Derived Tumor Xenografts to Predict Clinical Trial Drug Response. *Nat. Med.* 2015, *21* (11), 1318–1325.

(50) Townsend, E. C.; Murakami, M. A.; Christodoulou, A.; Christie, A. L.; Köster, J.; DeSouza, T. A.; Morgan, E. A.; Kallgren, S. P.; Liu, H.; Wu, S.-C.; Plana, O.; Montero, J.; Stevenson, K. E.; Rao, P.; Vadhi, R.; Andreeff, M.; Armand, P.; Ballen, K. K.; Barzaghi-Rinaudo, P.; Cahill, S.; Clark, R. A.; Cooke, V. G.; Davids, M. S.; DeAngelo, D. J.; Dorfman, D. M.; Eaton, H.; Ebert, B. L.; Etchin, J.; Firestone, B.; Fisher, D. C.; Freedman, A. S.; Galinsky, I. A.; Gao, H.; Garcia, J. S.; Garnache-Ottou, F.; Graubert, T. A.; Gutierrez, A.; Halilovic, E.; Harris, M. H.; Herbert, Z. T.; Horwitz, S. M.; Inghirami, G.; Intlekofer, A. M.; Ito, M.; Izraeli, S.; Jacobsen, E. D.; Jacobson, C. A.; Jeay, S.; Jeremias, I.; Kelliher, M. A.; Koch, R.; Konopleva, M.; Kopp, N.; Kornblau, S. M.; Kung, A. L.; Kupper, T. S.; LeBoeuf, N. R.; LaCasce, A. S.; Lees, E.; Li, L. S.; Look, A. T.; Murakami, M.; Muschen, M.; Neuberg, D.; Ng, S. Y.; Odejide, O. O.; Orkin, S. H.; Paquette, R. R.; Place, A. E.; Roderick, J. E.; Ryan, J. A.; Sallan, S. E.; Shoji, B.; Silverman, L. B.; Soiffer, R. J.; Steensma, D. P.; Stegmaier, K.; Stone, R. M.; Tamburini, J.; Thorner, A. R.; van Hummelen, P.; Wadleigh, M.; Wiesmann, M.; Weng, A. P.; Wuerthner, J. U.; Williams, D. A.; Wollison, B. M.; Lane, A. A.; Letai, A.; Bertagnolli, M. M.; Ritz, J.; Brown, M.; Long, H.; Aster, J. C.; Shipp, M. A.; Griffin, J. D.; Weinstock, D. M. The Public Repository of Xenografts Enables Discovery and Randomized Phase II-like Trials in Mice. *Cancer Cell* 2016, *30* (1), 183.

(51) Fernandez-Martinez, A.; Krop, I. E.; Hillman, D. W.; Polley, M.-Y.; Parker, J. S.; Huebner, L.; Hoadley, K. A.; Shepherd, J.; Tolaney, S.; Henry, N. L.; Dang, C.; Harris, L.; Berry, D.; Hahn, O.; Hudis, C.; Winer, E.; Partridge, A.; Perou, C. M.; Carey, L. A. Survival, Pathologic Response, and Genomics in CALGB 40601 (Alliance), a Neoadjuvant Phase III Trial of Paclitaxel-Trastuzumab With or Without Lapatinib in HER2-Positive Breast Cancer. *J. Clin. Oncol.* 2020, *38* (35), 4184–4193.

(52) O'Leary, B.; Cutts, R. J.; Liu, Y.; Hrebien, S.; Huang, X.; Fenwick, K.; André, F.; Loibl, S.; Loi, S.; Garcia-Murillas, I.; Cristofanilli, M.; Huang Bartlett, C.; Turner, N. C. The Genetic Landscape and Clonal Evolution of Breast Cancer Resistance to Palbociclib plus Fulvestrant in the PALOMA-3 Trial. *Cancer Discov.* 2018, *8* (11), 1390–1403.

(53) Wolf, D. M.; Yau, C.; Wulfkuhle, J.; Brown-Swigart, L.; Gallagher, R. I.; Lee, P. R. E.; Zhu, Z.; Magbanua, M. J.; Sayaman, R.; O'Grady, N.; Basu, A.; Delson, A.; Coppé, J. P.; Lu, R.; Braun, J.; I-SPY2 Investigators; Asare, S. M.; Sit, L.; Matthews, J. B.; Perlmutter, J.; Hylton, N.; Liu, M. C.; Pohlmann, P.; Symmans, W. F.; Rugo, H. S.; Isaacs, C.; DeMichele, A. M.; Yee, D.; Berry, D. A.; Pusztai, L.; Petricoin, E. F.; Hirst, G. L.; Esserman, L. J.; van 't Veer, L. J. Redefining Breast Cancer Subtypes to Guide Treatment Prioritization and Maximize Response: Predictive Biomarkers across 10 Cancer Therapies. *Cancer Cell* 2022, *40* (6),

609-623.e6.

(54) Shepherd, J. H.; Ballman, K.; Polley, M.-Y. C.; Campbell, J. D.; Fan, C.; Selitsky, S.; Fernandez-Martinez, A.; Parker, J. S.; Hoadley, K. A.; Hu, Z.; Li, Y.; Soloway, M. G.; Spears, P. A.; Singh, B.; Tolaney, S. M.; Somlo, G.; Port, E. R.; Ma, C.; Kuzma, C.; Mamounas, E.; Golshan, M.; Bellon, J. R.; Collyar, D.; Hahn, O. M.; Hudis, C. A.; Winer, E. P.; Partridge, A.; Hyslop, T.; Carey, L. A.; Perou, C. M.; Sikov, W. M. CALGB 40603 (Alliance): Long-Term Outcomes and Genomic Correlates of Response and Survival After Neoadjuvant Chemotherapy With or Without Carboplatin and Bevacizumab in Triple-Negative Breast Cancer. *J. Clin. Oncol.* 2022, *40* (12), 1323–1334.

(55) Zhu, Z.; Turner, N. C.; Loi, S.; André, F.; Martin, M.; Diéras, V.; Gelmon, K. A.; Harbeck, N.; Zhang, C.; Cao, J. Q.; Yan, Z.; Lu, D. R.; Wei, P.; VanArsdale, T. L.; Rejto, P. A.; Huang, X.; Rugo, H. S.; Loibl, S.; Cristofanilli, M.; Finn, R. S.; Liu, Y. Comparative Biomarker Analysis of PALOMA-2/3 Trials for Palbociclib. *NPJ Precis Oncol* 2022, *6* (1), 56.

(56) van der Velden, D. L.; Hoes, L. R.; van der Wijngaart, H.; van Berge Henegouwen, J. M.; van Werkhoven, E.; Roepman, P.; Schilsky, R. L.; de Leng, W. W. J.; Huitema, A. D. R.; Nuijen, B.; Nederlof, P. M.; van Herpen, C. M. L.; de Groot, D. J. A.; Devriese, L. A.; Hoeben, A.; de Jonge, M. J. A.; Chalabi, M.; Smit, E. F.; de Langen, A. J.; Mehra, N.; Labots, M.; Kapiteijn, E.; Sleijfer, S.; Cuppen, E.; Verheul, H. M. W.; Gelderblom, H.; Voest, E. E. The Drug Rediscovery Protocol Facilitates the Expanded Use of Existing Anticancer Drugs. *Nature* 2019, *574* (7776), 127–131.

(57) Ma, X.; Liu, Y.; Liu, Y.; Alexandrov, L. B.; Edmonson, M. N.; Gawad, C.; Zhou, X.; Li, Y.; Rusch, M. C.; Easton, J.; Huether, R.; Gonzalez-Pena, V.; Wilkinson, M. R.; Hermida, L. C.; Davis, S.; Sioson, E.; Pounds, S.; Cao, X.; Ries, R. E.; Wang, Z.; Chen, X.; Dong, L.; Diskin, S. J.; Smith, M. A.; Guidry Auvil, J. M.; Meltzer, P. S.; Lau, C. C.; Perlman, E. J.; Maris, J. M.; Meshinchi, S.; Hunger, S. P.; Gerhard, D. S.; Zhang, J. Pan-Cancer Genome and Transcriptome Analyses of 1,699 Paediatric Leukaemias and Solid Tumours. *Nature* 2018, *555* (7696), 371–376.

(58) Quevedo, R.; Smirnov, P.; Tkachuk, D.; Ho, C.; El-Hachem, N.; Safikhani, Z.; Pugh, T. J.; Haibe-Kains, B. Assessment of Genetic Drift in Large Pharmacogenomic Studies. *Cell Syst* 2020, *11* (4), 393-401.e2.

(59) Ben-David, U.; Siranosian, B.; Ha, G.; Tang, H.; Oren, Y.; Hinohara, K.; Strathdee, C. A.; Dempster, J.; Lyons, N. J.; Burns, R.; Nag, A.; Kugener, G.; Cimini, B.; Tsvetkov, P.; Maruvka, Y. E.; O'Rourke, R.; Garrity, A.; Tubelli, A. A.; Bandopadhayay, P.; Tsherniak, A.; Vazquez, F.; Wong, B.; Birger, C.; Ghandi, M.; Thorner, A. R.; Bittker, J. A.; Meyerson, M.; Getz, G.; Beroukhim, R.; Golub, T. R. Genetic and Transcriptional Evolution Alters Cancer Cell Line Drug Response. *Nature* 2018, *560* (7718), 325–330.

(60) Trastulla, L.; Noorbakhsh, J.; Vazquez, F.; McFarland, J.; Iorio, F. Computational Estimation of Quality and Clinical Relevance of Cancer Cell Lines. *Mol. Syst. Biol.* 2022, *18* (7), e11017.

(61) Rae, C.; Amato, F.; Braconi, C. Patient-Derived Organoids as a Model for Cancer Drug Discovery. *Int. J. Mol. Sci.* 2021, *22* (7).

(62) Golebiewska, A.; Hau, A.-C.; Oudin, A.; Stieber, D.; Yabo, Y. A.; Baus, V.; Barthelemy, V.;

Klein, E.; Bougnaud, S.; Keunen, O.; Wantz, M.; Michelucci, A.; Neirinckx, V.; Muller, A.; Kaoma, T.; Nazarov, P. V.; Azuaje, F.; De Falco, A.; Flies, B.; Richart, L.; Poovathingal, S.; Arns, T.; Grzyb, K.; Mock, A.; Herold-Mende, C.; Steino, A.; Brown, D.; May, P.; Miletic, H.; Malta, T. M.; Noushmehr, H.; Kwon, Y.-J.; Jahn, W.; Klink, B.; Tanner, G.; Stead, L. F.; Mittelbronn, M.; Skupin, A.; Hertel, F.; Bjerkvig, R.; Niclou, S. P. Patient-Derived Organoids and Orthotopic Xenografts of Primary and Recurrent Gliomas Represent Relevant Patient Avatars for Precision Oncology. *Acta Neuropathol.* 2020, *140* (6), 919–949.

(63) Hidalgo, M.; Amant, F.; Biankin, A. V.; Budinská, E.; Byrne, A. T.; Caldas, C.; Clarke, R. B.; de Jong, S.; Jonkers, J.; Mælandsmo, G. M.; Roman-Roman, S.; Seoane, J.; Trusolino, L.; Villanueva, A. Patient-Derived Xenograft Models: An Emerging Platform for Translational Cancer Research. *Cancer Discov.* 2014, *4* (9), 998–1013.

(64) He, J.; Zhang, C.; Ozkan, A.; Feng, T.; Duan, P.; Wang, S.; Yang, X.; Xie, J.; Liu, X. Patient-Derived Tumor Models and Their Distinctive Applications in Personalized Drug Therapy. *Mechanobiology in Medicine* 2023, *1* (2), 100014.

(65) Nugent, B. M.; Madabushi, R.; Buch, B.; Peiris, V.; Crentsil, V.; Miller, V. M.; Bull, J.; R Jenkins, M. Heterogeneity in Treatment Effects across Diverse Populations. *Pharm. Stat.* 2021, *20* (5), 929–938.

(66) Chakraborty, S.; Hosen, M. I.; Ahmed, M.; Shekhar, H. U. Onco-Multi-OMICS Approach: A New Frontier in Cancer Research. *Biomed Res. Int.* 2018, *2018*, 9836256.

(67) Dawood, M.; Vu, Q. D.; Young, L. S.; Branson, K.; Jones, L.; Rajpoot, N.; Minhas, F. U. A. A. Cancer Drug Sensitivity Prediction from Routine Histology Images. *NPJ Precis Oncol* 2024, *8* (1), 5.

(68) Nakajima, E. C.; Simpson, A.; Bogaerts, J.; de Vries, E. G. E.; Do, R.; Garalda, E.; Goldmacher, G.; Kinahan, P. E.; Lambin, P.; LeStage, B.; Li, Q.; Lin, F.; Litière, S.; Perez-Lopez, R.; Petrick, N.; Schwartz, L.; Seymour, L.; Shankar, L.; Laurie, S. A. Tumor Size Is Not Everything: Advancing Radiomics as a Precision Medicine Biomarker in Oncology Drug Development and Clinical Care. A Report of a Multidisciplinary Workshop Coordinated by the RECIST Working Group. *JCO Precis Oncol* 2024, *8*, e2300687.

(69) Zhou, H.; Luo, Q.; Wu, W.; Li, N.; Yang, C.; Zou, L. Radiomics-Guided Checkpoint Inhibitor Immunotherapy for Precision Medicine in Cancer: A Review for Clinicians. *Front. Immunol.* 2023, *14*, 1088874.

(70) Thompson, J. C.; Scholes, D. G.; Carpenter, E. L.; Aggarwal, C. Molecular Response Assessment Using Circulating Tumor DNA (CtDNA) in Advanced Solid Tumors. *Br. J. Cancer* 2023, *129* (12), 1893–1902.

(71) Patelli, G.; Mauri, G.; Tosi, F.; Amatu, A.; Bencardino, K.; Bonazzina, E.; Pizzutilo, E. G.; Villa, F.; Calvanese, G.; Agostara, A. G.; Stabile, S.; Ghezzi, S.; Crisafulli, G.; Di Nicolantonio, F.; Marsoni, S.; Bardelli, A.; Siena, S.; Sartore-Bianchi, A. Circulating Tumor DNA to Drive Treatment in Metastatic Colorectal Cancer. *Clin. Cancer Res.* 2023, *29* (22), 4530–4539.

(72) Bengio, Y.; Delalleau, O. On the Expressive Power of Deep Architectures. In *Algorithmic Learning Theory*; Springer Berlin Heidelberg, 2011; pp 18–36.

(73) Poole, B.; Lahiri, S.; Raghu, M.; Sohl-Dickstein, J. N.; Ganguli, S. Exponential Expressivity in Deep Neural Networks through Transient Chaos. *Adv. Neural Inf. Process. Syst.* 2016, 3360–3368.

(74) Jin, I.; Nam, H. HiDRA: Hierarchical Network for Drug Response Prediction with Attention. *J. Chem. Inf. Model.* 2021, *61* (8), 3858–3867.

(75) Zhao, X.; Singhal, A.; Park, S.; Kong, J.; Bachelder, R.; Ideker, T. Cancer Mutations Converge on a Collection of Protein Assemblies to Predict Resistance to Replication Stress. *Cancer Discov.* 2024, *14* (3), 508–523.

(76) Park, S.; Silva, E.; Singhal, A.; Kelly, M. R.; Licon, K.; Panagiotou, I.; Fogg, C.; Fong, S.; Lee, J. J. Y.; Zhao, X.; Bachelder, R.; Parker, B. A.; Yeung, K. T.; Ideker, T. A Deep Learning Model of Tumor Cell Architecture Elucidates Response and Resistance to CDK4/6 Inhibitors. *Nat. Cancer* 2024, *5* (7), 996–1009.

(77) Briscoe, E.; Feldman, J. Conceptual Complexity and the Bias/Variance Tradeoff. *Cognition* 2011, *118* (1), 2–16.

(78) Domingos, P. The Role of Occam's Razor in Knowledge Discovery. *Data Min. Knowl. Discov.* 1999, *3* (4), 409–425.

(79) Thrun, S.; Pratt, L. *Learning to Learn*; Springer US, 1998.

(80) Raedt, D. *Advances in Inductive Logic Programming*, 1st ed.; IOS Press: NLD, 1996.

(81) Cohen, W. W. Compiling Prior Knowledge Into an Explicit Bias. In *Machine Learning Proceedings 1992*; Sleeman, D., Edwards, P., Eds.; Morgan Kaufmann: San Francisco (CA), 1992; pp 102–110.

(82) Tibshirani, R. Regression Shrinkage and Selection Via the Lasso. *J. R. Stat. Soc. Series B Stat. Methodol.* 2018, *58* (1), 267–288.

(83) Friedman, J.; Hastie, T.; Tibshirani, R. Regularization Paths for Generalized Linear Models via Coordinate Descent. *J. Stat. Softw.* 2010, *33* (1), 1–22.

(84) Quinlan, J. R. Simplifying Decision Trees. *Int. J. Man. Mach. Stud.* 1987, *27* (3), 221–234.

(85) Gou, J.; Yu, B.; Maybank, S. J.; Tao, D. Knowledge Distillation: A Survey. *Int. J. Comput. Vis.* 2021, *129* (6), 1789–1819.

(86) CO2 Emissions and the 🤗 Hub: Leading the Charge https://huggingface.co/blog/carbon-emissions-on-the-hub (accessed Jan 22, 2024).

(87) Friedman, J. H. Greedy Function Approximation: A Gradient Boosting Machine. *aos* 2001, *29* (5), 1189–1232.

(88) Firoozbakht, F.; Yousefi, B.; Schwikowski, B. An Overview of Machine Learning Methods for Monotherapy Drug Response Prediction. *Brief. Bioinform.* 2022, *23* (1).

(89) Park, A.; Lee, Y.; Nam, S. A Performance Evaluation of Drug Response Prediction Models

for Individual Drugs. *Sci. Rep.* 2023, *13* (1), 11911.

(90) Zhu, Y.; Brettin, T.; Evrard, Y. A.; Partin, A.; Xia, F.; Shukla, M.; Yoo, H.; Doroshow, J. H.; Stevens, R. L. Ensemble Transfer Learning for the Prediction of Anti-Cancer Drug Response. *Sci. Rep.* 2020, *10* (1), 18040.

(91) Sharifi-Noghabi, H.; Peng, S.; Zolotareva, O.; Collins, C. C.; Ester, M. AITL: Adversarial Inductive Transfer Learning with Input and Output Space Adaptation for Pharmacogenomics. *Bioinformatics* 2020, *36* (Suppl_1), i380–i388.

(92) Lee, K.; Cho, D.; Jang, J.; Choi, K.; Jeong, H.-O.; Seo, J.; Jeong, W.-K.; Lee, S. RAMP: Response-Aware Multi-Task Learning with Contrastive Regularization for Cancer Drug Response Prediction. *Brief. Bioinform.* 2023, *24* (1).

(93) Li, Y.; Hostallero, D. E.; Emad, A. Interpretable Deep Learning Architectures for Improving Drug Response Prediction Performance: Myth or Reality? *Bioinformatics* 2023, *39* (6).

(94) Tang, Y.-C.; Gottlieb, A. Explainable Drug Sensitivity Prediction through Cancer Pathway Enrichment. *Sci. Rep.* 2021, *11* (1), 3128.

(95) Stone, M. Cross-Validatory Choice and Assessment of Statistical Predictions. *J. R. Stat. Soc.* 1974, *36* (2), 111–133.

(96) Eisenhauer, E. A.; Therasse, P.; Bogaerts, J.; Schwartz, L. H.; Sargent, D.; Ford, R.; Dancey, J.; Arbuck, S.; Gwyther, S.; Mooney, M.; Rubinstein, L.; Shankar, L.; Dodd, L.; Kaplan, R.; Lacombe, D.; Verweij, J. New Response Evaluation Criteria in Solid Tumours: Revised RECIST Guideline (Version 1.1). *Eur. J. Cancer* 2009, *45* (2), 228–247.

(97) Feaster, D. J.; Mitrani, V. B.; Burns, M. J.; McCabe, B. E.; Brincks, A. M.; Rodriguez, A. E.; Asthana, D.; Robbins, M. S. A Randomized Controlled Trial of Structural Ecosystems Therapy for HIV Medication Adherence and Substance Abuse Relapse Prevention. *Drug Alcohol Depend.* 2010, *111* (3), 227–234.

(98) Schulman, K. L.; Berenson, K.; Tina Shih, Y.-C.; Foley, K. A.; Ganguli, A.; de Souza, J.; Yaghmour, N. A.; Shteynshlyuger, A. A Checklist for Ascertaining Study Cohorts in Oncology Health Services Research Using Secondary Data: Report of the ISPOR Oncology Good Outcomes Research Practices Working Group. *Value Health* 2013, *16* (4), 655–669.

(99) Partin, A.; Brettin, T.; Zhu, Y.; Dolezal, J. M.; Kochanny, S.; Pearson, A. T.; Shukla, M.; Evrard, Y. A.; Doroshow, J. H.; Stevens, R. L. Data Augmentation and Multimodal Learning for Predicting Drug Response in Patient-Derived Xenografts from Gene Expressions and Histology Images. *Front. Med.* 2023, *10*, 1058919.

(100) He, D.; Liu, Q.; Wu, Y.; Xie, L. A Context-Aware Deconfounding Autoencoder for Robust Prediction of Personalized Clinical Drug Response from Cell-Line Compound Screening. *Nature Machine Intelligence* 2022, *4* (10), 879–892.

(101) Moore, D. H., II. Classification and Regression Trees, by Leo Breiman, Jerome H. Friedman, Richard A. Olshen, and Charles J. Stone. Brooks/Cole Publishing, Monterey, 1984,358 Pages, $27.95. *Cytometry* 1987, *8* (5), 534–535.

(102) Ma, J.; Yu, M. K.; Fong, S.; Ono, K.; Sage, E.; Demchak, B.; Sharan, R.; Ideker, T. Using Deep Learning to Model the Hierarchical Structure and Function of a Cell. *Nat. Methods* 2018, *15* (4), 290–298.

(103) Kuenzi, B. M.; Park, J.; Fong, S. H.; Sanchez, K. S.; Lee, J.; Kreisberg, J. F.; Ma, J.; Ideker, T. Predicting Drug Response and Synergy Using a Deep Learning Model of Human Cancer Cells. *Cancer Cell* 2020, *38* (5), 672-684.e6.

(104) Elmarakeby, H. A.; Hwang, J.; Arafeh, R.; Crowdis, J.; Gang, S.; Liu, D.; AlDubayan, S. H.; Salari, K.; Kregel, S.; Richter, C.; Arnoff, T. E.; Park, J.; Hahn, W. C.; Van Allen, E. M. Biologically Informed Deep Neural Network for Prostate Cancer Discovery. *Nature* 2021, *598* (7880), 348–352.

(105) Huang, X.; Huang, K.; Johnson, T.; Radovich, M.; Zhang, J.; Ma, J.; Wang, Y. ParsVNN: Parsimony Visible Neural Networks for Uncovering Cancer-Specific and Drug-Sensitive Genes and Pathways. *NAR Genom Bioinform* 2021, *3* (4), lqab097.

(106) Ba-Alawi, W.; Nair, S. K.; Li, B.; Mammoliti, A.; Smirnov, P.; Mer, A. S.; Penn, L. Z.; Haibe-Kains, B. Bimodal Gene Expression in Patients with Cancer Provides Interpretable Biomarkers for Drug Sensitivity. *Cancer Res.* 2022, *82* (13), 2378–2387.

(107) Ribeiro, M. T.; Singh, S.; Guestrin, C. "Why Should I Trust You?": Explaining the Predictions of Any Classifier. In *Proceedings of the 22nd ACM SIGKDD International Conference on Knowledge Discovery and Data Mining*; KDD '16; Association for Computing Machinery: New York, NY, USA, 2016; pp 1135–1144.

(108) Office of the Commissioner. Artificial intelligence and medical products https://www.fda.gov/science-research/science-and-research-special-topics/artificial-intelligence-and-medical-products (accessed Apr 4, 2024).

(109) Using artificial intelligence & machine learning in the development of drug and biological products https://www.fda.gov/media/167973 (accessed Apr 4, 2024).

(110) Narla, A.; Kuprel, B.; Sarin, K.; Novoa, R.; Ko, J. Automated Classification of Skin Lesions: From Pixels to Practice. *J. Invest. Dermatol.* 2018, *138* (10), 2108–2110.

(111) Winkler, J. K.; Fink, C.; Toberer, F.; Enk, A.; Deinlein, T.; Hofmann-Wellenhof, R.; Thomas, L.; Lallas, A.; Blum, A.; Stolz, W.; Haenssle, H. A. Association Between Surgical Skin Markings in Dermoscopic Images and Diagnostic Performance of a Deep Learning Convolutional Neural Network for Melanoma Recognition. *JAMA Dermatol.* 2019, *155* (10), 1135–1141.

(112) DeGrave, A. J.; Janizek, J.; Lee, S.-I. AI for Radiographic COVID-19 Detection Selects Shortcuts over Signal. *Nature Machine Intelligence* 2021, *3* (7), 610–619.

(113) Peng, R. D.; Hicks, S. C. Reproducible Research: A Retrospective. *Annu. Rev. Public Health* 2021, *42*, 79–93.

(114) Wilkinson, M. D.; Dumontier, M.; Aalbersberg, I. J. J.; Appleton, G.; Axton, M.; Baak, A.; Blomberg, N.; Boiten, J.-W.; da Silva Santos, L. B.; Bourne, P. E.; Bouwman, J.; Brookes, A. J.; Clark, T.; Crosas, M.; Dillo, I.; Dumon, O.; Edmunds, S.; Evelo, C. T.; Finkers, R.;

Gonzalez-Beltran, A.; Gray, A. J. G.; Groth, P.; Goble, C.; Grethe, J. S.; Heringa, J.; 't Hoen, P. A. C.; Hooft, R.; Kuhn, T.; Kok, R.; Kok, J.; Lusher, S. J.; Martone, M. E.; Mons, A.; Packer, A. L.; Persson, B.; Rocca-Serra, P.; Roos, M.; van Schaik, R.; Sansone, S.-A.; Schultes, E.; Sengstag, T.; Slater, T.; Strawn, G.; Swertz, M. A.; Thompson, M.; van der Lei, J.; van Mulligen, E.; Velterop, J.; Waagmeester, A.; Wittenburg, P.; Wolstencroft, K.; Zhao, J.; Mons, B. The FAIR Guiding Principles for Scientific Data Management and Stewardship. *Sci Data* 2016, *3*, 160018.

(115) Models - Hugging Face https://huggingface.co/models (accessed Jan 22, 2024).

(116) MHub - The New Deployment Standard for Medical Imaging AI https://mhub.ai/ (accessed Jan 22, 2024).

(117) Wilson, S. L.; Way, G. P.; Bittremieux, W.; Armache, J.-P.; Haendel, M. A.; Hoffman, M. M. Sharing Biological Data: Why, When, and How. *FEBS Lett.* 2021, *595* (7), 847–863.

(118) Heil, B. J.; Hoffman, M. M.; Markowetz, F.; Lee, S.-I.; Greene, C. S.; Hicks, S. C. Reproducibility Standards for Machine Learning in the Life Sciences. *Nat. Methods* 2021, *18* (10), 1132–1135.

(119) Haibe-Kains, B.; Adam, G. A.; Hosny, A.; Khodakarami, F.; Massive Analysis Quality Control (MAQC) Society Board of Directors; Waldron, L.; Wang, B.; McIntosh, C.; Goldenberg, A.; Kundaje, A.; Greene, C. S.; Broderick, T.; Hoffman, M. M.; Leek, J. T.; Korthauer, K.; Huber, W.; Brazma, A.; Pineau, J.; Tibshirani, R.; Hastie, T.; Ioannidis, J. P. A.; Quackenbush, J.; Aerts, H. J. W. L. Transparency and Reproducibility in Artificial Intelligence. *Nature* 2020, *586* (7829), E14–E16.

(120) *Ethics and Governance of Artificial Intelligence for Health: WHO Guidance*; World Health Organization, 2021.

(121) Corrêa, N. K.; Galvão, C.; Santos, J. W.; Del Pino, C.; Pinto, E. P.; Barbosa, C.; Massmann, D.; Mambrini, R.; Galvão, L.; Terem, E.; de Oliveira, N. Worldwide AI Ethics: A Review of 200 Guidelines and Recommendations for AI Governance. *Patterns (N Y)* 2023, *4* (10), 100857.

(122) Social determinants of health https://www.who.int/health-topics/social-determinants-of-health (accessed May 22, 2024).

(123) International Classification of Diseases (ICD) https://www.who.int/standards/classifications/classification-of-diseases (accessed May 22, 2024).

(124) ICD-10-CM Official Guidelines for Coding and Reporting FY 2023 -- UPDATED April 1, 2023 (October 1, 2022 - September 30, 2023). 2023.

(125) Domingues, B.; Lopes, J. M.; Soares, P.; Pópulo, H. Melanoma Treatment in Review. *Immunotargets Ther* 2018, *7*, 35–49.

(126) Byeon, S.; Cho, H. J.; Jang, K.-T.; Kwon, M.; Lee, J.; Lee, J.; Kim, S. T. Molecular Profiling of Asian Patients with Advanced Melanoma Receiving Check-Point Inhibitor Treatment. *ESMO Open* 2021, *6* (1), 100002.

(127) Castellani, G.; Buccarelli, M.; Arasi, M. B.; Rossi, S.; Pisanu, M. E.; Bellenghi, M.; Lintas, C.; Tabolacci, C. BRAF Mutations in Melanoma: Biological Aspects, Therapeutic Implications, and Circulating Biomarkers. *Cancers* 2023, *15* (16).

(128) Mosher, J. T.; Pemberton, T. J.; Harter, K.; Wang, C.; Buzbas, E. O.; Dvorak, P.; Simón, C.; Morrison, S. J.; Rosenberg, N. A. Lack of Population Diversity in Commonly Used Human Embryonic Stem-Cell Lines. *N. Engl. J. Med.* 2010, *362* (2), 183–185.

(129) Badal, S. Ethnically Diverse Cancer Cell Lines for Drug Testing. *Nat. Rev. Cancer* 2022, *22* (2), 65–66.

(130) Verma, S.; Rubin, J. Fairness Definitions Explained. In *Proceedings of the International Workshop on Software Fairness*; FairWare '18; Association for Computing Machinery: New York, NY, USA, 2018; pp 1–7.

(131) Vaughn, L. *Bioethics: Principles, Issues, and Cases*; Oxford University Press, 2020.

(132) Tännsjö, T.; Tännsjö, T. *Setting Health-Care Priorities: What Ethical Theories Tell Us*; Oxford University Press, 2019.

(133) Arneson, R. J. *Prioritarianism*; Cambridge University Press, 2022.

(134) Ma, J.; Fong, S. H.; Luo, Y.; Bakkenist, C. J.; Shen, J. P.; Mourragui, S.; Wessels, L. F. A.; Hafner, M.; Sharan, R.; Peng, J.; Ideker, T. Few-Shot Learning Creates Predictive Models of Drug Response That Translate from High-Throughput Screens to Individual Patients. *Nat Cancer* 2021, *2* (2), 233–244.

(135) So, E.; Yu, F.; Wang, B.; Haibe-Kains, B. Reusability Report: Evaluating Reproducibility and Reusability of a Fine-Tuned Model to Predict Drug Response in Cancer Patient Samples. *Nature Machine Intelligence* 2023, *5* (7), 792–798.

(136) Meyers, R. M.; Bryan, J. G.; McFarland, J. M.; Weir, B. A.; Sizemore, A. E.; Xu, H.; Dharia, N. V.; Montgomery, P. G.; Cowley, G. S.; Pantel, S.; Goodale, A.; Lee, Y.; Ali, L. D.; Jiang, G.; Lubonja, R.; Harrington, W. F.; Strickland, M.; Wu, T.; Hawes, D. C.; Zhivich, V. A.; Wyatt, M. R.; Kalani, Z.; Chang, J. J.; Okamoto, M.; Stegmaier, K.; Golub, T. R.; Boehm, J. S.; Vazquez, F.; Root, D. E.; Hahn, W. C.; Tsherniak, A. Computational Correction of Copy Number Effect Improves Specificity of CRISPR–Cas9 Essentiality Screens in Cancer Cells. *Nat. Genet.* 2017, *49* (12), 1779–1784.

(137) Smirnov, P.; Smith, I.; Safikhani, Z.; Ba-Alawi, W.; Khodakarami, F.; Lin, E.; Yu, Y.; Martin, S.; Ortmann, J.; Aittokallio, T.; Hafner, M.; Haibe-Kains, B. Evaluation of Statistical Approaches for Association Testing in Noisy Drug Screening Data. *BMC Bioinformatics* 2022, *23* (1), 188.

(138) Lenhof, K.; Gerstner, N.; Kehl, T.; Eckhart, L.; Schneider, L.; Lenhof, H.-P. MERIDA: A Novel Boolean Logic-Based Integer Linear Program for Personalized Cancer Therapy. *Bioinformatics* 2021, *37* (21), 3881–3888.

(139) Aharonov, R.; Dinstag, G.; Shulman, E.; Elis, E.; Ben-Zvi, D.; Tirosh, O.; Hoang, D.-T.; SInha, S.; Apolo, A. B.; Dahut, W. L.; Lipkowitz, S.; Berger, R.; Kurzrock, R.; Papanicolau-Sengos, A.; Karzai, F.; Rajagopal, P. S.; Gilbert, M. R.; Aldape, K. D.; Beker, T.; Ruppin, E.

ENLIGHT: Pancancer Response Prediction to Targeted and Immunotherapies via Tumor Transcriptomics. *J. Clin. Orthod.* 2022, *40* (16_suppl), e13556–e13556.

(140) Knijnenburg, T. A.; Klau, G. W.; Iorio, F.; Garnett, M. J.; McDermott, U.; Shmulevich, I.; Wessels, L. F. A. Logic Models to Predict Continuous Outputs Based on Binary Inputs with an Application to Personalized Cancer Therapy. *Sci. Rep.* 2016, *6*, 36812.

(141) The Bletchley Declaration by Countries Attending the AI Safety Summit, 1-2 November 2023 https://www.gov.uk/government/publications/ai-safety-summit-2023-the-bletchley-declaration/the-bletchley-declaration-by-countries-attending-the-ai-safety-summit-1-2-november-2023 (accessed May 22, 2024).

(142) Russell, R. G.; Lovett Novak, L.; Patel, M.; Garvey, K. V.; Craig, K. J. T.; Jackson, G. P.; Moore, D.; Miller, B. M. Competencies for the Use of Artificial Intelligence-Based Tools by Health Care Professionals. *Acad. Med.* 2023, *98* (3), 348–356.

(143) Lee, T. C.; Shah, N. U.; Haack, A.; Baxter, S. L. Clinical Implementation of Predictive Models Embedded within Electronic Health Record Systems: A Systematic Review. *Informatics (MDPI)* 2020, *7* (3).

(144) Adam, G. A.; Chang, C.-H. K.; Haibe-Kains, B.; Goldenberg, A. Hidden Risks of Machine Learning Applied to Healthcare: Unintended Feedback Loops Between Models and Future Data Causing Model Degradation. In *Proceedings of the 5th Machine Learning for Healthcare Conference*; Doshi-Velez, F., Fackler, J., Jung, K., Kale, D., Ranganath, R., Wallace, B., Wiens, J., Eds.; Proceedings of Machine Learning Research; PMLR, 07--08 Aug 2020; Vol. 126, pp 710–731.

(145) Sahiner, B.; Chen, W.; Samala, R. K.; Petrick, N. Data Drift in Medical Machine Learning: Implications and Potential Remedies. *Br. J. Radiol.* 2023, *96* (1150), 20220878.

(146) Choudhury, A. Factors Influencing Clinicians' Willingness to Use an AI-Based Clinical Decision Support System. *Front Digit Health* 2022, *4*, 920662.

Chapter 2 Multiscale community detection in Cytoscape

2.1 Abstract

Detection of community structure has become a fundamental step in the analysis of biological networks with application to protein function annotation, disease gene prediction, and drug discovery. This recent impact creates a need to make these techniques and their accompanying visualization schemes available to a broad range of biologists. Here we present a service-oriented, end-to-end software framework, CDAPS (Community Detection APplication and Service), that integrates the identification, annotation, visualization, and interrogation of multiscale network communities, accessible within the popular Cytoscape network analysis platform. With novel design principles, CDAPS addresses unmet new challenges, such as identifying hierarchical community structures, comparison of outputs generated from diverse network resources, and easy deployment of new algorithms, to facilitate community-sourced science. We demonstrate that the CDAPS framework can be applied to high-throughput protein-protein interaction networks to gain novel insights, such as the identification of putative new members of known protein complexes.

2.2 Introduction

One of the fundamental features of a complex network is the notion of community, which can be defined as a group of nodes that are more densely connected with each other than they are to the rest of the network. Community detection is a class of pattern recognition methods that assign network nodes to groups, or communities, based on the network‘s structural organization. As an important technique to probe the structural organization of a complex network, it has been successfully applied to many problem domains in systems biology, such as identifying protein complexes[1–4], cataloging ‘omics profiles[5–8], and prioritizing new disease genes[9–11].

Clustering, which relates to community detection at a single scale, is a well-established technique in network analysis and is supported by many applications such as Clustermaker2[12],

CytoCluster[13], ClusterViz[14], and MCODE[15], which have been made available in bioinformatics environments like Cytoscape[16]. Recent work in multiscale network community detection makes it possible to build hierarchical representations of biological structure and function directly from networks[17–19]. These developments create a new challenge: to make multiscale community detection techniques and their accompanying visualization schemes available to a broad range of biologists.

Here, we present a software infrastructure to address these challenges, termed CDAPS (Community Detection APplication and Service), deployed as an App in the Cytoscape platform for network analysis. CDAPS has several novel aspects in its design relative to existing applications in the field of bioinformatics. First, beyond assigning nodes in an input network to a set of clusters, multiscale community detection in CDAPS summarizes a network's underlying multiscale structure in a separate hierarchical ontology, where each node represents a community. Second, CDAPS invokes community detection and functional enrichment algorithms via REST (REpresentational State Transfer) queries to a remote service outside of the Java-based Cytoscape desktop environment (Figure 2.1). On that service, community detection algorithms are encapsulated using Docker containers[20], enabling them to run in their native language and environment. Further, the use of remote servers allows incorporation of new algorithms without the need to update the App, and it removes the computational overhead of running these algorithms in the Cytoscape desktop application. Overall, CDAPS provides an end-to-end pipeline that creates, annotates, visualizes, and interrogates hierarchical models based on multiscale patterns in networks.

2.3 Design and implementation

The CDAPS framework contains two major components: CD App and CD service. CD App is part of the Cytoscape desktop application and acts as a client to the CD service. The CD service, as a typical service-oriented architecture[21], performs the community detection computation on a remote server. In the CD App, the user chooses a community detection

algorithm to be applied to a given *interaction network* and then the pertinent data is sent to the CD service, where a Docker image hosting the algorithm is invoked to produce a hierarchical network. The results are returned to the CD App, which generates a new *hierarchy network*, or ontology, which contains information of the resulting communities (as nodes) and their hierarchical relationships (as edges). The whole framework provides efficient interfaces among different modular components of the pipeline (Figure 2.1).

2.3.1 CD App

CD App is an App for Cytoscape[16] which acts as a client for the CD service, providing a convenient user interface through menu options. Below we briefly describe its functions:

1. **Community detection**: In this initial release, we provide four algorithms: Louvain[22], Infomap[23,24], OSLOM[25], and CliXO[26]. Louvain, Infomap, and OSLOM are popular community detection algorithms which are highly scalable and capable of organizing multiscale communities as a hierarchy. We also include our previously described CliXO algorithm, which uniquely organizes communities hierarchically in the form of a directed acyclic graph (DAG), i.e. a community is allowed to be part of different overlapping communities. These algorithms have previously been implemented without graphical user interfaces, making it difficult for new users to tune their parameters. Through CDAPS, we provide an interactive interface to tune parameters, such as the “resolution parameters” in Louvain (via Reichardt-Bornholdt configuration model[27] implemented in http://github.com/vtraag/louvain-igraph), Infomap (via the Markov time parameter in the Infomap package[28]), and OSLOM that control the granularity of the resulting communities. Because community detection is an active research field, and many new algorithms are proposed every year[29], the CD app is designed to be easily extended by packaging new algorithms as Docker images in a standardized format and adding them to the CD service (see details in "CD service").

2. **Functional enrichment**: One of the key downstream analyses of community detection is to annotate the resultant protein communities by determining their overlap with gene sets associated with known functional or biological entities. We currently provide interfaces with the following external functional enrichment tools: g:Profiler[30], Enrichr[31], and iQuery (iquery.ndexbio.org). These tools can be applied to all or a subset of communities.
3. **Interaction sub-networks**: We also provide a feature to enable interrogation of the communities in the hierarchical model by retrieving the subgraph of the interaction network corresponding to the genes in a given community.

Functional enrichment and sub-network interrogation can be invoked by menu options associated with any node (i.e. a community) in the hierarchy network. The CDAPS framework considers a hierarchy network and its source interaction network as two separate entities. We link these networks by keeping a simple reference to the source interaction network as an attribute of the hierarchy network. For a given interaction network, users can generate many alternative hierarchies with different algorithms and parameter settings, and they can save and manage them independently. For reproducibility, the CD App stores the name of the algorithms and the accompanying parameters as an attribute of the hierarchy network.

2.3.2 CD service

CD service is a REST web service that acts as a bridge between the Cytoscape desktop app and the hierarchical community detection algorithms. The service provides a platform-independent endpoint that is accessible to CD App and other tools such as a website or Jupyter notebook[32]. To facilitate easy installation and reproducibility, community detection algorithms are packaged as Docker images that are called by the CD Service on remote servers (Figure 2.1). An additional advantage of using remote servers is to avoid problems on platforms that do not support direct invocation of Docker images.

The infrastructure of the CD service facilitates updates and extends the capabilities of the CD app by enabling new Docker images to be incorporated into the CD service to support additional algorithms. Updates to the CD service are transparent to users because the CD App automatically updates its interface by querying the service to find the latest algorithms and their parameters. In addition to the community detection algorithms, the CD Service interfaces to external functional enrichment tools to find annotations that can help label a community and provide insight into its function (see the "CD App" section above).

2.4 Results

As proof of concept, we explored a workflow for creating a hierarchical model from a large protein interaction network in Cytoscape. Without loss of generality, we chose to use OSLOM[25] as the community detection algorithm and BioPlex 2.0[4] as the interaction network. BioPlex is a physical protein-protein interaction network containing 10,961 proteins and 56,553 interactions determined by the affinity-purification mass-spectrometry (AP-MS) technique. The goal of the analysis was to reveal meaningful structures of this complex network, as well as to discover *de novo* protein modules or novel extensions of previously identified protein modules. We then used a functional enrichment tool, g:Profiler[30], to generate labels for communities based on significant overlap with gene sets in databases. We describe the steps of this workflow as follows.

1. Download and install Cytoscape from http://www.cytoscape.org/.
2. Start Cytoscape and instantiate a new session.
3. Install the app. **Apps > App Manager > Select "CyCommunityDetection" > Install**.
4. Import the example network. Click **NDEx icon > Import Network from NDEx > Search "BioPlex" > Select "BioPlex 2.0 (56,000 interactions)" > Close.** The DOI of this network is http://doi.org/10.18119/N91597.
5. Execute OSLOM for BioPlex (Figure 2.2). Click **Apps > Community Detection > Run Community Detection > Select "OSLOM" from the algorithm drop-down > Set "coverage**

parameter" to 0.2 > Set "random number seed" to 1 > Run. This step creates a hierarchy network. Note that community detection algorithms are in general stochastic, and thus they may generate different results if the random seed parameter is not fixed. The parameters of community detection, including (if applicable) the random seed, are stored as a property of this hierarchical network to ensure the reproducibility of this workflow (column "description" of network table).

6. Run functional enrichment on the hierarchy network. Click **Apps > Community Detection > Run Functional Enrichment > Select g:Profiler from the algorithm drop-down > Set "minimum overlap" to 0.05 > Run.** This step adds annotations to the hierarchy network (Figures 2.3A and 2.3B).

7. Without loss of generality, with the hierarchy network in the viewport, type "mediator" in the search box at the upper-right corner of Cytoscape to highlight the two nodes annotated as "mediator complex". This is because the "mediator complex" is the best-matched gene set in reference databases of g:Profiler for both communities (Figure 2.3C). Between these two communities, the smaller one with 51 genes better matches the reference version of the "mediator complex" (CORUM:230; Jaccard index 0.64; relevant information can be found in columns "CD_AnnotatedMembers_SourceTerm" and "CD_AnnotatedMembers_Overlap").

8. For this node, copy the content in the attribute "CD_NonAnnotatedMembers" in the "Node Table" of the hierarchy network, which represents a subset of proteins in the community that is not recorded in the database entry of "mediator complex" queried by g:Profiler (i.e. CORUM:230 in this example).

9. **Right-click the node > Apps > Community Detection > View Interactions for Selected Node.** It creates a sub-network of the BioPlex 2.0, which contains only the proteins in this community (51 nodes, 269 edges) (Figure 2.3D).

10. With the interaction sub-network in the viewport, paste the string copied from Step 8 in the search box above the upper right corner of the viewport. It highlights some nodes in the interaction sub-network.

11. From the results, it can be noticed that several proteins that have not been known as members of the mediator complex (e.g. BIRC5, LZIC, NR1I3, TCL1B) have many interactions with known mediator complex members[33] (Figure 2.3D). These proteins are putative novel components of the mediator complex based on the BioPlex 2.0 network.

In support of their association with Mediator, BIRC5 and NR1I3 have reported roles as transcriptional activators[34,35], in agreement with the function of the Mediator complex which transduces signals from transcriptional activators bound to enhancers to the basal transcription machinery (including RNA polymerase II)[33], suggesting that these physical interactions are functionally relevant.

To test the performance of the CDAPS framework, we ran three community detection algorithms, Louvain, Infomap, and OSLOM[22,23,25], available through CDAPS, on popular biological networks and recorded the time taken by the algorithms inside the CD service along with the runtime corresponding to overhead (time taken transmitting the network and visualizing/constructing the resultant hierarchy). We observed that the fraction of time spent on overhead decreases sharply as the total runtime increases, suggesting that our implementation of CDAPS efficiently integrates the algorithms into the Cytoscape interface. For instance, for the Bioplex 2.0 network[4], the total runtime with OSLOM is about 43.85 seconds, including the CDAPS overhead time of 0.99 seconds, 2.3% of the total runtime (Table 2.1). In general, for any network for which the total runtime exceeds 50 seconds, the time overhead of running a community detection algorithm through CDAPS has a median of less than 1%. The CD service is currently hosted on an Intel(R) Xeon(R) E5-2687W v3 processor with 32 GB of memory. All the Docker containers are run with the default configuration and, thus, each container has all the resources of the host processor.

2.5 Availability and future directions

Flexibility and extensibility are the two main strengths of the CDAPS framework, allowing us and others to continue to grow and evolve the repertoire of community detection algorithms available to users. The use of Docker images to encapsulate algorithms will reduce the need for customization and simplify their deployment to the service. As new algorithms are deployed to CDAPS, the CD App will fetch the list of currently available algorithms from the CD service and update the CD app interface in Cytoscape without requiring any action on the part of users.

To enable a web-based, interactive investigation of hierarchical models of network communities, a compelling future direction is to create a pipeline that connects the CDAPS to our HiView platform[35]. HiView provides an intuitive visualization of hierarchical/nested structures with a powerful “circle packing” layout[34], as well as the ability to use any community-defined gene list to probe the support of the same community in orthogonal network datasets hosted on the NDEx database[36].

We will also apply workflows that use the results of community detection to select particular communities of high interest, such as those that significantly aggregate the disease-related statistical signals of individual genes/proteins extracted from large-scale genomic studies including GWAS (Genome-Wide Association Studies)[11,37] and cancer whole-exome sequencing.

The source code of CD App, along with the user documentation, is available at https://github.com/cytoscape/cy-community-detection. CD App can be directly installed through the Cytoscape Application Manager. The codebase of CD service and its documentation is available at https://github.com/cytoscape/communitydetection-rest-server.

2.6 Figures

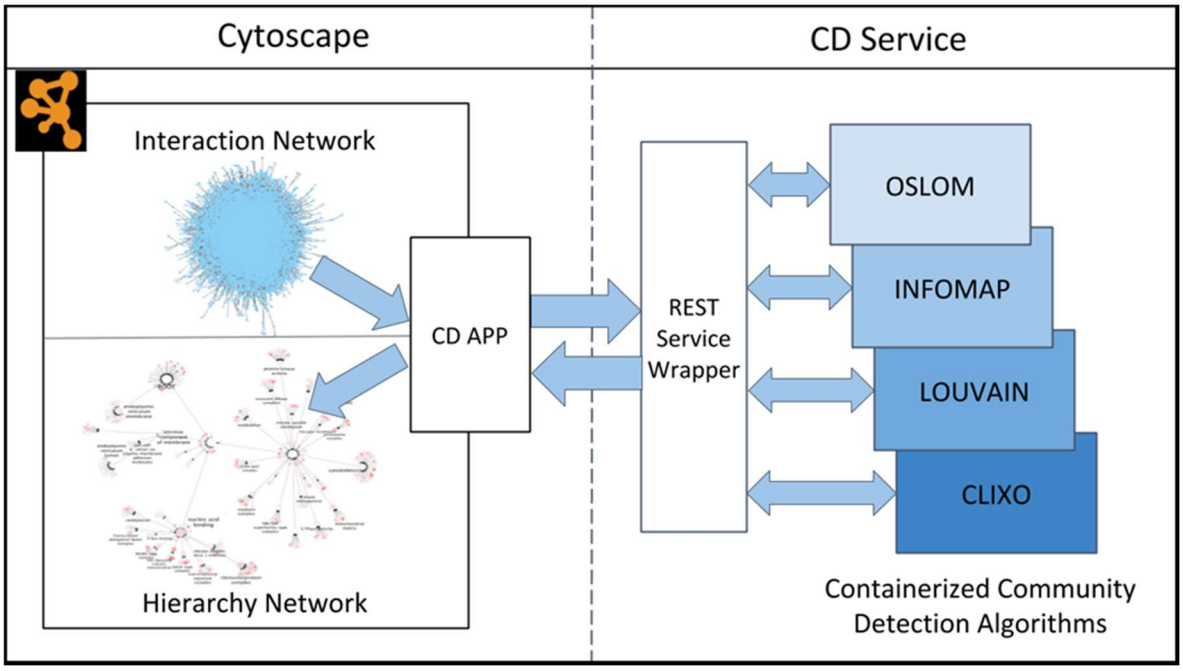

Figure 2.1: Overview of the CDAPS workflow.

A flowchart illustrating various components of the CDAPS framework and the data flow between them. The CD app can send edges of an interaction network for community detection to the CD service. The service then launches the corresponding Docker image which executes the required task and sends back a hierarchy network to the CD app for visualization and community labeling.

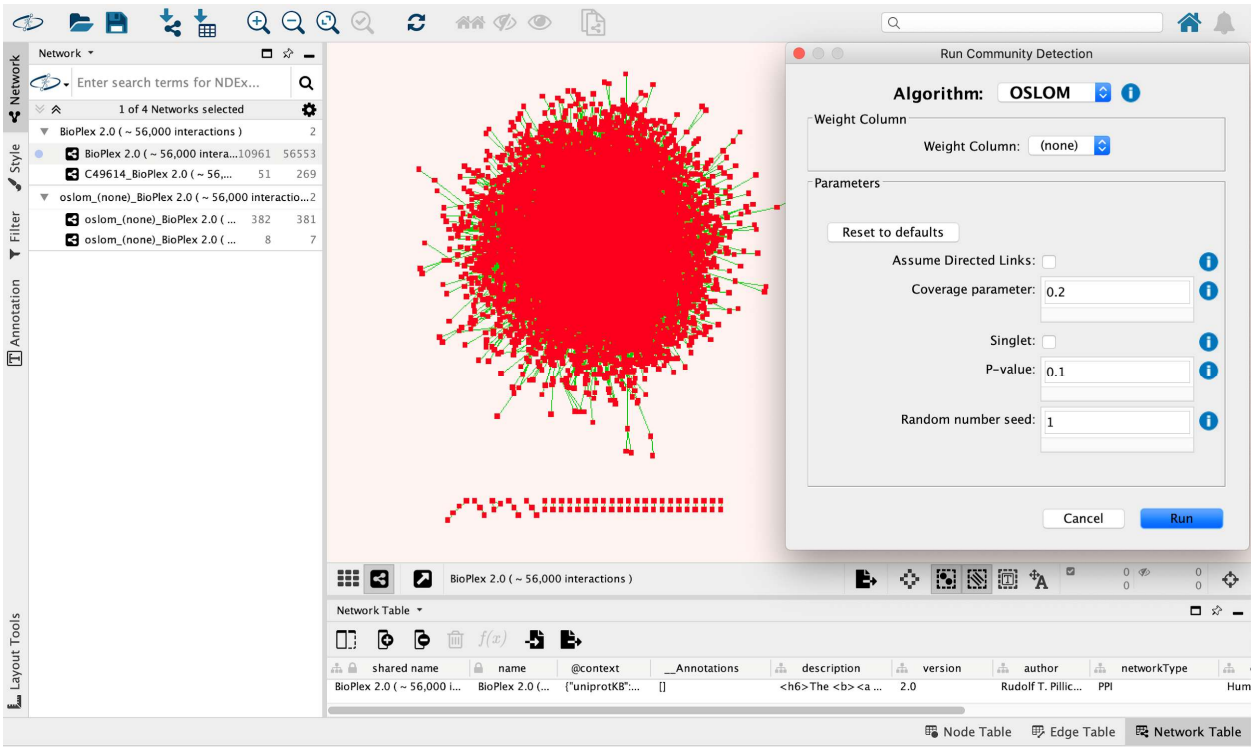

Figure 2.2: Run community detection on a protein-protein interaction network.

A Cytoscape example screenshot showing the BioPlex 2.0 network[4] imported from NDEx (http://doi.org/10.18119/N91597), along with settings for running OSLOM[25]. Related to steps 4-5 in the example workflow.

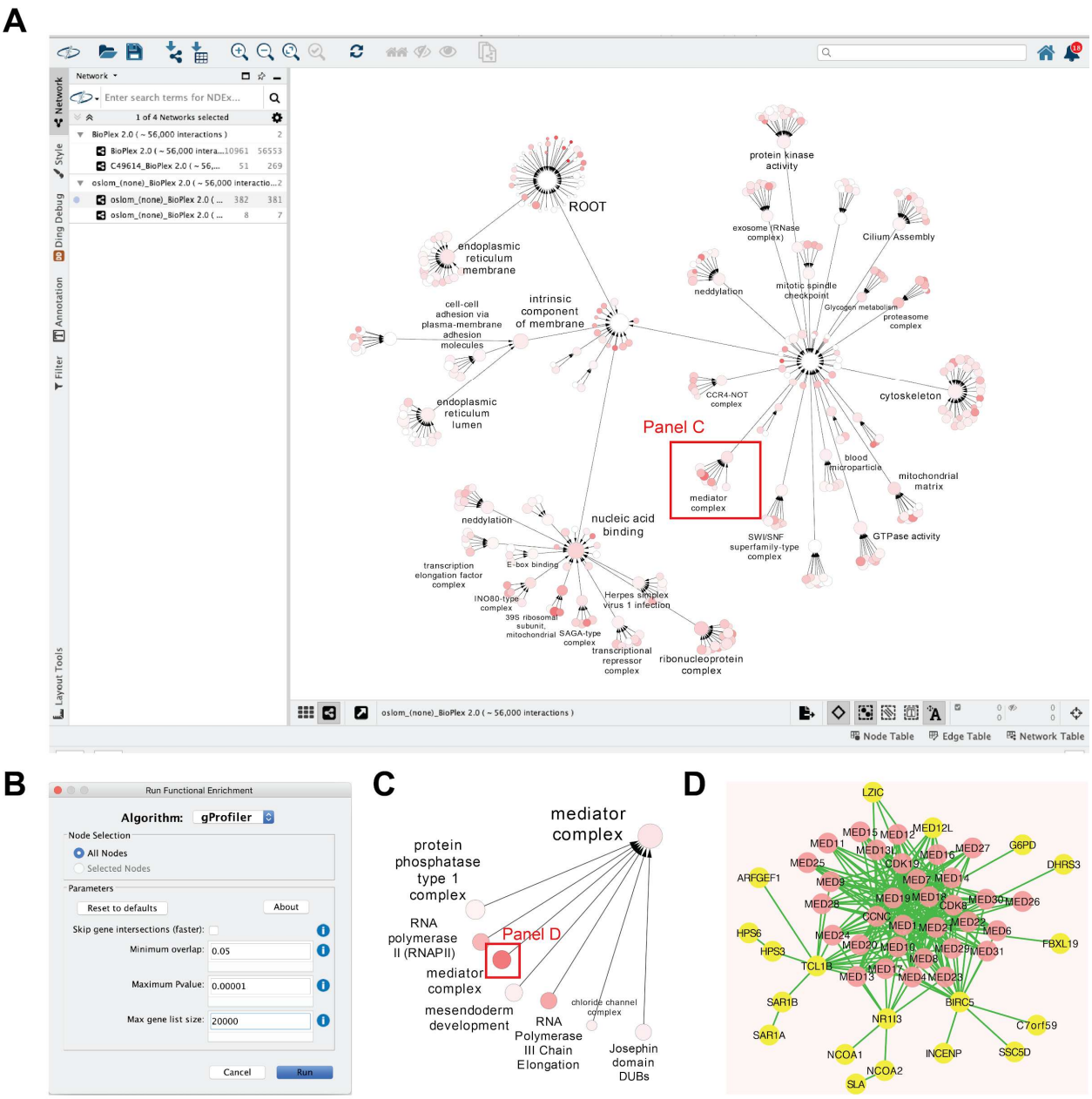

Figure 2.3: Results of hierarchical community detection and downstream analyses.

(A) A hierarchy derived from the BioPlex 2.0[4] interaction network with OSLOM[25] and annotated by g:Profiler. *Red rectangle*: a subregion in the hierarchy related to the mediator complex. (B) The menu to set up functional annotation with g:Profiler. (C) A zoom-in view of the sub-hierarchy highlighted in panel A. *Red rectangle:* a community to be further explored. (D) The interaction subnetwork of the community highlighted in panel C. Proteins, not known as members of the mediator complex, are highlighted (*yellow*). Related to steps 6-11 in the example workflow. *Node color*: The overlap (Jaccard Index) between a community and the gene set corresponding to its annotation (panels A and C). Networks can be found on NDEx: http://www.ndexbio.org/#/network/380d5904-bd9f-11ea-aaef-0ac135e8bacf (panel A). http://www.ndexbio.org/#/network/28fdd535-bbe5-11ea-aaef-0ac135e8bacf (panel D).

2.7 Tables

Table 2.1: Run-time performance of CDAPS.

Input Network (*nodes/edges*)	Louvain Runtime (T1*/T2†/T3⧫ in s)	Infomap Runtime (T1*/T2†/T3⧫ in s)	OSLOM Runtime (T1*/T2†/T3⧫ in s)
Drugbank Database - v4.1 (*7,093/13,239*)	1.09/2.16/2.31	0.97/1.10/1.48	20.79/21.21/21.60
BioPlex 2.0 (*10,961/56,553*)	1.58/2.09/2.38	1.35/2.17/2.70	42.86/43.30/43.85
BioGRID: Protein-Protein Interactions (D. melanogaster) (*9,337/61,188*)	1.92/2.19/2.39	3.26/4.18/4.42	73.15/73.40/73.65
HumanNet - PI (*15,351/158,499*)	2.60/3.18/3.38	3.34/4.21/4.62	382.15/382.66/383.23
STRING - Human Protein Links - High Confidence (Score >= 0.7) (*17,185/420,534*)	4.01/4.39/4.63	11.57/12.42/12.89	191.02/192.25/193.97
Human Gene Regulatory Network of Mesothelioma (*17,490/631,556*)	8.03/8.56/8.88	20.35/21.58/22.11	421.13/422.28/422.80
DisGeNet - Gene-Disease-PMID Associations (*41,710/1,573,979*)	11.76/13.29/13.88	14.80/16.15/17.10	922.33/924.54/940.62

*T1 indicates the time taken by a community detection algorithm inside the CD Service.
†T2 indicates T1 plus the network transmission time to and from the CD Service.
⧫T3 indicates T2 plus network creation time in Cytoscape.

2.8 Author contributions

Conceptualization - DP, SF, FZ, TI

Formal Analysis - AS, SC

Funding Acquisition - DP, TI

Investigation - AS, SC, CC, FZ

Methodology - AS, SC, CC, FZ

Project Administration - AS, DP

Resources - DP, TI

Software - AS, SC, CC

Supervision - DP, TI

Validation - AS, SC, CC, DP, FZ

Visualization - AS, FZ

Writing – Original Draft Preparation - AS, SC, CC, FZ

Writing – Review & Editing - AS, DP, SF, FZ, TI

2.9 Acknowledgements

Chapter 2, in full, is a reformatted reprint of the material as it appears as “Multiscale community detection in Cytoscape” in PLOS Computational Biology, 2020 by Singhal, Akshat; Cao, Song; Churas, Chris; Pratt, Dexter; Fortunato, Santo; Zheng, Fan; Ideker, Trey. The dissertation author was a primary investigator and author of this paper.

2.10 References

(1) Li, X.; Wu, M.; Kwoh, C.-K.; Ng, S.-K. Computational Approaches for Detecting Protein Complexes from Protein Interaction Networks: A Survey. BMC Genomics 2010, 11 Suppl 1, S3.

(2) Palla, G.; Derényi, I.; Farkas, I.; Vicsek, T. Uncovering the Overlapping Community Structure of Complex Networks in Nature and Society. Nature 2005, 435 (7043), 814–818.

(3) Nepusz, T.; Yu, H.; Paccanaro, A. Detecting Overlapping Protein Complexes in Protein-Protein Interaction Networks. Nat. Methods 2012, 9 (5), 471–472.

(4) Huttlin, E. L.; Bruckner, R. J.; Paulo, J. A.; Cannon, J. R.; Ting, L.; Baltier, K.; Colby, G.; Gebreab, F.; Gygi, M. P.; Parzen, H.; Szpyt, J.; Tam, S.; Zarraga, G.; Pontano-Vaites, L.; Swarup, S.; White, A. E.; Schweppe, D. K.; Rad, R.; Erickson, B. K.; Obar, R. A.; Guruharsha, K. G.; Li, K.; Artavanis-Tsakonas, S.; Gygi, S. P.; Harper, J. W. Architecture of the Human Interactome Defines Protein Communities and Disease Networks. Nature 2017, 545 (7655), 505–509.

(5) Levine, J. H.; Simonds, E. F.; Bendall, S. C.; Davis, K. L.; Amir, E.-A. D.; Tadmor, M. D.; Litvin, O.; Fienberg, H. G.; Jager, A.; Zunder, E. R.; Finck, R.; Gedman, A. L.; Radtke, I.; Downing, J. R.; Pe'er, D.; Nolan, G. P. Data-Driven Phenotypic Dissection of AML Reveals Progenitor-like Cells That Correlate with Prognosis. Cell 2015, 162 (1), 184–197.

(6) Wolf, F. A.; Angerer, P.; Theis, F. J. SCANPY: Large-Scale Single-Cell Gene Expression Data Analysis. Genome Biol. 2018, 19 (1), 15.

(7) Butler, A.; Hoffman, P.; Smibert, P.; Papalexi, E.; Satija, R. Integrating Single-Cell Transcriptomic Data across Different Conditions, Technologies, and Species. Nat. Biotechnol. 2018, 36 (5), 411–420.

(8) Kiselev, V. Y.; Andrews, T. S.; Hemberg, M. Challenges in Unsupervised Clustering of Single-Cell RNA-Seq Data. Nat. Rev. Genet. 2019, 20 (5), 273–282.

(9) Cantini, L.; Medico, E.; Fortunato, S.; Caselle, M. Detection of Gene Communities in Multi-Networks Reveals Cancer Drivers. Sci. Rep. 2015, 5, 17386.

(10) Boyle, E. A.; Pritchard, J. K.; Greenleaf, W. J. High-Resolution Mapping of Cancer Cell Networks Using Co-Functional Interactions. Mol. Syst. Biol. 2018, 14 (12), e8594.

(11) Choobdar, S.; Ahsen, M. E.; Crawford, J.; Tomasoni, M.; Fang, T.; Lamparter, D.; Lin, J.; Hescott, B.; Hu, X.; Mercer, J.; Natoli, T.; Narayan, R.; DREAM Module Identification Challenge Consortium; Subramanian, A.; Zhang, J. D.; Stolovitzky, G.; Kutalik, Z.; Lage, K.; Slonim, D. K.; Saez-Rodriguez, J.; Cowen, L. J.; Bergmann, S.; Marbach, D. Assessment of Network Module Identification across Complex Diseases. Nat. Methods 2019, 16 (9), 843–852.

(12) Morris, J. H.; Apeltsin, L.; Newman, A. M.; Baumbach, J.; Wittkop, T.; Su, G.; Bader, G. D.; Ferrin, T. E. ClusterMaker: A Multi-Algorithm Clustering Plugin for Cytoscape. BMC Bioinformatics 2011, 12, 436.

(13) Li, M.; Li, D.; Tang, Y.; Wu, F.; Wang, J. CytoCluster: A Cytoscape Plugin for Cluster Analysis and Visualization of Biological Networks. Int. J. Mol. Sci. 2017, 18 (9).

(14) Wang, J.; Zhong, J.; Chen, G.; Li, M.; Wu, F.-X.; Pan, Y. ClusterViz: A Cytoscape APP for Cluster Analysis of Biological Network. IEEE/ACM Trans. Comput. Biol. Bioinform. 2015, 12 (4), 815–822.

(15) Bader, G. D.; Hogue, C. W. V. An Automated Method for Finding Molecular Complexes in Large Protein Interaction Networks. BMC Bioinformatics 2003, 4, 2.

(16) Shannon, P.; Markiel, A.; Ozier, O.; Baliga, N. S.; Wang, J. T.; Ramage, D.; Amin, N.;

Schwikowski, B.; Ideker, T. Cytoscape: A Software Environment for Integrated Models of Biomolecular Interaction Networks. Genome Res. 2003, 13 (11), 2498–2504.

(17) Ravasz, E.; Barabási, A.-L. Hierarchical Organization in Complex Networks. Phys. Rev. E Stat. Nonlin. Soft Matter Phys. 2003, 67 (2 Pt 2), 026112.

(18) Clauset, A.; Moore, C.; Newman, M. E. J. Hierarchical Structure and the Prediction of Missing Links in Networks. Nature 2008, 453 (7191), 98–101.

(19) Dutkowski, J.; Kramer, M.; Surma, M. A.; Balakrishnan, R.; Cherry, J. M.; Krogan, N. J.; Ideker, T. A Gene Ontology Inferred from Molecular Networks. Nat. Biotechnol. 2013, 31 (1), 38–45.

(20) Merkel, D. Docker: Lightweight Linux Containers for Consistent Development and Deployment. Linux J. 2014, 2014 (239), 2.

(21) Fowler, M.; Lewis, J. Microservices. Viittattu 2014, 28, 2015.

(22) Blondel, V. D.; Guillaume, J.-L.; Lambiotte, R.; Lefebvre, E. Fast Unfolding of Communities in Large Networks. J. Stat. Mech. 2008, 2008 (10), P10008.

(23) Rosvall, M.; Bergstrom, C. T. Maps of Random Walks on Complex Networks Reveal Community Structure. Proc. Natl. Acad. Sci. U. S. A. 2008, 105 (4), 1118–1123.

(24) Rosvall, M.; Bergstrom, C. T. Multilevel Compression of Random Walks on Networks Reveals Hierarchical Organization in Large Integrated Systems. PLoS One 2011, 6 (4), e18209.

(25) Lancichinetti, A.; Radicchi, F.; Ramasco, J. J.; Fortunato, S. Finding Statistically Significant Communities in Networks. PLoS One 2011, 6 (4), e18961.

(26) Kramer, M.; Dutkowski, J.; Yu, M.; Bafna, V.; Ideker, T. Inferring Gene Ontologies from Pairwise Similarity Data. Bioinformatics 2014, 30 (12), i34-42.

(27) Reichardt, J.; Bornholdt, S. Statistical Mechanics of Community Detection. Phys. Rev. E Stat. Nonlin. Soft Matter Phys. 2006, 74 (1 Pt 2), 016110.

(28) Kheirkhahzadeh, M.; Lancichinetti, A.; Rosvall, M. Efficient Community Detection of Network Flows for Varying Markov Times and Bipartite Networks. Phys Rev E 2016, 93 (3), 032309.

(29) Fortunato, S.; Hric, D. Community Detection in Networks: A User Guide. Phys. Rep. 2016, 659, 1–44.

(30) Raudvere, U.; Kolberg, L.; Kuzmin, I.; Arak, T.; Adler, P.; Peterson, H.; Vilo, J. G:Profiler: A Web Server for Functional Enrichment Analysis and Conversions of Gene Lists (2019 Update). Nucleic Acids Res. 2019, 47 (W1), W191–W198.

(31) Kuleshov, M. V.; Jones, M. R.; Rouillard, A. D.; Fernandez, N. F.; Duan, Q.; Wang, Z.; Koplev, S.; Jenkins, S. L.; Jagodnik, K. M.; Lachmann, A.; McDermott, M. G.; Monteiro, C. D.; Gundersen, G. W.; Ma'ayan, A. Enrichr: A Comprehensive Gene Set Enrichment Analysis Web Server 2016 Update. Nucleic Acids Res. 2016, 44 (W1), W90-7.

(32) Kluyver, T.; Ragan-Kelley, B.; Pérez, F.; Granger, B. E.; Bussonnier, M.; Frederic, J.; Kelley, K.; Hamrick, J. B.; Grout, J.; Corlay, S.; Others. Jupyter Notebooks-a Publishing Format for Reproducible Computational Workflows. In ELPUB; 2016; pp 87–90.

(33) Soutourina, J. Transcription Regulation by the Mediator Complex. Nat. Rev. Mol. Cell Biol. 2018, 19 (4), 262–274.

(34) Wang, W.; Wang, H.; Dai, G.; Wang, H. Visualization of Large Hierarchical Data by Circle Packing. In Proceedings of the SIGCHI Conference on Human Factors in Computing Systems; CHI ’06; ACM: New York, NY, USA, 2006; pp 517–520.

(35) Yu, M. K.; Ma, J.; Ono, K.; Zheng, F.; Fong, S. H.; Gary, A.; Chen, J.; Demchak, B.; Pratt, D.; Ideker, T. DDOT: A Swiss Army Knife for Investigating Data-Driven Biological Ontologies. Cell Syst 2019, 8 (3), 267-273.e3.

(36) Pratt, D.; Chen, J.; Welker, D.; Rivas, R.; Pillich, R.; Rynkov, V.; Ono, K.; Miello, C.; Hicks, L.; Szalma, S.; Stojmirovic, A.; Dobrin, R.; Braxenthaler, M.; Kuentzer, J.; Demchak, B.; Ideker, T. NDEx, the Network Data Exchange. Cell Syst 2015, 1 (4), 302–305.

(37) Lamparter, D.; Marbach, D.; Rueedi, R.; Kutalik, Z.; Bergmann, S. Fast and Rigorous Computation of Gene and Pathway Scores from SNP-Based Summary Statistics. PLoS Comput. Biol. 2016, 12 (1), e1004714.

Chapter 3 A deep learning model of tumor cell architecture elucidates response and resistance to CDK4/6 inhibitors

3.1 Abstract

Cyclin-dependent kinase 4 and 6 inhibitors (CDK4/6is) have revolutionized breast cancer therapy. However, <50% of patients have an objective response, and nearly all patients develop resistance during therapy. To elucidate the underlying mechanisms, we constructed an interpretable deep learning model of the response to palbociclib, a CDK4/6i, based on a reference map of multiprotein assemblies in cancer. The model identifies eight core assemblies that integrate rare and common alterations across 90 genes to stratify palbociclib-sensitive versus palbociclib-resistant cell lines. Predictions translate to patients and patient-derived xenografts, whereas single-gene biomarkers do not. Most predictive assemblies can be shown by CRISPR–Cas9 genetic disruption to regulate the CDK4/6i response. Validated assemblies relate to cell-cycle control, growth factor signaling and a histone regulatory complex that we show promotes S-phase entry through the activation of the histone modifiers KAT6A and TBL1XR1 and the transcription factor RUNX1. This study enables an integrated assessment of how a tumor's genetic profile modulates CDK4/6i resistance.

3.2 Introduction

Cell-cycle activation and sustained proliferation are hallmarks of cancer[1]. Cyclin-dependent kinases 4 and 6 (CDK4 and CDK6) trigger cells to pass the G_1/S cell-cycle restriction point by phosphorylating the retinoblastoma transcriptional repressor (RB) and its paralogs. Inhibiting these kinases has been of high interest in cancer drug development[2,3]. Thus far three CDK4/6 inhibitors (palbociclib, ribociclib, abemaciclib) have been approved in combination with endocrine therapy for the treatment of hormone receptor-positive, human epidermal growth factor receptor-negative (HR+, HER2–) breast cancer, and clinical trials are underway in a spectrum of other tissue types[4]. In metastatic breast cancer, these agents have appreciably improved

treatment outcomes, increasing progression-free and overall survival with manageable side effects[4,5]. However, objective tumor response is observed in fewer than 50% of patients who receive CDK4/6 inhibitors as first-line therapy, and nearly all initially responsive patients develop drug resistance with subsequent fatality[6,7].

Studies of resistance to these drugs have largely defined two groups of molecular biomarkers: loss-of-function alterations to anti-proliferative CDK-pathway genes (e.g. *CDKN2A/B/C* or *RB1)*, or gain-of-function alterations to pro-growth genes (e.g. *CDK2*, *CDK4/6*, *CCND1*, *CCNE1*, *E2F*, or *PIK3CA)*. These markers have been characterized predominantly in preclinical *in-vitro* studies, with clinical assessments obtained primarily *via* retrospective analyses[4,5]. *RB1* mutation bears the strongest burden of evidence, as it has been extensively associated with CDK4/6 drug resistance in both cell lines and patient cohorts[8]. However, it and other markers have met with inconsistent results in prospective clinical trials[8], suggesting that our understanding of this drug response is still incomplete.

Deep learning is a powerful general methodology in precision medicine, including the use of molecular profiles to predict drug responses[9]. Such models are typically trained to maximize outcome prediction accuracy (e.g. whether a patient will respond to a drug), without attempting to reveal the internal cellular and molecular mechanisms by which that outcome is achieved. In this regard, it is notoriously difficult to interpret which molecular features are relevant and even more difficult to describe how these features integrate with one another in the logic of molecular pathways[10]. To create models that are both predictive and interpretable[11,12], we and others have advanced a series of “visible” neural network (VNN) architectures[13–16] which are guided by knowledge maps of cellular components and functions. For example, using such a model, Elmarakeby *et al.* found that metastatic outcomes in prostate cancer were well-predicted by convergent genetic alterations within an MDM-TP53 inhibition pathway, implicating *MDM4* in resistance to anti-androgen therapy[15].

Thus far, VNN models have been structured using the Gene Ontology[17] or Reactome[18], two general human expert-curated databases of known cellular components and functions which have not been explicitly designed to capture the molecular pathways of cancer. To systematically define and discover cancer mechanisms, we recently developed a hierarchical map of multi-protein assemblies called NeST (Nested Systems in Tumors)[19]. To build this map, we used affinity purification mass spectrometry (AP-MS) to interrogate the physical interactions of a broad set of frequently altered cancer proteins. These data were integrated with other systematic 'omics datasets to create a large cancer protein-protein association network. Structural analysis of this network revealed a hierarchy of protein assemblies in which small, specific complexes nest within larger communities corresponding to broad processes and organelles. NeST was defined as the final hierarchy of 395 assemblies found to be under significant selection pressure for somatic mutations in one or more adult tumor types (Figure 3.1a)[19]. Beyond identification of the mutated protein assemblies, NeST had not yet been used to inform drug response models.

Here, we use this experimentally derived NeST map as the foundation for a visible deep learning approach to understand how patterns of genetic alterations govern the tumor response to CDK4/6 inhibition. This model is both functionally predictive of palbociclib treatment outcomes and can be structurally interpreted, revealing a focal set of protein assemblies on which both common and rare cancer mutations converge to affect drug resistance or sensitivity (Figure 3.1b).

3.3 Results

3.3.1 Implementation of a cancer-oriented visible neural network

We defined a set of 718 genes that are assessed by one or more clinical cancer gene panels/studies, including the FoundationOne CDx[20] panel, Tempus xT[21], or Project GENIE (Genomics Evidence Neoplasia Information Exchange)[22]. We then queried NeST to extract a hierarchy of 131 protein assemblies containing proteins encoded by the clinically assessed genes. This hierarchy was used to guide the architecture of a visible neural network (VNN) following a

previously described approach[13] (Figure 3.1b, Supplementary Figure 3.1a, Methods). This model of cancer cell structure and response, which we call NeST-VNN, allowed for three binary input features per gene, describing the presence/absence of point mutation/insertion/deletion, copy number amplification (CNA), or copy number deletion (CND) (Figure 3.1b, Methods). These gene-level input features were integrated within their respective protein assemblies in subsequent layers of the NeST-VNN, with each assembly represented by a bank of artificial neurons, reflecting its biological state or "*in-silico* activity" (Supplementary Figure 3.1a). Connections were also established between the neurons of an assembly and those of larger assemblies that contain it (Supplementary Figure 3.1b), allowing for the flow of genetic information from small focal assemblies (e.g. "CDK holoenzyme complex") to larger-scale assemblies and super-assemblies (e.g., "Cell cycle"). The final protein assembly at the root of the hierarchy represented the model output — the predicted drug response of a tumor sample given the input set of genetic alterations (Figure 3.1b).

To train NeST-VNN, we leveraged drug response data for 1244 genomically-characterized tumor cell lines[23], obtained by harmonizing the Cancer Therapeutics Response Portal (CTRP)[24,25] and the Genomics of Drug Sensitivity in Cancer (GDSC)[26,27] databases (Methods). These data included the response to the CDK4/6 inhibitor palbociclib, which had been well-characterized in 947 cell lines. For comparative benchmarking, we also examined 50 non-CDK-related drugs, investigated in at least 200 cell lines, for which the cellular responses displayed sufficient variability, with many examples of sensitivity and resistance (Methods).

3.3.2 Evaluation of prediction performance

We constructed NeST-VNN drug response models for palbociclib, and separately for each of the 50 benchmark drugs, using standard neural network learning procedures based on back-propagation (Methods). Each model was trained to use the gene alteration profile of a cell line to predict the corresponding Area Under the dose-response Curve (AUC). Training and performance

assessment was conducted using nested five-fold cross-validation (Methods), with each fold setting aside 64% of cell lines for training, 16% for validation (used for tuning hyper-parameters), and 20% for testing. While nested cross-validation is computationally intensive, it fully insulates model testing from parameter tuning while maximizing the amount of testing that can be performed. We compared the NeST-VNN approach to three state-of-the-art alternatives: ElasticNet, Random Forest, and a conventional black box artificial neural network (ANN) (Supplementary Figure 3.2a,b, Table 3.1). The overall performance of NeST-VNN was generally comparable to the state-of-art models and often better, with NeST-VNN achieving the best performance for more than half of the tested drugs (62.7%, Supplementary Figure 3.2a,b). NeST-VNN trained for palbociclib was one of the top-performing models, significantly outperforming ElasticNet and ANN models and slightly, but not significantly, outperforming Random Forest (Supplementary Figure 3.2c, Table 3.1).

To translate predictions to discrete tumor response outcomes, we thresholded the AUC such that predictions below a value t_{low} were labeled “sensitive”, those above a value t_{high} were labeled “resistant,” and those between these two thresholds were labeled “undefined” (Figure 3.2a). At the most inclusive setting, t_{low} = t_{high} = median[AUC], NeST-VNN could accurately discriminate between actual sensitive and resistant cell lines in held-out test data with a diagnostic odds ratio (OR) of 6.0. Discriminative power increased substantially with more stringent thresholds. For instance, setting the thresholds one standard deviation from the median (t_{low} , t_{high}= median[AUC] ± stdev[AUC]), yielded a very high OR of 40.1, indicating that samples predicted as resistant were approximately 40 times more likely to test as resistant than samples predicted as sensitive (Figure 3.2b). The trade-off for higher accuracy was that samples were left undefined (66%), increasing specificity but lowering sensitivity (Supplementary Figure 3.2d).

3.3.3 Translation to patient-derived xenografts and patients

Next, we examined NeST-VNN performance in a study of patient-derived xenografts (PDX)[28] including *n*=172 samples treated with a CDK4/6 inhibitor (ribociclib). Each PDX sample was classified as sensitive, resistant, or undefined, using thresholds at one standard deviation from the median (t_{low} , t_{high} = median[AUC] ± stdev[AUC]). PDX samples predicted to be sensitive exhibited significantly longer progression-free survival (duration from start of treatment until the tumor volume has doubled) than those predicted to be resistant, suggesting that predicted sensitivity was associated with impaired tumor growth (log-rank p=0.04, Hazard Ratio=0.53, 95% Confidence Interval 0.30-0.97, Figure 3.2c, Methods).

Following this analysis in xenografts, we then evaluated model performance in predicting treatment outcomes for 226 breast cancer patients from the GENIE metastatic breast cancer cohort[22]. These patients had been treated with baseline endocrine therapy with (*n*=67) or without (*n*=159) a CDK4/6 inhibitor. Each patient was classified as “sensitive” or “resistant”, using the threshold $t_{low} = t_{high}$ = median[AUC] (no “undefined” category was used since the number of treated samples was less than for the earlier PDX or cell-line analysis). The resistant category was further equally split to denote "partially resistant" and "strongly resistant" subgroups. For patients treated with a CDK4/6 inhibitor, those predicted to be sensitive had significantly longer survival than those predicted to be strongly resistant (log-rank p=0.02, Hazard Ratio=0.21, 95% Confidence Interval 0.05-0.91, Figure 3.2c). Moreover, for the strongly resistant subgroup, addition of the CDK4/6 inhibitor failed to demonstrate a significant increase in overall survival compared to baseline therapy (p=0.37). These predictions outperformed single-gene markers of palbociclib resistance[29] (*RB1* mutation) or sensitivity[30,31] (*CCND1* CNA) which had been previously suggested, consistent with the mixed results of these markers in clinical trials[8] (Supplementary Figure 3.2e,f). Among patients who did not receive a CDK4/6 inhibitor, no significant survival differences were observed among the predicted sensitive/resistant/strongly-resistant class labels (all comparisons with log-rank p>0.1, Figure 3.2c). These results indicated that the NeST-VNN palbociclib model translates

to breast cancer patient populations and is specifically predictive of response rather than generally prognostic of patient survival.

3.3.4 Interpreting the model to identify important protein assemblies

Having seen that the NeST-VNN model was predictive of drug response in tumor cell lines, PDX samples and patients, we sought to interpret which protein assemblies were important to this process. Similar to a previous method[13], we computed a quantitative importance score for each assembly according to how well its *in-silico* activity was associated with the final drug response prediction (Figure 3.3a, Table 3.2, Methods). Assemblies containing the primary Cdk4 and Cdk6 drug targets were of significantly higher importance than expected by chance, serving as positive controls ($p=5\times10^{-5}$, Figure 3.3a, Table 3.2). For example, one of the important CDK assemblies was NeST:110 (CDK holoenzyme complex I, Figure 3.3b,c), comprised of the CyclinD-CDK4-CDK6 complex along with upstream inhibitors (CDKN1/2 protein families) and downstream targets (RB1). Positive-control assemblies were also observed for other top-performing drug models; the model for the drug Nutlin-3a, which targets TP53 activity through MDM2, placed high importance on assemblies containing these proteins ($p=6.8\times10^{-10}$, Supplementary Figure 3.2a & 3.3a).

For all drug models, assembly importance tended to increase with size and depth in the hierarchy, reflecting the progressive integration of genetic information. Assembly importance was similar between cell lines and patient tumors (Figure 3.3d) or PDX samples (Figure 3.3e). In contrast, little correlation was observed between cell-line versus clinical samples when examining the importance of individual gene mutations (Figure 3.3f) or copy-number aberrations (Supplementary Figure 3.3b,c). These results were consistent with the premise that most individual genetic alterations are rare, with variable incidence across contexts[32], and suggested that effects of genetic alterations on protein assemblies can be substantially more stable.

Of 33 assemblies that were of high importance for palbociclib response prediction in cell lines (importance ≥ 0.5), we focused on 8 distinct minimally overlapping assemblies whose importance scores remained significant under multiple-hypothesis correction (hereafter referred to as 'core assemblies', Methods). Beyond regulation of CDK activity, core assemblies spanned histone and chromatin regulation, DNA damage response, and growth factor signaling (Figure 3.3a) and integrated rare and common genetic alterations across 90 genes (Supplementary Figure 3.3d). Most core assemblies were also important for predicting outcomes in clinical and PDX samples (Figure 3.3d,e).

3.3.5 Systematic validation of core assemblies by loss-of-function screens

We next sought to validate the palbociclib core assemblies using two CRISPR loss-of-function screens (Figure 3.4a): a published chemogenetic screen involving genome-wide KO of single genes in combination with palbociclib treatment[33] and a *de-novo* dual CRISPR screen in which we paired gene KOs in selected NeST-VNN assemblies with a second gene KO targeting *CDK4* or *CDK6* (Figure 3.4a, Methods). For the chemogenetic screen, we assessed each assembly in NeST for the enrichment of genes whose knockouts modulate cell fitness in the context of palbociclib treatment (Methods). The enrichments of the eight core assemblies tended to be significantly higher than those of non-important controls (p=0.005, Mann-Whitney U-test), with four of these assemblies in particular (Regulation of CDK activity, Histone-mediated transcription regulation, DNA damage response, PML body) showing stronger effects than any assembly in the control set (Figure 3.4b). Such enrichment was due to knockouts in a diversity of genes, including roughly a dozen with extreme loss of fitness phenotypes (Figure 3.4c, e.g. BCL6, CCND3, CDK4, CDK5, RAD51C, TOP2A, BARD, AURKA, AURKB) and several causing gain of fitness (e.g. BRCA2, CTNNB1, CDKN2B, MSH6, MLH3). Enrichment was not observed for a genome-wide KO screen without palbociclib treatment[34], indicating that at least some of the effect was due to gene-drug interactions rather than independent gene essentiality (Methods, Figure

3.4d). We then moved on to our *de novo* dual CRISPR KO screen and noted that this screen and the earlier chemogenetic screen were reasonably consistent with respect to gene KO fitness effects (Pearson ρ=0.48, Figure 3.4e). Disruptions in all six of the core assemblies with sufficient coverage in our gene KO panel displayed a trend toward increased cell fitness (Figure 3.4f,g). Taken together, these results indicated that engineered genetic disruptions in protein assemblies identified by the NeST-VNN can influence tumor cell growth in the setting of CDK4/6 inhibition, whether such inhibition is induced by a drug (Figure 3.4b) or CDK4/6 knockout (Figure 3.4f,g).

3.3.6 Exploration of gain-of-function alterations in a histone transcriptional assembly

One open question is how CDK4/6 and the G_1/S transcriptional program interact with other cell functions, including upstream modulators and downstream effectors. A notable assembly in this regard was NeST:85 (Histone mediated transcription regulation), a densely-connected assembly of 15 proteins with roles in histone acetylation, deacetylation, and transcriptional activation (Figure 3.5a). This assembly was important for CDK4/6i response in cell lines (Figure 3.3a), PDX samples (Figure 3.3e, Supplementary Figure 3.4b) and patients (Figure 3.3d). It had also been validated by CRISPR loss-of-function analysis (Figure 3.4b). However, most of the frequent genetic alterations affecting this assembly in tumor cell lines patients were not loss-of-function events but gene copy-number amplifications (Figure 3.5b), which were especially prevalent in lung, oropharyngeal, and gynecologic tumors (frequencies 15-35%, Supplementary Figure 3.4a). CNA also accounted for the top five genetic alterations in this assembly that were most predictive of palbociclib resistance, in particular of *MYC*, *TERT*, *KAT6A*, *TBL1XR1* and *RUNX1* (Figure 3.5c, Methods). Each of these amplifications had a resistance odds ratio of around 2.0, indicating that cells harboring CNA are twice as likely to exhibit resistance to palbociclib compared to cells without amplification (Figure 3.5c).

Motivated by these findings, we turned to the technique of CRISPR activation (CRISPRa), which uses the dCAS9-VPR transcriptional activator to increase expression from gene promoters

targeted with CRISPR single-guide RNAs (Figure 3.5d). For these experiments we selected A549 lung carcinoma epithelial cells, which harbor few genetic alterations in the NeST:85 assembly compared to many other common tumor cell models, for which multiple genes are already amplified (Figure 3.5b). We transfected short guide RNAs (sgRNAs) targeting *KAT6A*, *TBL1XR1*, *RUNX1*, *TERT*, or *MYC* into A549 cells expressing dCAS9-VPR, confirming by quantitative PCR that constructs exhibited substantial overexpression of the target gene in comparison to non-targeting control sgRNAs (all except for *MYC*, Supplementary Figure 3.4c). sgRNAs targeting *MYC* did not have significant effect, consistent with prior reports that this gene is already highly expressed in A549[35]. We used the fluorescent thymidine analog, 5-ethynyl-2'-deoxyuridine (EdU), to count the fraction of cells undergoing active DNA replication in S phase. Over-expression of the histone modifiers *KAT6A* and *TBL1XR1* produced significant increases in the proportion of cells entering S-phase under palbociclib treatment compared to the untreated group (Figure 3.5e,f; approx. 2.5-fold; $p<0.05$); the transcription factor *RUNX1* also led to significant increases albeit to a lesser degree (1.5-fold). We also examined the effects of *KAT6A* or *TBL1XR1* overexpression on phosphorylation status of Rb1, the direct target of the CDK4/6/CyclinD complex. Capillary western blot analysis demonstrated that overexpression of these factors is indeed associated with a >2-fold increase in phospho-Rb levels (Figure 3.5g,h, Supplementary Figure 3.4d, Methods). Together, these results indicated several NeST:85 genes whose overexpression serves to promote cell cycle, in support of our earlier observation (Figure 3.5c) that CNAs in these genes are predictive of palbociclib resistance.

3.4 Discussion

CDK4/6 inhibitors are a well-studied class of drugs for which numerous candidate biomarkers have been identified[8]. Why has prediction of CDK4/6i responses remained challenging? One reason is that markers with promise in cell lines (e.g. *CCND1* amplification) do not consistently translate to patient populations[30,31]. Another is that individual genetic alterations

that are clinically predictive may occur too rarely to have broad utility (e.g. RB1 deletion or mutation). A wider, more integrative analysis is needed to fully understand CDKi resistance[5,8]. Towards this goal, NeST-VNN synthesizes both rare and common genetic events across a repertoire of drug response pathways, with the aim of facilitating a quantitative, integrated assessment of drug response. The modeling process begins with a map of tumor cell components, which is used to guide the topology of deep neural network models as they learn to translate genetic alterations to drug responses (Supplementary Figure 3.1). The key subcellular assemblies of models which accurately capture drug responses *in vitro* and that translate to *in-vivo* (e.g. PDX) and clinical settings (Figure 3.2) can be validated through directed CRISPR loss-of-function and/or activation screens (Figure 3.4,3.5). Assemblies that pass this validation pipeline are a source of candidate biomarkers in downstream precision medicine applications. Alternatively, a model can be used in its entirety to produce a single resistance score integrating the mutational status of all proteins and assemblies.

NeST-VNN is based on NeST, a whole-cell map of cancer protein complexes derived from systematic proteomics data (see 'Structural architecture of the NeST-VNN model' section in Methods). Previous drug response models have generally not incorporated outside knowledge of cell structure (many approaches, reviewed here[9,36]) or have modeled structure using databases of cellular components or pathways drawn from literature curation[9,14,15]. Biological insights informed by NeST-VNN are uniquely dependent on the composition of NeST, generating both strengths and limitations. One strength is that the model can incorporate information from numerous rare mutations in predicting a drug response, insofar as these rare alterations aggregate to affect the activity of commonly altered protein assemblies with documented cancer relevance. A limitation is that NeST almost certainly does not include all relevant protein assemblies (false negatives), and some assemblies that are included may be imperfect or irrelevant to a given tumor population (false positives). Regardless, the NeST knowledgebase positions the precision medicine model as a dynamic entity, which can be updated either

functionally, with new incoming drug response data, or structurally, as NeST (or other future map) is improved by additional data. These new data need not be limited to AP-MS experiments (the primary source informing NeST thus far[37]), but in the future might incorporate information from complementary proteomics technologies such as proximity ligation[38], size exclusion chromatography[39,40], or spatial imaging[41]. While pathway databases are sometimes treated as gold standards (especially literature-curated databases like GO and Reactome), knowledge of molecular pathways remains incomplete, particularly as it relates to specific tumor states and subtypes.

Using this platform, we identified a set of eight core assemblies for which genetic alterations associate with anti-CDK4/6 response, seven of which were validated by one or more CRISPR screens (Figure 3.4,3.5). These assemblies are not focused solely on cyclin-dependent control of cell cycle (Figure 3.3a). Nonetheless, ample literature support can be found for the involvement of many of these other assemblies in anti-CDK responses, such as those related to androgen receptor signaling[42], EGF/FGF signaling[43], DNA damage response[44], and the MDM2-p53 pathway[45]. Regarding the identification of an EGF/FGF growth-factor signaling assembly, recent studies have found that the *EGFR* and *ERBB2* epidermal growth-factor receptors are associated with palbociclib response[46], and that the genetic alteration status of *FGFR1/2* and its associated FGF ligand have promise as markers of acquired resistance[43]. Furthermore, ongoing clinical trials are assessing the combination of anti-CDK4/6 treatments with insulin-like growth factor (IGF) inhibition (trial # NCT03099174) or with EGFR inhibition (trial # NCT03065387) in various tumor types. In NeST-VNN, the EGF/FGF complex combines each of these alterations, which have largely been reported separately, into a single integrated effect including alterations in yet additional receptor tyrosine kinases (e.g. ERBB3/4).

The model also highlights a notable role for NeST:85 (Histone-mediated transcriptional regulation), which integrates both well-known and under studied factors. Treatment with CDK4/6 inhibitors induces remodeling of chromatin structure mediated by histone acetyltransferases and

deacetylases, leading to expression signatures of senescence and cell differentiation[3]. Accordingly, genetic alterations affecting proteins of the NeST:85 assembly, including histone acetylases *CREBBP* and *EP300*[47], deacetylases *HDAC1* and *HDAC2*[48], and transcription factors such as *TP53*[49] and *MYC*[50], have been previously documented to modulate the anti-CDK4/6 drug response. Using CRISPRa to model the effects of copy-number amplifications, we observed that increased expression of *KAT6A* and *TBL1XR1,* which are also components of the NeST:85 assembly, leads to increased S-phase entry (Figure 3.5). *KAT6A*, also known as *MYST3*/*MOZ*, encodes a histone lysine acetyltransferase that is amplified in many cancer types[51] (Figure 3.5b). Relevant to the NeST:85 assembly, *KAT6A* has been previously documented to regulate cell-cycle arrest and differentiation via transcription factors p53[52] and RUNX1[53]; it is a frequent translocation partner of other assembly members such as EP300 and CREBBP[54]. TBL1XR1, also known as TBLR1, is an F-box-like protein involved in recruitment of the ubiquitin-conjugation system to histone modifier and transcriptional repression complexes[55,56]. Subsequent proteasomal degradation of these complexes is essential for transcriptional activation by *AR*, as captured by the NeST:85 assembly, as well as other transcription factors such as *ER*[57]. Notably, increases in *KAT6A* and *TBL1XR1* expression were associated with higher phosphorylation levels of Rb, the central transcriptional repressor targeted by CDK cell-cycle control (Figure 3.5g,h), suggesting they may promote drug resistance by elevating the transcription, abundance, or activity of the upstream CDK4/6/CyclinD regulatory complex. The possible combination of HDAC-inhibitor therapies with cell cycle inhibitors has been previously proposed[48]; this study further underscores this potential and delineates alternative targets. Indeed, KAT6A inhibitors are under development and have demonstrated promising effectiveness for inducing cellular senescence[58–60] (Clinical trial NCT04606446). In the tumor cells characterized here (A549, Figure 3.5), *TBL1XR1* has a T290A missense mutation of unknown significance whose impact will require further investigation.

In summary, the predictive models presented in this study build from, and significantly develop, the concept of an integrated response to therapy. In such an integrated response, diverse effects converge on biological machinery at multiple levels to produce an overall treatment outcome. This concept may explain the difficulty in identifying individual genetic biomarkers of palbociclib drug response. It also speaks to the challenge of patient-to-patient heterogeneity, and illustrates one means by which knowledge of cellular machinery can be used to score a diverse population of cancer patients presenting unique patterns of mutational aberrations. Such an integrated model may provide a worthwhile asset in achieving improved outcomes for patients, as well as in efforts to evaluate novel therapeutics to overcome resistance.

3.5 Methods

3.5.1 Drug response data for model training

Drug response data were retrieved from the GDSC and CTRP[24–27], covering a total of 692,859 cell line/drug pairs, comprising 1244 cell lines and 888 drugs. The data from the two datasets were harmonized as follows. Drug information: Each molecule's published name, synonym, or SMILES string was queried using PubChemPy. The associated InChiKey was extracted and used to identify duplicate drugs (within or between datasets). Cell viability data: For CTRP, the vehicle control-normalized average percent viability files were used. For GDSC1 and GDSC2, data were normalized to "cells-only" and "DMSO control" wells, respectively, on a per-plate basis. Data were averaged across replicates within each dataset. For drug response measurement, we used Area Under the dose-response Curve (AUC) where AUC = 0 corresponds to complete cell killing and AUC = 1 corresponds to no cell killing; AUC > 1 represents a growth advantage conferred by the drug. AUCs calculated in this study agreed with AUCs reported by the original consortia (Pearson correlations of 0.92, 0.83, 0.91, and 0.91 for CTRP1, CTRP2, GDSC1, and GDSC2, respectively). For multiple AUCs for the same drug across different consortia, we used each replicate sample as a separate training instance. Genetic alteration data:

A panel of 718 clinical genes was assembled from the union of genes assessed by FoundationOne CDx[20], Tempus xT[21], PALOMA-3 trial[61], or Project GENIE[22], each of which assesses mutations and/or copy number aberrations. To compile genotypes for all cell lines, we extracted non-synonymous coding mutations and copy number alterations for the 718 clinical panel genes from the Cancer Cell Line Encyclopedia (CCLE, release 22Q1)[23]. Genes were marked as either mutated ("1") or unmutated ("0") with mutations filtered for the following types: missense/nonsense/nonstop mutations, frame-shift insertions/deletions, splice site/region variations, and in-frame insertions/deletions. Similarly, genes were marked as amplified ("1") or unamplified ("0"), and deleted ("1") or undeleted ("0"). Together, mutations, CNA, and CND served as features for each of the clinical panel genes. Of 888 drugs available from CCLE and/or GDSC, we selected the 51 drugs (including palbociclib and 50 others) with highest variation in the observed drug responses across cell lines (corresponding to standard deviation ≥ 0.3).

3.5.2 Structural architecture of the NeST-VNN model

Construction of the NeST hierarchy of cancer protein assemblies has been thoroughly detailed elsewhere[19]. Briefly, AP-MS protein interaction data for 61 known cancer proteins were integrated with a compendium of other systematically generated datasets informing protein-protein associations, including protein-protein-interaction (PPI), mRNA co-expression, protein co-expression, genetic co-dependency, and sequence similarity. Such integration resulted in a large network of approximately 1.8×10^8 PPIs among 19,035 proteins. Multi-scale community detection was performed to detect approximately 2,300 densely connected sets of proteins, herein called protein assemblies. Assemblies were nested, i.e. organized hierarchically, with larger assemblies containing smaller ones forming (parent-child) assembly relations. This hierarchy has been used earlier[19] to perform a comprehensive analysis of somatic coding mutations in The Cancer Genome Atlas[62], identifying significant convergence of mutations on a set of 395 protein assemblies, named NeST (Nested Systems in Tumors)[19]. Here, we filtered the NeST hierarchy

to identify the subset of assemblies encoded by at least five genes represented on the 718-gene clinical panel, producing a final hierarchy of 131 assemblies distributed over seven layers.

3.5.3 Model training

The filtered NeST hierarchy was used to embed a deep neural network for drug response prediction, which we refer to as NeST-VNN (Supplementary Figure 3.1a). We define an $m \times 3$ input matrix as I_g, where $I_{i,j} \in \{0,1\}$, with m denoting the number of genes and 3 the number of gene alteration types (mutation, CNA, and CND). For any input sample (tumor cell line, PDX or patient tumor), somatic genetic alterations for each gene and type are marked by 1, otherwise 0. The first layer in NeST-VNN converts these input features to gene-level representations $I_g \in \mathbb{R}^m$, as follows:

$$I_g = BatchNorm(Tanh(Linear(I)))$$

$BatchNorm$ indicates Batch Normalization[63], $Tanh$ indicates a hyperbolic tangent function and $Linear$ indicates a linear transformation. Here, the linear transformation is applied for each row in I so that the three gene alteration values for each gene are converted into a single value. The remaining seven layers of NeST-VNN follow the structure of the NeST protein assembly hierarchy, where each assembly is represented by some number of neurons N, a hyperparameter. Dropout[64] of 0.3 (selected through hyperparameter optimization) was added to the last four layers. Assembly state is defined as a function of the states of its K child assemblies and M additional genes (genes for which the protein products are not present in any descendant assemblies). Denoting an assembly input vector as I_s and output vector as O_s, we have:

$$O_s = BatchNorm(Tanh(Linear(Dropout(I_s))))$$

Here, I_s has dimension $N * (N * K + M)$ and O_s has dimension N. We define '*in-silico activity*', a representative singular value for assembly state, as the first principal component from principal component analysis[65]. The NeST-VNN objective function ($Loss$) aggregates the mean squared error (MSE) across every assembly in the hierarchy:

$$Loss = MSE(Linear(O_{root}), y) + \alpha \sum_{s \neq roo} MSE(Linear(O_s), y) + \beta ||W||$$

The parameter α was set to 0.3; β is a tuned hyperparameter. $Linear$ denotes the linear function used for transforming the vector O_i to a scalar. W denotes the weights of the neural network. Weight optimization was performed using AdamW[66].

3.5.4 Model benchmarking

For baseline benchmarking we trained Random Forest[67], ElasticNet[68] and a black-box artificial neural network[69] (allotted the same number of neurons and layers as the NeST-VNN model). models using Python scikit-learn[70]. For all models, including Nest-VNN, we used nested five-fold cross-validation[71], producing five models for each drug. For each fold setting, we split 64% of cell lines as a training set, 16% as a validation set (used for hyperparameter tuning), and 20% as a test set, ensuring that cell line replicate measurements (e.g. from different datasets) were not split between test and training sets. Hyperparameters were optimized with Optuna[72]. NeST-VNN was implemented in PyTorch and trained using five GPU servers containing four Nvidia Tesla V100s each with 5120 CUDA cores and 32GB GDDR6 RAM. All five NeST-VNN models were evaluated in downstream analyses.

3.5.5 Translation to cancer patients

Data from the AACR Project GENIE metastatic breast cohort[22] were used to validate the performance of the NeST-VNN model in retrospective clinical application. We extracted non-synonymous coding mutations, CNAs, and CNDs across 360 genes for 226 ER+ HER2– metastatic breast cancer patients along with their overall survival months and censorship information. We did not consider gender or sex. Of these patients, 67 had been treated with a CDK4/6 inhibitor and an endocrine therapy. The remaining 159 patients were treated with endocrine therapy only. Patients were excluded if they had been treated with additional targeted therapies, such as mTOR or AKT inhibitors. Tumor genomic data were converted to (0=unaltered,

1=altered) calls for all gene mutation, CNA, and CND features. Features used by NeST-VNN that were not assessed in the clinical trial were represented as unaltered. We predicted patient response to CDK4/6 inhibition using the average AUC over the five pre-trained palbociclib models, then thresholded this value as described in the main text (Figure 3.2c). Subjects whose status label was still “living” at 120 months were censored.

3.5.6 Translation to patient-derived xenografts

We analyzed a patient-derived xenograft (PDX) dataset[28], which contained 172 tumor samples treated with a CDK4/6 inhibitor (ribociclib) across five tumor types (breast carcinoma, non-small cell lung carcinoma, cutaneous melanoma, colorectal cancer, and pancreatic ductal carcinoma). Treatment responses had been measured by changes in the volume of the tumor xenograft over time, with an accompanying determination of treatment time as well as a classification according to the RECIST standard (Response Evaluation Criteria In Solid Tumors, includes categories of Progressive Disease, Stable Disease, Partial Response, or Complete Response). PDX samples had been genomically characterized, covering 660 out of 718 genes in the NeST-VNN gene set. Similar to the procedure for cell lines and patients, tumor genomic data were converted to calls (0=unaltered, 1=altered) for all gene mutation, CNA, and CND features. Features used by NeST-VNN that were not assessed in the PDX data were represented as unaltered. We predicted responses of PDX tumors to CDK4/6 inhibition as the average AUC over the five pre-trained NeST-VNN models for palbociclib, then thresholded this score as described in the main text (Figure 3.2d).

3.5.7 Model dependence on number of genes used for prediction

Given the difference in the number of genes used for prediction in cell lines (n=718) versus GENIE analysis (n=360) or PDX analysis (n=660), we systematically studied the dependence of model performance on the number of genes for which genetic alteration data are provided. We computed the average predictive performance of the pre-trained NeST-VNN model when it is

supplied with data for diminishing numbers of genes (Supplementary Figure 3.5a). We found that, at a gene set size of 350 (similar to the number of genes characterized in the GENIE study), the average performance is only slightly less than that obtained when using all genes (ρ=0.30 versus ρ=0.33), with a more precipitous fall in performance seen for 200 genes or fewer. A similar pattern was observed when we compared the assembly importance scores with their enrichments for gene KOs that modulate the response to palbociclib treatment (Supplementary Figure 3.5b). Notably, we also found that the precise panel of genes used by GENIE performs better than expected compared to a random subsampling (Supplementary Figure 3.5).

3.5.8 Identifying important assemblies and genes (model interpretation)

To determine which assemblies were important for drug response prediction in cell lines, PDX or clinical samples, we adopted a variation of "Relative Local Improvement in Predictive Power" method as previously reported[13]. Each assembly was modeled using linear regression, with the aim to evaluate how well its NeST-VNN neuron values capture the NeST-VNN overall drug response prediction. Each assembly k was assigned a $g\ x\ N$ matrix P_k, where g is the number of samples and N is the number of neurons. P_k was then used in a linear Ridge Regression[73] model to predict the NeST-VNN drug response D, creating models $M_1, M_2, \ldots M_k$. The following function was minimized for each model:

$$min_w ||P_k w - D||_2^2 + \alpha ||w||_2^2$$

where w is a vector of coefficients of length N and α imposes an L2 penalty on coefficient complexity. Assembly "importance" (Figure 3.3; Supplementary Figures 3.3, 3.5) is the Spearman correlation (ρ) between M_k and D. The mean correlation of the five Nest-VNN models was reported. A higher score indicates an assembly whose neuron values contributed strongly to NeST-VNN predictions and can therefore be considered important. To assess statistical significance, we generated a null distribution of assembly importance scores, as follows. We randomly rearranged gene-assembly memberships in the NeST-VNN while preserving the

assembly size and parent-child relationships. We trained 500 null models with these random rearrangements and calculated assembly importance for each null. One-tailed t-tests were used to evaluate whether assembly importance from the five NeST–VNN models were greater than assembly importance scores from the nulls, with Benjamini–Hochberg control for false discovery rate (Figure 3.3a). Finally, we defined 'core assemblies' as those with an importance score of ≥ 0.5 and a False Discovery Rate (FDR) of ≤ 0.1, while excluding less important assemblies if redundant assemblies (Jaccard similarity > 0.5 and parent-child relationships) exist. To identify specific genetic alterations in the NeST:85 assembly associated with palbociclib resistance (Figure 3.5c), we performed L1-norm regularized logistic regression[74,75]. Genetic alterations (mutations, CNA, CND) for the 15 assembly genes were used as regression features to predict AUCs. AUC values in the top 30% were encoded as 1 to represent resistance, while AUC values in the bottom 30% were encoded as 0 to represent sensitivity. Non-zero coefficients from the fitted model were recognized as significant alterations governing drug response, with the sign indicating whether the presence of alterations contributed to resistance (plus) or sensitivity (minus). We used scikit-learn implementation[70] with Logistic Regression settings of penalty = 'l1', C=0.01 (default for other parameters).

3.5.9 Comparison of interpretability of NeST-VNN versus Random Forest

We systematically evaluated the assembly importance scores provided by the NeST-VNN versus Random Forests[67] (RF) using the genome-wide loss-of-function screen for palbociclib treatment. To determine the assembly importance score for the RF model, we performed gene set enrichment analysis (GSEA[76], implemented with GSEApy[77]) on the gene list ranked according to the gene-level feature importance scores derived from the RF models. The absolute normalized enrichment scores (NES) generated from GSEA were used as assembly importance scores for RF models. Assembly importances in the NeST-VNN versus RF models were moderately but not completely correlated (ρ = 0.31, Supplementary Figure 3.6a). Relevant to the differences, we

found that the NeST-VNN importance of an assembly was also moderately correlated with its enrichment for gene KOs conferring palbociclib sensitivity or resistance (ρ = 0.33; Supplementary Figure 3.6b); in contrast, RF assembly importance showed a correlation that was substantially weaker (ρ = 0.07; Supplementary Figure 3.6c). Note that while RF models can achieve comparable predictive performance by identifying individual gene mutations that are indicative of drug response (Supplementary Figure 3.2a,c), NeST-VNN demonstrates its strength by integrating the effects of such mutations within predictive cancer protein assemblies.

3.5.10 Genome-wide CRISPR KO chemogenetic screen

Core protein assemblies were validated using a genome-wide CRISPR/Cas9 screen in MCF7 cells exposed to palbociclib treatment[33] (Figure 3.4a) (GEO: GSE192525). This screen had been run previously using the GeCKO v2 library (Genome-wide CRISPR Knock Out library). Gene-level Z-scores (referred to as normZ) from that study were used to indicate the effects of gene knockout (KO) on cell fitness in the context of CDK4/6 inhibition (Figure 3.4b). As a reference, the cell fitnesses of gene KOs (provided as Chronos score[78]) in the MCF7 cell line in the absence of CDK4/6i treatment (Figure 3.4c) were obtained from the Dependency Map (DepMap) project[34] (https://depmap.org/portal/).

3.5.11 Dual CRISPR KO combinatorial screen

The genome-wide chemogenetic data (above Methods) were complemented by a *de-novo* dual CRISPR screen performed in-house in MCF7 (HTB-22 ATCC), MCF10A (CRL-10317, ATCC), and MDAMB231 (CRM-HTB-26, ATCC) cell lines (Figure 3.4a). Cells were grown in DMEM with 10% FBS, screened for *Mycoplasma* contamination by PCR and verified by STR testing (Idexx Bioanalytics, 2019, 2018 and 2018, respectively). CRISPR-Cas9 nuclease was stably integrated by lentivirus. LentiCas9-Blast (Addgene plasmid # 52962) and lentiCRISPR v2 (Addgene plasmid #52961) were gifts from Dr. Feng Zhang[79]. Blasticidin was used to select Cas9 stable integrants. Cas9 protein expression was confirmed by capillary western (Wes, Protein

Simple). We constructed a library of double gRNA constructs targeting druggable targets (such as CDK4 and CDK6), tumor suppressors, and oncogenes. Here we analyze a subset of data from individual genes from core assemblies (sgRNA1) together with *CDK4* or *CDK6* (sgRNA2). The library was packaged into lentiviruses, and cells were infected to achieve a multiplicity of infection of 0.3. Puromycin selection (2.5 mg/mL) was started two days after transduction. Selection continued for seven days, after which puromycin was removed for the remainder of the screen. Cells were maintained in exponential growth by harvesting and removing a fraction of cells every two to three days. We analyzed data from two time points at approximately 14 and 21 days. DNA was extracted from cells with a Blood and Cell Culture DNA Mini Kit (Qiagen). To assess the relative frequencies of gRNAs before and after selection, gRNA sequences were amplified by PCR from genomic DNA and prepared for HiSeq4000 sequencing (Illumina). Standard Illumina primers were used for library preparation, and 100-bp paired-end reads were collected. Data quality was assessed with FastQC. Fitness effects of gene KOs at a time point were determined as the fold enrichment of a construct compared to the relative abundance of that construct in the plasmid library. Fitness measurements were normalized to the median fitness for non-targeting guides. The mean z-score across two biological replicates, two time points, and genes in each assembly was then determined and plotted (Figure 3.4b).

3.5.12 Production of dCas9-expressing stable cell line

CRISPR activation (CRISPRa) experiments were performed in A549 cells stably expressing dead Cas9 endonuclease (dCas9) together with the VPR transcriptional activation complex. For this purpose, 293T cells (ATCC CRL-3216) were co-transfected with a second-generation packaging plasmid (pCMV-dR8.2, Addgene 8455), VSV-G envelope-expressing plasmid (pMD2.G, Addgene 12259), and dCas9-VPR lentiviral plasmid (hCMV-Blast-dCas9-VPR, Horizon Discovery) using Lipofectamine3000 (Invitrogen, L3000015). Viral supernatant was collected and cleared of cell debris via centrifugation and Steriflip column (Millipore

SEIM003M00). Lentivirus was concentrated using Amicon Ultra-15 centrifugal filters (Millipore Z706345). Viral titer was determined via serial dilution. Subsequently, A549 cells (ATCC CCL-185) were grown in virus-containing media (DMEM/F12: 10% FBS, 100 IU/mL penicillin/streptomycin) with 8 µg/mL polybrene for 72 hours, followed by media washout and selection with blasticidin (3.5 µg/mL) for six days. Following selection, cells were cultured with maintenance-dose blasticidin (0.35 µg/mL) every other passage. The identity of stable dCas9 A549 cells were confirmed by STR testing (Idexx Bioanalytics, 8/31/2020).

3.5.13 CRISPRa screen

A custom panel of sgRNA expression plasmids targeting genes in the NeST:85 assembly was obtained from Horizon Discovery (Figure 3.5). Controls included a non-targeting control (NTC) sgRNA and an overexpression positive control sgRNA targeting OCT4 (not a component of NeST:85). dCas9-VPR-stable A549 cells were plated in complete media and were transfected next day with sgRNA plasmids for 24 hours using FuGENE HD (Promega). Cells were selected with puromycin (0.44 µg/mL) for 48 hours then lifted onto appropriate plates for further experimentation, where they were permitted to recover for 72 hours. RNA was collected using TRIzol Reagent (Invitrogen, 15596026) and RNeasy Mini Kit (Qiagen, 74104). cDNA was synthesized using iScript cDNA kit (Bio-Rad, 1708891). qPCR was performed using SYBR green and cycle threshold (Ct) values were compared for genes overexpressed by CRISPRa versus NTC samples (Figure 3.5e).

3.5.14 EdU assays for S-phase entry

Transfected cells were plated in collagen-coated glass-bottom 96-well plates in complete media containing palbociclib (4 µM) for 24 hours. Components of EdU Click-iT (Thermo Fisher, C10337) were prepared as instructed. Cells were labeled for 4 hours with 10 µM EdU-labeling solution in media and then counterstained with Hoechst dye (1:10,000) for 10 minutes. Cells were fixed in 3.75% formaldehyde for 10 minutes at room temperature and were then washed,

permeabilized, and stained according to manufacturer instructions. Images were collected using a Keyence microscope (BZ-X800) fitted with a 4x objective and GFP/FITC (Chroma C209879) and DAPI (Chroma C209877) filters. Images were processed in bulk using scikit-image[80]. Cells were identified using Hoechst counterstain and were then assessed for EdU incorporation (Figure 3.5f,g).

3.5.15 Capillary western assays for Rb status

Transfected cells were treated with palbociclib for 24 hours and were then trypsinized, washed in cold PBS; pellets were frozen at –80°C. Protein was extracted in hot 1X MES SDS running buffer (Invitrogen NP0002) for 10 minutes. Cooled samples were vortexed for 2 minutes with glass beads (Sigma G8772). cOmplete, EDTA-free Protease Inhibitor cocktail (Roche 04693132001) and PhoStop (Roche, 4906845001) were added to cleared lysate. Protein was quantified using Pierce 660 nm Protein Assay (Thermo Scientific, 22662). Protein analysis was performed on a capillary-based western blot system (Wes, ProteinSimple, product number 004–600) according to the manufacturer's instructions using the 12–230 kDa Separation Module (ProteinSimple SM-W001) and either the Anti-Rabbit Detection Module (ProteinSimple DM-001) or the Anti-Mouse Detection Module (ProteinSimple DM-002. Protein samples were diluted to 1 µg/ml in 0.1X sample buffer (ProteinSimple 042-195), then mixed with Fluorescent Master Mix and heated at 95°C for 5 min. Primary antibodies were one of anti-phospho-RB Ser807/811 (Mouse mAb clone D20B12, 1:100, Cell Signaling, #8516), anti-actin (rabbit polyclonal, 2µM, Novus, NB600-532), or HRP-conjugated secondary antibodies (ProteinSimple DM-001). Program settings were as follows: separation at 375 V 25 minutes; blocking reagent 15 minutes; 20-second wash (for runs with pRB only); primary antibody blocking 35 minutes; two 150-second washes; secondary antibody blocking 35 minutes; 150-second wash; chemiluminescence detection from 1 to 512 seconds. Electropherograms (Figure 3.5g,h) were inspected to check whether automatic peak detection required manual correction.

3.6 Statistics & Reproducibility

All wet lab experiments were performed in biological duplicate with three to four technical replicates. No statistical method was used to predetermine sample size. The experiments were not randomized. The investigators were not blinded to allocation during experiments or outcome assessment. EdU assays were evaluated computationally with data quality threshold filters as described above. For the survival analysis, patients were excluded if they had been documented to receive a targeted therapy other than a CDK4/6 inhibitor (i.e. mTOR or AKT inhibitor) as these other targeted therapies were not the focus of our study. Statistical tests were performed as described in each section above assuming data was normally distributed where appropriate, though this was not formally tested.

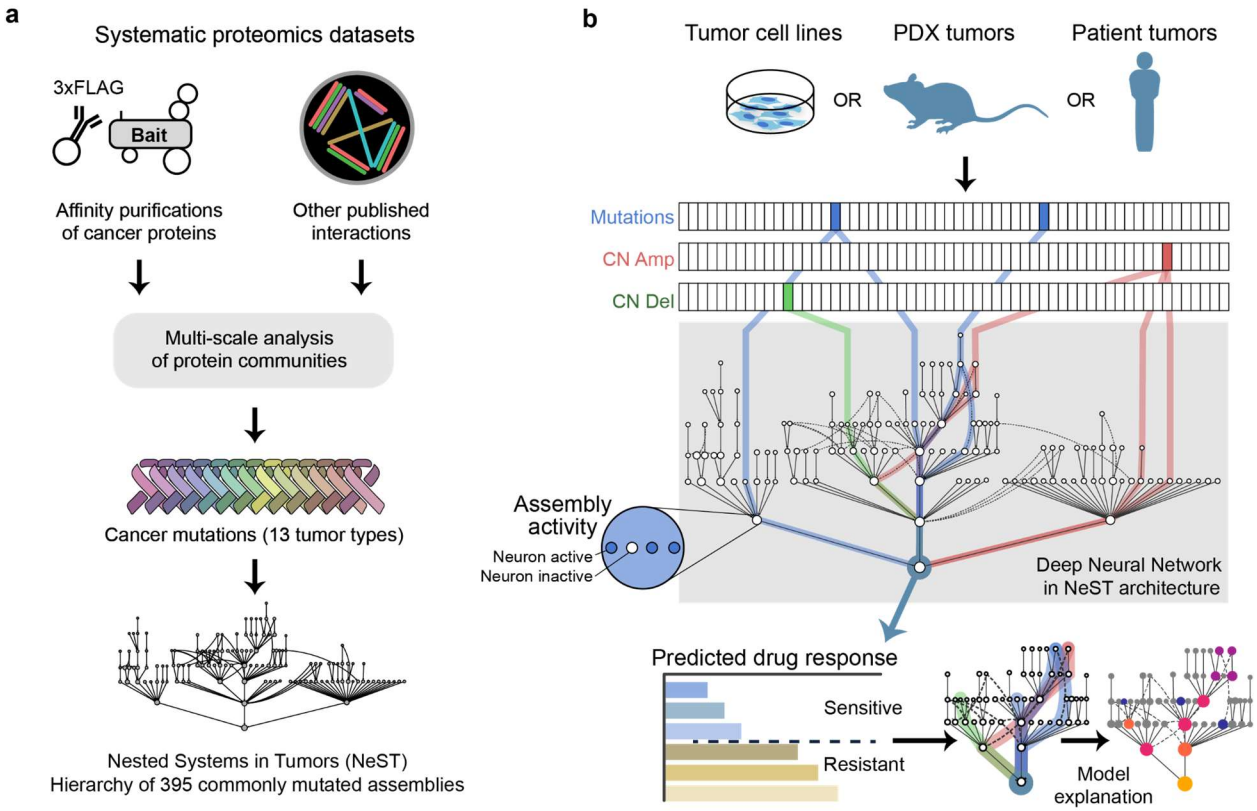

Figure 3.1: Architecture and features of the visible deep learning model.

a, Workflow depicting the construction of the NeST hierarchy of cancer protein assemblies by Zheng et al[19]. Affinity purification–mass spectrometry (AP-MS) data for 61 cancer protein baits were combined with a compendium of other systematic proteomic and 'omic datasets to produce an integrated protein network. This network was analyzed by multi-scale community detection to identify a hierarchy of nested protein assemblies. Those assemblies under mutational selection pressure in different tumor types were then identified, yielding the NeST map. **b**, Visible neural network (VNN) architecture for translating tumor genetic alterations (top) to drug responses (bottom) by genetic flow through the NeST map (middle). NeST is reduced to the 131 assemblies that involve genes measured by clinical gene panels (see text). CN Amp and CN Del refer to Copy Number Amplification and Copy Number Deletion, respectively.

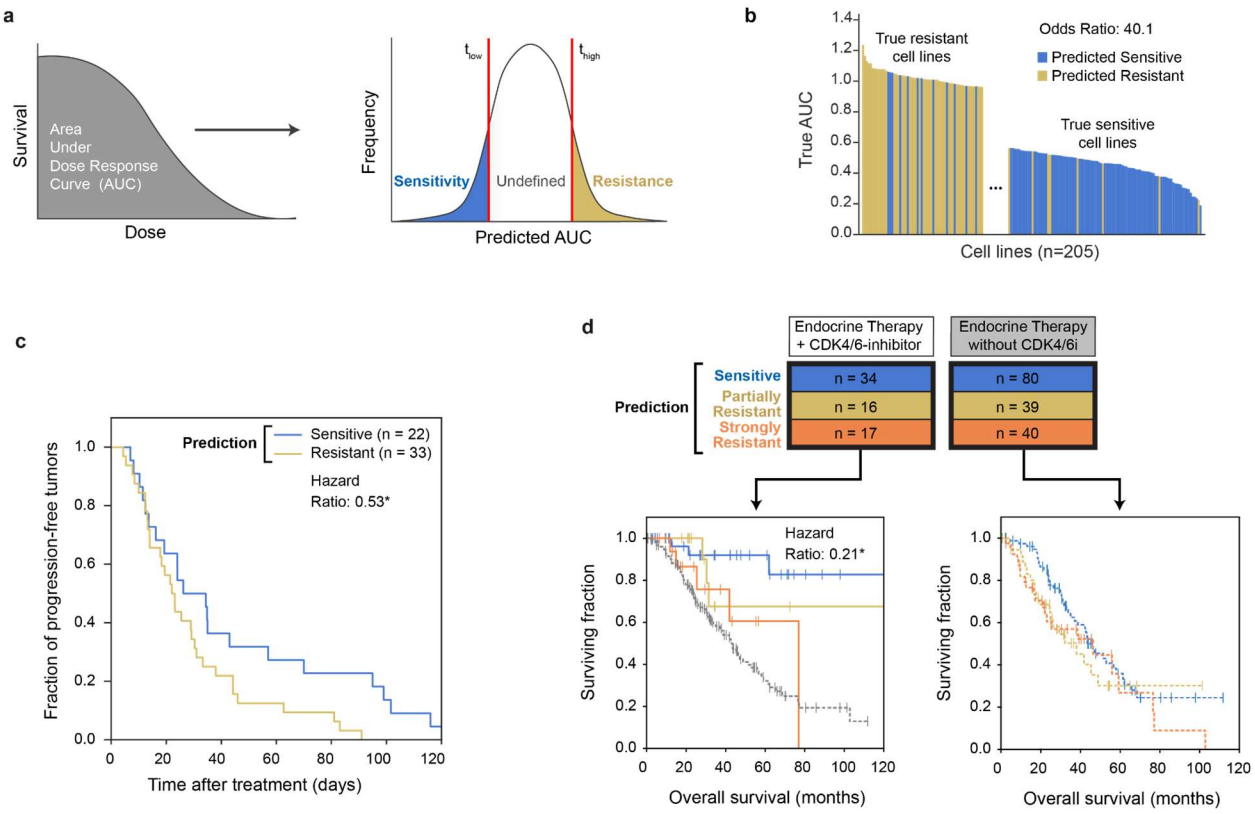

Figure 3.2: Predictive performance of the palbociclib model.

a, Scanning cell survival to measure a continuous area under the dose-response curve (AUC) which is thresholded to assign class labels (sensitive/undefined/resistant). **b,** Waterfall plot showing true dose responses of tumor cell lines, with colors indicating the predicted class of each. Predicted AUC is thresholded to produce (sensitive, resistant) class labels (see text). **c**, Survival curve analysis obtained when predicting sensitive/resistant status for PDX samples. *p<0.05 by log-rank test. **d,** Survival curve analysis for GENIE clinical trial patients treated with CDK4/6 inhibitor and endocrine therapy (left), or endocrine therapy alone (right). Colors denote class labels for predicted CDK4/6i-sensitive (blue) and CDK4/6i-resistant (yellow/orange) patients, with additional stratification of a strongly resistant category (orange). Patients not treated with CDK4/6 inhibitor therapy are shown in gray. Hazard ratio 0.21 for strongly resistant versus sensitive predicted subgroups. *p<0.05 by log-rank test.

Figure 3.3: Interpretation of palbociclib response mechanisms.

a, NeST-VNN interpretation of the palbociclib response. Nodes indicate assemblies, while node sizes indicate assembly sizes in numbers of proteins. Colors indicate degrees of importance for response prediction: Yellow, assemblies with importance > 0.5; Red: “core” assemblies, which bring the additional requirement of False Discovery Rate (FDR) ≤ 0.1 and exclude redundant assemblies of lesser importance (Jaccard similarity > 0.5). Assemblies containing CDK4 or CDK6 marked with small black squares. **b,** Protein interaction network defining the Cyclin D holoenzyme complex I (NeST:110), which contains CDK4 and CDK6. Edges represent biophysical protein-protein associations, with the edge weight reflecting the strength of evidence for association. **c,** Diagram of known functional associations among NeST:110 proteins in the context of cell-cycle progression. The CyclinD-CDK complex inhibits Rb1 by phosphorylation, such that it no longer transcriptionally represses genes required for entry into S-phase and subsequent DNA replication. **d** Scatter plot of assembly importance in clinical vs. cell line contexts (x vs. y-axes). **e,** Scatter plot of assembly importance in PDX vs. cell lines contexts (x vs. y-axes). **f,** Scatter plot of gene mutation importance in clinical vs. cell line contexts (x vs. y-axes).

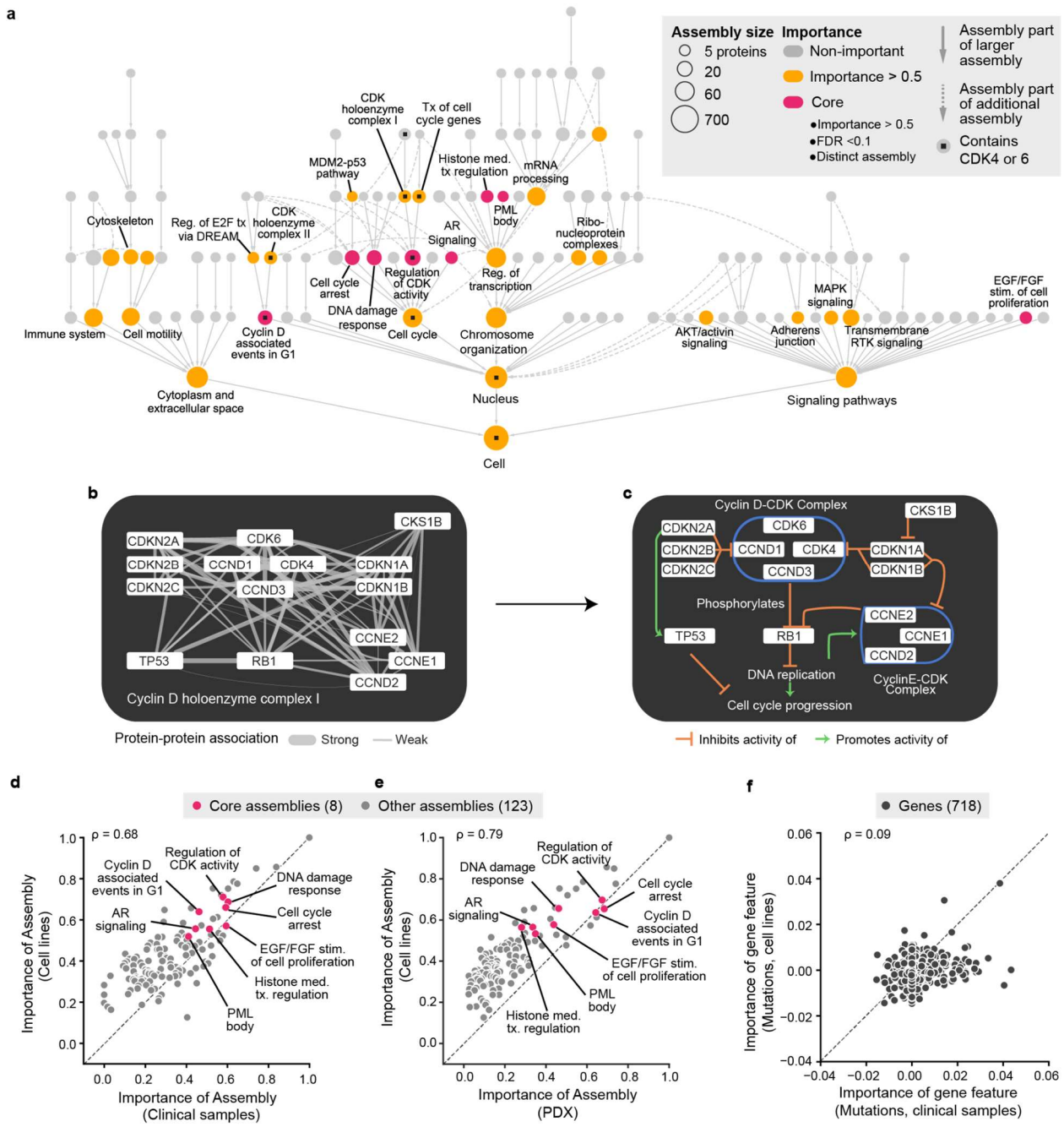
a
Assembly size
5 proteins
20
60
700
Importance
Non-important
Importance > 0.5
Core
•Importance > 0.5
•FDR <0.1
•Distinct assembly
Assembly part of larger assembly
Assembly part of additional assembly
Contains CDK4 or 6
CDK holoenzyme complex I
Tx of cell cycle genes
MDM2-p53 pathway
Histone med. tx regulation
mRNA processing
PML body
Cytoskeleton
Reg. of E2F tx via DREAM
CDK holoenzyme complex II
AR Signaling
Ribo-nucleoprotein complexes
Cell cycle arrest
Regulation of CDK activity
Reg. of transcription
DNA damage response
Cell cycle
MAPK signaling
EGF/FGF stim. of cell proliferation
Immune system
Cell motility
Cyclin D associated events in G1
Chromosome organization
AKT/activin signaling
Adherens junction
Transmembrane RTK signaling
Cytoplasm and extracellular space
Nucleus
Signaling pathways
Cell
b
CKS1B
CDKN2A
CDK6
CDKN2B
CCND1
CDK4
CDKN1A
CDKN2C
CCND3
CDKN1B
CCNE2
TP53
RB1
CCNE1
CCND2
Cyclin D holoenzyme complex I
Protein-protein association
Strong
Weak
c
Cyclin D-CDK Complex
CKS1B
CDKN2A
CDK6
CDKN2B
CCND1
CDK4
CDKN1A
CDKN2C
CCND3
CDKN1B
Phosphorylates
CCNE2
TP53
RB1
CCNE1
CCND2
DNA replication
CyclinE-CDK Complex
Cell cycle progression
Inhibits activity of
Promotes activity of
d
Core assemblies (8)
Other assemblies (123)
ρ = 0.68
Importance of Assembly (Cell lines)
Importance of Assembly (Clinical samples)
Regulation of CDK activity
Cyclin D associated events in G1
DNA damage response
AR signaling
Cell cycle arrest
EGF/FGF stim. of cell proliferation
Histone med. tx. regulation
PML body
e
ρ = 0.79
Importance of Assembly (Cell lines)
Importance of Assembly (PDX)
Regulation of CDK activity
DNA damage response
Cell cycle arrest
AR signaling
Cyclin D associated events in G1
EGF/FGF stim. of cell proliferation
PML body
Histone med. tx. regulation
f
Genes (718)
ρ = 0.09
Importance of gene feature (Mutations, cell lines)
Importance of gene feature (Mutations, clinical samples)

Figure 3.4: Systematic validation of palbociclib response mechanisms.

a, Schematic overview of CRISPR screens in MCF7 breast tumor cells. Individual sgRNAs targeting genes in protein assemblies are combined with palbociclib (CDK4/6i) or a second sgRNA targeting *CDK4* or *CDK6*. Cells harboring Cas9 nuclease are infected with lentiviral-packaged sgRNAs and propagated under selection. Palbociclib screen from Carpintero-Fernández et al.; CDK4 and CDK6 KO screens newly generated in present study. **b**, Violin plots illustrating enrichment of assemblies for gene KOs modulating cell fitness in context of palbociclib treatment, comparing core assemblies defined by NeST-VNN versus the same number of non-important assemblies (randomly selected among those with importance < 0.5). **p<0.01 by one-tailed Mann-Whitney U-test. Gene set enrichment analysis[76] was conducted for calculating enrichment scores. **c**, Left: Violin plot illustrating the effects on cell fitness due to CRISPR knockouts of each gene in the top four enriched assemblies shown in panel a. Point color indicates assembly relevant to each gene. Right: Similar plot showing effects for gene KOs in non-important assemblies (right, negative control). Cell fitness is z-score normalized across all tested gene KOs, with z>0 indicating increased fitness relative to average, and z<0 indicating decreased fitness. *p<0.05 by two-tailed Mann-Whitney U-test. **d,** Violin plots illustrating enrichment of assemblies for gene KOs modulating cell fitness without palbociclib treatment, comparing the core assemblies versus the same number of non-important assemblies. NS, not significant by one-tailed Mann-Whitney U-test. **e**, Scatter plot of cell fitness of gene KOs in the context of CDK4/6i (x-axis) versus CDK6 KO (y-axis). Genes are shown from the top four assemblies in panel **a** (n=18). **f**, Violin plots illustrating the mean fitness across gene KOs in core assemblies versus the same number of gene KOs from non-important assemblies in combination with CDK4 KO. **p<0.01 by two-tailed Mann–Whitney U-test. **g**, Same as panel **f**, except gene KOs are combined with CDK6 KO. *p<0.05 by two-tailed Mann–Whitney U-test. In panels f and g, two core assemblies did not have sufficient coverage in the gene panel, thus 6 of 8 were tested.

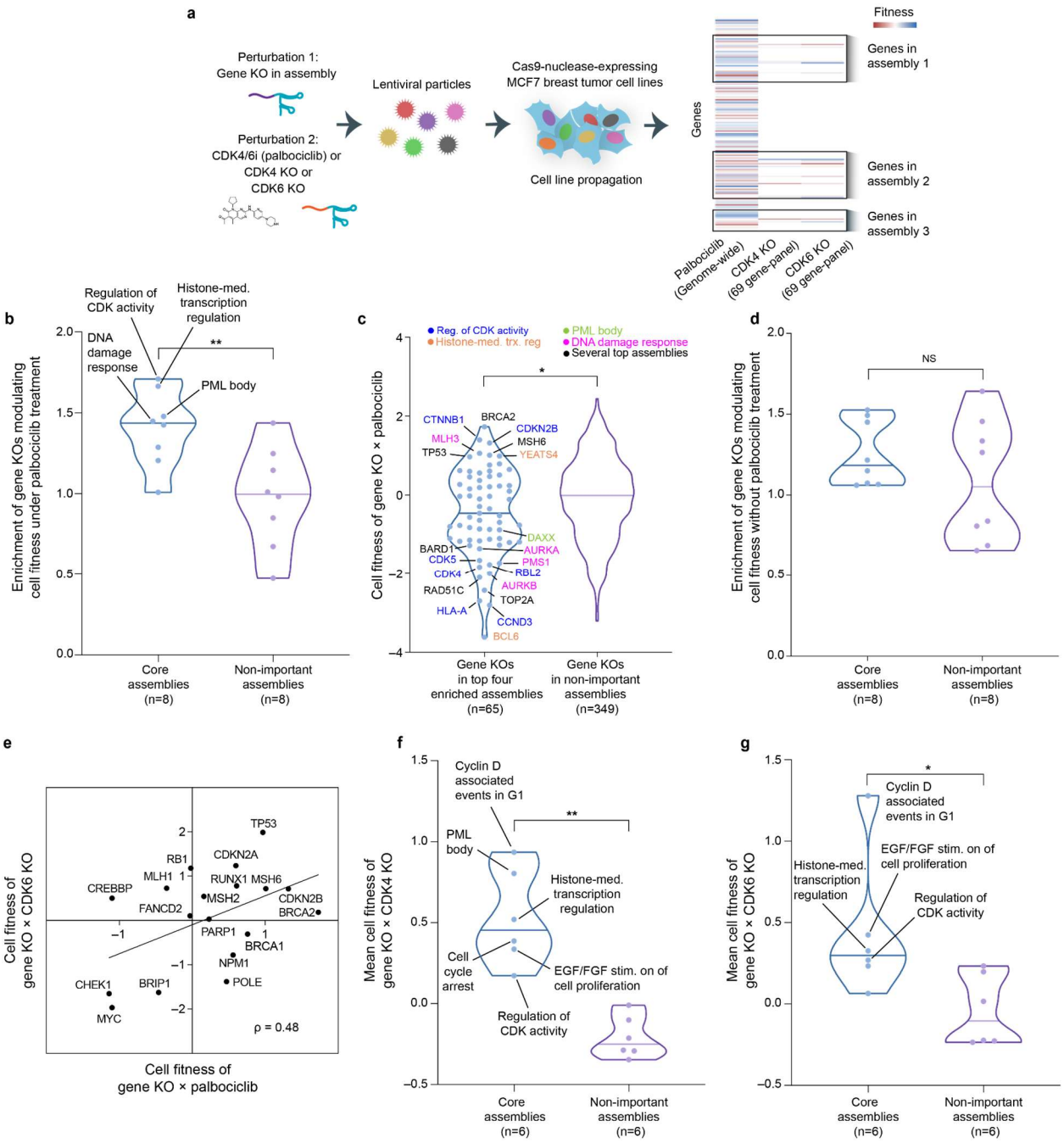
a
Perturbation 1:
Gene KO in assembly
Perturbation 2:
CDK4/6i (palbociclib) or
CDK4 KO or
CDK6 KO
Lentiviral particles
Cas9-nuclease-expressing
MCF7 breast tumor cell lines
Cell line propagation
Fitness
Genes
Genes in assembly 1
Genes in assembly 2
Genes in assembly 3
Palbociclib (Genome-wide)
CDK4 KO (69 gene-panel)
CDK6 KO (69 gene-panel)
b
Regulation of CDK activity
Histone-med. transcription regulation
DNA damage response
PML body
**
Enrichment of gene KOs modulating cell fitness under palbociclib treatment
Core assemblies (n=8)
Non-important assemblies (n=8)
c
Reg. of CDK activity
Histone-med. trx. reg
PML body
DNA damage response
Several top assemblies
*
Cell fitness of gene KO × palbociclib
CTNNB1
BRCA2
CDKN2B
MLH3
MSH6
TP53
YEATS4
DAXX
BARD1
AURKA
CDK5
PMS1
CDK4
RBL2
RAD51C
AURKB
TOP2A
HLA-A
CCND3
BCL6
Gene KOs in top four enriched assemblies (n=65)
Gene KOs in non-important assemblies (n=349)
d
NS
Enrichment of gene KOs modulating cell fitness without palbociclib treatment
Core assemblies (n=8)
Non-important assemblies (n=8)
e
Cell fitness of gene KO × CDK6 KO
TP53
RB1
CDKN2A
MLH1
RUNX1
MSH6
CREBBP
MSH2
CDKN2B
FANCD2
BRCA2
PARP1
BRCA1
NPM1
CHEK1
BRIP1
POLE
MYC
ρ = 0.48
Cell fitness of gene KO × palbociclib
f
Cyclin D associated events in G1
**
PML body
Histone-med. transcription regulation
Cell cycle arrest
EGF/FGF stim. on of cell proliferation
Regulation of CDK activity
Mean cell fitness of gene KO × CDK4 KO
Core assemblies (n=6)
Non-important assemblies (n=6)
g
*
Cyclin D associated events in G1
EGF/FGF stim. on of cell proliferation
Histone-med. transcription regulation
Regulation of CDK activity
Mean cell fitness of gene KO × CDK6 KO
Core assemblies (n=6)
Non-important assemblies (n=6)

Figure 3.5: Exploring the NeST:85 histone-related assembly in the palbociclib response.

a, Network diagram of NeST:85, depicting the Histone-mediated transcription regulation assembly. Edges show protein-protein biophysical associations, with thickness corresponding to the strength of evidence for association. Three subgroups of protein functions are indicated in boxes. **b,** OncoPrint illustrating genetic alteration patterns of NeST:85 genes (rows) in patient tumors of the TCGA/ICGC pan-cancer cohort (columns) along with representative cell lines (far-right columns). Genes sorted based on relative importance for drug resistance, then by alteration frequency within each important and non-important group. **c,** Odds ratios of important gene amplifications in NeST:85 with respect to palbociclib resistance in the TCGA/ICGC pan-cancer cohort. **d,** Schematic overview of CRISPRa gene overexpression screen. sgRNAs targeting the promoter regions of target genes were transfected into cells expressing the dCAS9-VPR transcriptional activator. Effects were characterized by EdU assay, which quantifies the number of cells undergoing active DNA synthesis, and by phosphorylation status of Rb, the molecular target of CDK4/6. Both palbociclib-treated and untreated conditions were examined. **e,** Cell microscopy images from EdU incorporation assay for non-targeting control (LEFT, NTC), TBL1XR1 overexpression (MIDDLE), or *KAT6A* overexpression (RIGHT). EdU-positive cells indicating active DNA synthesis are stained in green versus nuclei stained in blue with DAPI (4′,6-diamidino-2-phenylindole). Images are shown for palbociclib untreated (TOP) versus treated (BOTTOM) cells. **f,** Bar plot depicting fold increase in cells undergoing active DNA synthesis (S-phase) due to overexpression of specific target genes (x-axis) relative to non-targeting control (NTC). * $p<0.05$ by two-tailed Welch's t-test. Bars indicate mean; error bars indicate ± standard error; individual replicates shown. Circle points indicate biological replicate 1 (number of technical replicates=3) and square points indicate biological replicate 2 (number of technical replicates=3). **g,** Capillary western blot analysis of phospho-Rb levels for non-targeting control (NTC), TBL1XR1 overexpression, or KAT6A overexpression, in palbociclib-treated or untreated (DMSO) conditions. A representative image from two independent experiments. **h,** Bar plot depicting fold increase in relative phospho-Rb level (phospho-Rb/Actin) for overexpression of specific target genes (x-axis) relative to non-targeting control (NTC). * $p<0.05$ by two-tailed Welch's t-test. Bars indicate mean; error bars indicate ± standard error; individual replicates shown. Circle points indicate biological replicate 1 (number of technical replicates=3) and square points indicate biological replicate 2 (number of technical replicates=4).

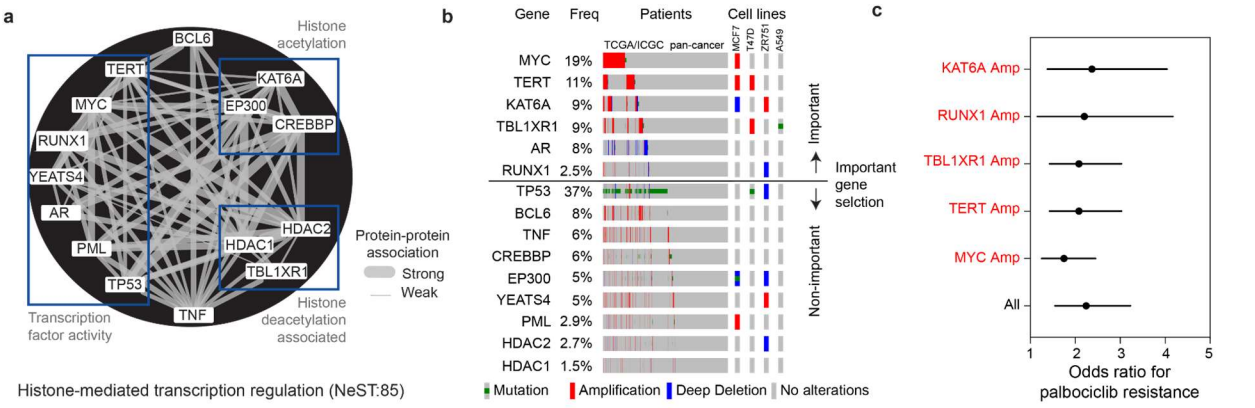
a
Histone acetylation
BCL6
TERT
KAT6A
MYC
EP300
CREBBP
RUNX1
YEATS4
AR
HDAC2
PML
HDAC1
TBL1XR1
TP53
TNF
Transcription factor activity
Histone deacetylation associated
Protein-protein association
Strong
Weak
Histone-mediated transcription regulation (NeST:85)
b
Gene
Freq
Patients
Cell lines
TCGA/ICGC pan-cancer
MCF7
147D
ZR751
A549
MYC 19%
TERT 11%
KAT6A 9%
TBL1XR1 9%
AR 8%
RUNX1 2.5%
TP53 37%
BCL6 8%
TNF 6%
CREBBP 6%
EP300 5%
YEATS4 5%
PML 2.9%
HDAC2 2.7%
HDAC1 1.5%
Important
Important gene selction
Non-important
Mutation
Amplification
Deep Deletion
No alterations
c
KAT6A Amp
RUNX1 Amp
TBL1XR1 Amp
TERT Amp
MYC Amp
All
1
2
3
4
5
Odds ratio for palbociclib resistance
d
sgRNAs
Target gene: KAT6A, RUNX1, TBL1XR1, TERT, MYC
sgRNA transfection
dCAS9-VPR expressing A549 cells
Selection with puromycin
Gene-overexpressed cell population
+/– palbociclib treatment
Entry into S phase (EdU assay)
Rb phosphorylation (western)
e
Control (NTC)
TBL1XR1 (+)
KAT6A (+)
Palbociclib (–)
Palbociclib (+)
50 μm
EdU positive cells
Nuclei
f
Fold change in cells undergoing S-phase compared to NTC control
Palbociclib (–)
Palbociclib (+)
TBL1XR1
KAT6A
RUNX1
TERT
MYC
Over-expressed gene
g
NTC
TBL1XR1
KAT6A
NTC
TBL1XR1
KAT6A
Palbociclib – – – + + +
Phospho Rb
Actin
h
Palbociclib (–)
Palbociclib (+)
Fold change in phospho-RB level compared to NTC
TBL1XR1
KAT6A
Over-expressed gene

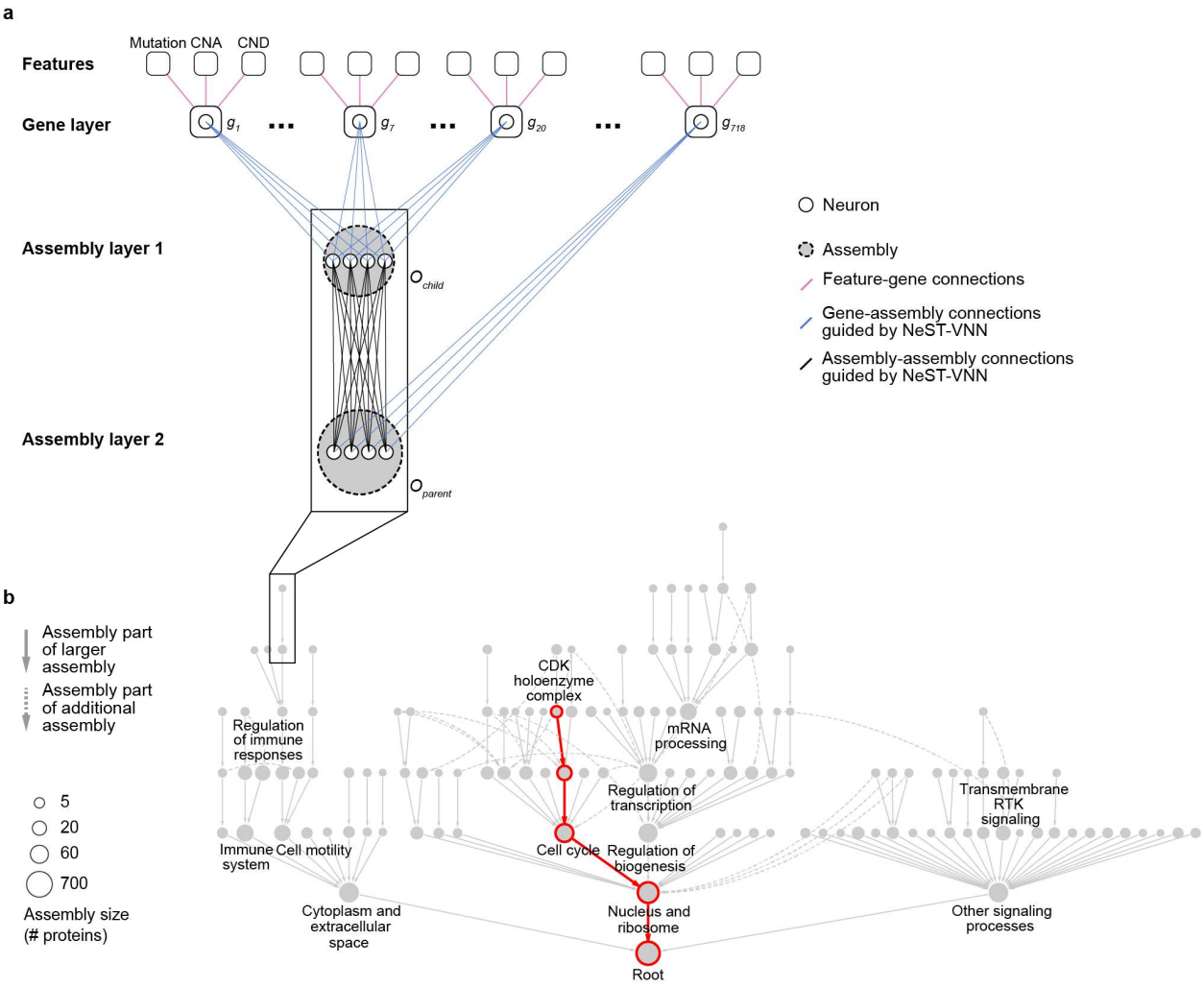

Supplementary Figure 3.1: NeST-VNN schematic.

a, The first layer of NeST-VNN incorporates gene-level features, including gene mutations, copy number amplifications (CNA), and copy number deletions (CND). Subsequent assembly layers aggregate gene-level features into assembly-level information, guided by the hierarchical relationships defined by the NeST map. The output state of each gene (*g*) and assembly (*O*) is represented by artificial neurons (one neuron per gene, multiple neurons per assembly). **b,** Position of the assemblies detailed in panel **a** within the greater NeST map. Each node indicates a protein assembly. An example path of information flow, from the neurons of CDK holoenzyme complex to Cell cycle through to the model Root, is shown in red.

Supplementary Figure 3.2: Supplemental model performance analysis.

a, Dot plot of model performance for each of 51 drugs for NeST-VNN (red) versus 3 alternate models: ElasticNet (green), Random Forest (purple), and a conventional Artificial Neural Network (ANN, blue). Palbociclib model highlighted in pink. **b,** Boxplot of performance for all drugs. Box plots show the 25th, 50th, and 75th percentiles of Pearson correlation. P-values reflect results of a one-tailed t-test assessing whether NeST-VNN outperforms baseline models. **c,** Bar chart of performance for palbociclib models. Error bars represent 95% confidence intervals with mean as the midpoint. P-values reflect results of one-tailed t-test. **d,** ROC curves for predicting resistance (yellow) or sensitivity (blue) to palbociclib. Marked points indicate cutoffs used to label samples as "resistant" or "sensitive" at different stringencies. Values in parenthesis indicate the (x,y) coordinate. **e,** Survival curves for CDK4/6i-treated patients stratified by somatic mutations or copy number deletions in *RB1.* **f,** Survival curves for CDK4/6i-treated patients stratified by somatic copy number amplifications in *CCND1*.

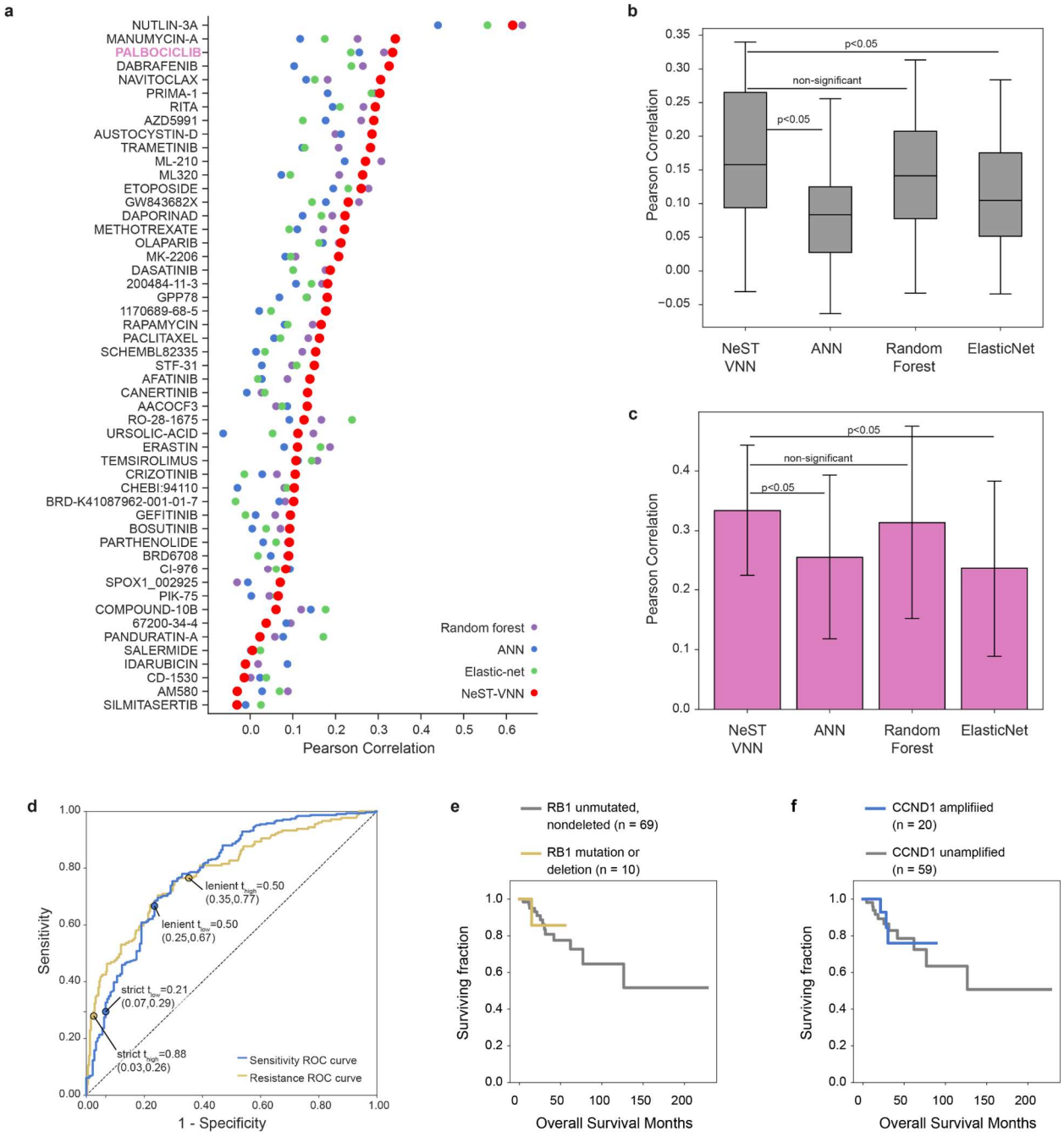
a
NUTLIN-3A
MANUMYCIN-A
PALBOCICLIB
DABRAFENIB
NAVITOCLAX
PRIMA-1
RITA
AZD5991
AUSTOCYSTIN-D
TRAMETINIB
ML-210
ML320
ETOPOSIDE
GW843682X
DAPORINAD
METHOTREXATE
OLAPARIB
MK-2206
DASATINIB
200484-11-3
GPP78
1170689-68-5
RAPAMYCIN
PACLITAXEL
SCHEMBL82335
STF-31
AFATINIB
CANERTINIB
AACOCF3
RO-28-1675
URSOLIC-ACID
ERASTIN
TEMSIROLIMUS
CRIZOTINIB
CHEBI:94110
BRD-K41087962-001-01-7
GEFITINIB
BOSUTINIB
PARTHENOLIDE
BRD6708
CI-976
SPOX1_002925
PIK-75
COMPOUND-10B
67200-34-4
PANDURATIN-A
SALERMIDE
IDARUBICIN
CD-1530
AM580
SILMITASERTIB
Random forest
ANN
Elastic-net
NeST-VNN
0.0 0.1 0.2 0.3 0.4 0.5 0.6
Pearson Correlation
b
Pearson Correlation
p<0.05
non-significant
p<0.05
NeST VNN
ANN
Random Forest
ElasticNet
c
Pearson Correlation
p<0.05
non-significant
p<0.05
NeST VNN
ANN
Random Forest
ElasticNet
d
Sensitivity
1 - Specificity
lenient t_high=0.50 (0.35,0.77)
lenient t_low=0.50 (0.25,0.67)
strict t_low=0.21 (0.07,0.29)
strict t_high=0.88 (0.03,0.26)
Sensitivity ROC curve
Resistance ROC curve
e
RB1 unmutated, nondeleted (n = 69)
RB1 mutation or deletion (n = 10)
Surviving fraction
Overall Survival Months
f
CCND1 amplifiied (n = 20)
CCND1 unamplified (n = 59)
Surviving fraction
Overall Survival Months

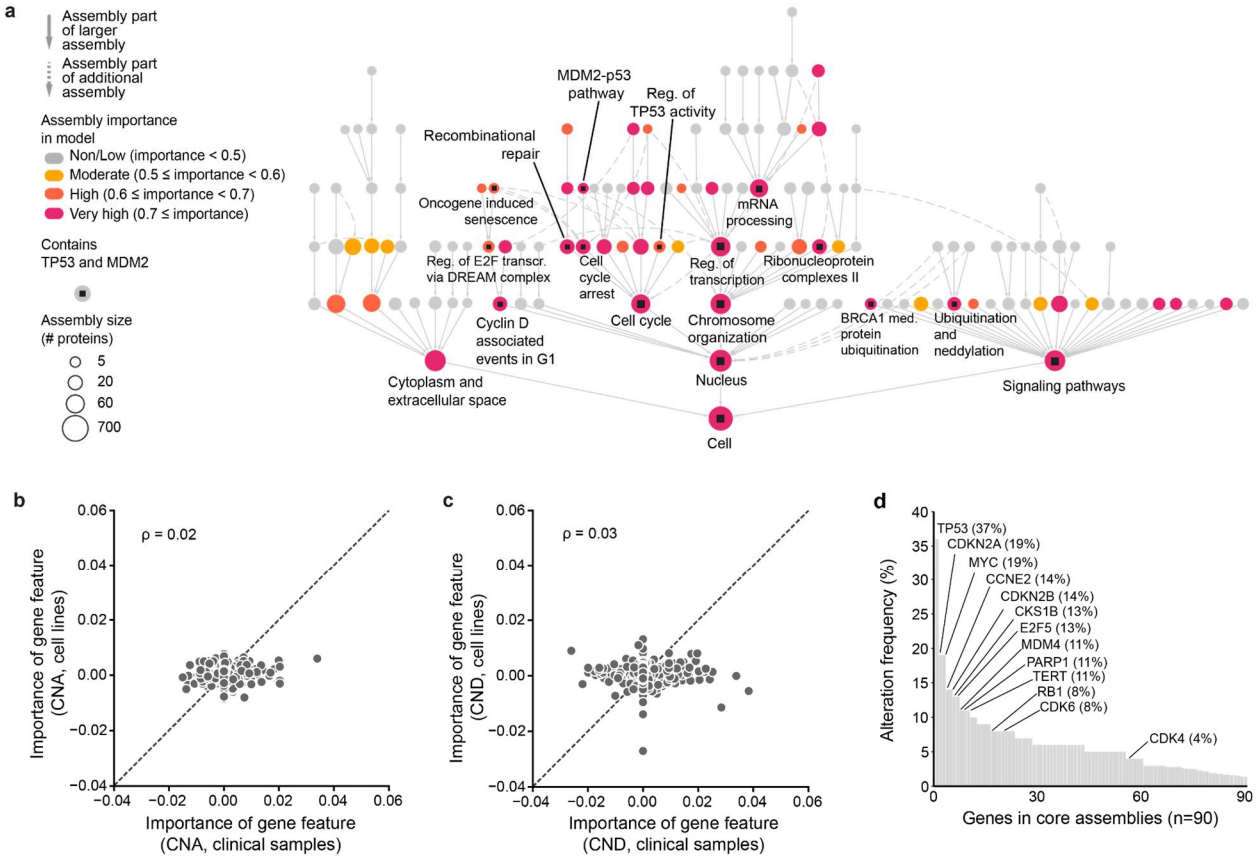

Supplementary Figure 3.3: Supplemental model interpretation.

a, NeST-VNN interpretation of the Nutlin-3a response. Nodes indicate assemblies; node sizes indicate assembly sizes in numbers of proteins; node colors indicate degrees of importance for response prediction; squares inside the nodes indicate whether the assembly contains TP53 and MDM2, drug targets of Nutlin-3a. **b,** Scatter plots of gene importance based on copy number amplifications (CNA) in clinical vs. cell line contexts (x vs. y). **c**, same as panel **b** except the gene importance is based on copy number deletions (CND). **d,** Alteration frequencies of genes within core assemblies. Includes somatic mutations, CNA, and CND observed in the TCGA/ICGC pan-cancer data.

Supplementary Figure 3.4: Analysis of Histone-mediated transcription regulation (NeST:85).

a, Alteration frequency of NeST:85 genes across tumor types**.** Frequency (y-axis) and type (color) of genetic alterations in NeST:85 genes *KAT6A*, *MYC*, *RUNX1*, *TBL1XR1*, and *TERT*, displayed across tumor cohorts documented by the cBioPortal (x-axis). Downloaded from cbioportal.org on 14 July 2023. **b,** Waterfall plot illustrating NeST:85 prediction (y-axis) in PDX samples (x-axis, n=41). The prediction was determined from the first principal component (PC1) of the in-silico activity of the NeST:85 assembly, thresholded (median ± stdev) to assign class labels (predicted sensitive/undefined/predicted resistant). Bar color represents true response of a PDX sample on a CDK4/6 inhibitor (ribociclib) based on the RECIST categories (yellow, resistance (PD); blue, sensitive (CR, PR, or SD)). **c,** Bar plot depicting fold increase in mRNA expression level due to overexpression of specific gene targets relative to non-targeting control (NTC). Bars indicate means of repeat experiments, with technical replicate data points shown (n=2). **d,** Full capillary western blot image of phospho-RB (pRB) level for nominal conditions (non-targeting control, NTC), TBL1XR1 overexpression, or KAT6A overexpression. A representative image from two independent experiments.

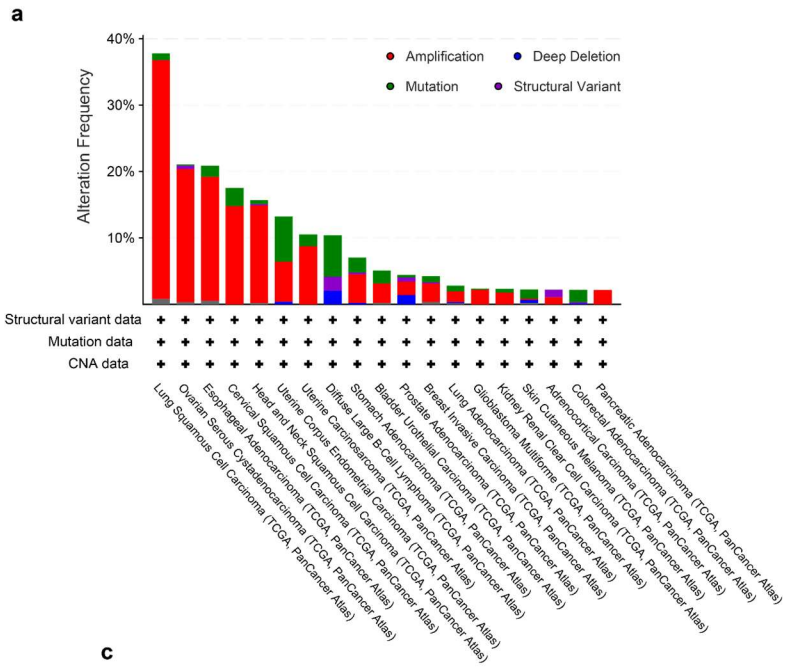
a
40%
30%
20%
10%
Alteration Frequency
Amplification
Deep Deletion
Mutation
Structural Variant
Structural variant data
Mutation data
CNA data
Lung Squamous Cell Carcinoma (TCGA, PanCancer Atlas)
Ovarian Serous Cystadenocarcinoma (TCGA, PanCancer Atlas)
Esophageal Adenocarcinoma (TCGA, PanCancer Atlas)
Cervical Squamous Cell Carcinoma (TCGA, PanCancer Atlas)
Head and Neck Squamous Cell Carcinoma (TCGA, PanCancer Atlas)
Uterine Corpus Endometrial Carcinoma (TCGA, PanCancer Atlas)
Diffuse Large B-Cell Lymphoma (TCGA, PanCancer Atlas)
Stomach Adenocarcinoma (TCGA, PanCancer Atlas)
Bladder Urothelial Carcinoma (TCGA, PanCancer Atlas)
Prostate Adenocarcinoma (TCGA, PanCancer Atlas)
Breast Invasive Carcinoma (TCGA, PanCancer Atlas)
Lung Adenocarcinoma (TCGA, PanCancer Atlas)
Glioblastoma Multiforme (TCGA, PanCancer Atlas)
Kidney Renal Clear Cell Carcinoma (TCGA, PanCancer Atlas)
Skin Cutaneous Melanoma (TCGA, PanCancer Atlas)
Adrenocortical Carcinoma (TCGA, PanCancer Atlas)
Colorectal Adenocarcinoma (TCGA, PanCancer Atlas)
Pancreatic Adenocarcinoma (TCGA, PanCancer Atlas)

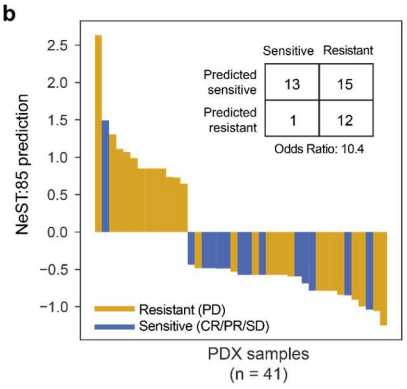
b
NeST:85 prediction
2.5
2.0
1.5
1.0
0.5
0.0
−0.5
−1.0
Sensitive
Resistant
Predicted sensitive
13
15
Predicted resistant
1
12
Odds Ratio: 10.4
Resistant (PD)
Sensitive (CR/PR/SD)
PDX samples
(n = 41)

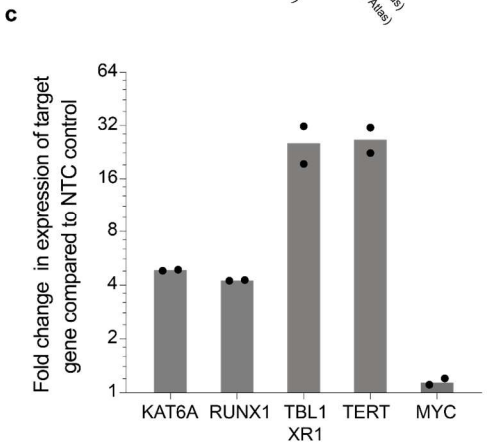
c
Fold change in expression of target gene compared to NTC control
64
32
16
8
4
2
1
KAT6A
RUNX1
TBL1 XR1
TERT
MYC

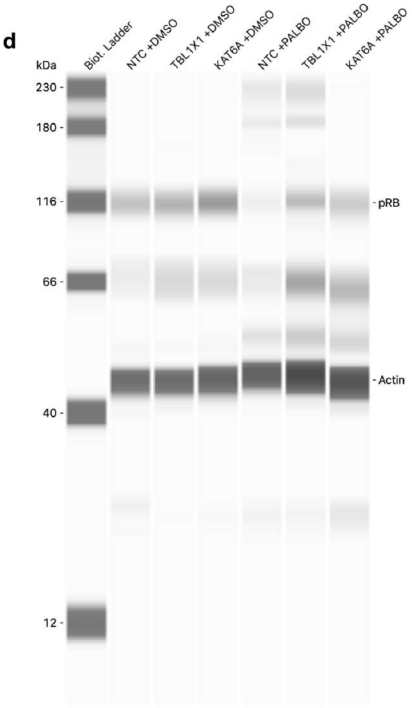
d
kDa
Biot. Ladder
NTC +DMSO
TBL1X1 +DMSO
KAT6A +DMSO
NTC +PALBO
TBL1X1 +PALBO
KAT6A +PALBO
230
180
116
66
40
12
pRB
Actin

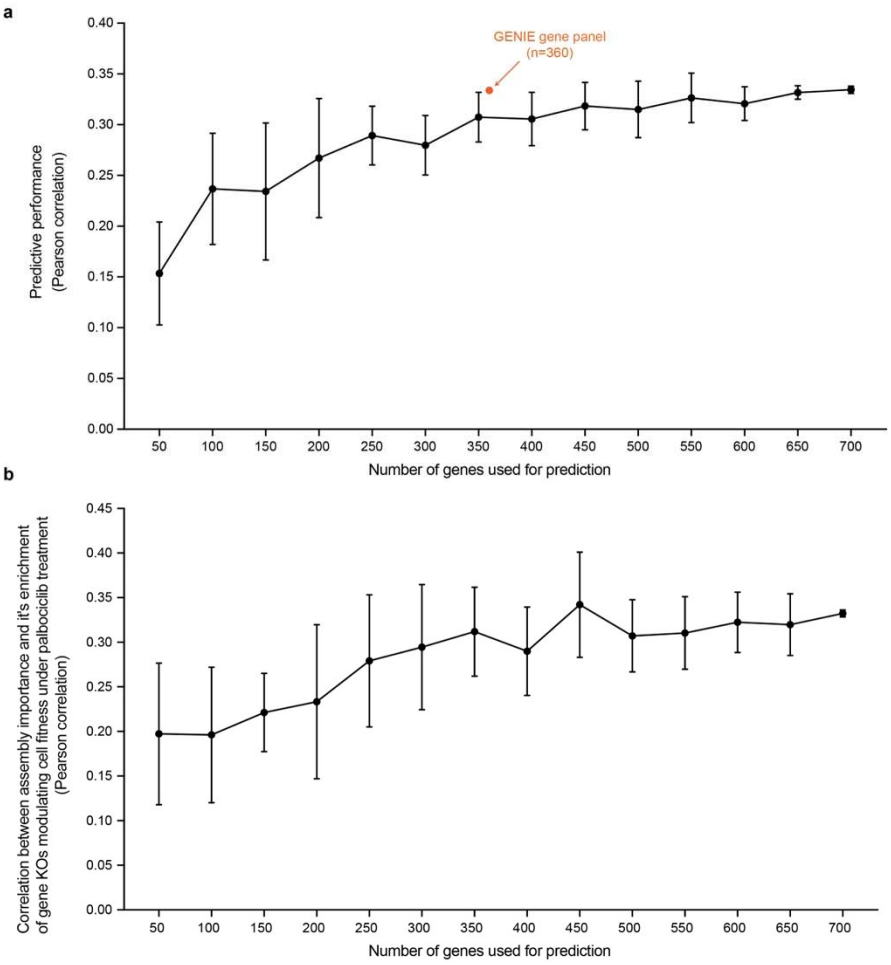

Supplementary Figure 3.5: Analysis of NeST-VNN robustness.

a, Predictive performance of NeST-VNN according to the number of genes used for prediction. Predictive performance is defined by the Pearson correlation between the predicted and actual drug responses. Each point represents the average predictive performance (y-axis) from 10 repeated experiments, with each experiment drawing a different random selection of genes of a given set size (x-axis). The error bar indicates the standard deviation of the predictive performance across these experiments. The orange point indicates the predictive performance (Pearson ρ=0.33) using the GENIE gene panel (n=360) for prediction. **b,** Correlation (Pearson ρ) between the importance of protein assemblies for model prediction and their enrichments for gene KOs that modulate palbociclib response (y-axis) as a function of the number of genes used for prediction (x-axis). Each point represents the average Pearson correlation from 10 repeated experiments, with each experiment drawing a different random selection of genes of a given set size. The error bar indicates the standard deviation of the Pearson correlation across these experiments.

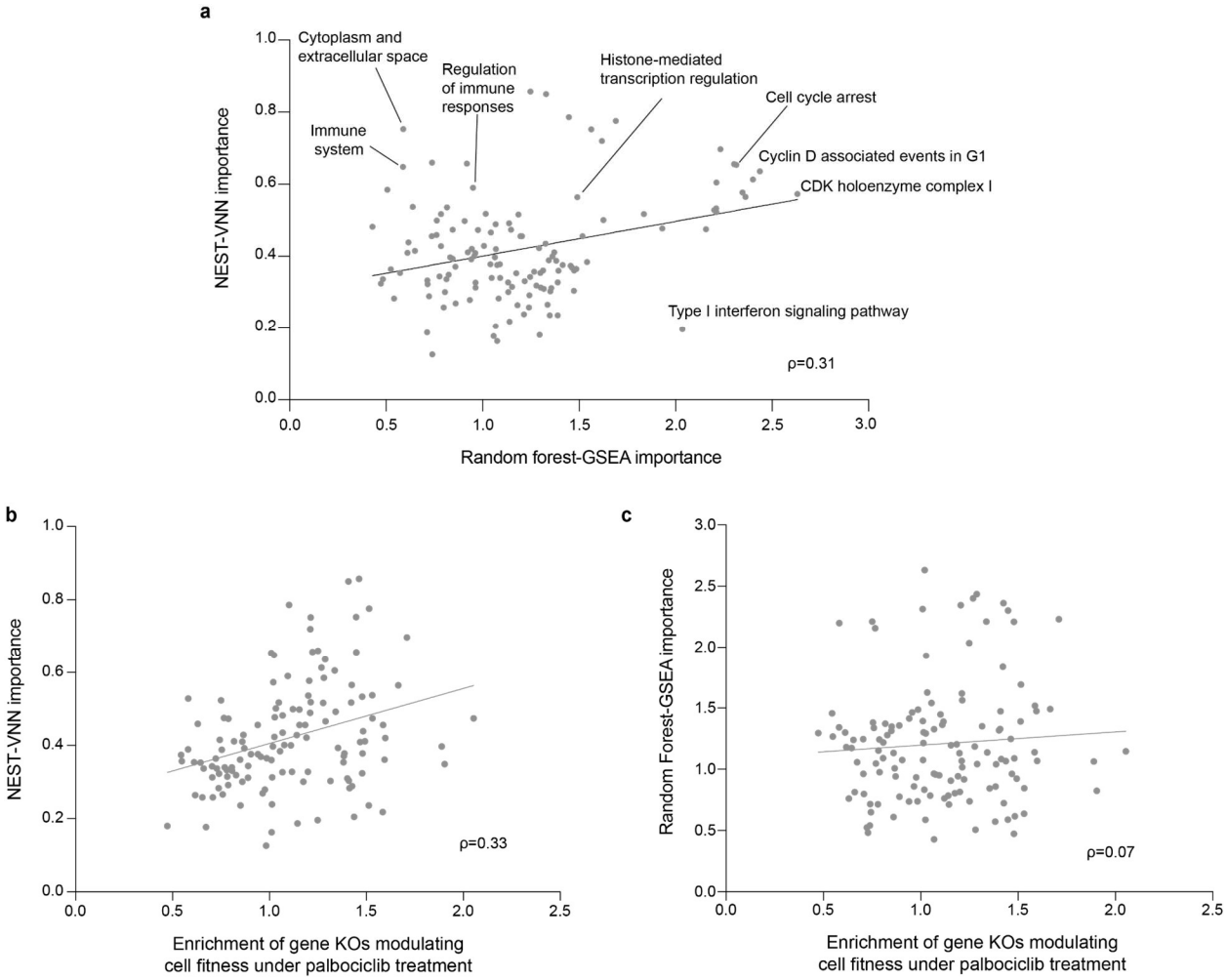

Supplementary Figure 3.6: Comparison of NeST-VNN versus Random Forest models.

a, Scatter plot of assembly importances from a Random forest-GSEA approach (x-axis) versus a NeST-VNN approach (y-axis). **b,** Scatter plot of assembly importance in the NeST-VNN model (y-axis) versus enrichment of gene KOs modulating cell fitness under palbociclib treatment (x-axis). Each dot represents an assembly (n=130). Rho (ρ) indicates the Pearson correlation. **c,** Same as panel **b** except the y-axis indicating Random Forest-GSEA importance.

3.8 Tables

Table 3.1: Summary of predictive performance for all 51 drugs.

Drug	Fold1	Fold2	Fold3	Fold4	Fold5	Average
Palbociclib	0.419	0.275	0.367	0.309	0.299	0.334
Trametinib	0.342	0.301	0.260	0.259	0.247	0.282
parthenolide	0.023	0.133	0.134	0.087	0.082	0.092
Dabrafenib	0.384	0.190	0.360	0.375	0.320	0.326
nutlin-3A	0.596	0.573	0.680	0.576	0.650	0.615
etoposide	0.275	0.240	0.261	0.284	0.241	0.260
paclitaxel	0.141	0.118	0.194	0.212	0.146	0.162
Rapamycin	0.115	0.158	0.180	0.188	0.190	0.166
Olaparib	0.242	0.217	0.138	0.217	0.250	0.213
Temsirolimus	0.126	0.103	0.136	0.087	0.083	0.107
MK-2206	0.228	0.153	0.220	0.166	0.270	0.207
Gefitinib	0.115	0.068	0.040	0.133	0.115	0.094
Ursolic-acid	-0.061	0.181	0.312	0.357	-0.229	0.112
Crizotinib	0.072	0.132	0.102	0.111	0.111	0.105
N-4-(1-BENZO	0.005	0.198	0.169	0.094	0.302	0.153
Salermide	0.099	-0.249	0.121	0.089	-0.034	0.005
200484-11-3	0.256	0.147	0.201	0.132	0.171	0.181
BRD6708	0.014	0.094	0.017	0.114	0.213	0.090
BRD-K41087962	-0.008	-0.049	0.196	0.278	0.093	0.102
PIK-75	0.199	0.023	0.097	-0.072	0.082	0.066
ML-210	0.424	0.303	0.197	0.107	0.320	0.270
Panduratin-A	-0.088	0.207	-0.127	0.020	0.102	0.023
Daporinad	0.239	0.264	0.245	0.094	0.270	0.222
67200-34-4	0.026	0.018	0.081	0.042	0.020	0.038
Bosutinib	0.073	0.112	0.059	0.120	0.098	0.093
AM580	-0.126	0.137	0.014	-0.023	-0.154	-0.030
STF-31	0.118	0.240	0.154	0.072	0.168	0.150
IDARUBICIN	0.033	-0.257	0.140	0.014	0.014	-0.011
Dasatinib	0.255	0.089	0.193	0.223	0.177	0.188
Austocystin-D	0.364	0.277	0.369	0.120	0.297	0.285
Ro-28-1675	0.170	0.051	0.297	0.101	0.013	0.126
AZD5991	0.306	0.301	0.417	0.194	0.230	0.290
Aacocf3	0.184	0.129	0.189	0.145	0.023	0.134
CD-1530	-0.063	0.059	-0.084	0.047	-0.028	-0.014
ERASTIN	0.151	-0.026	0.132	0.294	0.004	0.111
CHEBI:94110	0.063	0.158	0.116	0.142	0.037	0.103
prima-1	0.317	0.283	0.278	0.279	0.361	0.304
RITA	0.272	0.247	0.350	0.331	0.267	0.293
methotrexate	0.235	0.176	0.255	0.170	0.268	0.221
Compound-10b	0.232	0.101	-0.068	0.007	0.030	0.061
Afatinib	0.154	0.139	0.179	0.166	0.062	0.140
SpOx1_002925	-0.049	-0.009	0.274	0.112	0.025	0.070
Manumycin-A	0.350	0.249	0.338	0.408	0.355	0.340
Silmitasertib	0.093	0.086	-0.113	-0.100	-0.121	-0.031
ml320	0.272	0.333	0.226	0.236	0.251	0.263
GPP78	0.203	0.157	0.239	0.157	0.147	0.181
1170689-68-5	0.246	0.133	0.213	0.154	0.143	0.178
Navitoclax	0.289	0.256	0.335	0.244	0.405	0.306
GW843682X	0.314	0.220	0.198	0.123	0.294	0.230
Canertinib	0.165	0.116	0.156	0.072	0.164	0.135
CI-976	0.060	0.166	0.144	-0.025	0.071	0.083

Table 3.2: Summary of assembly importance and statistical significance.

Assembly ID	Assembly Name	Assembly Importance	t_test - FDR
NEST	NeST	1.00	0.90
NEST:1	Other signaling processes	0.86	0.90
NEST:10	mRNA processing	0.72	0.81
NEST:102	CDK holoenzyme complex II	0.52	0.80
NEST:104	MAPK and MAP2K activation	0.40	1.00
NEST:105	Protein neddylation	0.31	1.00
NEST:107	HDACs deacetylate histones	0.47	1.00
NEST:108	Adherens junction	0.50	0.81
NEST:11	Metabolic pathways	0.36	1.00
NEST:110	CDK holoenzyme complex I	0.57	0.02
NEST:112	Androgen receptor signaling pathway	0.57	0.03
NEST:117	Regulation of TP53 Activity	0.42	1.00
NEST:119	Regulation of E2F tx via DREAM complex	0.53	0.02
NEST:12	Membrane trafficking	0.46	1.00
NEST:121	Extended cohesin complex	0.34	0.81
NEST:123	PML body	0.53	0.01
NEST:125	Extended mismatch repair complex	0.33	1.00
NEST:126	NEST:126	0.39	1.00
NEST:127	Intrinsic pathway for apoptosis	0.34	1.00
NEST:129	BAF (SWI/SNF) complex	0.31	1.00
NEST:13	Ribosome biogenesis	0.46	1.00
NEST:130	Homologous recombination	0.39	1.00
NEST:132	EGF/FGF stimulation of cell proliferation	0.58	0.02
NEST:133	Histone methyltransferase subcomplex	0.26	1.00
NEST:134	RPA complex associated proteins	0.34	0.90
NEST:137	AKT/MTOR pathway II	0.40	0.81
NEST:138	PIK3/AKT/PTEN signaling	0.42	1.00
NEST:14	Cytoskeleton	0.54	1.00
NEST:142	EGF/beta-catenin signaling	0.41	1.00
NEST:145	AKT/MTOR pathway I	0.36	0.46
NEST:146	SMAD-TGFbeta signaling	0.29	1.00
NEST:15	Cell cycle	0.78	0.28
NEST:150	G1 to S cell cycle control	0.48	0.69
NEST:153	PIK3-EGFR signaling	0.43	1.00
NEST:155	H3 acetylation and H3K4 methylation crosstalk	0.29	1.00
NEST:158	Histone modifications in DNA damage response	0.18	1.00
NEST:16	NEST:16	0.52	1.00
NEST:163	NEST:163	0.33	1.00
NEST:165	Transcription coactivator activity	0.35	0.68
NEST:168	CBP and p300 binds NF-kB complex	0.44	0.95
NEST:169	AKT1 activation	0.33	1.00
NEST:17	Ribonucleoprotein complexes II	0.54	1.00
NEST:170	Phosphatase 2A catalytic subunit	0.18	1.00
NEST:174	Extended beta-catenin destruction complex	0.32	1.00
NEST:177	TP53 regulates transcription of cell cycle genes	0.37	0.34
NEST:18	Regulation of immune responses	0.59	1.00
NEST:182	Beta-catenin-TCF complex	0.38	0.92
NEST:186	MDM2-p53 pathway	0.52	0.01
NEST:19	mRNA splicing	0.37	1.00
NEST:193	Resolution of D-loop structures	0.40	0.93
NEST:195	NEST:195	0.37	0.81
NEST:196	Cohesin complex	0.32	0.69
NEST:199	Oncogene induced senescence	0.48	0.01
NEST:2	Cytoplasm and extracellular space	0.75	1.00
NEST:20	Extracellular matrix organization	0.44	0.98

Table 3.2: Summary of assembly importance and statistical significance. (Continued)

Assembly ID	Assembly Name	Assembly Importance	t_test - FDR
NEST:202	MHC class I including non-classical MHCs	0.16	1.00
NEST:21	Protein processing in endoplasmic reticulum	0.34	0.90
NEST:210	Regulation of AR signaling	0.30	0.98
NEST:212	RAS-RAF-MAPK signaling	0.34	1.00
NEST:22	Structural constituent of muscle	0.22	1.00
NEST:221	Non-canonical Wnt signaling pathway	0.32	0.93
NEST:23	Actin filament-based process	0.41	0.98
NEST:231	MutS homologs	0.26	1.00
NEST:239	Beta-catenin destruction complex	0.28	1.00
NEST:24	Keratinization	0.33	1.00
NEST:25	Lymphocyte activation	0.48	1.00
NEST:254	EGFR-insulin receptor cross-talk	0.35	0.98
NEST:256	FGFR-ERBB-RAS signaling	0.32	1.00
NEST:26	Spliceosomal-snRNP complex	0.35	1.00
NEST:27	Contractile fiber	0.21	1.00
NEST:277	MutL alpha/beta complex	0.24	1.00
NEST:29	NEST:29	0.46	0.90
NEST:293	RBL-TP53 complex	0.33	0.70
NEST:3	Nucleus and ribosome	0.85	0.81
NEST:30	DNA metabolic process	0.66	0.03
NEST:31	Extracellular matrix	0.39	0.81
NEST:32	Ubiquitination and neddylation	0.47	1.00
NEST:33	Ribosome abundance control	0.47	0.81
NEST:34	Histone modification	0.61	0.27
NEST:35	Spliceosomal complex	0.13	1.00
NEST:36	Interferon signaling	0.24	1.00
NEST:38	Transmembrane RTK signaling	0.66	1.00
NEST:39	Regulation of mRNA processing	0.19	1.00
NEST:4	Regulation of biogenesis	0.79	0.81
NEST:40	Actin filaments	0.38	1.00
NEST:42	Transcription elongation	0.36	0.98
NEST:43	Type I interferon signaling pathway	0.20	1.00
NEST:44	Nuclear transport	0.42	0.10
NEST:45	Mediator/CCR-NOT complex	0.30	1.00
NEST:47	Apoptosis	0.46	0.98
NEST:48	Actin cytoskeleton	0.30	0.98
NEST:49	NEST:49	0.34	1.00
NEST:5	Cell motility	0.66	1.00
NEST:50	Regulation of CDK activity	0.70	0.03
NEST:51	ECM-cytoskeleton assembly	0.38	0.57
NEST:52	AKT/activin signaling	0.52	1.00
NEST:53	Integrator-PP2A complex	0.42	1.00
NEST:54	Cell-extracellular matrix interactions	0.28	1.00
NEST:55	Nucleosome remodeling	0.49	0.81
NEST:57	Histone acetyltransferase complex	0.46	0.98
NEST:58	Cyclin D associated events in G1	0.64	0.05
NEST:59	Chromosome centrometric region	0.35	0.98
NEST:6	Regulation of transcription	0.75	0.98
NEST:60	Nuclear receptor transcription pathway	0.49	0.98
NEST:61	COP9-Cul4-RING ubiquitin E3 ligase complex	0.30	1.00
NEST:63	Actin and actin-associated proteins	0.31	0.98
NEST:65	Cell cycle arrest	0.65	0.03
NEST:66	PcG protein complex	0.39	0.98
NEST:69	SUMOylation for nuclear transport	0.41	0.10
NEST:7	Metabolism	0.41	1.00

Table 3.2: Summary of assembly importance and statistical significance. (Continued)

Assembly ID	Assembly Name	Assembly Importance	t_test - FDR
NEST:70	BRCA1 mediated protein ubiquitination	0.47	0.81
NEST:73	MAPK signaling	0.52	1.00
NEST:77	COP9 signalosome-ubiquitin E3 ligase complex	0.26	1.00
NEST:78	NEST:78	0.24	1.00
NEST:79	Recombinational repair	0.50	1.00
NEST:8	Immune system	0.65	1.00
NEST:80	NEST:80	0.28	1.00
NEST:81	TGF-beta pathway/SMAD protein complex	0.27	1.00
NEST:82	Extended PRC1 complex	0.38	0.98
NEST:83	TNF signaling pathway	0.43	1.00
NEST:84	JAK-STAT signaling pathway	0.40	1.00
NEST:85	NEST:85	0.56	0.10
NEST:89	Erb and JAK-STAT signaling	0.50	1.00
NEST:9	Ribonucleoprotein complexes	0.59	0.98
NEST:90	Mediator complex	0.27	1.00
NEST:91	NEST:91	0.61	0.03
NEST:92	Polybromo- and BAF containing complex	0.36	1.00
NEST:93	tRNA transport	0.38	0.14
NEST:94	Nucleosome assembly	0.37	1.00
NEST:97	Ephrin receptor activity	0.31	1.00
NEST:98	Histone methyltransferase complex	0.36	1.00

3.9 Data availability

The datasets used in this study are all publicly available. GDSC version 1: https://www.cancerrxgene.org/downloads/bulk_download; GDSC version 2: https://www.cancerrxgene.org/downloads/bulk_download; CTRP version 1: https://portals.broadinstitute.org/ctrp.v1/; CTRP version 2: https://portals.broadinstitute.org/ctrp.v2.1/; DepMap 22Q1: https://doi.org/10.6084/m9.figshare.19139906.v1; PDX: https://www.nature.com/articles/nm.3954; Project GENIE: https://genie.cbioportal.org/study/summary?id=brca_akt1_genie_2019; Genome-wide CRISPR KO chemogenetic screen: https://www.ncbi.nlm.nih.gov/geo/query/acc.cgi?acc=GSE192525 (GEO accession number: GSE192525). The Cytoscape session containing the NeST-VNN hierarchy and the pre-trained models are available on GitHub. Cytoscape session: https://github.com/idekerlab/nest_vnn/blob/main/misc/NeST_VNN_Palbociclib.cys; pre-trained models: https://github.com/idekerlab/nest_vnn/tree/main/pretrained_models/palbociclib

3.10 Code availability

The source code of NeST-VNN is available on GitHub (https://github.com/idekerlab/nest_vnn). Other supporting software is available as follows: Scikit-learn: http://scikit-learn.org/stable/index.html; PyTorch: http://pytorch.org.

3.11 Author Contributions Statement

S.P., E.S., and A.S. contributed equally to the manuscript. S.P., E.S., A.S., and T.I. conceived the idea. S.P., E.S., and A.S. developed the methods. S.P., E.S., A.S., M.K., and T.I. interpreted the results. K.L., I.P., and C.F., conducted the CRISPRa experiment. S.F. and J.L. conducted the dual CRISPR KO combinatorial screen experiment. M.K., X.Z., R.B., and T.I. reviewed the experimental analyses. X.Z., B.A.P, K.T.Y, and T.I, reviewed the data analyses. S.P., E.S., A.S., and T.I. wrote the manuscript. All authors reviewed the manuscript.

3.12 Acknowledgments

We are grateful to Dr. Anthony Sun and Dr. Jianzhu Ma for their very helpful comments. This work was supported by the National Institutes of Health via the Cancer Cell Map Initiative (CA274502), the National Resource for Network Biology (GM103504), the Network Data Exchange (CA184427), and the NCI (CA236404 and F30CA236404).

Chapter 3, in full, is a reformatted reprint of the material as it appears as “A deep learning model of tumor cell architecture elucidates response and resistance to CDK4/6 inhibitors” in Nature Cancer, 2024 by Park, Sungjoon; Silva, Erica; Singhal, Akshat; Kelly, Marcus R.; Licon, Kate; Panagiotou, Isabella; Fogg, Catalina; Fong, Samson; Lee, John J. Y.; Zhao, Xiaoyu; Bachelder, Robin; Parker, Barbara A.; Yeung, Kay T.; Ideker, Trey. The dissertation author was a primary investigator and author of this paper.

3.13 References

(1) Hanahan, D.; Weinberg, R. A. The Hallmarks of Cancer. *Cell* 2000, *100* (1), 57–70.

(2) Goel, S.; Bergholz, J. S.; Zhao, J. J. Targeting CDK4 and CDK6 in Cancer. *Nat. Rev. Cancer* 2022, *22* (6), 356–372.

(3) Watt, A. C.; Goel, S. Cellular Mechanisms Underlying Response and Resistance to CDK4/6 Inhibitors in the Treatment of Hormone Receptor-Positive Breast Cancer. *Breast Cancer Res.* 2022, *24* (1), 17.

(4) Fassl, A.; Geng, Y.; Sicinski, P. CDK4 and CDK6 Kinases: From Basic Science to Cancer Therapy. *Science* 2022, *375* (6577), eabc1495.

(5) Xu, X.-Q.; Pan, X.-H.; Wang, T.-T.; Wang, J.; Yang, B.; He, Q.-J.; Ding, L. Intrinsic and Acquired Resistance to CDK4/6 Inhibitors and Potential Overcoming Strategies. *Acta Pharmacol. Sin.* 2021, *42* (2), 171–178.

(6) Gao, J. J.; Cheng, J.; Bloomquist, E.; Sanchez, J.; Wedam, S. B.; Singh, H.; Amiri-Kordestani, L.; Ibrahim, A.; Sridhara, R.; Goldberg, K. B.; Theoret, M. R.; Kluetz, P. G.; Blumenthal, G. M.; Pazdur, R.; Beaver, J. A.; Prowell, T. M. CDK4/6 Inhibitor Treatment for Patients with Hormone Receptor-Positive, HER2-Negative, Advanced or Metastatic Breast Cancer: A US Food and Drug Administration Pooled Analysis. *Lancet Oncol.* 2020, *21* (2), 250–260.

(7) Li, J.; Huo, X.; Zhao, F.; Ren, D.; Ahmad, R.; Yuan, X.; Du, F.; Zhao, J. Association of Cyclin-Dependent Kinases 4 and 6 Inhibitors With Survival in Patients With Hormone Receptor-Positive Metastatic Breast Cancer: A Systematic Review and Meta-Analysis.

JAMA Netw Open 2020, *3* (10), e2020312.

(8) McCartney, A.; Migliaccio, I.; Bonechi, M.; Biagioni, C.; Romagnoli, D.; De Luca, F.; Galardi, F.; Risi, E.; De Santo, I.; Benelli, M.; Malorni, L.; Di Leo, A. Mechanisms of Resistance to CDK4/6 Inhibitors: Potential Implications and Biomarkers for Clinical Practice. *Front. Oncol.* 2019, *9*, 666.

(9) Rafique, R.; Islam, S. M. R.; Kazi, J. U. Machine Learning in the Prediction of Cancer Therapy. *Comput. Struct. Biotechnol. J.* 2021, *19*, 4003–4017.

(10) Yu, M. K.; Ma, J.; Fisher, J.; Kreisberg, J. F.; Raphael, B. J.; Ideker, T. Visible Machine Learning for Biomedicine. *Cell* 2018, *173* (7), 1562–1565.

(11) Kim, Y.-A.; Sarto Basso, R.; Wojtowicz, D.; Liu, A. S.; Hochbaum, D. S.; Vandin, F.; Przytycka, T. M. Identifying Drug Sensitivity Subnetworks with NETPHIX. *iScience* 2020, *23* (10), 101619.

(12) Jin, I.; Nam, H. HiDRA: Hierarchical Network for Drug Response Prediction with Attention. *J. Chem. Inf. Model.* 2021, *61* (8), 3858–3867.

(13) Ma, J.; Yu, M. K.; Fong, S.; Ono, K.; Sage, E.; Demchak, B.; Sharan, R.; Ideker, T. Using Deep Learning to Model the Hierarchical Structure and Function of a Cell. *Nat. Methods* 2018, *15* (4), 290–298.

(14) Kuenzi, B. M.; Park, J.; Fong, S. H.; Sanchez, K. S.; Lee, J.; Kreisberg, J. F.; Ma, J.; Ideker, T. Predicting Drug Response and Synergy Using a Deep Learning Model of Human Cancer Cells. *Cancer Cell* 2020, *38* (5), 672-684.e6.

(15) Elmarakeby, H. A.; Hwang, J.; Arafeh, R.; Crowdis, J.; Gang, S.; Liu, D.; AlDubayan, S. H.; Salari, K.; Kregel, S.; Richter, C.; Arnoff, T. E.; Park, J.; Hahn, W. C.; M Van Allen, E. Biologically Informed Deep Neural Network for Prostate Cancer Discovery. *Nature* 2021.

(16) Huang, X.; Huang, K.; Johnson, T.; Radovich, M.; Zhang, J.; Ma, J.; Wang, Y. ParsVNN: Parsimony Visible Neural Networks for Uncovering Cancer-Specific and Drug-Sensitive Genes and Pathways. *NAR Genom Bioinform* 2021, *3* (4), lqab097.

(17) Ashburner, M.; Ball, C. A.; Blake, J. A.; Botstein, D.; Butler, H.; Cherry, J. M.; Davis, A. P.; Dolinski, K.; Dwight, S. S.; Eppig, J. T.; Harris, M. A.; Hill, D. P.; Issel-Tarver, L.; Kasarskis, A.; Lewis, S.; Matese, J. C.; Richardson, J. E.; Ringwald, M.; Rubin, G. M.; Sherlock, G. Gene Ontology: Tool for the Unification of Biology. The Gene Ontology Consortium. *Nat. Genet.* 2000, *25* (1), 25–29.

(18) Gillespie, M.; Jassal, B.; Stephan, R.; Milacic, M.; Rothfels, K.; Senff-Ribeiro, A.; Griss, J.; Sevilla, C.; Matthews, L.; Gong, C.; Deng, C.; Varusai, T.; Ragueneau, E.; Haider, Y.; May, B.; Shamovsky, V.; Weiser, J.; Brunson, T.; Sanati, N.; Beckman, L.; Shao, X.; Fabregat, A.; Sidiropoulos, K.; Murillo, J.; Viteri, G.; Cook, J.; Shorser, S.; Bader, G.; Demir, E.; Sander, C.; Haw, R.; Wu, G.; Stein, L.; Hermjakob, H.; D'Eustachio, P. The Reactome Pathway Knowledgebase 2022. *Nucleic Acids Res.* 2022, *50* (D1), D687–D692.

(19) Zheng, F.; Kelly, M. R.; Ramms, D. J.; Heintschel, M. L.; Tao, K.; Tutuncuoglu, B.; Lee, J. J.; Ono, K.; Foussard, H.; Chen, M.; Herrington, K. A.; Silva, E.; Liu, S. N.; Chen, J.;

Churas, C.; Wilson, N.; Kratz, A.; Pillich, R. T.; Patel, D. N.; Park, J.; Kuenzi, B.; Yu, M. K.; Licon, K.; Pratt, D.; Kreisberg, J. F.; Kim, M.; Swaney, D. L.; Nan, X.; Fraley, S. I.; Gutkind, J. S.; Krogan, N. J.; Ideker, T. Interpretation of Cancer Mutations Using a Multiscale Map of Protein Systems. *Science* 2021, *374* (6563), eabf3067.

(20) Frampton, G. M.; Fichtenholtz, A.; Otto, G. A.; Wang, K.; Downing, S. R.; He, J.; Schnall-Levin, M.; White, J.; Sanford, E. M.; An, P.; Sun, J.; Juhn, F.; Brennan, K.; Iwanik, K.; Maillet, A.; Buell, J.; White, E.; Zhao, M.; Balasubramanian, S.; Terzic, S.; Richards, T.; Banning, V.; Garcia, L.; Mahoney, K.; Zwirko, Z.; Donahue, A.; Beltran, H.; Mosquera, J. M.; Rubin, M. A.; Dogan, S.; Hedvat, C. V.; Berger, M. F.; Pusztai, L.; Lechner, M.; Boshoff, C.; Jarosz, M.; Vietz, C.; Parker, A.; Miller, V. A.; Ross, J. S.; Curran, J.; Cronin, M. T.; Stephens, P. J.; Lipson, D.; Yelensky, R. Development and Validation of a Clinical Cancer Genomic Profiling Test Based on Massively Parallel DNA Sequencing. *Nat. Biotechnol.* 2013, *31* (11), 1023–1031.

(21) Beaubier, N.; Tell, R.; Lau, D.; Parsons, J. R.; Bush, S.; Perera, J.; Sorrells, S.; Baker, T.; Chang, A.; Michuda, J.; Iguartua, C.; MacNeil, S.; Shah, K.; Ellis, P.; Yeatts, K.; Mahon, B.; Taxter, T.; Bontrager, M.; Khan, A.; Huether, R.; Lefkofsky, E.; White, K. P. Clinical Validation of the Tempus XT Next-Generation Targeted Oncology Sequencing Assay. *Oncotarget* 2019, *10* (24), 2384–2396.

(22) Smyth, L. M.; Zhou, Q.; Nguyen, B.; Yu, C.; Lepisto, E. M.; Arnedos, M.; Hasset, M. J.; Lenoue-Newton, M. L.; Blauvelt, N.; Dogan, S.; Micheel, C. M.; Wathoo, C.; Horlings, H.; Hudecek, J.; Gross, B. E.; Kundra, R.; Sweeney, S. M.; Gao, J.; Schultz, N.; Zarski, A.; Gardos, S. M.; Lee, J.; Sheffler-Collins, S.; Park, B. H.; Sawyers, C. L.; André, F.; Levy, M.; Meric-Bernstam, F.; Bedard, P. L.; Iasonos, A.; Schrag, D.; Hyman, D. M.; AACR Project GENIE Consortium. Characteristics and Outcome of AKT1 E17K-Mutant Breast Cancer Defined through AACR Project GENIE, a Clinicogenomic Registry. *Cancer Discov.* 2020, *10* (4), 526–535.

(23) Barretina, J.; Caponigro, G.; Stransky, N.; Venkatesan, K.; Margolin, A. A.; Kim, S.; Wilson, C. J.; Lehár, J.; Kryukov, G. V.; Sonkin, D.; Reddy, A.; Liu, M.; Murray, L.; Berger, M. F.; Monahan, J. E.; Morais, P.; Meltzer, J.; Korejwa, A.; Jané-Valbuena, J.; Mapa, F. A.; Thibault, J.; Bric-Furlong, E.; Raman, P.; Shipway, A.; Engels, I. H.; Cheng, J.; Yu, G. K.; Yu, J.; Aspesi, P., Jr; de Silva, M.; Jagtap, K.; Jones, M. D.; Wang, L.; Hatton, C.; Palescandolo, E.; Gupta, S.; Mahan, S.; Sougnez, C.; Onofrio, R. C.; Liefeld, T.; MacConaill, L.; Winckler, W.; Reich, M.; Li, N.; Mesirov, J. P.; Gabriel, S. B.; Getz, G.; Ardlie, K.; Chan, V.; Myer, V. E.; Weber, B. L.; Porter, J.; Warmuth, M.; Finan, P.; Harris, J. L.; Meyerson, M.; Golub, T. R.; Morrissey, M. P.; Sellers, W. R.; Schlegel, R.; Garraway, L. A. The Cancer Cell Line Encyclopedia Enables Predictive Modelling of Anticancer Drug Sensitivity. *Nature* 2012, *483* (7391), 603–607.

(24) Seashore-Ludlow, B.; Rees, M. G.; Cheah, J. H.; Cokol, M.; Price, E. V.; Coletti, M. E.; Jones, V.; Bodycombe, N. E.; Soule, C. K.; Gould, J.; Alexander, B.; Li, A.; Montgomery, P.; Wawer, M. J.; Kuru, N.; Kotz, J. D.; Hon, C. S.-Y.; Munoz, B.; Liefeld, T.; Dančík, V.; Bittker, J. A.; Palmer, M.; Bradner, J. E.; Shamji, A. F.; Clemons, P. A.; Schreiber, S. L. Harnessing Connectivity in a Large-Scale Small-Molecule Sensitivity Dataset. *Cancer Discov.* 2015, *5* (11), 1210–1223.

(25) Basu, A.; Bodycombe, N. E.; Cheah, J. H.; Price, E. V.; Liu, K.; Schaefer, G. I.; Ebright, R. Y.; Stewart, M. L.; Ito, D.; Wang, S.; Bracha, A. L.; Liefeld, T.; Wawer, M.; Gilbert, J. C.;

Wilson, A. J.; Stransky, N.; Kryukov, G. V.; Dancik, V.; Barretina, J.; Garraway, L. A.; Hon, C. S.-Y.; Munoz, B.; Bittker, J. A.; Stockwell, B. R.; Khabele, D.; Stern, A. M.; Clemons, P. A.; Shamji, A. F.; Schreiber, S. L. An Interactive Resource to Identify Cancer Genetic and Lineage Dependencies Targeted by Small Molecules. *Cell* 2013, *154* (5), 1151–1161.

(26) Garnett, M. J.; Edelman, E. J.; Heidorn, S. J.; Greenman, C. D.; Dastur, A.; Lau, K. W.; Greninger, P.; Thompson, I. R.; Luo, X.; Soares, J.; Liu, Q.; Iorio, F.; Surdez, D.; Chen, L.; Milano, R. J.; Bignell, G. R.; Tam, A. T.; Davies, H.; Stevenson, J. A.; Barthorpe, S.; Lutz, S. R.; Kogera, F.; Lawrence, K.; McLaren-Douglas, A.; Mitropoulos, X.; Mironenko, T.; Thi, H.; Richardson, L.; Zhou, W.; Jewitt, F.; Zhang, T.; O'Brien, P.; Boisvert, J. L.; Price, S.; Hur, W.; Yang, W.; Deng, X.; Butler, A.; Choi, H. G.; Chang, J. W.; Baselga, J.; Stamenkovic, I.; Engelman, J. A.; Sharma, S. V.; Delattre, O.; Saez-Rodriguez, J.; Gray, N. S.; Settleman, J.; Futreal, P. A.; Haber, D. A.; Stratton, M. R.; Ramaswamy, S.; McDermott, U.; Benes, C. H. Systematic Identification of Genomic Markers of Drug Sensitivity in Cancer Cells. *Nature* 2012, *483* (7391), 570–575.

(27) Iorio, F.; Knijnenburg, T. A.; Vis, D. J.; Bignell, G. R.; Menden, M. P.; Schubert, M.; Aben, N.; Gonçalves, E.; Barthorpe, S.; Lightfoot, H.; Cokelaer, T.; Greninger, P.; van Dyk, E.; Chang, H.; de Silva, H.; Heyn, H.; Deng, X.; Egan, R. K.; Liu, Q.; Mironenko, T.; Mitropoulos, X.; Richardson, L.; Wang, J.; Zhang, T.; Moran, S.; Sayols, S.; Soleimani, M.; Tamborero, D.; Lopez-Bigas, N.; Ross-Macdonald, P.; Esteller, M.; Gray, N. S.; Haber, D. A.; Stratton, M. R.; Benes, C. H.; Wessels, L. F. A.; Saez-Rodriguez, J.; McDermott, U.; Garnett, M. J. A Landscape of Pharmacogenomic Interactions in Cancer. *Cell* 2016, *166* (3), 740–754.

(28) Gao, H.; Korn, J. M.; Ferretti, S.; Monahan, J. E.; Wang, Y.; Singh, M.; Zhang, C.; Schnell, C.; Yang, G.; Zhang, Y.; Balbin, O. A.; Barbe, S.; Cai, H.; Casey, F.; Chatterjee, S.; Chiang, D. Y.; Chuai, S.; Cogan, S. M.; Collins, S. D.; Dammassa, E.; Ebel, N.; Embry, M.; Green, J.; Kauffmann, A.; Kowal, C.; Leary, R. J.; Lehar, J.; Liang, Y.; Loo, A.; Lorenzana, E.; Robert McDonald, E., 3rd; McLaughlin, M. E.; Merkin, J.; Meyer, R.; Naylor, T. L.; Patawaran, M.; Reddy, A.; Röelli, C.; Ruddy, D. A.; Salangsang, F.; Santacroce, F.; Singh, A. P.; Tang, Y.; Tinetto, W.; Tobler, S.; Velazquez, R.; Venkatesan, K.; Von Arx, F.; Wang, H. Q.; Wang, Z.; Wiesmann, M.; Wyss, D.; Xu, F.; Bitter, H.; Atadja, P.; Lees, E.; Hofmann, F.; Li, E.; Keen, N.; Cozens, R.; Jensen, M. R.; Pryer, N. K.; Williams, J. A.; Sellers, W. R. High-Throughput Screening Using Patient-Derived Tumor Xenografts to Predict Clinical Trial Drug Response. *Nat. Med.* 2015, *21* (11), 1318–1325.

(29) Li, Z.; Razavi, P.; Li, Q.; Toy, W.; Liu, B.; Ping, C.; Hsieh, W.; Sanchez-Vega, F.; Brown, D. N.; Da Cruz Paula, A. F.; Morris, L.; Selenica, P.; Eichenberger, E.; Shen, R.; Schultz, N.; Rosen, N.; Scaltriti, M.; Brogi, E.; Baselga, J.; Reis-Filho, J. S.; Chandarlapaty, S. Loss of the FAT1 Tumor Suppressor Promotes Resistance to CDK4/6 Inhibitors via the Hippo Pathway. *Cancer Cell* 2018, *34* (6), 893-905.e8.

(30) Finn, R. S.; Crown, J. P.; Lang, I.; Boer, K.; Bondarenko, I. M.; Kulyk, S. O.; Ettl, J.; Patel, R.; Pinter, T.; Schmidt, M.; Shparyk, Y.; Thummala, A. R.; Voytko, N. L.; Fowst, C.; Huang, X.; Kim, S. T.; Randolph, S.; Slamon, D. J. The Cyclin-Dependent Kinase 4/6 Inhibitor Palbociclib in Combination with Letrozole versus Letrozole Alone as First-Line Treatment of Oestrogen Receptor-Positive, HER2-Negative, Advanced Breast Cancer (PALOMA-1/TRIO-18): A Randomised Phase 2 Study. *Lancet Oncol.* 2015, *16* (1), 25–35.

(31) DeMichele, A.; Clark, A. S.; Tan, K. S.; Heitjan, D. F.; Gramlich, K.; Gallagher, M.; Lal, P.;

Feldman, M.; Zhang, P.; Colameco, C.; Lewis, D.; Langer, M.; Goodman, N.; Domchek, S.; Gogineni, K.; Rosen, M.; Fox, K.; O'Dwyer, P. CDK 4/6 Inhibitor Palbociclib (PD0332991) in Rb+ Advanced Breast Cancer: Phase II Activity, Safety, and Predictive Biomarker Assessment. *Clin. Cancer Res.* 2015, *21* (5), 995–1001.

(32) Garraway, L. A.; Lander, E. S. Lessons from the Cancer Genome. *Cell* 2013, *153* (1), 17–37.

(33) Carpintero-Fernández, P.; Borghesan, M.; Eleftheriadou, O.; Pan-Castillo, B.; Fafián-Labora, J. A.; Mitchell, T. P.; Yuste, A.; Ogrunc, M.; Nightingale, T. D.; Mayan, M.; O'Loghlen, A. Genome Wide CRISPR/Cas9 Screen Identifies the Coagulation Factor IX (F9) as a Regulator of Senescence. *Cell Death Dis.* 2022, *13* (2), 163.

(34) Tsherniak A, Vazquez F, Montgomery PG, et al. Defining a Cancer Dependency Map. *Cell* 2017, *170* (3), 564-576.e16.

(35) Fukazawa, T.; Maeda, Y.; Matsuoka, J.; Yamatsuji, T.; Shigemitsu, K.; Morita, I.; Faiola, F.; Durbin, M. L.; Soucek, L.; Naomoto, Y. Inhibition of Myc Effectively Targets KRAS Mutation-Positive Lung Cancer Expressing High Levels of Myc. *Anticancer Res.* 2010, *30* (10), 4193–4200.

(36) Adam, G.; Rampášek, L.; Safikhani, Z.; Smirnov, P.; Haibe-Kains, B.; Goldenberg, A. Machine Learning Approaches to Drug Response Prediction: Challenges and Recent Progress. *NPJ Precis Oncol* 2020, *4*, 19.

(37) Richards, A. L.; Eckhardt, M.; Krogan, N. J. Mass Spectrometry-Based Protein–Protein Interaction Networks for the Study of Human Diseases. *Mol. Syst. Biol.* 2021, *17* (1), e8792.

(38) Go, C. D.; Knight, J. D. R.; Rajasekharan, A.; Rathod, B.; Hesketh, G. G.; Abe, K. T.; Youn, J.-Y.; Samavarchi-Tehrani, P.; Zhang, H.; Zhu, L. Y.; Popiel, E.; Lambert, J.-P.; Coyaud, É.; Cheung, S. W. T.; Rajendran, D.; Wong, C. J.; Antonicka, H.; Pelletier, L.; Palazzo, A. F.; Shoubridge, E. A.; Raught, B.; Gingras, A.-C. A Proximity-Dependent Biotinylation Map of a Human Cell. *Nature* 2021, *595* (7865), 120–124.

(39) Salas, D.; Stacey, R. G.; Akinlaja, M.; Foster, L. J. Next-Generation Interactomics: Considerations for the Use of Co-Elution to Measure Protein Interaction Networks. *Mol. Cell. Proteomics* 2020, *19* (1), 1–10.

(40) Heusel, M.; Bludau, I.; Rosenberger, G.; Hafen, R.; Frank, M.; Banaei-Esfahani, A.; van Drogen, A.; Collins, B. C.; Gstaiger, M.; Aebersold, R. Complex-Centric Proteome Profiling by SEC-SWATH-MS. *Mol. Syst. Biol.* 2019, *15* (1), e8438.

(41) Qin, Y.; Huttlin, E. L.; Winsnes, C. F.; Gosztyla, M. L.; Wacheul, L.; Kelly, M. R.; Blue, S. M.; Zheng, F.; Chen, M.; Schaffer, L. V.; Licon, K.; Bäckström, A.; Vaites, L. P.; Lee, J. J.; Ouyang, W.; Liu, S. N.; Zhang, T.; Silva, E.; Park, J.; Pitea, A.; Kreisberg, J. F.; Gygi, S. P.; Ma, J.; Harper, J. W.; Yeo, G. W.; Lafontaine, D. L. J.; Lundberg, E.; Ideker, T. A Multi-Scale Map of Cell Structure Fusing Protein Images and Interactions. *Nature* 2021, *600* (7889), 536–542.

(42) Ji, W.; Shi, Y.; Wang, X.; He, W.; Tang, L.; Tian, S.; Jiang, H.; Shu, Y.; Guan, X. Combined Androgen Receptor Blockade Overcomes the Resistance of Breast Cancer Cells to

Palbociclib. *Int. J. Biol. Sci.* 2019, *15* (3), 522–532.

(43) Mao, P.; Cohen, O.; Kowalski, K. J.; Kusiel, J. G.; Buendia-Buendia, J. E.; Cuoco, M. S.; Exman, P.; Wander, S. A.; Waks, A. G.; Nayar, U.; Chung, J.; Freeman, S.; Rozenblatt-Rosen, O.; Miller, V. A.; Piccioni, F.; Root, D. E.; Regev, A.; Winer, E. P.; Lin, N. U.; Wagle, N. Acquired FGFR and FGF Alterations Confer Resistance to Estrogen Receptor (ER) Targeted Therapy in ER+ Metastatic Breast Cancer. *Clin. Cancer Res.* 2020, *26* (22), 5974–5989.

(44) Wang, T.-H.; Chen, C.-C.; Leu, Y.-L.; Lee, Y.-S.; Lian, J.-H.; Hsieh, H.-L.; Chen, C.-Y. Palbociclib Induces DNA Damage and Inhibits DNA Repair to Induce Cellular Senescence and Apoptosis in Oral Squamous Cell Carcinoma. *J. Formos. Med. Assoc.* 2021, *120* (9), 1695–1705.

(45) Fernández-Aroca, D. M.; Roche, O.; Sabater, S.; Pascual-Serra, R.; Ortega-Muelas, M.; Sánchez Pérez, I.; Belandia, B.; Ruiz-Hidalgo, M. J.; Sánchez-Prieto, R. P53 Pathway Is a Major Determinant in the Radiosensitizing Effect of Palbociclib: Implication in Cancer Therapy. *Cancer Lett.* 2019, *451*, 23–33.

(46) Pancholi, S.; Ribas, R.; Simigdala, N.; Schuster, E.; Nikitorowicz-Buniak, J.; Ressa, A.; Gao, Q.; Leal, M. F.; Bhamra, A.; Thornhill, A.; Morisset, L.; Montaudon, E.; Sourd, L.; Fitzpatrick, M.; Altelaar, M.; Johnston, S. R.; Marangoni, E.; Dowsett, M.; Martin, L.-A. Tumour Kinome Re-Wiring Governs Resistance to Palbociclib in Oestrogen Receptor Positive Breast Cancers, Highlighting New Therapeutic Modalities. *Oncogene* 2020, *39* (25), 4781–4797.

(47) Shu, S.; Wu, H.-J.; Ge, J. Y.; Zeid, R.; Harris, I. S.; Jovanović, B.; Murphy, K.; Wang, B.; Qiu, X.; Endress, J. E.; Reyes, J.; Lim, K.; Font-Tello, A.; Syamala, S.; Xiao, T.; Reddy Chilamakuri, C. S.; Papachristou, E. K.; D'Santos, C.; Anand, J.; Hinohara, K.; Li, W.; McDonald, T. O.; Luoma, A.; Modiste, R. J.; Nguyen, Q.-D.; Michel, B.; Cejas, P.; Kadoch, C.; Jaffe, J. D.; Wucherpfennig, K. W.; Qi, J.; Liu, X. S.; Long, H.; Brown, M.; Carroll, J. S.; Brugge, J. S.; Bradner, J.; Michor, F.; Polyak, K. Synthetic Lethal and Resistance Interactions with BET Bromodomain Inhibitors in Triple-Negative Breast Cancer. *Mol. Cell* 2020, *78* (6), 1096-1113.e8.

(48) Zhou, M.; Yuan, M.; Zhang, M.; Lei, C.; Aras, O.; Zhang, X.; An, F. Combining Histone Deacetylase Inhibitors (HDACis) with Other Therapies for Cancer Therapy. *Eur. J. Med. Chem.* 2021, *226*, 113825.

(49) Wang, B.; Varela-Eirin, M.; Brandenburg, S. M.; Hernandez-Segura, A.; van Vliet, T.; Jongbloed, E. M.; Wilting, S. M.; Ohtani, N.; Jager, A.; Demaria, M. Pharmacological CDK4/6 Inhibition Reveals a P53-Dependent Senescent State with Restricted Toxicity. *EMBO J.* 2022, *41* (6), e108946.

(50) Ji, W.; Zhang, W.; Wang, X.; Shi, Y.; Yang, F.; Xie, H.; Zhou, W.; Wang, S.; Guan, X. C-Myc Regulates the Sensitivity of Breast Cancer Cells to Palbociclib via c-Myc/MiR-29b-3p/CDK6 Axis. *Cell Death Dis.* 2020, *11* (9), 760.

(51) Wiesel-Motiuk, N.; Assaraf, Y. G. The Key Roles of the Lysine Acetyltransferases KAT6A and KAT6B in Physiology and Pathology. *Drug Resist. Updat.* 2020, *53*, 100729.

(52) Rokudai, S.; Laptenko, O.; Arnal, S. M.; Taya, Y.; Kitabayashi, I.; Prives, C. MOZ Increases P53 Acetylation and Premature Senescence through Its Complex Formation with PML. *Proc. Natl. Acad. Sci. U. S. A.* 2013, *110* (10), 3895–3900.

(53) Kitabayashi, I.; Aikawa, Y.; Nguyen, L. A.; Yokoyama, A.; Ohki, M. Activation of AML1-Mediated Transcription by MOZ and Inhibition by the MOZ-CBP Fusion Protein. *EMBO J.* 2001, *20* (24), 7184–7196.

(54) Borrow, J.; Stanton, V. P., Jr; Andresen, J. M.; Becher, R.; Behm, F. G.; Chaganti, R. S.; Civin, C. I.; Disteche, C.; Dubé, I.; Frischauf, A. M.; Horsman, D.; Mitelman, F.; Volinia, S.; Watmore, A. E.; Housman, D. E. The Translocation t(8;16)(P11;P13) of Acute Myeloid Leukaemia Fuses a Putative Acetyltransferase to the CREB-Binding Protein. *Nat. Genet.* 1996, *14* (1), 33–41.

(55) Li, J. Y.; Daniels, G.; Wang, J.; Zhang, X. TBL1XR1 in Physiological and Pathological States. *Am J Clin Exp Urol* 2015, *3* (1), 13–23.

(56) Tomita, A.; Buchholz, D. R.; Shi, Y.-B. Recruitment of N-CoR/SMRT-TBLR1 Corepressor Complex by Unliganded Thyroid Hormone Receptor for Gene Repression during Frog Development. *Mol. Cell. Biol.* 2004, *24* (8), 3337–3346.

(57) Perissi, V.; Scafoglio, C.; Zhang, J.; Ohgi, K. A.; Rose, D. W.; Glass, C. K.; Rosenfeld, M. G. TBL1 and TBLR1 Phosphorylation on Regulated Gene Promoters Overcomes Dual CtBP and NCoR/SMRT Transcriptional Repression Checkpoints. *Mol. Cell* 2008, *29* (6), 755–766.

(58) Priebbenow, D. L.; Leaver, D. J.; Nguyen, N.; Cleary, B.; Lagiakos, H. R.; Sanchez, J.; Xue, L.; Huang, F.; Sun, Y.; Mujumdar, P.; Mudududdla, R.; Varghese, S.; Teguh, S.; Charman, S. A.; White, K. L.; Shackleford, D. M.; Katneni, K.; Cuellar, M.; Strasser, J. M.; Dahlin, J. L.; Walters, M. A.; Street, I. P.; Monahan, B. J.; Jarman, K. E.; Jousset Sabroux, H.; Falk, H.; Chung, M. C.; Hermans, S. J.; Downer, N. L.; Parker, M. W.; Voss, A. K.; Thomas, T.; Baell, J. B. Discovery of Acylsulfonohydrazide-Derived Inhibitors of the Lysine Acetyltransferase, KAT6A, as Potent Senescence-Inducing Anti-Cancer Agents. *J. Med. Chem.* 2020, *63* (9), 4655–4684.

(59) Baell, J. B.; Leaver, D. J.; Hermans, S. J.; Kelly, G. L.; Brennan, M. S.; Downer, N. L.; Nguyen, N.; Wichmann, J.; McRae, H. M.; Yang, Y.; Cleary, B.; Lagiakos, H. R.; Mieruszynski, S.; Pacini, G.; Vanyai, H. K.; Bergamasco, M. I.; May, R. E.; Davey, B. K.; Morgan, K. J.; Sealey, A. J.; Wang, B.; Zamudio, N.; Wilcox, S.; Garnham, A. L.; Sheikh, B. N.; Aubrey, B. J.; Doggett, K.; Chung, M. C.; de Silva, M.; Bentley, J.; Pilling, P.; Hattarki, M.; Dolezal, O.; Dennis, M. L.; Falk, H.; Ren, B.; Charman, S. A.; White, K. L.; Rautela, J.; Newbold, A.; Hawkins, E. D.; Johnstone, R. W.; Huntington, N. D.; Peat, T. S.; Heath, J. K.; Strasser, A.; Parker, M. W.; Smyth, G. K.; Street, I. P.; Monahan, B. J.; Voss, A. K.; Thomas, T. Inhibitors of Histone Acetyltransferases KAT6A/B Induce Senescence and Arrest Tumour Growth. *Nature* 2018, *560* (7717), 253–257.

(60) Su, J.; Wang, X.; Bai, Y.; Sun, M.; Yao, Y.; Duan, Y. The Role of MOZ/KAT6A in Hematological Malignancies and Advances in MOZ/KAT6A Inhibitors. *Pharmacol. Res.* 2021, *174*, 105930.

(61) Lira, M. E.; Xie, T.; Deng, S.; Kinong, J.; Gao, J.; Zhu, Z.; Lee, N.; Rejto, P.; Bienkowska,

J.; Hardwick, J.; Wang, K.; Huang, S. Abstract 2749: Liquid Biopsy Testing Allows Highly-Sensitive Detection of Plasma CfDNA Mutations in 87 Breast Cancer-Related Genes. *Cancer Res.* 2017, *77* (13 Supplement), 2749–2749.

(62) Bailey, M. H.; Tokheim, C.; Porta-Pardo, E.; Sengupta, S.; Bertrand, D.; Weerasinghe, A.; Colaprico, A.; Wendl, M. C.; Kim, J.; Reardon, B.; Kwok-Shing Ng, P.; Jeong, K. J.; Cao, S.; Wang, Z.; Gao, J.; Gao, Q.; Wang, F.; Liu, E. M.; Mularoni, L.; Rubio-Perez, C.; Nagarajan, N.; Cortés-Ciriano, I.; Zhou, D. C.; Liang, W.-W.; Hess, J. M.; Yellapantula, V. D.; Tamborero, D.; Gonzalez-Perez, A.; Suphavilai, C.; Ko, J. Y.; Khurana, E.; Park, P. J.; Van Allen, E. M.; Liang, H.; MC3 Working Group; Cancer Genome Atlas Research Network; Lawrence, M. S.; Godzik, A.; Lopez-Bigas, N.; Stuart, J.; Wheeler, D.; Getz, G.; Chen, K.; Lazar, A. J.; Mills, G. B.; Karchin, R.; Ding, L. Comprehensive Characterization of Cancer Driver Genes and Mutations. *Cell* 2018, *174* (4), 1034–1035.

(63) Ioffe, S.; Szegedy, C. Batch Normalization: Accelerating Deep Network Training by Reducing Internal Covariate Shift. In *Proceedings of the 32nd International Conference on Machine Learning*; Bach, F., Blei, D., Eds.; Proceedings of Machine Learning Research; PMLR: Lille, France, 07--09 Jul 2015; Vol. 37, pp 448–456.

(64) Srivastava, N.; Hinton, G.; Krizhevsky, A.; Sutskever, I.; Salakhutdinov, R. Dropout: A Simple Way to Prevent Neural Networks from Overfitting. *J. Mach. Learn. Res.* 2014, *15* (1), 1929–1958.

(65) Jolliffe, I. Principal Component Analysis. In *Wiley StatsRef: Statistics Reference Online*; John Wiley & Sons, Ltd, 2014.

(66) Loshchilov, I.; Hutter, F. Decoupled Weight Decay Regularization. *arXiv [cs.LG]*, 2017.

(67) Breiman, L. Random Forests. *Machine Learning* 2001, *45* (1), 5–32.

(68) Friedman, J.; Hastie, T.; Tibshirani, R. Regularization Paths for Generalized Linear Models via Coordinate Descent. *J. Stat. Softw.* 2010, *33* (1), 1–22.

(69) Hinton, G. E. Connectionist Learning Procedures. *Artif. Intell.* 1989, *40*, 185–234.

(70) Pedregosa, F.; Varoquaux, G.; Gramfort, A.; Michel, V.; Thirion, B.; Grisel, O.; Blondel, M.; Prettenhofer, P.; Weiss, R.; Dubourg, V.; Others. Scikit-Learn: Machine Learning in Python. *Journal of Machine Learning Research* 2011, *12*, 2825–2830.

(71) Stone, M. Cross-Validatory Choice and Assessment of Statistical Predictions. *Journal of the Royal Statistical Society: Series B (Methodological)*. 1974, pp 111–133.

(72) Akiba, T.; Sano, S.; Yanase, T.; Ohta, T.; Koyama, M. Optuna: A Next-Generation Hyperparameter Optimization Framework. In *Proceedings of the 25th ACM SIGKDD International Conference on Knowledge Discovery & Data Mining*; KDD '19; Association for Computing Machinery: New York, NY, USA, 2019; pp 2623–2631.

(73) Hoerl, A. E.; Kennard, R. W. Ridge Regression: Biased Estimation for Nonorthogonal Problems. *Technometrics*. 2000, pp 80–86.

(74) McCullagh, P.; Nelder, J. A. *Generalized Linear Models, Second Edition*; CRC Press, 1989.

(75) Stanford University. Department of Statistics; Tibshirani, R. *Regression Shrinkage and Selection Via the Lasso*; 1994.

(76) Subramanian, A.; Tamayo, P.; Mootha, V. K.; Mukherjee, S.; Ebert, B. L.; Gillette, M. A.; Paulovich, A.; Pomeroy, S. L.; Golub, T. R.; Lander, E. S.; Mesirov, J. P. Gene Set Enrichment Analysis: A Knowledge-Based Approach for Interpreting Genome-Wide Expression Profiles. *Proc. Natl. Acad. Sci. U. S. A.* 2005, *102* (43), 15545–15550.

(77) Akalin, A. *Computational Genomics with R*; CRC Press, 2020.

(78) Dempster, J. M.; Boyle, I.; Vazquez, F.; Root, D. E.; Boehm, J. S.; Hahn, W. C.; Tsherniak, A.; McFarland, J. M. Chronos: A Cell Population Dynamics Model of CRISPR Experiments That Improves Inference of Gene Fitness Effects. *Genome Biol.* 2021, *22* (1), 1–23.

(79) Sanjana, N. E.; Shalem, O.; Zhang, F. Improved Vectors and Genome-Wide Libraries for CRISPR Screening. *Nat. Methods* 2014, *11* (8), 783–784.

(80) van der Walt, S.; Schönberger, J. L.; Nunez-Iglesias, J.; Boulogne, F.; Warner, J. D.; Yager, N.; Gouillart, E.; Yu, T.; scikit-image contributors. Scikit-Image: Image Processing in Python. *PeerJ* 2014, *2*, e453.

Chapter 4 Cancer mutations converge on a collection of protein assemblies to predict resistance to replication stress.

4.1 Abstract

Rapid proliferation is a hallmark of tumor cells, associated with sensitivity to therapeutics that cause DNA replication stress (RS). Many tumors exhibit drug resistance, however, via molecular pathways that are incompletely understood. Here, we develop an ensemble of predictive models that elucidate how cancer mutations impact the response to common RS-inducing (RSi) agents. The models implement recent advances in deep learning to facilitate multi-drug prediction and mechanistic interpretation. Initial studies in tumor cells identify 41 molecular assemblies that integrate alterations in hundreds of genes for accurate drug response prediction. These cover roles in transcription, repair, cell-cycle checkpoints, and growth signaling, of which 30 are shown by loss-of-function genetic screens to regulate drug sensitivity or replication restart. The model translates to cisplatin-treated cervical cancer patients, highlighting an RTK-JAK-STAT assembly governing resistance. This study defines a compendium of mechanisms by which mutations affect therapeutic responses, with implications for drug selection and combination.

4.2 Introduction

DNA replication is central to cell division and proliferation, involving closely orchestrated functions among hundreds of proteins[1,2]. Although the replication machinery is highly accurate, it faces challenges from both extrinsic and intrinsic factors[3]. These challenges can result in stalled replication forks, occurrence of DNA breaks, reduced replication precision, and other factors collectively known as RS[4]. Accordingly, cells have evolved a robust RS response which activates DNA damage repair signaling, or alternatively induces cell death, to maintain genome integrity within the cell population[5–9]. Due to sustained proliferative signaling and/or defective DNA repair, cancer cells undergo persistent replication stress[10,11] making them strongly RS response

dependent. A consequence of this dependency is that replication stress becomes an exploitable therapeutic vulnerability in cancer treatment[12,13].

A multitude of cancer therapeutics leverage replication stress to eliminate cancer cells, employing a diversity of RSi mechanisms (Supplementary Figure 4.1). Classical chemotherapeutic agents induce RS by directly affecting DNA integrity. Examples include DNA crosslinkers and alkylating agents (e.g., cisplatin, methotrexate), topoisomerase I and II inhibitors (e.g., camptothecin, etoposide, doxorubicin), ribonucleotide reductase inhibitors (gemcitabine, hydroxyurea), and nucleotide analogues (5-fluorouracil)[12,14,15]. Other agents elevate RS by targeting DNA polymerases or DNA damage response proteins. Some of these have progressed to advanced stages of preclinical and clinical development, including inhibitors of the DNA polymerase (e.g., CD437), the base-excision repair factors PARP1 and PARP2 (e.g, olaparib), ATR-CHK1 signaling (e.g, ceralasertib), or the WEE1 checkpoint kinase (e.g, MK-1775)[13,16]. Treatment outcomes vary widely due to significant differences in drug sensitivity and resistance across tumors, motivating efforts to better understand response mechanisms. These efforts have led to an expanding catalog of genetic alterations associated with sensitivity or resistance to RSi drugs, including mutations in *BRCA1*, *BRCA2*, *ATM*, or *ATR* (Figure 4.1A)[17–26]. This list is almost certainly not exhaustive, since the vast majority of genetic alterations identified are rare rather than common in tumors. Moreover, it is unclear how these multiple single-gene effects integrate to constitute an overall drug response.

Currently, two machine learning (ML) methodologies are emerging as particularly useful in understanding the effects of genetic alterations in precision medicine applications. The first methodology, known as “interpretable” ML, includes a wide array of approaches that attempt to gain insight into the mechanisms or rationale underlying a model’s predictions (arXiv 1206.4656)[27]. In this regard, we and others have developed a series of “visible” neural network (VNN) models which guide the internal architecture of the model using knowledge maps of biological components and functions[28–34]. In contrast to conventional “black box’’ neural

networks[35], a prime advantage of VNNs is that they not only learn to predict biomedical outcomes from sparse genetic feature sets but their predictions can be mapped to internal state changes in molecular mechanisms and pathways, allowing for model interpretation. To initiate a proteomics-driven resource of molecular mechanisms in cancer, we recently used affinity purification mass spectrometry to delineate the physical interactions of a broad set of cancer proteins. We integrated these interactions with other 'omics datasets to create a large cancer protein-protein association network, which was iteratively clustered to generate a map of frequently altered protein assemblies (NeST, Nested Systems in Tumors, Supplementary Figure 4.2)[36]. This map exhibits hierarchical structure, whereby individual cancer proteins converge to form protein complexes and larger assemblies which, in turn, incorporate into broad processes and organelles (Figure 4.1A and Supplementary Figure 4.2B). The second ML methodology is multi-task learning, whereby several learning tasks are solved at the same time while exploiting commonalities and differences across these tasks[37]. Multi-task learning has been previously used to boost the efficacy of drug response and mechanism of action prediction[38,39] (bioRxiv 2020.11.17.385757), although it has not yet been combined with knowledge bases of cancer pathways like NeST or (to our knowledge) applied to understand the response to RSi drugs.

Motivated by these challenges and advancements, here we describe and evaluate interpretable deep learning models of RSi drug response (Figure 4.1B). Starting from the genetic alterations detected in a tumor sample, the models predict the sensitivity or resistance to specific RSi drugs. The architecture of these models is based on knowledge of cancer protein complexes in NeST, meaning their predictions can be interpreted mechanistically, and both single-drug and multi-task (multi-drug) models are evaluated. These models identify a constellation of protein assemblies that integrate genetic alterations to predict drug sensitivity or resistance, which we show can be validated by multiple types of genome-wide functional assays and by their utility in predicting responses to previously unseen RSi agents as well as in chemotherapy-treated patients (Figure 4.1B).

4.3 Results

4.3.1 A cancer-oriented interpretable neural network

To model responses to RSi drugs, we focused on the set of 718 genes assessed by current clinical cancer gene panels, including one or more of FoundationOne CDx[40], Tempus xT[41], and Project GENIE[42]. The genomic alteration status of these genes in a tumor sample, including the presence/absence of mutation and copy number aberration (CNA), was used as input (Supplementary Figure 4.3A). Models were trained using drug response data for genomically-characterized tumor cell lines harmonized from the Cancer Therapeutics Response Portal (CTRP)[43,44] and the Genomics of Drug Sensitivity in Cancer (GDSC)[45,46] databases. These databases included the measured responses to many RSi drugs targeting DNA replication or DNA damage response. In another recent study, Olivieri and colleagues employed genome-wide CRISPR chemogenetic screens to investigate DNA damage response against genotoxic agents. Therefore, we initially focused on six RSi agents characterized by Olivieri (cisplatin, gemcitabine, camptothecin, etoposide, olaparib, CD437) (Figure 4.2A) which had also been examined in CTRP or GDSC[47].

Instead of associating genetic alterations with drug responses via classical “black-box” machine learning, we implemented visible neural network models (VNN) in which the layers of artificial neurons are designed to propagate the effects of individual gene mutations over the NeST map of cancer protein assemblies[36]. In constructing the VNN, each protein assembly encoded by genes on the clinical panel (131 assemblies, Table 4.1) was assigned a bank of artificial neurons to represent the *in silico* activity of that system (Supplementary Figure 4.3A; Methods). The use of multiple neurons allowed protein assemblies to be multifunctional, with the ability to adopt a range of values along several dimensions. For the neurons assigned to an assembly, weighted input connections were permitted from the neurons assigned to each of its subassemblies in the preceding layers of the NeST hierarchy. This design enabled genetic

information to flow from the input gene alterations to small protein complexes (e.g., “CDK holoenzyme complex”) then larger scale assemblies (e.g., “checkpoint-regulated DNA repair”), and finally to the root assembly, representing the whole cell (Supplementary Figure 4.3B). Connection weights were learned during training so that the integrated activity of the root neurons represented the predicted drug response of a tumor sample given its genetic alteration profile. In the multi-drug configuration, this architecture was extended so that the activity of the root was provided as input to an additional (final) neuronal processing layer that was optimized separately for each drug response (Supplementary Figure 4.3C; Methods).

4.3.2 Training and performance analysis of the models

We first trained single-drug VNN models for predicting the response to each of the six RSi agents (Figure 4.2A). Training was conducted by minimizing the mean squared error between the predicted and observed drug responses using standard back-propagation techniques (Methods). The accuracy of drug response prediction was assessed for each model using nested cross-validation, in which 64% of cell lines were randomly selected for model training, 16% for model validation and hyperparameter tuning, and 20% as held-out cell lines not yet seen during training or validation (this entire procedure was repeated over five folds, Methods). This assessment produced predictive odds ratios (OR) in the range of 2.2 to 3.2 across the six RSi-drug models (Figure 4.2B, orange points). These models generally demonstrated performance that was comparable to, or better than, matched black-box neural networks (Figure 4.2B, blue points; ORs of 1.8 to 3.3; $P = 0.04$). Their performance was significantly better than that of two general pan-drug models (DrugCell, DeepCDR) which had not been specifically developed for RSi drug prediction[30,48] (Figure 4.2B, cyan and purple points; with P-values of 2.5×10^{-8} and 1.2×10^{-10} respectively).

We also used multi-task learning to train a unified multi-drug VNN with six outputs, predicting the response to each of the six RSi drugs (Supplementary Figure 4.3C; Methods). This

unified model yielded ORs of 3.0 to 4.9 (Figure 4.2B, red points), significantly outperforming both the single-task models ($P = 4.3\times10^{-5}$) and the matched black-box models ($P = 2.1\times10^{-7}$). To further test the generality of this multi-drug model, we evaluated its accuracy in predicting cell-line responses to additional RSi agents not yet seen in this study (predictions based on the average of model outputs, Methods). The new agents included RS-inducing chemotherapies such as doxorubicin, 5-fluorouracil, methotrexate, and bleomycin-a2 as well as drugs targeting DNA damage response factors such as ceralasertib (ATR inhibitor) and MK-1775 (WEE1 inhibitor). The predictive ORs were significant for all new RSi drugs (mean OR 3.2, Figure 4.2C red points, Table 4.2), and they were significantly higher than ORs obtained when predicting responses to a broad panel of 33 agents not associated with replication stress (mean OR 1.8, $P = 3.1\times10^{-4}$; Figure 4.2C blue points). Furthermore, the performance of the multi-drug model decreased considerably when, during training, some of the RSi drug responses were substituted with unrelated drug responses (Supplementary Figure 4.4A). These results were consistent with the expectation that RSi drugs share common response pathways, a finding that was also reflected by varying degrees of similarity in their drug response profiles across tumor cell lines (Supplementary Figure 4.4B).

4.3.3 Molecular assemblies important for RSi drug response prediction

We next scored all protein assemblies to rank their importance in prediction of RSi drug responses (Table 4.3). For this purpose, we computed a system importance (SI) score, which measures the dependence of the drug response prediction on genetic alterations within an assembly, captured by changes in the in silico activity of that assembly's neurons (Methods). We created an importance profile for each RSi agent using the single-drug models, then mapped these to the NeST protein assembly hierarchy (Figure 4.3A); SI profiles were also computed for the multi-drug model, with qualitatively consistent results (Supplementary Figure 4.4C; Table 4.3).

Due to the progressive integration of genetic information, we noted that importance scores for all models tended to increase with assembly size and depth in the hierarchy. To thus highlight distinct protein assemblies important to RSi drugs, we focused our examination on small-to-medium scale assemblies (124 assemblies with fewer than 100 genes), identifying 41 that were high scoring in the single- or multi-drug RSi models (Figures 4.3A and 4.3B; Supplementary Figure 4.4C; Methods). These “RSi assemblies” recovered proteins associated with known drug indications or mechanisms of action, where applicable (camptothecin: TOP1; etoposide: TOP2A; olaparib: BRCA1, BRCA2, PARP1; the CD437 target POLA1 was absent from clinical gene panels). For example, in predicting etoposide response we identified “Checkpoint-regulated DNA repair” and “G1/S phase” assemblies, which contained the etoposide target, topoisomerase 2α (TOP2A) (Table 4.3). Turning from positive to negative controls, we found that the various RSi drug models yielded assembly importance scores that were distinct from those of non-RSi drugs but similar to one another (Figure 4.3C). Moreover, these RSi assemblies were specifically important for the prediction of the cellular response to RSi drugs, as opposed to non-RS drugs (Figure 4.3D).

4.3.4 Validation of specific protein assemblies using genome-wide functional assays

For the assemblies identified as important to the RSi drug models, we investigated whether engineered genetic perturbations impacting each of these assemblies were able to predictably affect the drug response. For this purpose, we turned to the recent work of Olivieri and colleagues[47], who had conducted genome-wide drug sensitivity screens in the presence of each of 27 genotoxic agents, including the 6 RSi drugs used to train the models in our study (Supplementary Figure 4.5A). For each drug, genes were scored by the degree to which loss-of-function by CRISPR/Cas9 modulates drug sensitivity in either direction (i.e. absolute z-score, capturing both increases and decreases in sensitivity). Using these scores, we found that 24 of the 41 RSi assemblies were significantly enriched for genes affecting sensitivity to one or more

RSi drugs, a rate higher than for non-RSi assemblies (59% versus 45%, $P < 0.001$; Supplementary Figure 4.5B). Such enrichment was particularly strong in the drug sensitivity screens for etoposide, camptothecin, and CD437 (Supplementary Figure 4.5C).

We then explored a second genome-wide loss-of-function screen, directly measuring immunofluorescent readouts of DNA damage and replication restart after an RS challenge[49]. This screen had measured the effect of siRNA gene knockdowns on phosphorylation of histone variant H2AX (γH2AX), a marker of stalled replication forks, and on incorporation of EdU in DNA, a marker of active genome replication (Figure 4.4A). The ratio of these two readouts, the "replication restart score" (RRS), was used to score all gene knockdowns for their importance in RS response. Genes that affected replication restart in either direction (absolute z-score) were enriched in 21 of the 41 RSi assemblies, a rate significantly higher than for non-RSi assemblies (51% versus 30%, $P < 0.001$; Figure 4.4B). In addition, we found that the converse enrichment relationship was also true, in that NeST assemblies enriched in genes affecting drug sensitivity or replication restart were significantly more important to RSi drug models than to non-RSi models (Figures 4.4C-4.4D; Supplementary Figures 4.5D–4.5J; with P-values of 1×10^{-9} and 3×10^{-6} respectively).

Summarizing the functional screening results, the 41 RSi assemblies included 30 with support from either the drug sensitivity or replication restart readouts (Figure 4.4E). Among these, 15 assemblies had support from both, including assemblies involved in mismatch and excision repair, homologous recombination, Fanconi anemia repair, checkpoint-regulated DNA repair, locomotion, ubiquitin/proteasomal assemblies, and the RTK-JAK-STAT pathway (Figure 4.4F; Table 4.4). The set of 30 assemblies and the subset of 15 assemblies were equally important for predicting RSi drug response, surpassing non-RSi drug response (Supplementary Figure 4.5K).

4.3.5 Prediction of clinical responses to cisplatin

Among adult solid tumors cataloged by The Cancer Genome Atlas (TCGA), five cancer subtypes commonly receive cisplatin therapy, with substantial numbers of associated samples

(>30 cisplatin-treated subjects per subtype, Figure 4.5A). Among these subtypes, we noted that patients with cervical and lung squamous carcinomas (CESC and LUSC) currently show cisplatin benefit, with long progression-free survival times (PFS, Figure 4.5B) that are significantly improved over patients not receiving cisplatin (Figures 4.5C and 4.5D; contrast to other types in Supplementary Figures 4.6A–4.6C). Despite this benefit, approximately 35% of cervical and lung tumors continue to progress after treatment (Figure 4.5B). Accordingly, we investigated whether these variable outcomes could be predicted by the cisplatin VNN (Figure 4.5E; Methods). Indeed, we found that cisplatin-treated patients with CESC or LUSC, who were predicted as sensitive to treatment, had significantly better progression-free survival outcomes than those who were predicted as resistant (CESC Hazard Ratio = 2.2 at $P = 0.02$, LUSC HR = 3.4 at $P = 0.03$; Figures 4.5F–4.5G). This performance was significantly better than baseline random forest or elastic net models (Figure 4.5H; with P-values of 9.1×10^{-5} and 1.0×10^{-2} for comparison with random forest and elastic net, respectively). Among the remaining cancer cohorts which failed to show cisplatin benefit—head-and-neck squamous cell carcinoma (HNSC), lung adenocarcinoma (LUAD), and ovarian carcinoma (OV)—we observed that the vast majority of these patients were predicted as resistant by the cisplatin VNN model, as expected (75%, Supplementary Figure 4.6D; compared to 25% for CESC and LUSC, Supplementary Figure 4.6E).

We next investigated which protein assemblies were responsible for the clinical predictions. Starting from the 29 assemblies found to be important to cisplatin response during training in cell lines (Figure 4.6A), we computed the *in silico* activity of each of these assemblies (per patient) as the first principal component of its neuron values (Methods). This activity was then investigated, separately for each assembly, as a quantitative marker for the prediction of cisplatin response in cervical cancer patients. We found that these 29 assembly activities were generally predictive of cisplatin treatment outcomes and tended to outperform those drawn from other protein assemblies in the NeST map (Figure 4.6B; Table 4.5). This observation also applied to the 41 RSi assemblies, as well as to the sets of assemblies that were validated in functional

screens. Notably, the 15 assemblies validated by both screening modes exhibited the highest predictive performance (Supplementary Figure 4.6F). They also surpassed the predictive power of single-gene biomarkers based on presence/absence of coding alterations in individual genes (Figure 4.6B). Some of the most predictive assemblies included roles in the regulation of β-catenin transcriptional activity, DNA repair, epigenetic modification, and RTK-JAK-STAT signaling (Figure 4.6B), most of which had also been validated in the earlier drug sensitivity or replication restart screens (Table 4.4).

For example, the top assembly with predictive power in patients was NeST:126 (Regulation of β-catenin transcriptional activity, Figures 4.4F and 4.6C), capturing activation of gene transcription by β-catenin via multiple mechanisms, including β-catenin co-activation (EP300, CREBBP)[50,51], negative regulation of β-catenin activity (HDAC2)[52], and regulation of β-catenin ubiquitination (TP53)[53]. The high *in silico* activity of this assembly was associated with significantly worse progression-free survival outcomes (Figure 4.6D), reflecting that genetic alteration of this complex predicts cisplatin resistance. Notably, single proteins in this assembly with frequent genetic alterations in cancer patients, such as TP53, were not individually predictive of drug response (Figure 4.6E; *TP53* mutation frequency 14% in TCGA cervical cancer). *BARD1* and *TOP2A*, two DNA repair genes that do not encode members of NeST:126, exhibited relatively high predictive accuracy but had limited predictive value due to the rare occurrence of alterations in these genes in cervical cancer patients, making them inapplicable to a large portion of the population (Figure 4.6E). The assembly as a whole, however, had both high alteration frequency and relatively high predictive accuracy (Figure 4.6E; 42% alteration frequency, C-index: 0.62).

4.3.6 The RTK-JAK-STAT assembly as a predictive marker of cisplatin response

The RTK-JAK-STAT assembly (NeST:89) provides an excellent illustration of how predictive accuracy is driven by the integration of multiple rare alterations in a protein assembly (Figure 4.7A). It consists of dense interactions of upstream growth factors (EGF) and receptor

tyrosine kinases (RTKs, including EGFR and ERBB2/3/4) with downstream signaling messengers and effectors (e.g. JAK1/2, STAT3/5A) (Figure 4.7B). Genetic alterations in this assembly had been initially identified as important for predicting cisplatin and gemcitabine responses in cell lines (Figure 4.3A). The impact of such alterations was subsequently validated in both the drug sensitivity and replication restart screens (Figures 4.4C and 4.4F; Supplementary Figure 4.5I; Table 4.4), and high activity of this assembly was shown to be predictive of drug resistance in cisplatin-treated cervical cancer patients (Figures 4.6B and 2.7C, HR = 2.8, P = 0.004).

Notably, none of the individual proteins in this complex were frequently genetically altered in cervical cancer, with all frequencies less than 10% (Figure 4.7D). As an integrator of these rare alterations, however, the complex as a whole showed a relatively high frequency of alteration (44.3% in TCGA cervical cancer) and predictive accuracy (C-index: 0.58) (Figure 4.7D). Perturbation of this complex (*in silico* activity > 0) was associated with drug resistance, driven predominantly by alterations spread over eight genes. These included copy number amplifications in *ERBB2*, *JAK2*, and *EGFR*, copy number deletions in *ERBB4*, *CBL*, and *IRS1*, and point mutations in *CBLB* and *PDGFRA* (Figure 4.7E, several of these genes had multiple alteration types). In general, the presence of any of these alterations was able to signal high assembly activity, and thus cisplatin resistance, following approximate OR-type Boolean logic (Figure 4.7F).

4.4 Discussion

Here we have advanced a set of interpretable deep learning models aimed at understanding genetic mechanisms of susceptibility and resistance to drugs that induce replication stress. Instead of associating single gene alterations with drug responses directly, the strategy is to project these alterations on a map of protein complexes and larger molecular assemblies associated with cancer. This approach is prompted and supported by the concept that cancer is a network-based disease arising from the action of hallmark cancer pathways[11,54]. According to this concept, a particular driving mutation may occur rarely in a tumor population,

but such rare events can sometimes be better understood and modeled by their impacts on common subcellular components. In this regard, our model identifies 41 protein assemblies in which genetic alterations modulate RSi drug responses, of which many could be corroborated by systematic gene loss-of-function assays (Figure 4.4 and Supplementary Figure 4.5) and/or predictive power in clinical cohorts (Figures 4.5–4.7).

4.4.1 Predictive assemblies identified by the models

It is widely recognized that cancer cells acquire resistance to the damage caused by cisplatin and other RSi agents through multiple mechanisms, with some of the key factors being the activation of DNA damage response pathways as well as rewiring of anti-apoptotic and pro-survival signaling cascades[24,55]. In agreement with these previous studies, our models highlight the significant roles of alterations in DNA repair-related assemblies, including mismatch and excision repair (NeST:30) as well as homologous recombination and Fanconi Anemia repair (NeST:79) (Figure 4.3A and Table 4.2). Such assemblies also capture the previously observed interactions of multiple DNA polymerases, including pol δ, ε, and η (POLD1, POLE, POLH)[56–58], with DNA repair proteins in regulating cisplatin resistance. Beyond DNA repair, an established component of cisplatin resistance is the dysregulation of cell growth and survival signaling, including the insulin receptor-PI3K-AKT-FOXO (INSR-FOXO, NeST:52)[59,60] and RAS-MAPK (NeST:73)[61] cascades, aspects that our models also capture (Figure 4.3A and Table 4.2).

In addition to these well-characterized response pathways, a growing body of evidence has begun to implicate aberrant epigenetic regulation cisplatin resistance, but the mechanistic details have remained unclear [62,63]. Here, all RSi-drug models (including the specific agent models and the multi-drug model) identify an assembly of epigenetic regulators in which alterations to multiple genes converge to modulate drug resistance in both cell lines and patients (Epigenetic modification, NeST:34; cell lines: Figure 4.3A and Supplementary Figure 4.4C; patients: Figure 4.6B). This assembly integrates genetic alterations across DNA methyltransferases (*DNMT1*,

DNMT3A, *DNMT3B*), histone methyltransferases (*EZH2*, *PRDM1*), histone demethylase (*KDM5A*), histone acetyltransferase (*CREBBP*), histone deacetylases (*HDAC1–3*), chromatin regulators (*SMARCA1, CHD4, MTA1*) and transcription factors (*RUNX1, ZBTB2, ZNF217, BRD4, TP53*). Among these, overexpression of the histone methyltransferase EZH2 has been shown to promote, and its inhibitor to effectively reverse, cisplatin resistance[64–66]. One possibility is that this and other epigenetic factors can affect cisplatin response via interactions with transcription factors in this assembly, such as RUNX1 and the zinc-finger proteins ZBTB2 and ZNF217. The impact of alterations to other proteins in NeST:34 on cisplatin response is less well-studied. Beyond this particular assembly, our model also highlights the importance of assemblies engaged in protein transport (NeST:12), locomotion (NeST:14), and regulation of immune responses (NeST:18). These predictive assemblies present promising avenues for further research and development.

4.4.2 The significance of integrating across many genetic alterations

Historically, drug response prediction has been pursued predominantly through the search for single-gene markers. Here, a key contribution of our work is to demonstrate how individual genetic alterations may be integrated into a unified quantitative assessment of drug resistance, calling attention to both well-known and understudied effects (Figure 4.1A). For example, the predictive NeST:89 assembly (RTK-JAK-STAT signaling, Figure 4.7) integrates and quantitatively weighs the effects of well-documented genetic markers of cisplatin resistance in cervical cancer, such as *EGFR*, *JAK2*, *STAT3* and *STAT5*[67–70]. It also integrates additional predictive features that have been less well-appreciated, including copy number deletion of *CBL* and *ERBB4*, as well as mutations of *PDGFRA*. Negative regulators like ubiquitin ligases (CBL, CBLB) may counterbalance the activation of EGFR and other RTKs, influencing the sensitivity to RSi agents like cisplatin. Unlike other oncogenic ERBB family proteins in this assembly, ERBB4 can form tumor-suppressing homodimers and negatively regulate STAT5A[71]. This unique aspect of the ERBB4 paralog may explain why, in our models, *ERBB4* deletions are predictive of cisplatin

resistance in cervical cancer patients (Figures 4.7E and 4.7F). More generally, the extensive interactions in this assembly interconnecting RTKs to JAK-STAT factors (Figure 4.7A) suggest that alterations of RTKs may trigger downstream JAK-STAT signaling to modulate the cellular response to cisplatin and potentially other RSi agents. Notably, the integration of all of these effects yields an integrated marker of cisplatin resistance with both high alteration frequency and predictive power (Figure 4.7D).

4.4.3 Comparison to previous ML models

Our work extends previous RSi drug response models along several lines. A first group of models, representing the majority of ML drug response modeling efforts[72], have focused on mRNA expression features for prediction. For example, Jin et al. used expression features very effectively in their state-of-the-art pan-drug-response model, which was also interpretable[73]. Here the VNN models are complementary, as they focus on the integration of rare and common genetic alterations, including somatic mutations and copy number aberrations. A second group of models have sought to identify gene signatures associated with responses to single RSi drugs[74–78] (medRxiv 19007757v1), such as Sui et al. who focused on predicting cisplatin resistance in non-small cell lung cancer[77]. Conversely, at the opposite end of the spectrum are models trained across very large numbers of drugs, including DeepCDR and DrugCell[30,48]. While such studies do not focus on RSi agents in particular, they nonetheless include representative RSi agents among hundreds of others, and some of these models also provide mechanistic pathway interpretation. Likely due to their generality, these models appear to sacrifice precision in RSi drug response prediction (e.g., see comparisons in Figure 4.2B). In this respect, the multi-task implementation presented here appears to strike a useful balance between single RSi-drug models and pan-drug models, in that it can capture both drug-specific features alongside general mechanisms underlying multiple RSi responses (Supplementary Figure 4.3C).

4.4.4 Systematic validation of assemblies via complementary functional assays

Our exploration of the predictive protein assemblies invoked two distinct types of genome-wide functional assay, with complementary insights. The first sought to confirm assemblies in which loss of gene function affects tumor cell fitness during a drug treatment[47]. This assay provides a direct test of the prediction that genetic alterations in an assembly affect a drug response, and it scales easily to multiple drugs using a pooled gene knockout library. On the other hand, drug sensitivity provides less information about the specific functions of an assembly, as it integrates the outputs of replication stress pathways with numerous other cellular responses such as growth signaling, apoptosis, immune response, drug export and so on. In contrast to this first screen, the second genome-wide assay sought to identify assemblies that relate specifically to mechanisms of DNA replication and replication restart[49]. This second screen offers richer phenotypic readouts than cell fitness, using dual markers for replication damage and restart, respectively, and thus is a more direct probe of RS responses. On the other hand, not all genes underlying a replication phenotype necessarily affect the ultimate drug response. Furthermore, the direct replication phenotypes were screened in an arrayed format, one gene at a time, and thus were only available for a single RSi agent in our study. Regardless, 24 assemblies important to the RSi drug models could be supported by drug sensitivity screens and 21 by replication restart screens, covering 30 assemblies total (Figure 4.4E).

4.4.5 Limitations and future directions

While we have mainly explored protein assemblies for their power as integrated genetic markers of drug response, a complementary direction will be to incorporate other layers of omics data, such as gene expression. Another compelling direction will be to explore the important assemblies as a source of drug targets. Targeted therapies that induce tumor-specific replication stress have emerged as a promising avenue for cancer treatment[12], as have synthetic combinations of RSi drugs with second points of intervention[79]. In this regard, we identified as

many as 41 important protein assemblies that mediate RSi drug responses, some of which may cause further replication stress when targeted. These assemblies might thus be used to design and conduct a systematic screen to disrupt and overexpress proteins from each RSi assembly in combination with a broad panel of FDA-approved drugs. These assemblies also serve as a valuable resource for elucidating the biology of DNA replication stress and its associated response pathways. Furthermore, the presence of common RSi drug regulatory mechanisms observed in non-RSi drugs (e.g., manumycin and ML210, Figures 4.2C and 4.3C) suggests the possibility that these drugs induce indirect or secondary effects on DNA replication or establish crosstalk between their primary effects and DNA damage responses. While these drugs are not originally designed to target RS, our study underscores the importance of a systematic elucidation of drug response mechanisms.

4.5 Methods

4.5.1 Preparation of therapeutics response data

Drug response data were retrieved from the Genomics of Drug Sensitivity in Cancer database (GDSC, with separate datasets GDSC1 and GDSC2) and the Cancer Therapeutics Response Portal (CTRP, with separate datasets CTRP1 and CTRP2) in July of 2022[43–46]. Together, these repositories covered a total of 692,859 cell line-drug pairs, comprising 1244 cell lines and 888 drugs with some pairs missing. The numbers of cell lines with response data informing each RSi drug were as follows: cisplatin (947), gemcitabine (1210), camptothecin (799), etoposide (1181), olaparib (1213), and CD437 (825). Data from both repositories were harmonized as follows. Drug information: Each molecule's published name, synonym, or SMILES string was queried using PubChemPy, and the corresponding associated InChiKey was extracted and stored. Duplicate drugs (within or between repositories) were then matched with one another using InChiKeys, and PubChemPy was used to extract isomeric SMILES strings. Some compounds with no matches were manually annotated. Cell viability data: For CTRP, the average

percent viability files, which have been normalized to vehicle control, were used. For GDSC1, data were normalized to 'cells-only' controls on a per-plate basis. For GDSC2, data were normalized to DMSO control wells on a per-plate basis. Data were then averaged across all replicates for each dataset separately. For drug response measurement, we used Area Under the dose-response Curve (AUC) where AUC = 0 corresponds to complete cell killing and AUC = 1 corresponds to no cell killing; AUC > 1 represents a growth advantage conferred by the drug. The harmonized AUCs calculated in this study were in agreement with AUCs reported by the original consortia (Pearson correlations of 0.92, 0.83, 0.91, and 0.91 for CTRP1, CTRP2, GDSC1, and GDSC2, respectively).

4.5.2 Selection of gene features

A set of 718 clinical genes was assembled from the union of those in which mutations and/or copy number aberrations are assessed by one or more of the following clinical panels: FoundationOne CDx[40], Tempus xT[41], PALOMA-3 trial[80], or Project GENIE[42]. To compile genotypes for all cell lines, we extracted non-synonymous coding mutations and copy number alterations for the clinical panel genes from the Cancer Cell Line Encyclopedia (CCLE, release 22Q1)[81]. Gene mutations were marked as either present ("1") or absent ("0"), with mutations filtered for the following types: missense, nonsense and non-stop mutations, frame-shift insertions and deletions, splice site and region variations, and in-frame insertions and deletions. Gene copy number deletions or amplifications were marked separately, also using binary (1/0) indications. Together, mutations, copy number deletions, and copy number amplifications served as features for each of the clinical panel genes.

4.5.3 Model architecture

We queried the NeST hierarchy of cancer protein assemblies[36] to identify those that contained clinical panel genes. We define a hierarchy of protein assemblies as a multi-layered treelike structure where individual genes recursively cluster together to form assemblies that are

connected to other assemblies in parent-child relationships all the way up to the root of the structure which represents a cancer cell (Supplementary Figure 4.2). In our models, protein assemblies were filtered to require ≥5 clinical panel genes or >1 child assembly, producing a final hierarchy consisting of 131 assemblies distributed over 7 layers. An assembly in NeST can have both single proteins and other assemblies as its children (Supplementary Figure 4.3A).

We trained six single-drug visible neural networks (VNNs)[29] and one multi-drug VNN (Figure 4.2A), where the VNN architecture followed the connections of the 718 genes and 131 assemblies in NeST (Supplementary Figure 4.3). Gene alterations (mutations, copy number deletions, and copy number amplifications) form the input feature layer, which connect together to form the gene layer (Supplementary Figure 4.3A). For any gene g_i, we denote the input features as a vector I_i and the output as g_i, where $i \in [1,718]$, $I_i \in [0,1]^3$ and $g_i \in R$. Hence, a gene-layer equation is given by:

$$g_i = BatchNorm(Tanh(Linear(I_i)))$$

$BatchNorm$ indicates Batch Normalization[82], $Tanh$ indicates a hyperbolic tangent function and $Linear$ indicates a weighted linear transformation.

The remaining layers of the model represent the 131 NeST assemblies, where each assembly is represented by n neurons, and every parent-child connection follows the edges in the hierarchical map. An assembly-gene pair is connected through $n \times 1$ connections and an assembly-assembly pair through $n \times n$ connections. The number of neurons is a hyperparameter. Dropout[83] with probability = 0.3 was added to layers five through eight after hyperparameter optimization. Given an assembly A_j connected to k child assemblies and m genes, its input is denoted by a vector I_j of dimension $n * (n * k + m)$ and output by a vector A_j of dimension n, where $A_j \in R^n$ and $j \in [1,131]$. Thus, the equation for an assembly is given by:

$$A_j = BatchNorm\left(Tanh\left(Linear\left(Dropout(I_j)\right)\right)\right)$$

The state of an assembly, which we refer to as the '*in silico* activity', is defined as a function of the states of its k child assemblies and m genes. To reduce *in silico* activity to a single dimension, we compute the first principal component resulting from principal component analysis (PCA)[84] of the set of neuron values for each assembly. The final output for a single-drug model is a linear transformation of the output of the root, resulting in a real number in the range [0,1]. For the multi-drug model, the output of the root node is connected to an additional layer of neurons, one for each of d drugs, resulting in an output vector $O \epsilon R^d$. Hence, the output-layer equation is given by:

$$O = Tanh(Linear(A_{root}))$$

The objective function $(Loss)$ of the VNN aggregates the mean squared error (MSE) across every assembly in the hierarchy. The loss function for a single-drug model can be defined as:

$$Loss = MSE(O, y) + \sum_{j \neq root} MSE\big(Linear(A_j), y\big) + \beta||W||$$

The parameter α was set to 0.3 whereas β was tuned by hyper-parameter optimization. $Linear$ denotes the linear function used for transforming the vector A_j to a scalar. Note that for the single-drug models, O is already a scalar. W denotes the weights of the neural network. AdamW (arXiv 1711.05101) was used to optimize weights. For the multi-drug model, the final loss is the sum of loss for each drug, given by:

$$Loss = \sum_d \left(MSE\big(O^d, y^d\big) + \sum_{j \neq roo} MSE\big(Linear(A_j), y^d\big) + \beta||W|| \right)$$

NB: Assembly states and weights remain the same because they are shared across all drugs.

4.5.4 Model training

All models were trained using a five-fold nested cross-validation procedure. For each fold setting, 64% of cell lines were split as a training set, 16% as a validation set (used in

hyperparameter tuning), and 20% as a test set, ensuring that cell line replicate measurements (e.g., from different GDSC or CTRP datasets) were not split between test and training sets. Hyperparameter optimization was performed using Optuna[85]. All VNN models were implemented in PyTorch and trained using five GPU servers containing four Nvidia Tesla V100s each with 5120 CUDA cores and 32GB GDDR6 RAM.

4.5.5 Alternate models for performance comparison

We assessed three models for benchmarking the performance of VNN models. We constructed a black-box artificial neural network (ANN)[35] using the Python scikit-learn library[86], which was allotted the same number of neurons and layers as the VNN model. The ANN was trained and optimized using the exact same procedure as the VNN models. We also evaluated two previously published models, DeepCDR[48] and DrugCell[30]. Both models were re-trained against the exact mutation calls and drug responses used for the VNN models using five-fold cross-validation. We assessed the performance of these models on held-out cell lines, as compared to the held-out drug-cell line pairs used originally in these studies.

4.5.6 Predicting drug response using the multi-drug model

To predict cellular response to each drug (6 discovery and 39 test drugs), first, we divided the cell lines into five held-out sets, one for each fold of the multi-drug model, such that no cell line was used in training the model. The model predicted six responses per cell line, one for each RSi drug (*O,* Supplementary Figure 4.3C). Since each fold predicted response to a distinct set of cell lines, the responses from all the folds were simply aggregated to calculate one odds ratio per discovery drug and six odds ratio values per test drug. The odds ratio and its confidence interval were reported for the discovery drugs (Figure 4.2B). The mean and standard error of the six odds ratios were used to compare the predictions across the test drugs (Figure 4.2C).

4.5.7 System importance (SI) score

To determine the importance scores of protein assemblies for drug response prediction, we adopted a variation of "Relative Local Improvement in Predictive Power" previously reported by Ma et al.[29]. For each of the five pre-trained models corresponding to each drug, we used Ridge Regression, an L2-norm regularized linear regression method, trained on assembly neuron values (*A*, Supplementary Figure 4.3A), to model the predicted drug response of an assembly (system). System importance was calculated using the Spearman correlation between the prediction of Ridge Regression and VNN drug response for the single-drug models and the *in silico* activity of the root node for the multi-drug model. Throughout the paper, the average scores of system importance were reported across all five models. A higher SI score indicated an assembly for which the neurons had a strong contribution to VNN predictions and could therefore be considered important; conversely, a low SI score indicated an assembly for which the neurons were weak predictors of VNN predictions and could therefore be considered of low importance. Assemblies with SI scores of ≥ 0.5 were referred to as important assemblies (Figure 4.3A).

4.5.8 Enrichment of important assemblies in functional screens

The function "gost" from the R package "g:Profiler"[87] was used to identify functional enrichment of genes in the NeST assemblies. An assembly-to-genes annotation file (.gmt) (Table 4.1) was created using the function "CreatePathwayCollection" in the R package "pathwayPCA". Genes were first rank-ordered by the degree (absolute z score) to which their loss-of-function modulates the response to an RSi drug in the CRISPR/Cas9 screens or the repair of replication fork[47,49]. The ranks in each of the chemogenetic screens or the RNAi screen were then loaded into "gost" as input to find the over-representation of functions from the NeST. The Benjamini-Hochberg procedure was utilized to adjust p-values for multiple comparisons. Over-representation with FDR < 0.1 was considered enrichment in the CRISPR/Cas9 screens. (Supplementary Figure 4.5). Note that the models identify assemblies important for sensitivity or

resistance, by integrating the effect of both gain and loss of function genetic events. However, the models currently only have binary annotations for mutations, without distinguishing gain or loss of function. Given the integrated bidirectional complexity of mutation functions and response outputs, we evaluated CRISPR knockouts or RNAi knockdowns as signless modifiers for systematic validations. A more detailed evaluation can be performed for a specific assembly by carefully examining individual patient mutations.

4.5.9 Preparation of cisplatin clinical data

Genotypes (mutations, copy number variations) for patients treated with cisplatin were queried from The Cancer Genome Atlas (TCGA, PanCancer Atlas) via cBioportal (https://www.cbioportal.org/datasets). Patients treated with multiple RSi drugs (cisplatin and etoposide; cisplatin and gemcitabine) were excluded, resulting in 368 cisplatin-treated patients with genomic profiles and clinical information. The patient population where cisplatin is the standard-of-care was selected for a focused model evaluation. We further selected cisplatin-treated cancer types with at least 30 patients. This resulted in five types, including 106 patients with cervical squamous cell carcinoma (CESC), 45 patients with lung squamous carcinoma (LUSC), 92 patients with head and neck squamous cell carcinoma (HNSC), 58 patients with lung adenocarcinoma (LUAD) and 67 patients with ovarian serous cystadenocarcinoma (OV) (Figure 4.5).

4.5.10 Model evaluation for cisplatin-treated patients

We evaluated the prediction performance of the cisplatin VNN model using the concordance index (C-index) and hazard ratio (HR)[88], which were calculated using “Lifelines”, a Python survival analysis library. C-index quantifies the fraction of concordant pairs in patients, comparing predicted AUC with actual survival time, out of all possible pairs. Those pairs were discarded if the earlier time was censored. For a given test set, its risk scores with event time and event status were used to calculate the C-index. A higher C-index value indicates a better time-

to-event prediction model, with a C-index of 1.0 indicating perfect prediction and a C-index of 0.5 indicating random prediction. C-index less than 0.5 indicates an anti-concordance relation. Hazard ratio (HR) is a statistical measure that compares the relative hazard rates between predicted resistant and sensitive patients, using the Cox proportional hazards regression method[89]. A hazard ratio greater than 1 indicates a higher risk in the predicted resistant group compared to the sensitive group (Figures 4.5–4.7 and Supplementary Figure 4.6). Beyond the cisplatin VNN, we also evaluated the performance of the other RSi drug models on prediction of cisplatin survival outcomes, including the single-drug and multi-drug models. While other single-drug VNNs were less accurate than the cisplatin VNN, their C-index generally outperformed the non-RSi VNNs (Supplementary Figure 4.6G). The multi-drug VNN was also able to stratify cisplatin-treated patients into resistant and sensitive groups with comparable accuracy to the cisplatin VNN (Supplementary Figure 4.6G).

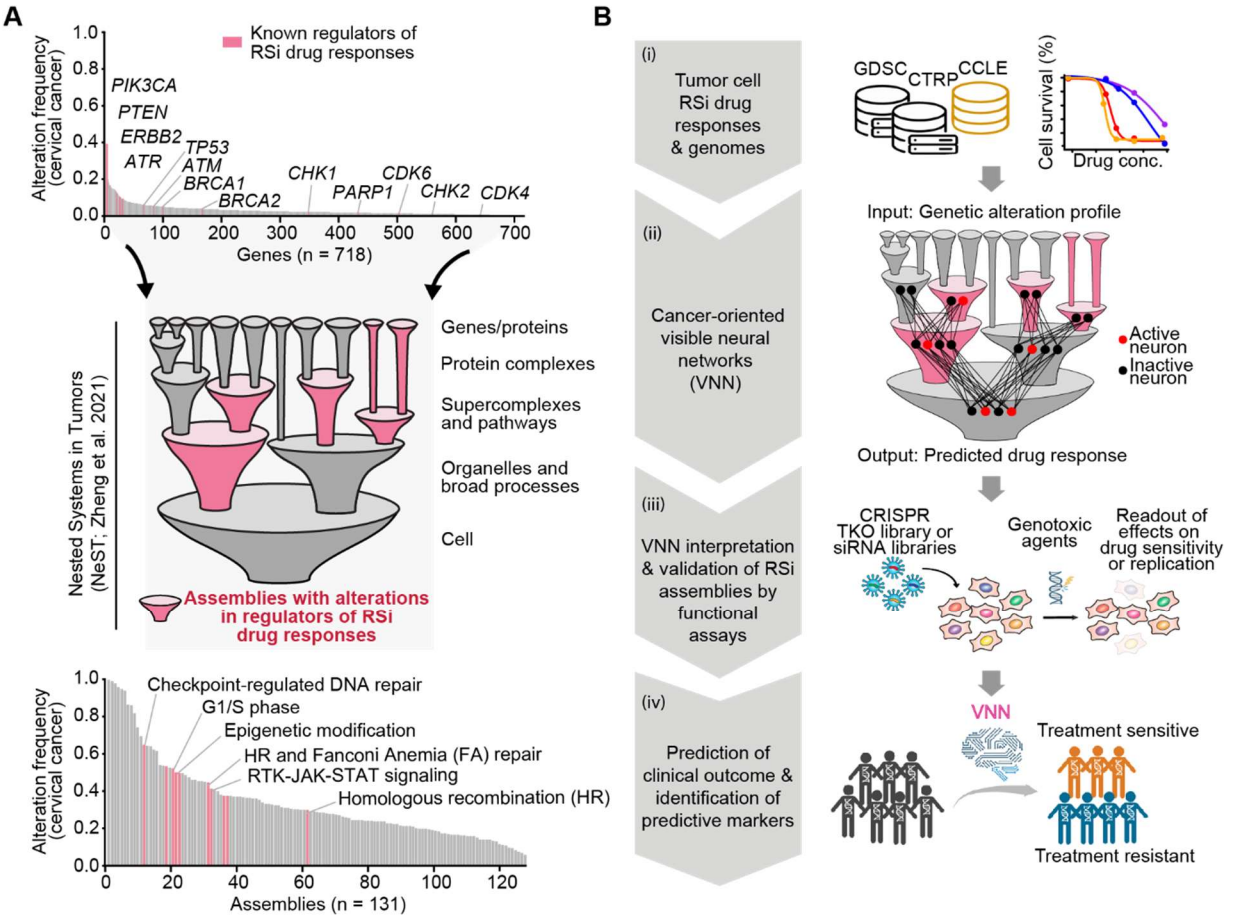

Figure 4.1: **Study overview.**

A, Genetic alterations that modulate replication stress-inducing (RSi) drug responses are typically rare but converge on multiscale protein assemblies in cancer. Top: Waterfall plot of gene alteration frequencies in The Cancer Genome Atlas (TCGA) cervical squamous carcinoma cohort, showing that most genetic alterations are rare. Alterations include somatic mutations and copy number aberrations of genes covered by clinical cancer gene panels. Middle: Genetic alterations converge on specific multi-protein assemblies in the NeST (Nested Systems in Tumors) hierarchy. Bottom: Waterfall plot showing genetic alteration frequencies of NeST protein assemblies which, by nature, tend to be higher than for individual genes. **B,** Pipeline for drug response prediction. (i) Acquisition of datasets used in this study. RSi drug response data from Genomics of Drug Sensitivity in Cancer (GDSC) and Cancer Therapeutics Response Portal (CTRP) databases. Tumor cell-line genome sequencing data from Cancer Cell Line Encyclopedia (CCLE). (ii) Construction of Visible Neural Network (VNN) models with architecture guided by NeST. (iii) Interpretation of VNN models to recognize assemblies for which genetic alterations are most important for RSi drug responses. Validation by genome-wide loss-of-function screens. (iv) Translation of VNNs to predict chemotherapy responses in cancer patients.

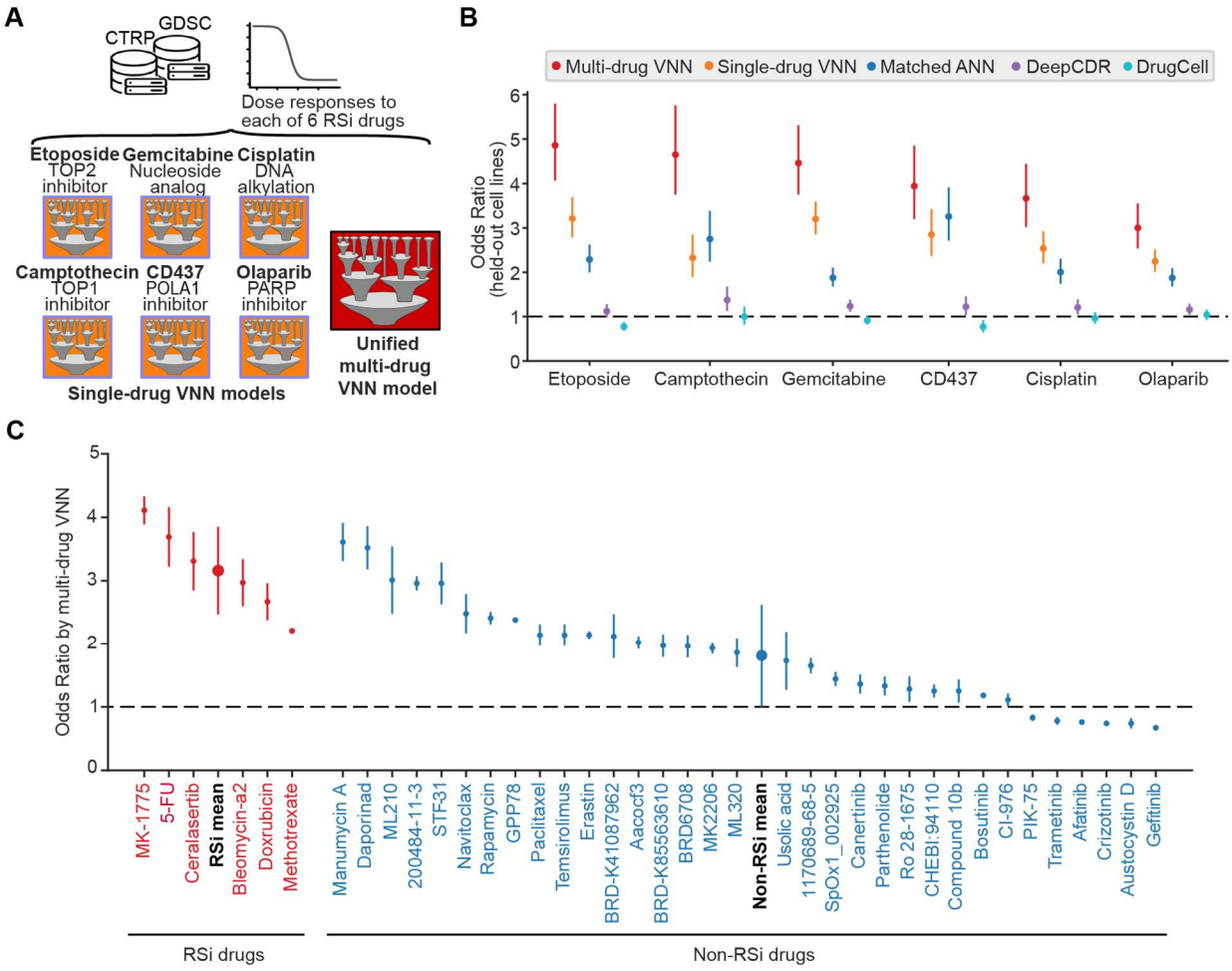

Figure 4.2: **Performance of RSi-drug response models.**

A, Schematic representation of the VNN models implemented in this study for single-drug and multi-drug scenarios. **B,** Accuracy (odds ratio) of drug response prediction for each of the initial six RSi agents. Multi-drug and single-drug VNNs (red, orange) are compared against black-box artificial neural networks with a matched number of parameters and layers (ANN, blue), DeepCDR (purple), and DrugCell (cyan). Error bars show the confidence interval of the odds ratio for each model. Performance was assessed on drug responses of held-out cell lines not seen during training. **C,** Accuracy (odds ratio) of drug response prediction by the multi-drug model, evaluated for additional RSi drugs (n = 6, red) and non-RSi drugs (n = 33, blue), none of which were seen during training. Error bars show standard deviation of the odds ratio for each drug. Performance was assessed using held-out cell lines. Statistical comparisons conducted with the Mann-Whitney U test.

Figure 4.3: **Identification of molecular mechanisms important for RSi drug responses.**

A, System Importance (SI) profiles for prediction of initial six RSi drug responses. Nodes indicate protein assemblies; node sizes denote assembly sizes in numbers of proteins; colors mark important assemblies for each drug response. The number of important assemblies is indicated in parentheses for each single-drug model. **B,** Venn diagram showing numbers of important assemblies identified by single-drug (n = 37, left) versus multi-drug VNNs (n = 36, right). The union set is defined as RSi assemblies (n = 41). **C,** UMAP projection of SI profiles of each drug model constructed in this study (points). The HDBSCAN algorithm is used to group drug models into clusters (colors) by similarity of important assemblies (SI profiles); gray models fall outside of stable clusters. Bold font face indicates RSi drug models, light font face indicates non-RSi drug models. **D,** RSi assemblies (defined in panel B) are plotted by their average importance scores for models trained on the initial RSi discovery agents (left), the later RSi test agents (middle), or non-RSi drug models (right). Horizontal line in each swarm represents the mean. ***$P < 0.01$; P-values by one-sided Mann-Whitney U test.

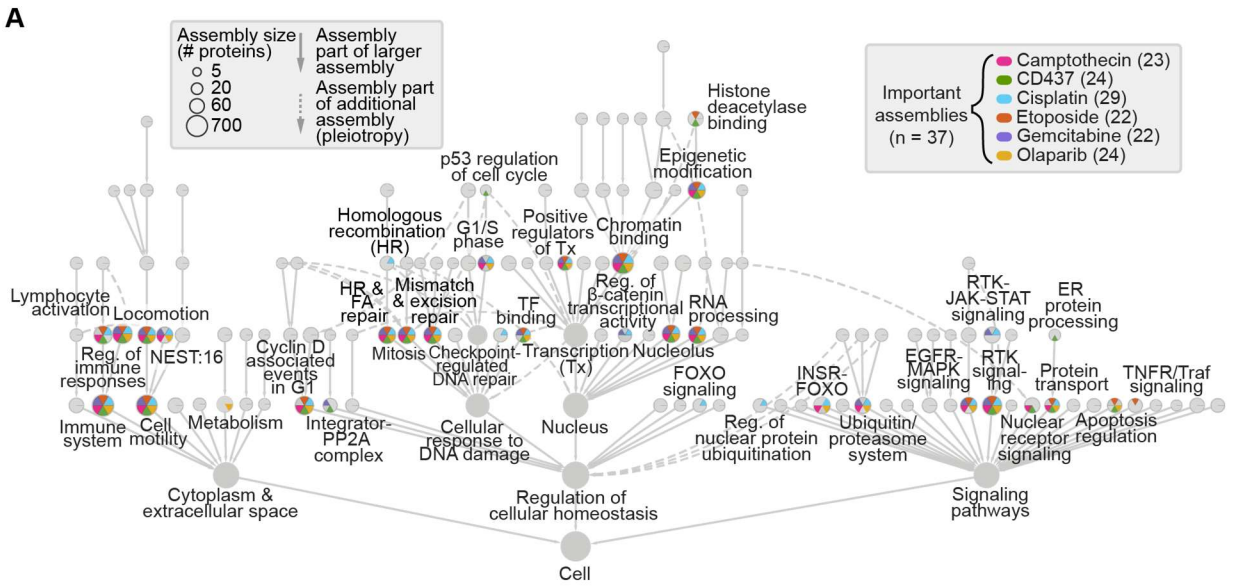
A
Assembly size (# proteins)
5
20
60
700
Assembly part of larger assembly
Assembly part of additional assembly (pleiotropy)
Important assemblies (n = 37)
Camptothecin (23)
CD437 (24)
Cisplatin (29)
Etoposide (22)
Gemcitabine (22)
Olaparib (24)
Histone deacetylase binding
p53 regulation of cell cycle
Epigenetic modification
Homologous recombination (HR)
G1/S phase
Positive regulators of Tx
Chromatin binding
Lymphocyte activation
Locomotion
HR & FA repair
Mismatch & excision repair
TF binding
Reg. of β-catenin transcriptional activity
RNA processing
RTK-JAK-STAT signaling
ER protein processing
Reg. of immune responses
NEST:16
Cyclin D associated events in G1
Mitosis
Checkpoint-regulated DNA repair
Transcription (Tx)
Nucleolus
FOXO signaling
INSR-FOXO
EGFR-MAPK signaling
RTK signal-ing
Protein transport
TNFR/Traf signaling
Immune system
Cell motility
Metabolism
Integrator-PP2A complex
Cellular response to DNA damage
Nucleus
Reg. of nuclear protein ubiquitination
Ubiquitin/ proteasome system
Nuclear receptor signaling
Apoptosis regulation
Cytoplasm & extracellular space
Regulation of cellular homeostasis
Signaling pathways
Cell
B
RSi assemblies (n= 41)
Assemblies important in ≥ 1 single-drug VNN (n = 37)
5
32
4
Assemblies important in multi-drug VNN (n = 36)
C
Clustering of models by SI profiles:
Cluster 1
Cluster 2
Outlier
Font face:
Bold: RSi drug model
Light: Non-RSi model
Ro-28-1675
Canertinib
BRD-K41087962
Ursolic acid
CI-976
BRD-K85563610
Parthenolide
GPP78
200484-11-3
CHEBI:94110
Crizotinib
STF-31
SpOx1_002925
PIK-75
BRD6708
Daporinad
Compound-10b
Trametinib
Erastin
5-FU
Ceralasertib
Aacocf3
Gefitinib
Paclitaxel
Bosutinib
Bleomycin-a2
ML-210
Rapamycin
ML320
Gemcitabine
Methotrexate
Manumycin-A
1170689-68-5
Afatinib
Cisplatin
MK-2206
Olaparib
Etoposide
Austocystin D
CD437
Navitoclax
Temsirolimus
Camptothecin
Doxorubicin
Multi-drug
MK-1775
D
***P = 1×10−12
***P = 2×10−8
Assembly importance score (mean SI assigned by models)
0.8
0.6
0.4
0.2
0.0
Showing RSi assemblies (n = 41)
Discovery RSi drug models
Test RSi drug models
Non-RSi drug models

Figure 4.4: Evaluation of important assemblies by systematic siRNA screening.

A, Assemblies are analyzed for their enrichment for gene knockdowns that affect RS response via the absolute value of the replication restart score |RRS|, defined as the ratio of γH2AX to EdU intensity readouts. RRS screening data by Kavanaugh et al. [49]. **B,** Percent of assemblies validated by enrichment in RRS assay, shown separately for those important to RSi drug models (left) versus all others (right). Error bars display the standard error of the proportion. ***P < 0.01; P-value by two sample z-test. **C,** NeST assemblies ranked by their degree of enrichment, from most to least significant. Assemblies with FDR < 0.1 are highlighted in red (n = 46). Selected RSi assemblies were labeled. **D,** Mean importance scores for the 46 RRS-enriched assemblies (highlighted in panel C), shown separately for RSi (left) and non-RSi drug models (right). ***P < 0.01; P-value by Mann-Whitney U test. **E,** Venn diagram showing numbers of RSi assemblies validated by enrichment in the RRS assay or a separate chemogenetic drug sensitivity analysis (Supplementary Figure 4.S5). **F,** Validated assemblies in the two functional assays are indicated on the NeST assemblies map.

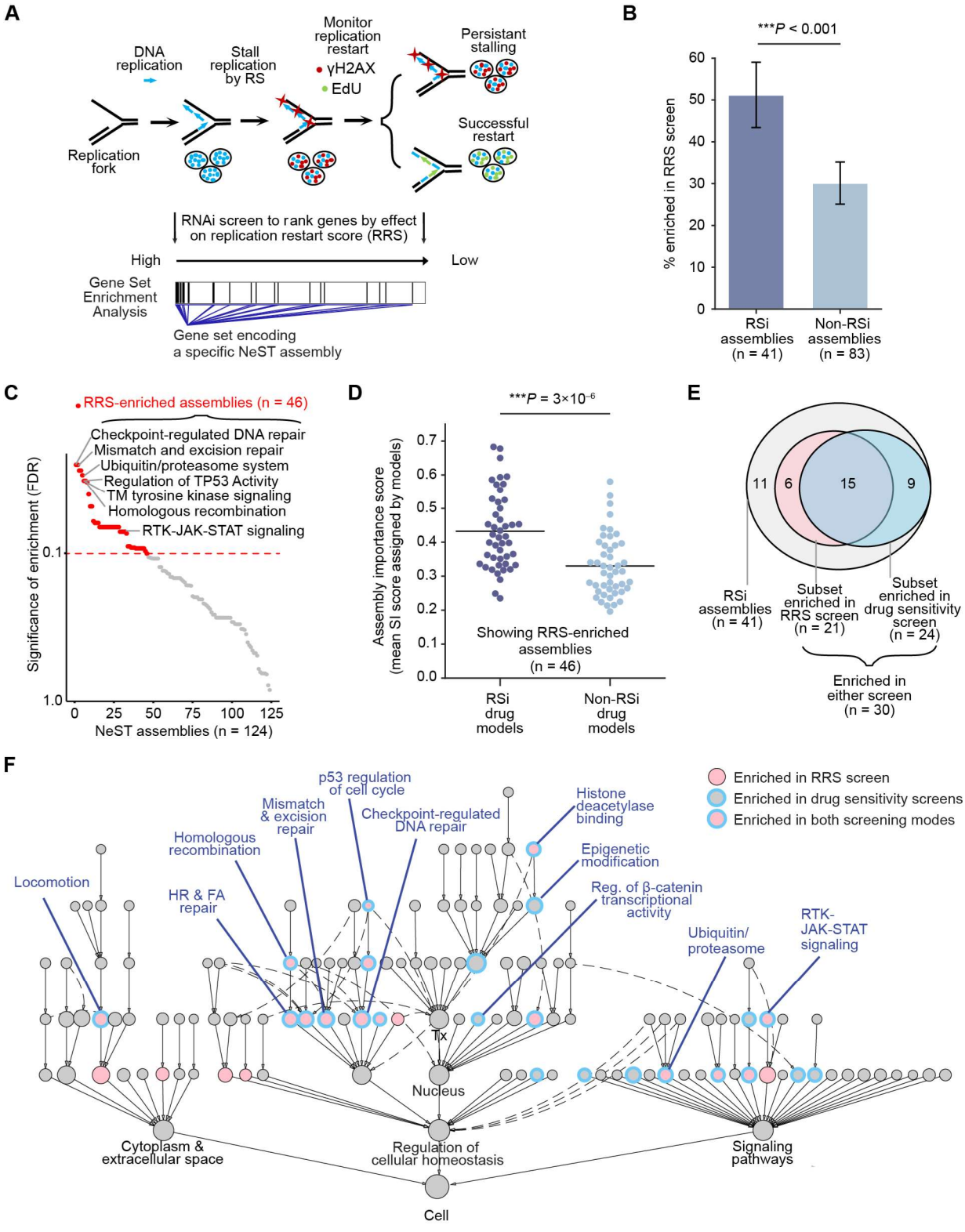
A
DNA replication
Stall replication by RS
Monitor replication restart
γH2AX
EdU
Persistant stalling
Successful restart
Replication fork
RNAi screen to rank genes by effect on replication restart score (RRS)
High
Low
Gene Set Enrichment Analysis
Gene set encoding a specific NeST assembly
B
***P < 0.001
% enriched in RRS screen
RSi assemblies (n = 41)
Non-RSi assemblies (n = 83)
C
RRS-enriched assemblies (n = 46)
Checkpoint-regulated DNA repair
Mismatch and excision repair
Ubiquitin/proteasome system
Regulation of TP53 Activity
TM tyrosine kinase signaling
Homologous recombination
RTK-JAK-STAT signaling
Significance of enrichment (FDR)
NeST assemblies (n = 124)
D
***P = 3×10⁻⁶
Assembly importance score (mean SI score assigned by models)
Showing RRS-enriched assemblies (n = 46)
RSi drug models
Non-RSi drug models
E
11
6
15
9
RSi assemblies (n = 41)
Subset enriched in RRS screen (n = 21)
Subset enriched in drug sensitivity screen (n = 24)
Enriched in either screen (n = 30)
F
Enriched in RRS screen
Enriched in drug sensitivity screens
Enriched in both screening modes
Locomotion
HR & FA repair
Homologous recombination
Mismatch & excision repair
p53 regulation of cell cycle
Checkpoint-regulated DNA repair
Histone deacetylase binding
Epigenetic modification
Reg. of β-catenin transcriptional activity
Ubiquitin/ proteasome
RTK-JAK-STAT signaling
Tx
Nucleus
Cytoplasm & extracellular space
Regulation of cellular homeostasis
Signaling pathways
Cell

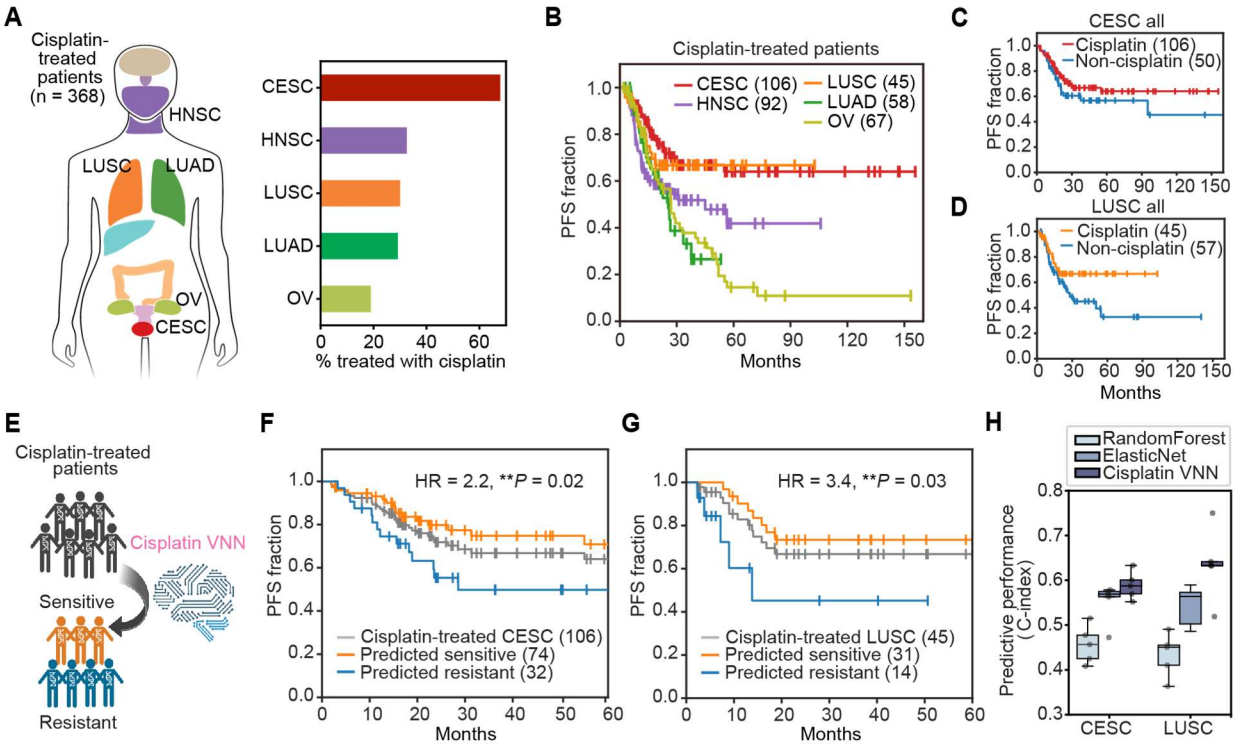

Figure 4.5: **Model translation to predict clinical outcomes in cervical and lung cancers.**

A, Top five cancer types in The Cancer Genome Atlas (TCGA) by largest number of patients treated by cisplatin: CESC, LUSC, HNSC, LUAD and OV. Right barplot shows the fraction of patients of each type that were treated with cisplatin. **B,** Kaplan-Meier survival curves of progression-free survival (PFS) for TCGA patients with various cancer types that are indicated by different colors. Patients with CESC or LUSC were chosen for the cisplatin VNN model validation because they showed the best outcome following cisplatin treatment. **C,** Kaplan-Meier survival curves of progression-free survival (PFS) for cisplatin-treated and non-cisplatin-treated patients with CESC. **D,** Kaplan-Meier survival curves of progression-free survival (PFS) for cisplatin-treated and non-cisplatin-treated patients with LUSC. **E,** Application of the cisplatin VNN to predict patient responses to cisplatin treatment. **F,** Kaplan-Meier survival curves of progression-free survival (PFS) for patients with CESC stratified by the cisplatin VNN prediction status (sensitive versus resistant, shown by orange versus blue). $^{**}P < 0.05$; P-value by log-rank test. **G,** Kaplan-Meier survival curves of progression-free survival (PFS) for patients with LUSC stratified by the cisplatin VNN prediction status (sensitive versus resistant, shown by orange versus blue). $^{**}P < 0.05$; P-value by log-rank test. HR, Hazard Ratio. **H,** Predictive performance in response to cisplatin of RandomForest, ElasticNet, and the cisplatin VNN models (boxplots of different colors) in patients with CESC (left) or LUSC (right). Performance measured using the Concordance index (C-index). Boxplot midline is median, box boundaries show upper and lower quartile, and whiskers show C-indices measured by five respective cross-validation modes of RandomForest, ElasticNet, and the cisplatin VNN models.

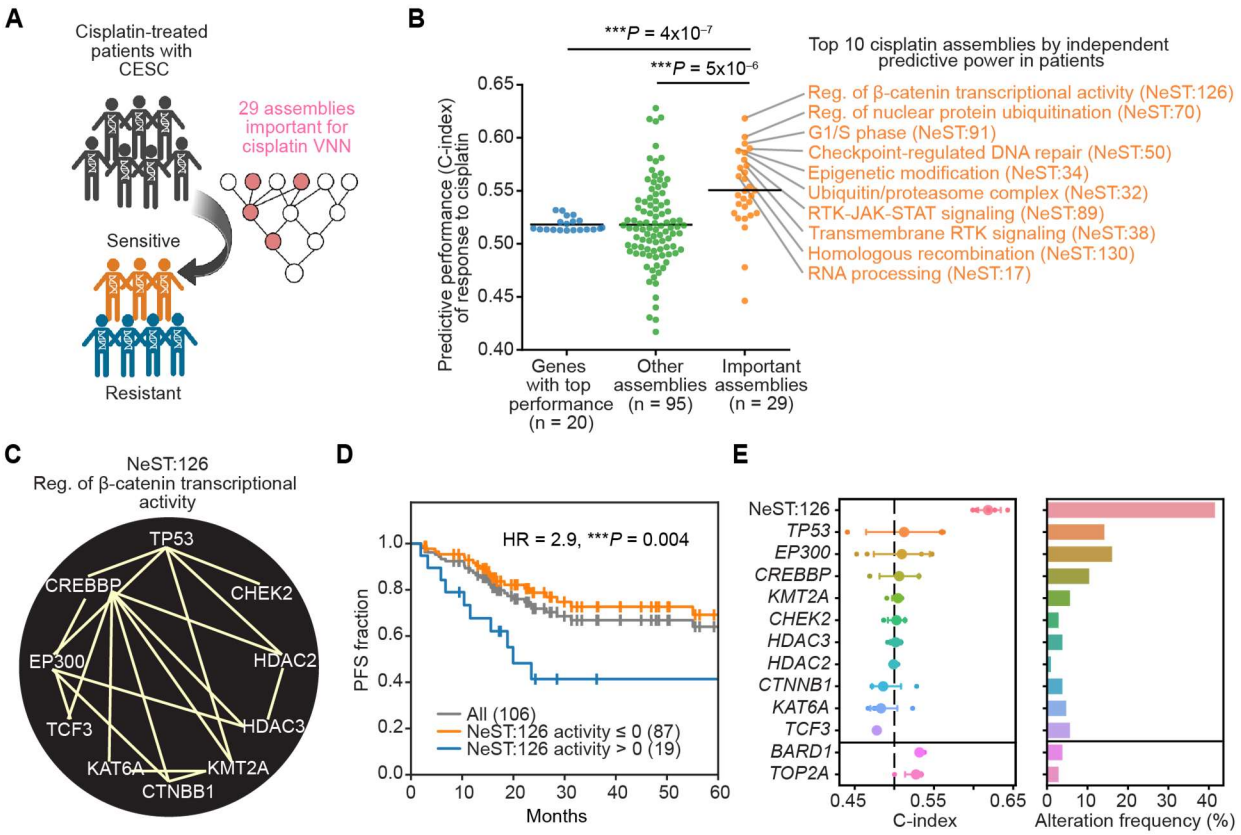

Figure 4.6: **Protein assemblies as biomarkers of cisplatin outcome.**

A, Evaluation of individual assemblies for prediction of responses to cisplatin in patients with CESC. **B,** Swarmplot showing the predictive performance (C-index) of genes and assemblies in response to cisplatin in patients with CESC. Assemblies are grouped into the 29 important for cisplatin response in cell lines (right) versus all other assemblies (middle). The top 10 predictive assemblies in patients with CESC are listed in orange. ***P < 0.01; P-value by Mann-Whitney U test. **C,** Interaction network of proteins in NeST:126. Edges denote Integrated Association Stringency (IAS) scores used to assemble the NeST map [36]. **D,** Kaplan-Meier survival curves of progression-free survival (PFS) for cisplatin-treated patients with CESC stratified by *in silico* activity of NeST:126. ***P < 0.01; P-value by log-rank test. HR, Hazard Ratio. **E,** LEFT: Predictive performance (C-index) of NeST:126 assembly (top row) and its genes (all other rows except BARD1 and TOP2A) for prediction of CESC cisplatin response. RIGHT: Corresponding frequency at which the assembly or its genes is genetically altered in patients with CESC. Large circles indicate the mean C-index over five models from cross-validation. Error bars denote 95% confidence intervals (CI). C-index and alteration frequency of the top two predictive genes BARD1 and TOP2A that are not members of NeST:126 are shown at bottom, separately.

Figure 4.7: **RTK-JAK-STAT assembly as an example predicting cisplatin resistance.**

A, Protein network defining NeST:89 (RTK-JAK-STAT signaling). Edges denote Integrated Association Stringency (IAS) scores used to assemble the NeST map. **B,** Oncogenic signaling pathways captured by NeST:89. **C,** Kaplan-Meier survival curves of progression-free survival (PFS) for cisplatin-treated patients with CESC stratified by *in silico* activity of NeST:89. HR, Hazard Ratio. ***$P < 0.01$; P-value by log-rank test. **D,** LEFT: Predictive performance (C-index) of NeST:89 assembly (top row) and its genes (all other rows except BARD1 and TOP2A) for prediction of CESC cisplatin response. RIGHT: Corresponding frequency at which the assembly or its genes is genetically altered in patients with CESC. Large circles represent the mean C-index over five models from cross-validation. Error bars denote 95% confidence intervals. C-index and alteration frequency of the top two predictive genes BARD1 and TOP2A that are not members of NeST:89 are shown at bottom, separately. **E,** OncoPrint showing NeST:89 genes (rows) by cisplatin-treated patients with CESC (columns). Patients stratified into binary response subtypes based on NeST:89 status (low activity at left, enriched for cisplatin-sensitive patients; high activity at right, enriched for cisplatin-resistant patients). Genes sorted from top-to-bottom based on alteration frequency in cisplatin-resistant subtype. **F,** Boolean circuit diagram representing the approximate logic function by which the genetic alteration status of eight NeST:89 genes predicts resistance to cisplatin in the CESC cohort. Inputs from activating or upregulating alterations are directly connected to the OR gates whereas inputs from inactivating or downregulating alterations are first negated to represent an opposite signal.

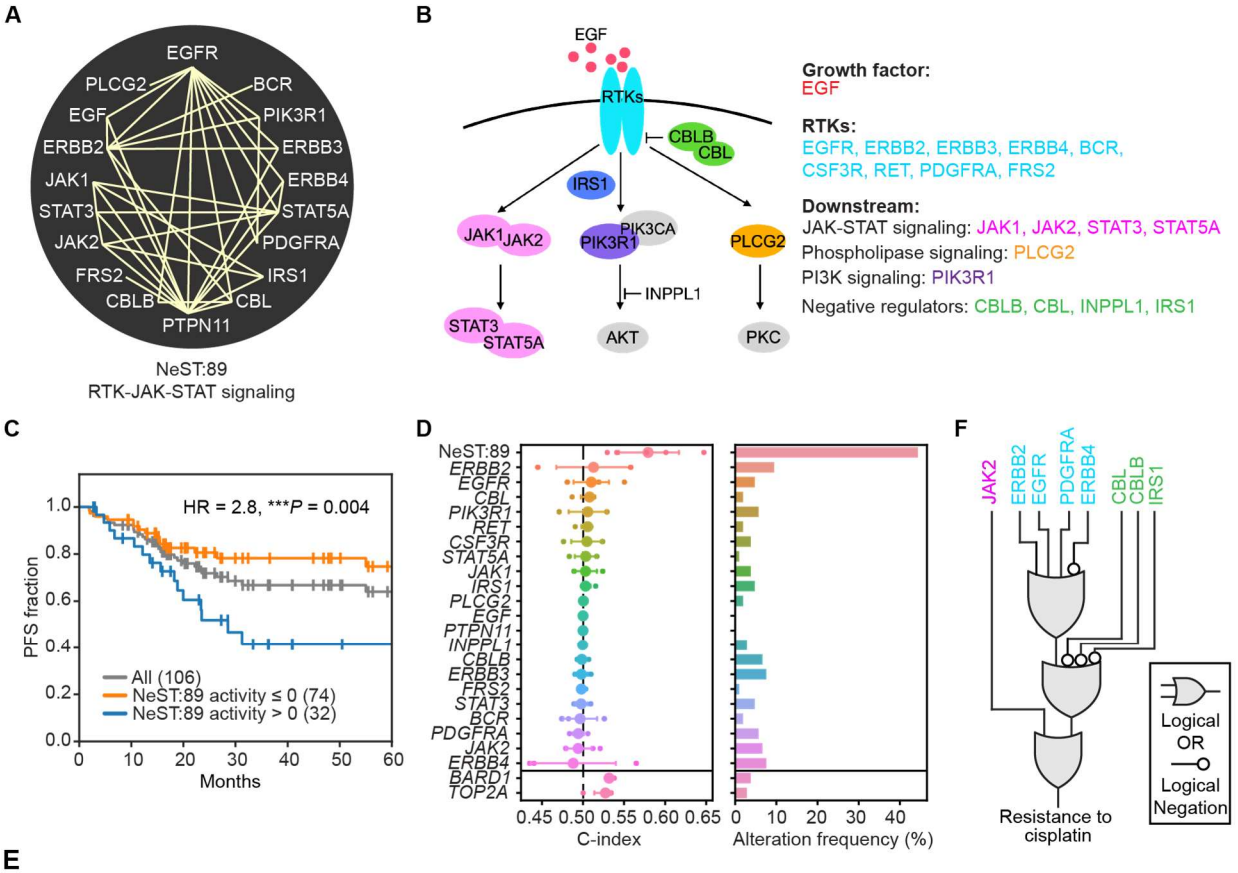
A
EGFR
PLCG2
BCR
EGF
PIK3R1
ERBB2
ERBB3
JAK1
ERBB4
STAT3
STAT5A
JAK2
PDGFRA
FRS2
IRS1
CBLB
CBL
PTPN11
NeST:89
RTK-JAK-STAT signaling
B
EGF
RTKs
CBLB
CBL
IRS1
JAK1
JAK2
PIK3CA
PIK3R1
PLCG2
INPPL1
STAT3
STAT5A
AKT
PKC
Growth factor:
EGF
RTKs:
EGFR, ERBB2, ERBB3, ERBB4, BCR,
CSF3R, RET, PDGFRA, FRS2
Downstream:
JAK-STAT signaling: JAK1, JAK2, STAT3, STAT5A
Phospholipase signaling: PLCG2
PI3K signaling: PIK3R1
Negative regulators: CBLB, CBL, INPPL1, IRS1
C
HR = 2.8, ***P = 0.004
PFS fraction
Months
All (106)
NeST:89 activity ≤ 0 (74)
NeST:89 activity > 0 (32)
D
NeST:89
ERBB2
EGFR
CBL
PIK3R1
RET
CSF3R
STAT5A
JAK1
IRS1
PLCG2
EGF
PTPN11
INPPL1
CBLB
ERBB3
FRS2
STAT3
BCR
PDGFRA
JAK2
ERBB4
BARD1
TOP2A
C-index
Alteration frequency (%)
F
JAK2
ERBB2
EGFR
PDGFRA
ERBB4
CBL
CBLB
IRS1
Logical
OR
Logical
Negation
Resistance to
cisplatin
E
Genes in
NeST:89
CESC with NeST:89 activity ≤ 0
CESC with NeST:89 activity > 0
Genetic alteration
Amplification
Deletion
Mutation
PFS status
1:Progression
0:Censored
PFS months
150
100
50
0
PFS status
PFS months

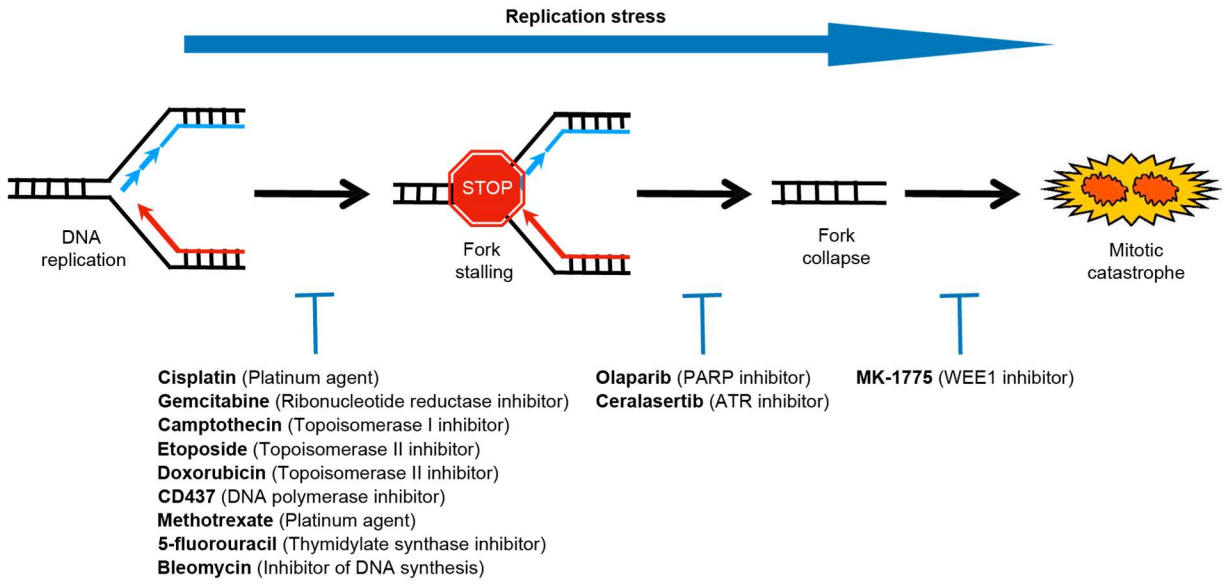

Supplementary Figure 4.1: Replication stress addressed by cancer therapeutics.

Cancer therapeutics can invoke diverse mechanisms to induce RS. Shown are nine conventional chemotherapeutics disrupting DNA integrity or replication (left), along with three inhibitors targeting DNA damage repair signaling cascades (middle and right).

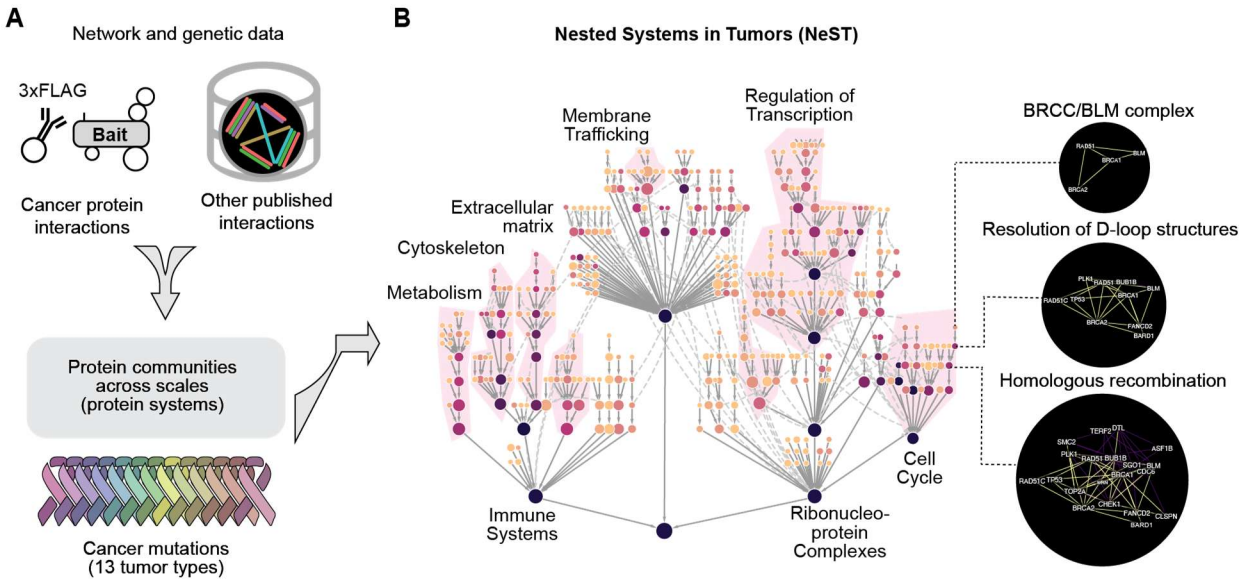

Supplementary Figure 4.2: Nested systems in tumors (NeST).

A, Workflow depicting construction of the NST hierarchy of protein assemblies in tumor cells. AP-MS data from 61 cancer protein baits were integrated with a compendium of published protein interaction data to produce an integrated protein network. **B**, Community detection identified nested protein assemblies inside the network. Protein assemblies under mutational selection pressure were identified, producing the NeST hierarchical map.

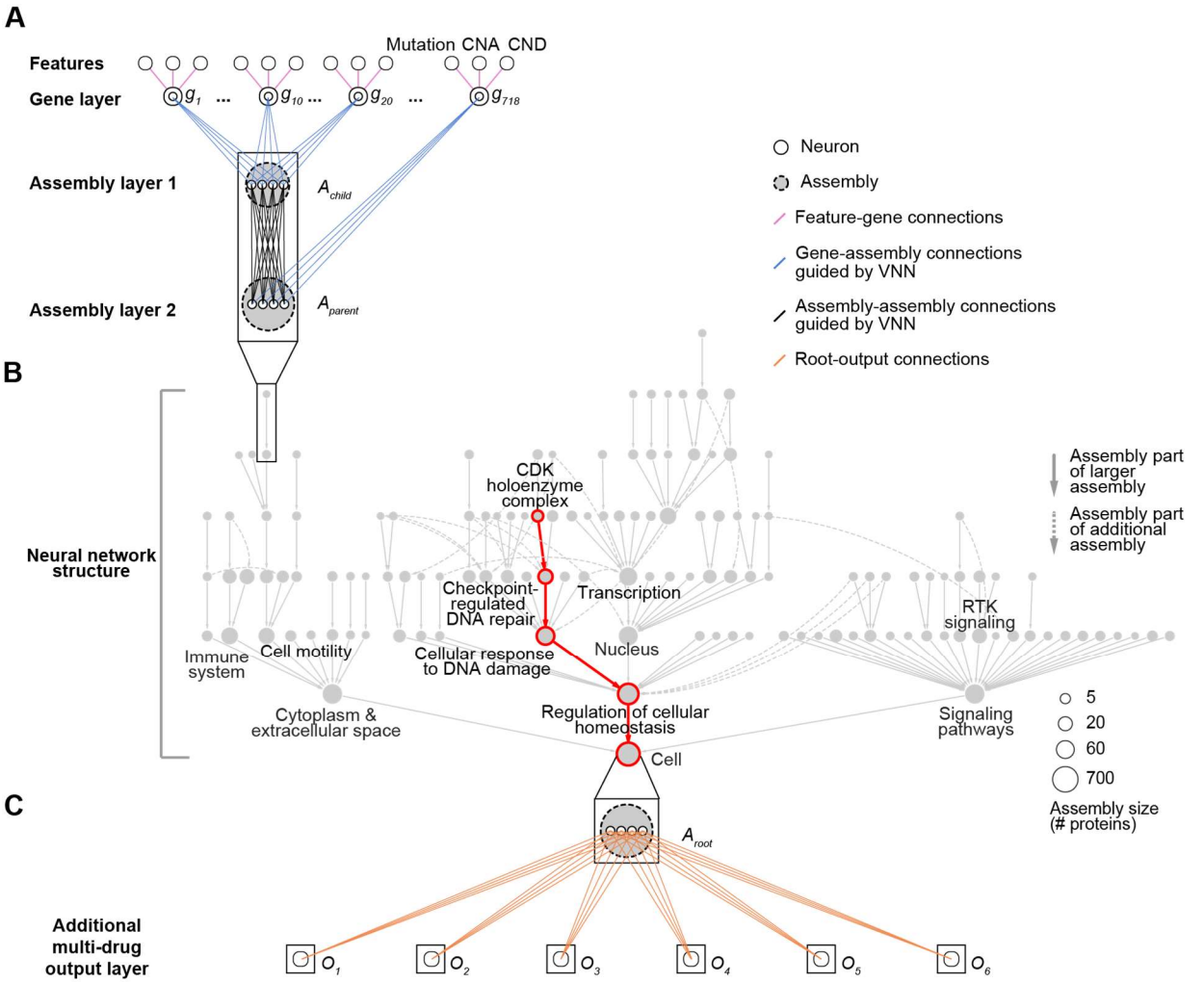

Supplementary Figure 4.3: VNN schematic.

A, The first layer of a VNN incorporates gene-level features, including gene mutations, copy number amplifications (CNA), and copy number deletions (CND). Subsequent layers aggregate gene-level features into assembly-level information, guided by the hierarchical relationships defined by the NeST map. The output state of each gene (g) and assembly (A) is represented by artificial neurons (one neuron per gene, multiple neurons per assembly). Hierarchical gene-to-assembly and assembly-to-assembly connections are assigned weights that are optimized during neural network training. **B**, Position of the assemblies detailed in panel (A) within the greater NeST map. Each node indicates a protein assembly. An example path of information flow, from the neurons of CDK holoenzyme complex to Cell cycle through to model Root, is shown in red. **C**, The additional layer in the multi-task (multi-drug) model enables a single model to be trained for multiple related agents by transforming the state of the Root into multiple outputs, one for each drug of interest. Apart from this final layer, all neural network weights are shared across drugs, yielding potential boosts in predictive power and model interpretation.

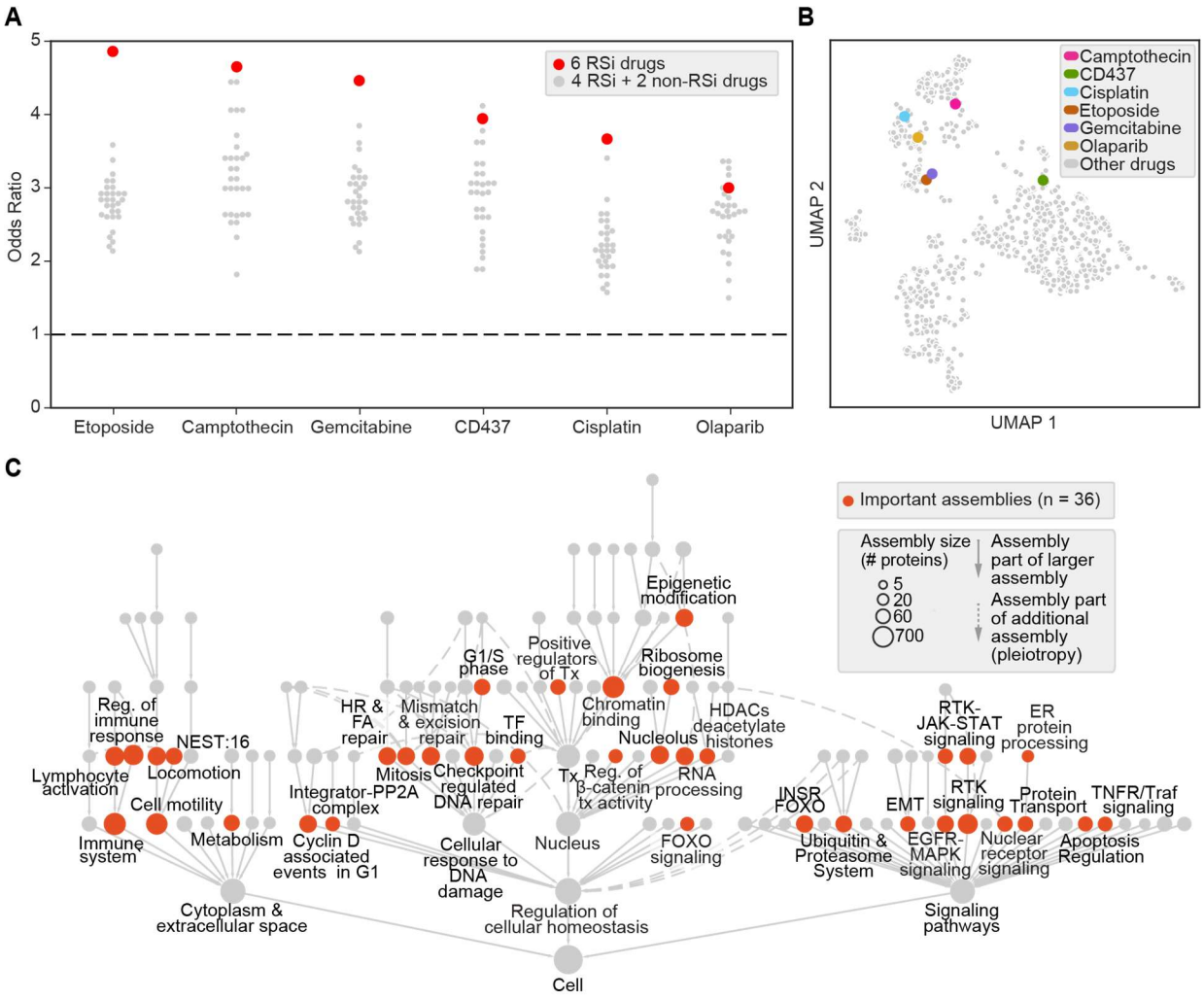

Supplementary Figure 4.4: Performance and interpretation of the multi-drug VNN.

A, Accuracy of the multi-drug VNN (odds ratio, y-axis) in predicting the cellular response to each of six RSi drugs (x-axis). The multi-drug VNN trained on six RSi drugs (red points) is compared to alternate multi-drug VNNs trained on combinations of RSi and non-RSi drugs (gray points). **B**, UMAP projection of drugs based on the response profiles across cell lines profiled in GDSC and CTRP. Note that all RSi drugs, save for CD437, cluster in the top left quadrant, indicating similarity in their response profiles across cell lines, with gemcitabine and etoposide showing particularly high similarity. **C**, System importance (SI) profile for the unified multi-drug VNN. The number of important assemblies is indicated in parentheses for multi-drug model.

Supplementary Figure 4.5: Evaluation of assemblies by systematic drug sensitivity screens.

A, Assemblies are analyzed for their enrichment for CRISPR/Cas9 gene knockouts that affect sensitivity to an RSi drug in either direction (increased or decreased sensitivity). Genetic screen and scoring by Olivieri et al. (47). **B**, Percent of assemblies enriched in drug sensitivity screens, shown separately for assemblies important to RSi drug models (left) versus all others (right). Error bars display the standard error of the proportion. ***P < 0.01; P-value by two sample z-test. **C**, Percent of important assemblies in single-drug VNN models enriched in each individual drug sensitivity screen. **D**, NeST assemblies ranked by their degree of enrichment in cisplatin screen, from most to least significant. Assemblies with FDR < 0.1 are highlighted in red. **E**, NeST assemblies ranked by their degree of enrichment in etoposide screen, from most to least significant. Assemblies with FDR < 0.1 are highlighted in red. **F**, NeST assemblies ranked by their degree of enrichment in camptothecin screen, from most to least significant. Assemblies with FDR < 0.1 are highlighted in red. **G**, NeST assemblies ranked by their degree of enrichment in CD437 screen, from most to least significant. Assemblies with FDR < 0.1 are highlighted in red. **H**, NeST assemblies ranked by their degree of enrichment in olaparib screen, from most to least significant. Assemblies with FDR < 0.1 are highlighted in red. **I**, NeST assemblies ranked by their degree of enrichment in gemcitabine screen, from most to least significant. Assemblies with FDR < 0.1 are highlighted in red. In panels D-I, selected RSi assemblies were labeled. **J**, Mean importance scores for assemblies enriched in one or more drug sensitivity screens (union from panels D-I, N = 61), shown separately for RSi (left) and non-RSi drug models (right). ***P < 0.01; P-value by Mann-Whitney U test. **K**, Mean importance scores for assemblies validated in functional screens, shown separately for RSi (left) and non-RSi drug models (right). ***P < 0.01; P-value by Mann-Whitney U test.

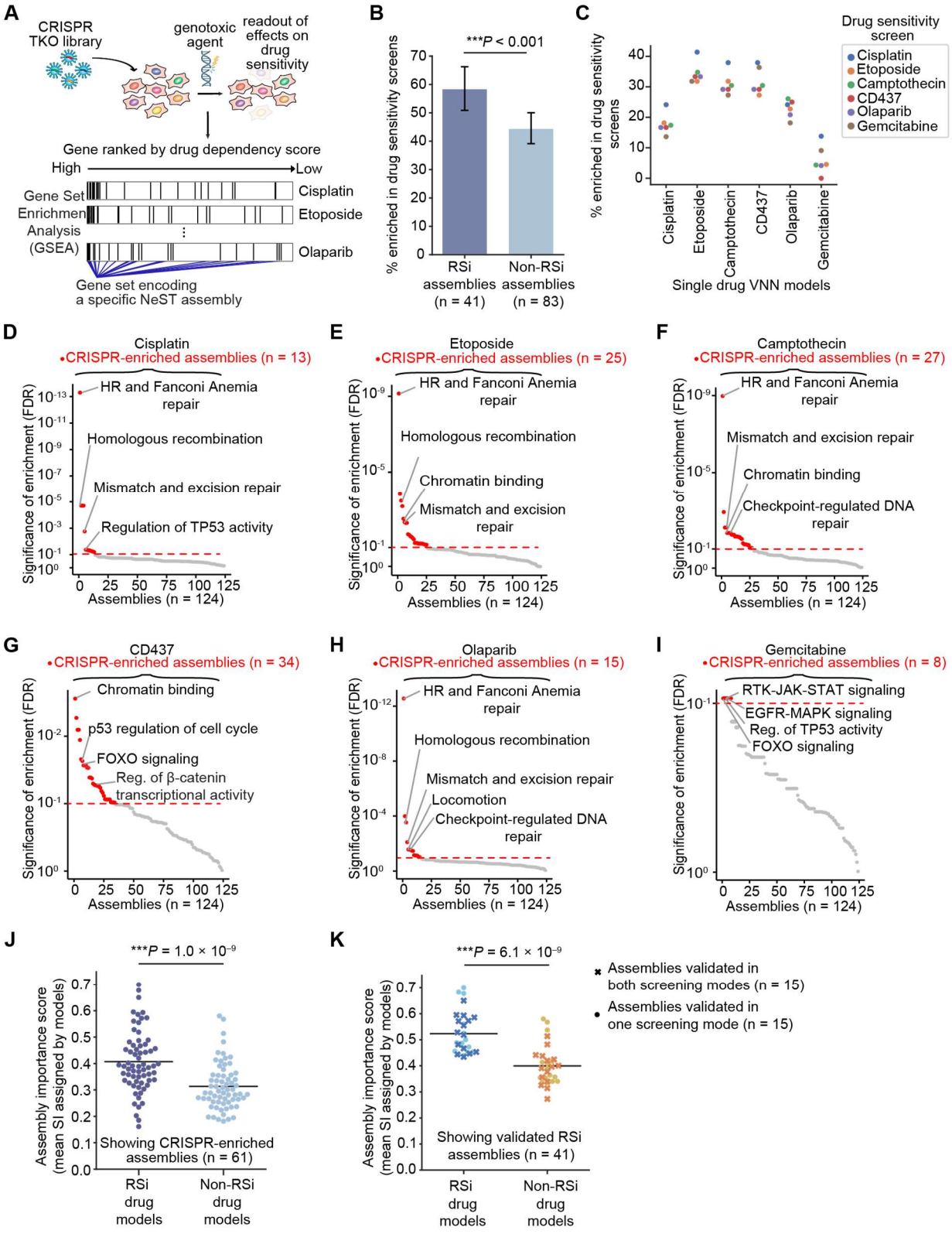
A
CRISPR TKO library
genotoxic agent
readout of effects on drug sensitivity
Gene ranked by drug dependency score
High
Low
Gene Set Enrichment Analysis (GSEA)
Cisplatin
Etoposide
Olaparib
Gene set encoding a specific NeST assembly
B
***P < 0.001
% enriched in drug sensitivity screens
RSi assemblies (n = 41)
Non-RSi assemblies (n = 83)
C
% enriched in drug sensitivity screens
Drug sensitivity screen
Cisplatin
Etoposide
Camptothecin
CD437
Olaparib
Gemcitabine
Single drug VNN models
D
Cisplatin
•CRISPR-enriched assemblies (n = 13)
HR and Fanconi Anemia repair
Homologous recombination
Mismatch and excision repair
Regulation of TP53 activity
Significance of enrichment (FDR)
Assemblies (n = 124)
E
Etoposide
•CRISPR-enriched assemblies (n = 25)
HR and Fanconi Anemia repair
Homologous recombination
Chromatin binding
Mismatch and excision repair
F
Camptothecin
•CRISPR-enriched assemblies (n = 27)
HR and Fanconi Anemia repair
Mismatch and excision repair
Chromatin binding
Checkpoint-regulated DNA repair
G
CD437
•CRISPR-enriched assemblies (n = 34)
Chromatin binding
p53 regulation of cell cycle
FOXO signaling
Reg. of β-catenin transcriptional activity
H
Olaparib
•CRISPR-enriched assemblies (n = 15)
HR and Fanconi Anemia repair
Homologous recombination
Mismatch and excision repair
Locomotion
Checkpoint-regulated DNA repair
I
Gemcitabine
•CRISPR-enriched assemblies (n = 8)
RTK-JAK-STAT signaling
EGFR-MAPK signaling
Reg. of TP53 activity
FOXO signaling
J
***P = 1.0 × 10⁻⁹
Assembly importance score (mean SI assigned by models)
Showing CRISPR-enriched assemblies (n = 61)
RSi drug models
Non-RSi drug models
K
***P = 6.1 × 10⁻⁹
Assembly importance score (mean SI assigned by models)
Showing validated RSi assemblies (n = 41)
RSi drug models
Non-RSi drug models
Assemblies validated in both screening modes (n = 15)
Assemblies validated in one screening mode (n = 15)

Supplementary Figure 4.6: Survival analysis of cisplatin-treated TCGA cohorts.

A–C, Kaplan-Meier progression-free survival (PFS) plots are shown for cisplatin-treated vs. non-cisplatin-treated patients from the TCGA head-and-neck squamous cell carcinoma (HNSC, panel A), lung adenocarcinoma (LUAD, B) and ovarian carcinoma (OV, C) cohorts. None of these panels show significant effects of cisplatin on PFS (all $P > 0.1$). **D**, Kaplan-Meier PFS plots for HNSC, OV, and LUAD patients stratified by the cisplatin VNN prediction status. **E**, Kaplan-Meier PFS plots for CESC and LUSC patients stratified by the cisplatin VNN prediction status. **F**, Swarmplot showing the predictive performance (C-index) of assemblies in response to cisplatin in patients with CESC. Assemblies are grouped into the 83 non-RSi assemblies, 41 RSi assemblies, 30 assemblies validated in at least one screening mode and 15 assemblies validated in both screening modes (from left to right). ***$P < 0.01$; *$P < 0.1$; P-value by Mann-Whitney U test. **G**, Performance comparison of 12 RSi drug models and 33 non-RSi drug models predicting response to cisplatin-treated patients with CESC. Performance measured by concordance index (C-index); **$P < 0.05$; P-value by Mann-Whitney U test. For all Kaplan-Meier plots, sensitive versus resistant shown respectively by blue versus orange; **$P < 0.05$; P-value by log-rank test.

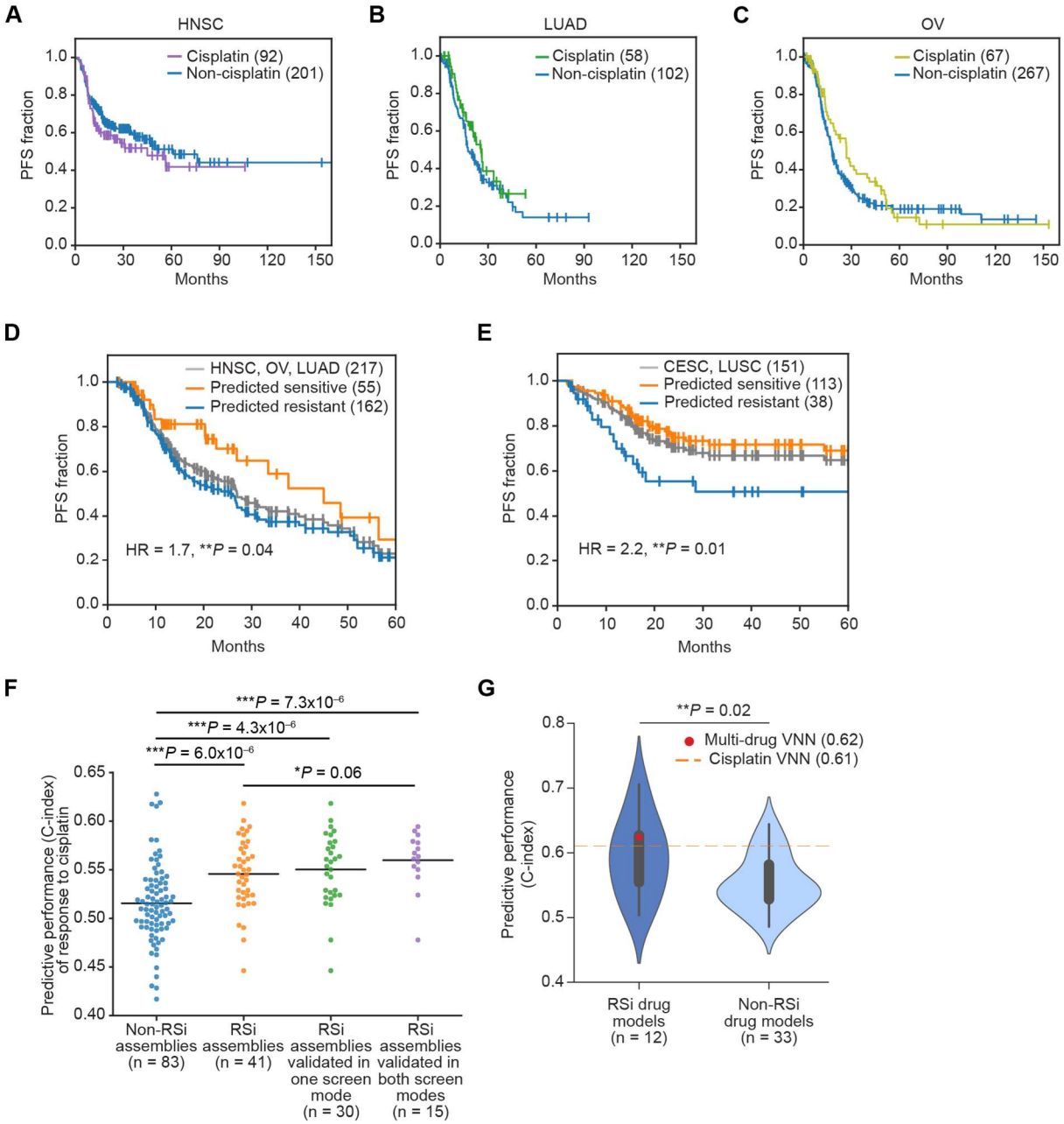
A
HNSC
Cisplatin (92)
Non-cisplatin (201)
PFS fraction
Months
B
LUAD
Cisplatin (58)
Non-cisplatin (102)
C
OV
Cisplatin (67)
Non-cisplatin (267)
D
HNSC, OV, LUAD (217)
Predicted sensitive (55)
Predicted resistant (162)
HR = 1.7, **P = 0.04
E
CESC, LUSC (151)
Predicted sensitive (113)
Predicted resistant (38)
HR = 2.2, **P = 0.01
F
***P = 7.3x10⁻⁶
***P = 4.3x10⁻⁶
***P = 6.0x10⁻⁶
*P = 0.06
Predictive performance (C-index) of response to cisplatin
Non-RSi assemblies (n = 83)
RSi assemblies (n = 41)
RSi assemblies validated in one screen mode (n = 30)
RSi assemblies validated in both screen modes (n = 15)
G
**P = 0.02
Multi-drug VNN (0.62)
Cisplatin VNN (0.61)
Predictive performance (C-index)
RSi drug models (n = 12)
Non-RSi drug models (n = 33)

4.7 Tables

Table 4.1: Annotation of NeST assemblies.

NeST ID	Annotation
NeST	Cell
NeST:1	Signaling pathways
NeST:10	Chromatin binding
NeST:102	CDK holoenzyme complex II
NeST:104	MAPK and MAP2K activation
NeST:105	Ubiquitin regulation of p53 activity
NeST:107	HDACs deacetylate histones
NeST:108	EMT
NeST:11	Metabolic pathways
NeST:110	CDK holoenzyme complex I
NeST:112	Transcription factor (TF) binding
NeST:117	Regulation of TP53 Activity
NeST:119	Regulation of E2F transcription via DREAM complex
NeST:12	Protein Transport
NeST:121	Extended cohesin complex
NeST:123	PML body
NeST:125	Extended mismatch repair complex
NeST:126	Regulation of beta catenin transcriptional activity
NeST:127	Fas
NeST:129	BAF (SWI/SNF) complex
NeST:13	Ribosome biogenesis
NeST:130	Homologous recombination
NeST:132	Cell Proliferation
NeST:133	Histone methyltransferase subcomplex
NeST:134	RPA complex associated proteins
NeST:137	mTOR regulation of autophagy/ribosome biogenesis
NeST:138	PIK3/AKT signaling
NeST:14	Locomotion
NeST:142	Regulation of adherens junction stability
NeST:145	mTOR regulation of mRNA translation
NeST:146	SMAD-TGFbeta signaling
NeST:15	Cellular response to DNA damage
NeST:150	G1 to S cell cycle control
NeST:153	EGFR/PI3K signaling
NeST:155	H3 acetylation and H3K4 methylation crosstalk
NeST:158	Histone modifications in DNA damage response
NeST:16	NeST:16
NeST:163	NeST:163
NeST:165	Transcription coactivator activity
NeST:168	Foxo signaling
NeST:169	Neg Regulation EGFR
NeST:17	RNA processing
NeST:170	Phosphatase 2A catalytic subunit
NeST:174	Wnt/beta-catenin
NeST:177	p53 regulation of cell cycle
NeST:18	Regulation of immune responses
NeST:182	Regulation of beta catenin transcription
NeST:186	MDM2-p53 pathway

Table 4.1: Annotation of NeST assemblies. (Continued)

NeST ID	Annotation
NeST:19	RNA metabolism
NeST:193	Resolution of D-loop structures
NeST:195	NeST:195
NeST:196	Cohesin
NeST:199	Oncogene induced senescence
NeST:2	Cytoplasm/extracellular space
NeST:20	Extracellular matrix organization
NeST:202	MHC class I including non-classical MHCs
NeST:21	Endoplasmic Reticulum protein processing
NeST:210	Regulation of androgen receptor signaling pathway
NeST:212	RAS-RAF-MAPK
NeST:22	Structural constituent of muscle
NeST:221	Beta-catenin
NeST:23	Actin filament-based process
NeST:231	MutS homologs
NeST:239	Beta-catenin destruction complex
NeST:24	Epithelial differentiation
NeST:25	Lymphocyte activation
NeST:254	PI3-K/Akt
NeST:256	MAPK signaling
NeST:26	RNA processing
NeST:27	Contractile fiber
NeST:277	MutL alpha/beta complex
NeST:29	NeST:29
NeST:293	RBL-TP53 complex
NeST:3	Regulation of cellular homeostasis
NeST:30	Mismatch and excision repair
NeST:31	Extracellular matrix
NeST:32	Ubiquitin/Proteasome System
NeST:33	Ribosome abundance control
NeST:34	Epigenetic modification
NeST:35	Spliceosomal complex
NeST:36	Interferon signaling
NeST:38	Transmembrane tyrosine kinase signaling
NeST:39	Regulation of mRNA processing
NeST:4	Nucleus
NeST:40	Actin filaments
NeST:42	Transcription elongation
NeST:43	Type I interferon signaling pathway
NeST:44	Nuclear transport
NeST:45	Mediator/CCR-NOT complex
NeST:47	Apoptosis Regulation
NeST:48	Actin cytoskeleton
NeST:49	NeST:49
NeST:5	Cell motility
NeST:50	Checkpoint-regulated DNA repair
NeST:51	ECM-cytoskeleton assembly
NeST:52	INSR-FOXO
NeST:53	Integrator-PP2A complex
NeST:54	Cell-extracellular matrix interactions
NeST:55	Histone deacetylase binding

Table 4.1: Annotation of NeST assemblies. (Continued)

NeST ID	Annotation
NeST:57	Histone acetyltransferase complex
NeST:58	Cyclin D associated events in G1
NeST:59	Chromosome centrometric region
NeST:6	Transcription
NeST:60	Nuclear receptor signaling
NeST:61	Culin-RIng uniqutin ligase complex
NeST:63	Actin and actin-associated proteins
NeST:65	Mitosis
NeST:66	PcG protein complex
NeST:69	Protein nuclear transport
NeST:7	Metabolism
NeST:70	Regulation of nuclear protein ubiquitiation
NeST:73	EGFR-MAPK signaling
NeST:77	Ubiquitin regulation of mitophagy
NeST:78	NeST:78
NeST:79	Homologous recombination (HR) and Fanconi Anemia repair
NeST:8	Immune system
NeST:80	NeST:80
NeST:81	TGF-beta/Smad signaling
NeST:82	Extended PRC1 complex
NeST:83	TNFR/Traf signaling
NeST:84	Lymphoid JAK/STAT signaling
NeST:85	Positive regulators of transcription
NeST:89	RTK-JAK-STAT signaling
NeST:9	Nucleolus
NeST:90	Mediator complex
NeST:91	G1/S phase
NeST:92	Polybromo- and BAF containing complex
NeST:93	Nuclear pore
NeST:94	p53 regulation
NeST:97	Cell projection morphogenesis
NeST:98	Histone methyltransferase complex

Table 4.2: Odds ratio for 45 drug response predictions with multi-drug model.

Drug	Odds Ratio	SD (Odds ratio)
MK-1775	4.11	0.22
5-fluorouracil	3.69	0.47
Ceralasertib	3.31	0.46
Bleomycin-a2	2.97	0.37
Doxorubicin	2.67	0.29
Methotrexate	2.21	0.04
Etoposide**	4.86	1.73
Gemcitabine**	4.46	1.56
Olaparib**	3	1.01
CD437**	3.94	1.65
Cisplatin**	3.67	1.42
Camptothecin**	4.65	2.01
Manumycin-A	3.61	0.3
Daporinad	3.52	0.34
ML-210	3.01	0.53
200484-11-3	2.96	0.11
STF-31	2.96	0.33
Navitoclax	2.48	0.31
Rapamycin	2.41	0.1
GPP78	2.38	0.04
Temsirolimus	2.14	0.17
ERASTIN	2.14	0.06
BRD-K41087962	2.12	0.35
Aacocf3	2.02	0.1
BRD-K85563610	1.97	0.18
BRD6708	1.96	0.18
MK-2206	1.93	0.09
ML320	1.86	0.23
Ursolic-acid	1.73	0.46
1170689-68-5	1.65	0.12
SpOx1_002925	1.44	0.11
Canertinib	1.36	0.15
Parthenolide	1.33	0.15
Ro-28-1675	1.28	0.2
Compound-10b	1.25	0.18
CHEBI:94110	1.25	0.1
Bosutinib	1.18	0.04
CI-976	1.11	0.1
PIK-75	0.83	0.05
Trametinib	0.78	0.06
Afatinib	0.76	0.03
Crizotinib	0.74	0.02
Austocystin-D	0.74	0.08
Gefitinib	0.67	0.01
Paclitaxel	2.14	0.17

** Discovery RSi drugs.

Table 4.3: Importance of assemblies in VNN models.

NeST ID	Single-drug VNN of discovery RSi drugs						Multi-drug	Single-drug VNN of test RSi drugs					
	D1	D2	D3	D4	D5	D6		D7	D8	D9	D10	D11	D12
NeST:10	0.71	0.69	0.72	0.72	0.72	0.66	0.74	0.65	0.71	0.70	0.72	0.65	0.70
NeST:102	0.43	0.40	0.43	0.46	0.44	0.47	0.43	0.34	0.45	0.33	0.50	0.38	0.31
NeST:104	0.45	0.44	0.41	0.44	0.48	0.45	0.50	0.37	0.43	0.50	0.39	0.38	0.47
NeST:105	0.38	0.34	0.25	0.39	0.40	0.39	0.32	0.28	0.35	0.33	0.36	0.31	0.46
NeST:107	0.38	0.42	0.44	0.47	0.44	0.45	0.54	0.43	0.38	0.48	0.46	0.37	0.43
NeST:108	0.48	0.43	0.46	0.36	0.44	0.46	0.50	0.48	0.30	0.46	0.46	0.36	0.46
NeST:11	0.38	0.41	0.37	0.34	0.41	0.33	0.42	0.34	0.40	0.47	0.28	0.36	0.44
NeST:110	0.39	0.38	0.41	0.37	0.43	0.44	0.41	0.41	0.45	0.33	0.49	0.37	0.30
NeST:112	0.55	0.58	0.53	0.55	0.53	0.48	0.60	0.47	0.50	0.58	0.55	0.40	0.50
NeST:117	0.47	0.41	0.50	0.41	0.50	0.44	0.49	0.50	0.51	0.41	0.44	0.34	0.48
NeST:119	0.34	0.40	0.41	0.39	0.42	0.36	0.43	0.39	0.38	0.39	0.45	0.36	0.34
NeST:12	0.48	0.51	0.53	0.56	0.50	0.53	0.58	0.40	0.49	0.47	0.49	0.32	0.46
NeST:121	0.27	0.18	0.23	0.16	0.28	0.24	0.25	0.22	0.22	0.10	0.17	0.11	0.21
NeST:123	0.41	0.43	0.41	0.44	0.42	0.40	0.47	0.42	0.43	0.52	0.42	0.37	0.48
NeST:125	0.30	0.33	0.24	0.30	0.30	0.31	0.38	0.28	0.28	0.37	0.34	0.24	0.35
NeST:126	0.52	0.44	0.49	0.47	0.54	0.48	0.50	0.50	0.39	0.53	0.51	0.25	0.52
NeST:127	0.30	0.31	0.38	0.29	0.36	0.34	0.32	0.39	0.36	0.34	0.31	0.28	0.26
NeST:129	0.34	0.31	0.37	0.31	0.37	0.31	0.35	0.30	0.28	0.41	0.30	0.28	0.43
NeST:13	0.48	0.40	0.38	0.50	0.49	0.46	0.52	0.48	0.45	0.39	0.45	0.38	0.45
NeST:130	0.44	0.40	0.50	0.35	0.54	0.42	0.44	0.53	0.46	0.44	0.42	0.41	0.46
NeST:132	0.39	0.38	0.36	0.45	0.38	0.43	0.46	0.48	0.43	0.40	0.45	0.41	0.48
NeST:133	0.29	0.27	0.36	0.29	0.33	0.32	0.33	0.30	0.32	0.36	0.38	0.22	0.32
NeST:134	0.35	0.31	0.40	0.24	0.37	0.37	0.36	0.31	0.27	0.30	0.29	0.23	0.31
NeST:137	0.40	0.34	0.47	0.39	0.40	0.39	0.48	0.31	0.39	0.40	0.40	0.24	0.43
NeST:138	0.34	0.29	0.29	0.31	0.33	0.35	0.30	0.24	0.24	0.34	0.30	0.27	0.34
NeST:14	0.61	0.62	0.59	0.62	0.59	0.59	0.70	0.52	0.61	0.55	0.62	0.51	0.58
NeST:142	0.42	0.39	0.39	0.35	0.35	0.36	0.44	0.42	0.31	0.40	0.40	0.28	0.40
NeST:145	0.30	0.23	0.29	0.25	0.24	0.28	0.35	0.19	0.27	0.32	0.28	0.22	0.31
NeST:146	0.31	0.40	0.32	0.33	0.35	0.32	0.38	0.32	0.20	0.36	0.33	0.16	0.31
NeST:150	0.36	0.37	0.41	0.38	0.42	0.43	0.40	0.33	0.41	0.30	0.50	0.36	0.25
NeST:153	0.43	0.40	0.45	0.35	0.46	0.38	0.48	0.47	0.32	0.48	0.44	0.36	0.40
NeST:155	0.39	0.33	0.38	0.37	0.37	0.30	0.38	0.33	0.38	0.40	0.32	0.38	0.38
NeST:158	0.29	0.28	0.29	0.29	0.25	0.25	0.26	0.31	0.24	0.33	0.28	0.24	0.29
NeST:16	0.51	0.39	0.55	0.41	0.51	0.51	0.52	0.50	0.55	0.38	0.44	0.34	0.47
NeST:163	0.22	0.22	0.32	0.24	0.26	0.27	0.34	0.20	0.24	0.34	0.23	0.24	0.32
NeST:165	0.34	0.32	0.37	0.36	0.39	0.39	0.38	0.29	0.31	0.27	0.40	0.29	0.20
NeST:168	0.48	0.47	0.46	0.44	0.52	0.42	0.51	0.38	0.30	0.52	0.40	0.34	0.49
NeST:169	0.41	0.36	0.37	0.36	0.32	0.28	0.43	0.31	0.34	0.43	0.37	0.31	0.38
NeST:17	0.62	0.54	0.55	0.54	0.58	0.54	0.63	0.55	0.59	0.49	0.53	0.52	0.53
NeST:170	0.33	0.28	0.41	0.34	0.37	0.35	0.35	0.30	0.33	0.27	0.35	0.18	0.31
NeST:174	0.36	0.33	0.39	0.38	0.35	0.35	0.43	0.33	0.24	0.44	0.40	0.27	0.36
NeST:177	0.40	0.46	0.44	0.53	0.45	0.41	0.49	0.42	0.47	0.45	0.52	0.34	0.39
NeST:18	0.63	0.57	0.57	0.63	0.61	0.67	0.67	0.60	0.56	0.52	0.64	0.53	0.52
NeST:182	0.35	0.27	0.26	0.28	0.35	0.37	0.37	0.32	0.22	0.36	0.34	0.17	0.38
NeST:186	0.37	0.37	0.45	0.31	0.47	0.41	0.40	0.45	0.41	0.39	0.37	0.34	0.37
NeST:19	0.43	0.44	0.36	0.47	0.43	0.36	0.44	0.40	0.47	0.41	0.46	0.40	0.38
NeST:193	0.35	0.33	0.36	0.25	0.42	0.35	0.35	0.41	0.42	0.40	0.21	0.37	0.40
NeST:195	0.37	0.32	0.43	0.32	0.48	0.45	0.40	0.32	0.32	0.27	0.35	0.23	0.30
NeST:196	0.25	0.14	0.19	0.12	0.23	0.20	0.20	0.14	0.17	0.09	0.14	0.09	0.14

Table 4.3: Importance of assemblies in VNN models. (Continued)

NeST ID	Single-drug VNN of discovery RSi drugs						Multi-drug	Single-drug VNN of test RSi drugs					
	D1	D2	D3	D4	D5	D6		D7	D8	D9	D10	D11	D12
NeST:199	0.28	0.37	0.37	0.25	0.39	0.32	0.41	0.37	0.34	0.38	0.42	0.33	0.29
NeST:20	0.40	0.33	0.36	0.38	0.36	0.40	0.40	0.37	0.40	0.31	0.36	0.38	0.39
NeST:202	0.09	0.16	0.07	0.20	0.15	0.16	0.16	0.14	0.15	0.16	0.19	0.12	0.18
NeST:21	0.41	0.47	0.46	0.51	0.43	0.43	0.53	0.32	0.39	0.39	0.43	0.21	0.35
NeST:210	0.28	0.36	0.34	0.43	0.30	0.27	0.42	0.30	0.32	0.40	0.39	0.21	0.27
NeST:212	0.38	0.33	0.37	0.34	0.33	0.33	0.40	0.26	0.37	0.41	0.26	0.33	0.28
NeST:22	0.32	0.22	0.33	0.22	0.29	0.32	0.30	0.29	0.35	0.22	0.26	0.15	0.31
NeST:221	0.28	0.30	0.18	0.21	0.26	0.33	0.22	0.28	0.22	0.33	0.24	0.21	0.40
NeST:23	0.34	0.30	0.38	0.25	0.32	0.40	0.41	0.32	0.35	0.35	0.33	0.31	0.27
NeST:231	0.25	0.25	0.24	0.22	0.22	0.26	0.29	0.22	0.24	0.28	0.31	0.12	0.31
NeST:239	0.25	0.27	0.20	0.24	0.24	0.24	0.26	0.19	0.16	0.35	0.15	0.20	0.28
NeST:24	0.33	0.28	0.33	0.24	0.34	0.34	0.34	0.29	0.20	0.25	0.25	0.23	0.34
NeST:25	0.49	0.54	0.41	0.56	0.52	0.55	0.55	0.45	0.40	0.43	0.55	0.39	0.46
NeST:254	0.31	0.34	0.29	0.31	0.30	0.33	0.36	0.30	0.24	0.25	0.29	0.28	0.29
NeST:256	0.34	0.28	0.28	0.35	0.37	0.39	0.37	0.28	0.24	0.34	0.28	0.20	0.33
NeST:26	0.41	0.42	0.36	0.45	0.39	0.30	0.44	0.43	0.39	0.44	0.41	0.41	0.37
NeST:27	0.32	0.22	0.32	0.20	0.29	0.31	0.29	0.28	0.32	0.21	0.23	0.14	0.26
NeST:277	0.31	0.30	0.27	0.18	0.29	0.26	0.30	0.23	0.24	0.28	0.33	0.18	0.33
NeST:29	0.40	0.31	0.41	0.38	0.42	0.43	0.40	0.44	0.45	0.37	0.38	0.33	0.41
NeST:293	0.31	0.32	0.42	0.36	0.35	0.33	0.35	0.28	0.31	0.30	0.39	0.26	0.17
NeST:30	0.56	0.57	0.62	0.60	0.65	0.63	0.65	0.60	0.55	0.51	0.61	0.51	0.54
NeST:31	0.31	0.26	0.31	0.28	0.33	0.31	0.32	0.33	0.30	0.28	0.25	0.32	0.33
NeST:32	0.50	0.50	0.53	0.48	0.53	0.55	0.54	0.48	0.57	0.49	0.56	0.45	0.57
NeST:33	0.50	0.44	0.42	0.45	0.44	0.49	0.49	0.41	0.45	0.46	0.32	0.37	0.46
NeST:34	0.58	0.58	0.54	0.63	0.56	0.54	0.63	0.52	0.57	0.55	0.59	0.50	0.50
NeST:35	0.23	0.20	0.27	0.18	0.22	0.15	0.20	0.25	0.20	0.11	0.17	0.15	0.07
NeST:36	0.21	0.19	0.23	0.20	0.28	0.24	0.23	0.29	0.28	0.23	0.17	0.22	0.19
NeST:38	0.70	0.70	0.67	0.66	0.70	0.70	0.77	0.68	0.69	0.59	0.69	0.60	0.65
NeST:39	0.29	0.28	0.25	0.33	0.22	0.22	0.29	0.24	0.21	0.18	0.33	0.19	0.22
NeST:40	0.32	0.26	0.37	0.22	0.32	0.35	0.36	0.30	0.30	0.34	0.27	0.31	0.27
NeST:42	0.39	0.34	0.47	0.29	0.39	0.40	0.43	0.38	0.34	0.44	0.30	0.24	0.40
NeST:43	0.17	0.15	0.20	0.17	0.21	0.20	0.20	0.23	0.22	0.14	0.16	0.19	0.18
NeST:44	0.33	0.25	0.34	0.27	0.24	0.39	0.37	0.21	0.30	0.30	0.23	0.19	0.27
NeST:45	0.33	0.25	0.19	0.31	0.35	0.25	0.29	0.31	0.32	0.36	0.31	0.23	0.25
NeST:47	0.50	0.54	0.53	0.51	0.44	0.49	0.50	0.48	0.42	0.46	0.50	0.36	0.38
NeST:48	0.24	0.21	0.30	0.16	0.22	0.30	0.29	0.10	0.21	0.20	0.15	0.17	0.18
NeST:49	0.24	0.18	0.22	0.28	0.29	0.26	0.29	0.28	0.33	0.34	0.26	0.29	0.34
NeST:5	0.70	0.71	0.69	0.68	0.69	0.71	0.76	0.65	0.71	0.58	0.72	0.57	0.70
NeST:50	0.65	0.64	0.66	0.67	0.68	0.62	0.68	0.65	0.63	0.67	0.70	0.56	0.64
NeST:51	0.31	0.20	0.26	0.26	0.27	0.29	0.29	0.30	0.27	0.25	0.24	0.26	0.30
NeST:52	0.49	0.47	0.54	0.45	0.56	0.53	0.53	0.44	0.44	0.53	0.54	0.35	0.51
NeST:53	0.51	0.41	0.47	0.50	0.42	0.44	0.52	0.45	0.45	0.41	0.45	0.36	0.46
NeST:54	0.26	0.20	0.25	0.14	0.28	0.25	0.27	0.20	0.19	0.24	0.14	0.19	0.22
NeST:55	0.47	0.52	0.43	0.57	0.48	0.41	0.49	0.42	0.45	0.50	0.52	0.43	0.38
NeST:57	0.42	0.34	0.37	0.36	0.43	0.49	0.45	0.35	0.34	0.38	0.32	0.33	0.41
NeST:58	0.48	0.51	0.52	0.55	0.51	0.51	0.53	0.49	0.52	0.44	0.61	0.43	0.41
NeST:59	0.37	0.42	0.42	0.41	0.46	0.40	0.48	0.38	0.35	0.35	0.50	0.31	0.33
NeST:60	0.41	0.44	0.50	0.51	0.48	0.50	0.55	0.41	0.45	0.50	0.52	0.38	0.43
NeST:61	0.42	0.39	0.36	0.36	0.43	0.42	0.42	0.36	0.34	0.39	0.34	0.34	0.48

Table 4.3: Importance of assemblies in VNN models. (Continued)

NeST ID	Single-drug VNN of discovery RSi drugs						Multi-drug	Single-drug VNN of test RSi drugs					
	D1	D2	D3	D4	D5	D6		D7	D8	D9	D10	D11	D12
NeST:63	0.27	0.22	0.36	0.13	0.26	0.29	0.34	0.20	0.28	0.24	0.23	0.24	0.21
NeST:65	0.55	0.60	0.60	0.61	0.60	0.56	0.63	0.61	0.57	0.61	0.70	0.49	0.60
NeST:66	0.37	0.32	0.34	0.36	0.31	0.32	0.40	0.29	0.34	0.30	0.35	0.33	0.30
NeST:69	0.33	0.25	0.35	0.30	0.17	0.37	0.38	0.21	0.26	0.31	0.21	0.21	0.28
NeST:7	0.46	0.47	0.50	0.39	0.49	0.42	0.51	0.37	0.50	0.49	0.43	0.40	0.45
NeST:70	0.45	0.46	0.49	0.44	0.51	0.44	0.50	0.50	0.47	0.40	0.48	0.33	0.45
NeST:73	0.51	0.54	0.53	0.48	0.55	0.54	0.58	0.51	0.54	0.53	0.51	0.50	0.54
NeST:77	0.38	0.33	0.22	0.40	0.35	0.36	0.30	0.24	0.36	0.32	0.38	0.17	0.44
NeST:78	0.35	0.37	0.38	0.35	0.39	0.38	0.44	0.28	0.33	0.36	0.37	0.27	0.42
NeST:79	0.55	0.57	0.63	0.58	0.63	0.60	0.63	0.58	0.53	0.47	0.57	0.52	0.55
NeST:8	0.66	0.67	0.66	0.70	0.65	0.71	0.73	0.62	0.61	0.61	0.66	0.59	0.63
NeST:80	0.19	0.15	0.21	0.26	0.29	0.27	0.24	0.24	0.30	0.31	0.19	0.27	0.33
NeST:81	0.37	0.38	0.38	0.28	0.40	0.37	0.38	0.31	0.25	0.38	0.26	0.16	0.33
NeST:82	0.34	0.27	0.28	0.35	0.29	0.29	0.35	0.29	0.32	0.28	0.35	0.29	0.30
NeST:83	0.46	0.53	0.48	0.49	0.40	0.49	0.54	0.44	0.33	0.39	0.55	0.31	0.38
NeST:84	0.37	0.41	0.38	0.40	0.45	0.38	0.39	0.40	0.42	0.44	0.36	0.37	0.41
NeST:85	0.51	0.46	0.53	0.48	0.56	0.55	0.56	0.48	0.46	0.50	0.46	0.43	0.55
NeST:89	0.53	0.50	0.48	0.39	0.52	0.44	0.54	0.51	0.52	0.45	0.51	0.42	0.45
NeST:9	0.59	0.53	0.60	0.57	0.65	0.56	0.64	0.60	0.58	0.54	0.55	0.50	0.54
NeST:90	0.29	0.22	0.16	0.27	0.33	0.24	0.21	0.24	0.28	0.32	0.28	0.26	0.23
NeST:91	0.55	0.56	0.57	0.59	0.60	0.56	0.59	0.58	0.54	0.61	0.67	0.45	0.58
NeST:92	0.39	0.36	0.37	0.27	0.42	0.38	0.39	0.34	0.29	0.42	0.35	0.28	0.48
NeST:93	0.33	0.19	0.34	0.27	0.17	0.34	0.37	0.17	0.24	0.26	0.20	0.19	0.25
NeST:94	0.36	0.28	0.31	0.29	0.46	0.37	0.36	0.34	0.33	0.29	0.28	0.34	0.35
NeST:97	0.32	0.31	0.28	0.26	0.30	0.33	0.34	0.26	0.27	0.28	0.29	0.25	0.28
NeST:98	0.37	0.37	0.41	0.38	0.35	0.39	0.41	0.34	0.37	0.46	0.40	0.32	0.40

D1=Gemcitabine; D2=Etoposide; D3=Olaparib; D4=CD437; D5=Cisplatin; D6=Camptothecin;
D7=Ceralasertib; D8=5-Fluorouracil; D9=Doxorubicin; D10=MK-1775; D11=Bleomycin-a2; D12=Methotrexate.

Table 4.4: Assembly enrichment in replication and drug sensitivity screens.

NeST ID	Significance of enrichment in drug sensitivity screens (FDR)						RRS screen (FDR)
	D1	D2	D3	D4	D5	D6	
NeST:10	0.170	0.003	0.178	0.003	0.253	0.015	0.149
NeST:104	0.170	0.196	0.261	0.466	0.303	0.092	0.219
NeST:107	0.376	0.544	0.376	0.506	0.303	0.225	0.164
NeST:108	0.337	0.242	0.301	0.069	0.427	0.421	0.089
NeST:112	0.242	0.402	0.483	0.484	0.586	0.433	0.066
NeST:117	0.094	0.005	0.151	0.058	0.057	0.025	0.032
NeST:12	0.197	0.262	0.222	0.103	0.057	0.421	0.598
NeST:126	0.395	0.171	0.229	0.054	0.551	0.450	0.105
NeST:13	0.412	0.897	0.904	0.614	0.965	0.869	0.270
NeST:130	0.460	0.000	0.000	0.054	0.000	0.019	0.033
NeST:14	0.213	0.231	0.027	0.103	0.249	0.237	0.066
NeST:16	0.341	0.623	0.541	0.369	0.776	0.566	0.298
NeST:168	0.094	0.063	0.151	0.027	0.174	0.025	0.203
NeST:17	0.197	0.255	0.301	0.042	0.704	0.450	0.066
NeST:177	0.292	0.067	0.313	0.023	0.308	0.340	0.092
NeST:18	0.262	0.962	0.460	0.850	0.859	0.954	0.216
NeST:21	0.376	0.505	0.235	0.295	0.249	0.653	0.270
NeST:25	0.394	1.000	0.490	0.979	0.876	0.954	0.146
NeST:30	0.421	0.005	0.008	0.155	0.002	0.008	0.025
NeST:32	0.171	0.032	0.376	0.052	0.451	0.165	0.029
NeST:34	0.480	0.022	0.151	0.168	0.493	0.023	0.123
NeST:38	0.126	0.234	0.207	0.133	0.319	0.218	0.032
NeST:47	0.262	0.209	0.251	0.197	0.427	0.167	0.153
NeST:5	0.245	0.234	0.138	0.144	0.303	0.318	0.066
NeST:50	0.376	0.062	0.027	0.096	0.071	0.015	0.025
NeST:52	0.197	0.062	0.074	0.158	0.149	0.019	0.130
NeST:53	0.397	0.128	0.285	0.108	0.303	0.218	0.066
NeST:55	0.611	0.062	0.074	0.103	0.501	0.061	0.092
NeST:58	0.480	0.234	0.264	0.116	0.249	0.209	0.048
NeST:60	0.292	0.262	0.098	0.448	0.427	0.285	0.203
NeST:65	0.188	0.162	0.199	0.065	0.255	0.029	0.066
NeST:7	0.126	0.128	0.311	0.700	0.532	0.433	0.096
NeST:70	0.126	0.071	0.079	0.151	0.085	0.059	0.144
NeST:73	0.094	0.262	0.178	0.299	0.208	0.318	0.066
NeST:79	0.197	0.000	0.000	0.029	0.000	0.000	0.066
NeST:8	0.344	0.974	0.666	0.711	0.686	0.914	0.146
NeST:83	0.292	0.137	0.383	0.190	0.208	0.162	0.146
NeST:85	0.392	0.116	0.294	0.117	0.232	0.162	0.164
NeST:89	0.094	0.234	0.158	0.184	0.303	0.408	0.071
NeST:9	0.292	0.449	0.571	0.190	0.808	0.753	0.270
NeST:91	0.401	0.058	0.301	0.086	0.451	0.225	0.073

D1=Gemcitabine; D2=Etoposide; D3=Olaparib; D4=CD437; D5=Cisplatin; D6=Camptothecin;

Table 4.5: Assembly performance in cisplatin-treated cervical cancer.

NeST ID	ci_1	ci_2	ci_3	ci_4	ci_5	mean ci
NeST	0.55	0.60	0.57	0.63	0.59	0.59
NeST:3	0.54	0.56	0.58	0.58	0.53	0.56
NeST:2	0.46	0.55	0.55	0.57	0.56	0.54
NeST:1	0.52	0.59	0.61	0.65	0.61	0.59
NeST:4	0.54	0.57	0.55	0.59	0.57	0.56
NeST:6	0.56	0.56	0.54	0.56	0.53	0.55
NeST:15	0.53	0.53	0.53	0.57	0.49	0.53
NeST:8	0.54	0.54	0.56	0.55	0.55	0.55
NeST:10	0.54	0.54	0.55	0.52	0.49	0.53
NeST:5	0.50	0.54	0.53	0.54	0.51	0.52
NeST:18	0.52	0.53	0.57	0.52	0.54	0.53
NeST:38	0.52	0.56	0.60	0.60	0.59	0.57
NeST:50	0.59	0.58	0.59	0.60	0.59	0.59
NeST:25	0.50	0.55	0.53	0.56	0.54	0.54
NeST:9	0.47	0.58	0.57	0.52	0.55	0.54
NeST:14	0.46	0.50	0.48	0.49	0.46	0.48
NeST:30	0.56	0.58	0.57	0.54	0.55	0.56
NeST:17	0.50	0.54	0.59	0.62	0.58	0.57
NeST:34	0.59	0.59	0.59	0.62	0.55	0.59
NeST:65	0.52	0.53	0.58	0.55	0.56	0.55
NeST:79	0.56	0.57	0.53	0.54	0.51	0.54
NeST:58	0.55	0.51	0.56	0.55	0.47	0.53
NeST:52	0.44	0.47	0.45	0.43	0.45	0.45
NeST:73	0.58	0.62	0.42	0.60	0.59	0.56
NeST:16	0.55	0.58	0.53	0.54	0.57	0.55
NeST:19	0.45	0.52	0.54	0.52	0.45	0.50
NeST:32	0.58	0.57	0.58	0.59	0.61	0.59
NeST:89	0.54	0.58	0.53	0.65	0.60	0.58
NeST:91	0.58	0.58	0.60	0.62	0.59	0.59
NeST:13	0.45	0.50	0.49	0.52	0.50	0.49
NeST:7	0.63	0.63	0.61	0.36	0.57	0.56
NeST:102	0.53	0.53	0.55	0.45	0.55	0.52
NeST:60	0.50	0.52	0.56	0.54	0.50	0.52
NeST:107	0.51	0.47	0.52	0.48	0.49	0.49
NeST:55	0.56	0.53	0.55	0.61	0.54	0.56
NeST:84	0.47	0.48	0.47	0.50	0.49	0.48
NeST:110	0.58	0.59	0.59	0.42	0.59	0.55
NeST:12	0.56	0.51	0.58	0.57	0.51	0.55
NeST:26	0.47	0.55	0.55	0.55	0.47	0.52
NeST:85	0.58	0.50	0.56	0.56	0.53	0.55
NeST:104	0.59	0.62	0.42	0.38	0.59	0.52
NeST:108	0.54	0.58	0.55	0.55	0.55	0.55
NeST:112	0.57	0.51	0.48	0.54	0.52	0.53
NeST:132	0.65	0.65	0.62	0.36	0.38	0.53
NeST:29	0.44	0.55	0.54	0.49	0.51	0.51
NeST:57	0.50	0.57	0.55	0.57	0.54	0.55
NeST:150	0.56	0.57	0.57	0.43	0.57	0.54
NeST:20	0.55	0.58	0.57	0.53	0.54	0.56
NeST:47	0.45	0.52	0.51	0.52	0.58	0.52
NeST:11	0.58	0.57	0.55	0.42	0.56	0.54
NeST:130	0.55	0.59	0.58	0.56	0.58	0.57

Table 4.5: Assembly performance in cisplatin-treated cervical cancer. (Continued)

NeST ID	ci_1	ci_2	ci_3	ci_4	ci_5	mean ci
NeST:33	0.50	0.45	0.47	0.49	0.48	0.48
NeST:53	0.50	0.54	0.51	0.52	0.49	0.51
NeST:83	0.57	0.59	0.62	0.63	0.55	0.59
NeST:92	0.44	0.42	0.40	0.41	0.41	0.42
NeST:117	0.49	0.51	0.53	0.55	0.55	0.52
NeST:119	0.57	0.54	0.55	0.54	0.53	0.54
NeST:138	0.46	0.49	0.39	0.39	0.42	0.43
NeST:153	0.59	0.61	0.62	0.66	0.61	0.62
NeST:23	0.48	0.52	0.48	0.46	0.46	0.48
NeST:70	0.59	0.61	0.62	0.61	0.58	0.60
NeST:94	0.51	0.51	0.51	0.53	0.51	0.51
NeST:98	0.54	0.49	0.49	0.53	0.57	0.52
NeST:125	0.53	0.52	0.53	0.54	0.53	0.53
NeST:126	0.62	0.60	0.60	0.64	0.63	0.62
NeST:142	0.56	0.57	0.53	0.57	0.56	0.56
NeST:168	0.53	0.50	0.49	0.52	0.53	0.52
NeST:78	0.46	0.56	0.55	0.55	0.52	0.53
NeST:105	0.57	0.59	0.58	0.58	0.58	0.58
NeST:123	0.52	0.49	0.49	0.54	0.55	0.52
NeST:193	0.55	0.59	0.58	0.55	0.59	0.57
NeST:45	0.51	0.49	0.50	0.54	0.50	0.51
NeST:66	0.41	0.46	0.55	0.52	0.52	0.49
NeST:129	0.43	0.43	0.43	0.42	0.43	0.43
NeST:137	0.50	0.52	0.50	0.53	0.48	0.51
NeST:174	0.52	0.52	0.49	0.52	0.53	0.52
NeST:186	0.57	0.56	0.58	0.57	0.56	0.57
NeST:202	0.46	0.47	0.44	0.53	0.49	0.47
NeST:24	0.49	0.47	0.51	0.51	0.51	0.50
NeST:31	0.54	0.57	0.53	0.52	0.52	0.53
NeST:36	0.52	0.49	0.51	0.47	0.49	0.50
NeST:40	0.48	0.50	0.48	0.46	0.46	0.48
NeST:42	0.49	0.47	0.47	0.51	0.51	0.49
NeST:49	0.48	0.52	0.52	0.51	0.49	0.50
NeST:61	0.53	0.53	0.53	0.56	0.55	0.54
NeST:77	0.57	0.57	0.55	0.55	0.56	0.56
NeST:82	0.58	0.55	0.57	0.52	0.51	0.55
NeST:97	0.44	0.47	0.49	0.46	0.45	0.46
NeST:127	0.53	0.54	0.60	0.43	0.58	0.54
NeST:163	0.44	0.43	0.52	0.45	0.47	0.46
NeST:182	0.61	0.65	0.61	0.60	0.62	0.62
NeST:199	0.59	0.58	0.57	0.59	0.57	0.58
NeST:212	0.53	0.58	0.54	0.47	0.53	0.53
NeST:39	0.45	0.53	0.54	0.56	0.46	0.51
NeST:43	0.52	0.48	0.51	0.45	0.49	0.49
NeST:44	0.50	0.53	0.48	0.50	0.47	0.49
NeST:59	0.47	0.55	0.53	0.50	0.53	0.52
NeST:80	0.51	0.52	0.52	0.50	0.49	0.51
NeST:81	0.53	0.53	0.48	0.49	0.52	0.51
NeST:121	0.49	0.50	0.56	0.57	0.48	0.52
NeST:133	0.44	0.43	0.43	0.53	0.52	0.47

Table 4.5: Assembly performance in cisplatin-treated cervical cancer. (Continued)

NeST ID	ci_1	ci_2	ci_3	ci_4	ci_5	mean ci
NeST:134	0.48	0.49	0.46	0.48	0.45	0.47
NeST:146	0.51	0.51	0.49	0.51	0.50	0.50
NeST:158	0.46	0.48	0.51	0.53	0.48	0.49
NeST:169	0.57	0.53	0.48	0.50	0.56	0.53
NeST:195	0.61	0.63	0.63	0.62	0.60	0.62
NeST:21	0.51	0.51	0.51	0.51	0.52	0.51
NeST:22	0.51	0.48	0.50	0.46	0.49	0.49
NeST:254	0.53	0.55	0.47	0.50	0.50	0.51
NeST:256	0.62	0.62	0.63	0.64	0.63	0.63
NeST:35	0.47	0.49	0.51	0.51	0.49	0.49
NeST:51	0.54	0.58	0.54	0.53	0.53	0.54
NeST:69	0.50	0.52	0.48	0.51	0.47	0.50
NeST:90	0.51	0.50	0.51	0.50	0.51	0.51
NeST:145	0.48	0.51	0.50	0.49	0.49	0.49
NeST:155	0.56	0.57	0.53	0.57	0.59	0.56
NeST:165	0.54	0.53	0.47	0.53	0.53	0.52
NeST:170	0.49	0.51	0.50	0.52	0.48	0.50
NeST:177	0.57	0.56	0.56	0.60	0.60	0.58
NeST:196	0.49	0.52	0.55	0.53	0.49	0.51
NeST:210	0.51	0.50	0.52	0.49	0.49	0.50
NeST:221	0.53	0.53	0.49	0.52	0.50	0.51
NeST:231	0.53	0.54	0.54	0.54	0.47	0.53
NeST:239	0.54	0.53	0.49	0.53	0.53	0.52
NeST:27	0.50	0.48	0.51	0.47	0.49	0.49
NeST:277	0.56	0.50	0.51	0.50	0.52	0.52
NeST:293	0.54	0.54	0.54	0.54	0.54	0.54
NeST:48	0.44	0.43	0.45	0.45	0.43	0.44
NeST:54	0.49	0.52	0.49	0.49	0.52	0.50
NeST:63	0.46	0.44	0.46	0.45	0.43	0.45
NeST:93	0.50	0.49	0.48	0.51	0.48	0.49

4.8 Data availability

The datasets used in this study are all publicly available: GDSC1 and GDSC2: https://www.cancerrxgene.org/; CTRP1: https://portals.broadinstitute.org/ctrp.v1/; CTRP2: https://portals.broadinstitute.org/ctrp.v2.1/; DepMap 22Q2: https://doi.org/10.6084/m9.figshare.19700056.v2; cBioportal (https://www.cbioportal.org/datasets); CRISPR and RNAi screen. The pre-trained models are available on GitHub in their respective repositories.

4.9 Code availability

The source codes are available at GitHub: VNN https://github.com/idekerlab/nest_vnn; multi-drug VNN https://github.com/idekerlab/mutlitask_vnn.

4.10 Acknowledgments

We are grateful to Drs. Erica Silva, Samson Fong, Yue Qin, Mark Kelly, and Ingoo Lee for their very insightful comments. This study was made possible by grants from the National Institutes of Health (NCI U54 CA274502, NIGMS P41 GM103504) and Merck KGaA (Darmstadt, Germany) and the Eric and Wendy Schmidt AI in Science Postdoctoral Fellowship, a Schmidt Futures program.

Chapter 4, in full, is a reformatted reprint of the material as it appears as “Cancer Mutations Converge on a Collection of Protein Assemblies to Predict Resistance to Replication Stress” in Cancer Discovery, 2024 by Zhao, Xiaoyu; Singhal, Akshat; Park, Sungjoon; Kong, JungHo; Bachelder, Robin; Ideker, Trey. The dissertation author was a primary investigator and author of this paper.

4.11 References

(1) Burgers, P. M. J.; Kunkel, T. A. Eukaryotic DNA Replication Fork. *Annu. Rev. Biochem.* 2017, *86*, 417–438.

(2) Fragkos, M.; Ganier, O.; Coulombe, P.; Méchali, M. DNA Replication Origin Activation in Space and Time. *Nat. Rev. Mol. Cell Biol.* 2015, *16* (6), 360–374.

(3) Zeman, M. K.; Cimprich, K. A. Causes and Consequences of Replication Stress. *Nat. Cell Biol.* 2014, *16* (1), 2–9.

(4) Saxena, S.; Zou, L. Hallmarks of DNA Replication Stress. *Mol. Cell* 2022, *82* (12), 2298–2314.

(5) Byun, T. S.; Pacek, M.; Yee, M.-C.; Walter, J. C.; Cimprich, K. A. Functional Uncoupling of MCM Helicase and DNA Polymerase Activities Activates the ATR-Dependent Checkpoint. *Genes Dev.* 2005, *19* (9), 1040–1052.

(6) Zellweger, R.; Dalcher, D.; Mutreja, K.; Berti, M.; Schmid, J. A.; Herrador, R.; Vindigni, A.; Lopes, M. Rad51-Mediated Replication Fork Reversal Is a Global Response to Genotoxic Treatments in Human Cells. *J. Cell Biol.* 2015, *208* (5), 563–579.

(7) Saldivar, J. C.; Cortez, D.; Cimprich, K. A. The Essential Kinase ATR: Ensuring Faithful Duplication of a Challenging Genome. *Nat. Rev. Mol. Cell Biol.* 2017, *18* (10), 622–636.

(8) Ge, X. Q.; Blow, J. J. Chk1 Inhibits Replication Factory Activation but Allows Dormant Origin Firing in Existing Factories. *J. Cell Biol.* 2010, *191* (7), 1285–1297.

(9) Toledo, L. I.; Altmeyer, M.; Rask, M.-B.; Lukas, C.; Larsen, D. H.; Povlsen, L. K.; Bekker-Jensen, S.; Mailand, N.; Bartek, J.; Lukas, J. ATR Prohibits Replication Catastrophe by Preventing Global Exhaustion of RPA. *Cell* 2013, *155* (5), 1088–1103.

(10) Macheret, M.; Halazonetis, T. D. DNA Replication Stress as a Hallmark of Cancer. *Annu. Rev. Pathol.* 2015, *10*, 425–448.

(11) Hanahan, D.; Weinberg, R. A. Hallmarks of Cancer: The next Generation. *Cell* 2011, *144* (5), 646–674.

(12) Ubhi, T.; Brown, G. W. Exploiting DNA Replication Stress for Cancer Treatment. *Cancer Res.* 2019, *79* (8), 1730–1739.

(13) Dobbelstein, M.; Sørensen, C. S. Exploiting Replicative Stress to Treat Cancer. *Nat. Rev. Drug Discov.* 2015, *14* (6), 405–423.

(14) Zhang, J.; Dai, Q.; Park, D.; Deng, X. Targeting DNA Replication Stress for Cancer Therapy. *Genes* 2016, *7* (8), 51.

(15) Vesela, E.; Chroma, K.; Turi, Z.; Mistrik, M. Common Chemical Inductors of Replication Stress: Focus on Cell-Based Studies. *Biomolecules* 2017, *7* (1).

(16) Zhang, J.; Chan, D. W.; Lin, S.-Y. Exploiting DNA Replication Stress as a Therapeutic Strategy for Breast Cancer. *Biomedicines* 2022, *10* (11).

(17) Shah, M. A.; Schwartz, G. K. Cell Cycle-Mediated Drug Resistance: An Emerging Concept in Cancer Therapy. *Clin. Cancer Res.* 2001, *7* (8), 2168–2181.

(18) Beretta, G. L.; Gatti, L.; Perego, P.; Zaffaroni, N. Camptothecin Resistance in Cancer: Insights into the Molecular Mechanisms of a DNA-Damaging Drug. *Curr. Med. Chem.* 2013, *20* (12), 1541–1565.

(19) Dias, M. P.; Moser, S. C.; Ganesan, S.; Jonkers, J. Understanding and Overcoming Resistance to PARP Inhibitors in Cancer Therapy. *Nat. Rev. Clin. Oncol.* 2021, *18* (12), 773–791.

(20) Cao, X.; Hou, J.; An, Q.; Assaraf, Y. G.; Wang, X. Towards the Overcoming of Anticancer Drug Resistance Mediated by P53 Mutations. *Drug Resist. Updat.* 2020, *49*, 100671.

(21) Li, L.-Y.; Guan, Y.-D.; Chen, X.-S.; Yang, J.-M.; Cheng, Y. DNA Repair Pathways in Cancer Therapy and Resistance. *Front. Pharmacol.* 2020, *11*, 629266.

(22) Jia, Y.; Xie, J. Promising Molecular Mechanisms Responsible for Gemcitabine Resistance in Cancer. *Genes Dis* 2015, *2* (4), 299–306.

(23) Galluzzi, L.; Senovilla, L.; Vitale, I.; Michels, J.; Martins, I.; Kepp, O.; Castedo, M.; Kroemer, G. Molecular Mechanisms of Cisplatin Resistance. *Oncogene* 2012, *31* (15), 1869–1883.

(24) Bhattacharjee, R.; Dey, T.; Kumar, L.; Kar, S.; Sarkar, R.; Ghorai, M.; Malik, S.; Jha, N. K.; Vellingiri, B.; Kesari, K. K.; Pérez de la Lastra, J. M.; Dey, A. Cellular Landscaping of Cisplatin Resistance in Cervical Cancer. *Biomed. Pharmacother.* 2022, *153*, 113345.

(25) Nasrpour Navaei, Z.; Khalili-Tanha, G.; Sadra Zangouei, A.; Reza Abbaszadegan, M.; Moghbeli, M. PI3K/AKT Signaling Pathway as a Critical Regulator of Cisplatin Response in Tumor Cells. *Oncol. Res.* 2021, *29* (4), 235–250.

(26) Kiss, R. C.; Xia, F.; Acklin, S. Targeting DNA Damage Response and Repair to Enhance Therapeutic Index in Cisplatin-Based Cancer Treatment. *Int. J. Mol. Sci.* 2021, *22* (15).

(27) Li, Y.; Hostallero, D. E.; Emad, A. Interpretable Deep Learning Architectures for Improving Drug Response Prediction Performance: Myth or Reality? *Bioinformatics* 2023, *39* (6).

(28) Deng, L.; Cai, Y.; Zhang, W.; Yang, W.; Gao, B.; Liu, H. Pathway-Guided Deep Neural Network toward Interpretable and Predictive Modeling of Drug Sensitivity. *J. Chem. Inf. Model.* 2020, *60* (10), 4497–4505.

(29) Ma, J.; Yu, M. K.; Fong, S.; Ono, K.; Sage, E.; Demchak, B.; Sharan, R.; Ideker, T. Using Deep Learning to Model the Hierarchical Structure and Function of a Cell. *Nat. Methods* 2018, *15* (4), 290–298.

(30) Kuenzi, B. M.; Park, J.; Fong, S. H.; Sanchez, K. S.; Lee, J.; Kreisberg, J. F.; Ma, J.; Ideker, T. Predicting Drug Response and Synergy Using a Deep Learning Model of Human Cancer Cells. *Cancer Cell* 2020, *38* (5), 672-684.e6.

(31) Elmarakeby, H. A.; Hwang, J.; Arafeh, R.; Crowdis, J.; Gang, S.; Liu, D.; AlDubayan, S. H.; Salari, K.; Kregel, S.; Richter, C.; Arnoff, T. E.; Park, J.; Hahn, W. C.; Van Allen, E. M. Biologically Informed Deep Neural Network for Prostate Cancer Discovery. *Nature* 2021, *598* (7880), 348–352.

(32) Chen, H.-I. H.; Chiu, Y.-C.; Zhang, T.; Zhang, S.; Huang, Y.; Chen, Y. GSAE: An Autoencoder with Embedded Gene-Set Nodes for Genomics Functional Characterization. *BMC Syst. Biol.* 2018, *12* (Suppl 8), 142.

(33) Hao, J.; Kim, Y.; Kim, T.-K.; Kang, M. PASNet: Pathway-Associated Sparse Deep Neural Network for Prognosis Prediction from High-Throughput Data. *BMC Bioinformatics* 2018, *19* (1), 510.

(34) Huang, X.; Huang, K.; Johnson, T.; Radovich, M.; Zhang, J.; Ma, J.; Wang, Y. ParsVNN: Parsimony Visible Neural Networks for Uncovering Cancer-Specific and Drug-Sensitive Genes and Pathways. *NAR Genomics and Bioinformatics* 2021, *3* (4), lqab097.

(35) Hinton, G. E. Connectionist Learning Procedures. *Artificial intelligence* 1989, *40* (1), 185–234.

(36) Zheng, F.; Kelly, M. R.; Ramms, D. J.; Heintschel, M. L.; Tao, K.; Tutuncuoglu, B.; Lee, J. J.; Ono, K.; Foussard, H.; Chen, M.; Herrington, K. A.; Silva, E.; Liu, S. N.; Chen, J.; Churas, C.; Wilson, N.; Kratz, A.; Pillich, R. T.; Patel, D. N.; Park, J.; Kuenzi, B.; Yu, M. K.; Licon, K.; Pratt, D.; Kreisberg, J. F.; Kim, M.; Swaney, D. L.; Nan, X.; Fraley, S. I.; Gutkind, J. S.; Krogan, N. J.; Ideker, T. Interpretation of Cancer Mutations Using a Multiscale Map of Protein Systems. *Science* 2021, *374* (6563), eabf3067.

(37) Caruana, R. Multitask Learning. *Machine Learning* 1997, *28* (1), 41–75.

(38) Douglass, E. F., Jr; Allaway, R. J.; Szalai, B.; Wang, W.; Tian, T.; Fernández-Torras, A.; Realubit, R.; Karan, C.; Zheng, S.; Pessia, A.; Tanoli, Z.; Jafari, M.; Wan, F.; Li, S.; Xiong, Y.; Duran-Frigola, M.; Bertoni, M.; Badia-I-Mompel, P.; Mateo, L.; Guitart-Pla, O.; Chung, V.; DREAM CTD-squared Pancancer Drug Activity Challenge Consortium; Tang, J.; Zeng, J.; Aloy, P.; Saez-Rodriguez, J.; Guinney, J.; Gerhard, D. S.; Califano, A. A Community Challenge for a Pancancer Drug Mechanism of Action Inference from Perturbational Profile Data. *Cell Rep Med* 2022, *3* (1), 100492.

(39) Yuan, H.; Paskov, I.; Paskov, H.; González, A. J.; Leslie, C. S. Multitask Learning Improves Prediction of Cancer Drug Sensitivity. *Sci. Rep.* 2016, *6*, 31619.

(40) Frampton, G. M.; Fichtenholtz, A.; Otto, G. A.; Wang, K.; Downing, S. R.; He, J.; Schnall-Levin, M.; White, J.; Sanford, E. M.; An, P.; Sun, J.; Juhn, F.; Brennan, K.; Iwanik, K.; Maillet, A.; Buell, J.; White, E.; Zhao, M.; Balasubramanian, S.; Terzic, S.; Richards, T.; Banning, V.; Garcia, L.; Mahoney, K.; Zwirko, Z.; Donahue, A.; Beltran, H.; Mosquera, J. M.; Rubin, M. A.; Dogan, S.; Hedvat, C. V.; Berger, M. F.; Pusztai, L.; Lechner, M.; Boshoff, C.; Jarosz, M.; Vietz, C.; Parker, A.; Miller, V. A.; Ross, J. S.; Curran, J.; Cronin, M. T.; Stephens, P. J.; Lipson, D.; Yelensky, R. Development and Validation of a Clinical Cancer Genomic Profiling Test Based on Massively Parallel DNA Sequencing. *Nat. Biotechnol.* 2013, *31* (11), 1023–1031.

(41) Beaubier, N.; Tell, R.; Lau, D.; Parsons, J. R.; Bush, S.; Perera, J.; Sorrells, S.; Baker, T.; Chang, A.; Michuda, J.; Iguartua, C.; MacNeil, S.; Shah, K.; Ellis, P.; Yeatts, K.; Mahon, B.; Taxter, T.; Bontrager, M.; Khan, A.; Huether, R.; Lefkofsky, E.; White, K. P. Clinical Validation of the Tempus XT Next-Generation Targeted Oncology Sequencing Assay. *Oncotarget* 2019, *10* (24), 2384–2396.

(42) Smyth, L. M.; Zhou, Q.; Nguyen, B.; Yu, C.; Lepisto, E. M.; Arnedos, M.; Hasset, M. J.; Lenoue-Newton, M. L.; Blauvelt, N.; Dogan, S.; Micheel, C. M.; Wathoo, C.; Horlings, H.; Hudecek, J.; Gross, B. E.; Kundra, R.; Sweeney, S. M.; Gao, J.; Schultz, N.; Zarski, A.; Gardos, S. M.; Lee, J.; Sheffler-Collins, S.; Park, B. H.; Sawyers, C. L.; André, F.; Levy, M.;

Meric-Bernstam, F.; Bedard, P. L.; Iasonos, A.; Schrag, D.; Hyman, D. M. Characteristics and Outcome of AKT1E17K-Mutant Breast Cancer Defined through AACR Project GENIE, a Clinicogenomic Registry. *Cancer Discov.* 2020, *10* (4), 526–535.

(43) Basu, A.; Bodycombe, N. E.; Cheah, J. H.; Price, E. V.; Liu, K.; Schaefer, G. I.; Ebright, R. Y.; Stewart, M. L.; Ito, D.; Wang, S.; Bracha, A. L.; Liefeld, T.; Wawer, M.; Gilbert, J. C.; Wilson, A. J.; Stransky, N.; Kryukov, G. V.; Dancik, V.; Barretina, J.; Garraway, L. A.; Hon, C. S.-Y.; Munoz, B.; Bittker, J. A.; Stockwell, B. R.; Khabele, D.; Stern, A. M.; Clemons, P. A.; Shamji, A. F.; Schreiber, S. L. An Interactive Resource to Identify Cancer Genetic and Lineage Dependencies Targeted by Small Molecules. *Cell* 2013, *154* (5), 1151–1161.

(44) Seashore-Ludlow, B.; Rees, M. G.; Cheah, J. H.; Cokol, M.; Price, E. V.; Coletti, M. E.; Jones, V.; Bodycombe, N. E.; Soule, C. K.; Gould, J.; Alexander, B.; Li, A.; Montgomery, P.; Wawer, M. J.; Kuru, N.; Kotz, J. D.; Hon, C. S.-Y.; Munoz, B.; Liefeld, T.; Dančík, V.; Bittker, J. A.; Palmer, M.; Bradner, J. E.; Shamji, A. F.; Clemons, P. A.; Schreiber, S. L. Harnessing Connectivity in a Large-Scale Small-Molecule Sensitivity Dataset. *Cancer Discov.* 2015, *5* (11), 1210–1223.

(45) Garnett, M. J.; Edelman, E. J.; Heidorn, S. J.; Greenman, C. D.; Dastur, A.; Lau, K. W.; Greninger, P.; Thompson, I. R.; Luo, X.; Soares, J.; Liu, Q.; Iorio, F.; Surdez, D.; Chen, L.; Milano, R. J.; Bignell, G. R.; Tam, A. T.; Davies, H.; Stevenson, J. A.; Barthorpe, S.; Lutz, S. R.; Kogera, F.; Lawrence, K.; McLaren-Douglas, A.; Mitropoulos, X.; Mironenko, T.; Thi, H.; Richardson, L.; Zhou, W.; Jewitt, F.; Zhang, T.; O'Brien, P.; Boisvert, J. L.; Price, S.; Hur, W.; Yang, W.; Deng, X.; Butler, A.; Choi, H. G.; Chang, J. W.; Baselga, J.; Stamenkovic, I.; Engelman, J. A.; Sharma, S. V.; Delattre, O.; Saez-Rodriguez, J.; Gray, N. S.; Settleman, J.; Futreal, P. A.; Haber, D. A.; Stratton, M. R.; Ramaswamy, S.; McDermott, U.; Benes, C. H. Systematic Identification of Genomic Markers of Drug Sensitivity in Cancer Cells. *Nature* 2012, *483* (7391), 570–575.

(46) Iorio, F.; Knijnenburg, T. A.; Vis, D. J.; Bignell, G. R.; Menden, M. P.; Schubert, M.; Aben, N.; Gonçalves, E.; Barthorpe, S.; Lightfoot, H.; Cokelaer, T.; Greninger, P.; van Dyk, E.; Chang, H.; de Silva, H.; Heyn, H.; Deng, X.; Egan, R. K.; Liu, Q.; Mironenko, T.; Mitropoulos, X.; Richardson, L.; Wang, J.; Zhang, T.; Moran, S.; Sayols, S.; Soleimani, M.; Tamborero, D.; Lopez-Bigas, N.; Ross-Macdonald, P.; Esteller, M.; Gray, N. S.; Haber, D. A.; Stratton, M. R.; Benes, C. H.; Wessels, L. F. A.; Saez-Rodriguez, J.; McDermott, U.; Garnett, M. J. A Landscape of Pharmacogenomic Interactions in Cancer. *Cell* 2016, *166* (3), 740–754.

(47) Olivieri, M.; Cho, T.; Álvarez-Quilón, A.; Li, K.; Schellenberg, M. J.; Zimmermann, M.; Hustedt, N.; Rossi, S. E.; Adam, S.; Melo, H.; Heijink, A. M.; Sastre-Moreno, G.; Moatti, N.; Szilard, R. K.; McEwan, A.; Ling, A. K.; Serrano-Benitez, A.; Ubhi, T.; Feng, S.; Pawling, J.; Delgado-Sainz, I.; Ferguson, M. W.; Dennis, J. W.; Brown, G. W.; Cortés-Ledesma, F.; Williams, R. S.; Martin, A.; Xu, D.; Durocher, D. A Genetic Map of the Response to DNA Damage in Human Cells. *Cell* 2020, *182* (2), 481-496.e21.

(48) Liu, Q.; Hu, Z.; Jiang, R.; Zhou, M. DeepCDR: A Hybrid Graph Convolutional Network for Predicting Cancer Drug Response. *Bioinformatics* 2020, *36* (Suppl_2), i911–i918.

(49) Kavanaugh, G.; Ye, F.; Mohni, K. N.; Luzwick, J. W.; Glick, G.; Cortez, D. A Whole Genome RNAi Screen Identifies Replication Stress Response Genes. *DNA Repair* 2015, *35*, 55–62.

(50) Takemaru, K. I.; Moon, R. T. The Transcriptional Coactivator CBP Interacts with Beta-Catenin to Activate Gene Expression. *J. Cell Biol.* 2000, *149* (2), 249–254.

(51) Hecht, A.; Vleminckx, K.; Stemmler, M. P.; van Roy, F.; Kemler, R. The P300/CBP Acetyltransferases Function as Transcriptional Coactivators of Beta-Catenin in Vertebrates. *EMBO J.* 2000, *19* (8), 1839–1850.

(52) Shen, Y.; Xu, L.; Ning, Z.; Liu, L.; Lin, J.; Chen, H.; Meng, Z. ARHGAP4 Regulates the Cell Migration and Invasion of Pancreatic Cancer by the HDAC2/β-Catenin Signaling Pathway. *Carcinogenesis* 2019, *40* (11), 1405–1414.

(53) Sadot, E.; Geiger, B.; Oren, M.; Ben-Ze'ev, A. Down-Regulation of Beta-Catenin by Activated P53. *Mol. Cell. Biol.* 2001, *21* (20), 6768–6781.

(54) Vogelstein, B.; Kinzler, K. W. Cancer Genes and the Pathways They Control. *Nat. Med.* 2004, *10* (8), 789–799.

(55) Lugones, Y.; Loren, P.; Salazar, L. A. Cisplatin Resistance: Genetic and Epigenetic Factors Involved. *Biomolecules* 2022, *12* (10), 1365.

(56) Fuchs, J.; Cheblal, A.; Gasser, S. M. Underappreciated Roles of DNA Polymerase δ in Replication Stress Survival. *Trends Genet.* 2021, *37* (5), 476–487.

(57) Rocha, C. R. R.; Silva, M. M.; Quinet, A.; Cabral-Neto, J. B.; Menck, C. F. M. DNA Repair Pathways and Cisplatin Resistance: An Intimate Relationship. *Clinics* 2018, *73* (suppl 1), e478s.

(58) Tian, W.; Ji, Z.; Wang, J.; Meng, J.; Bi, R.; Ren, Y.; Shan, B.; Yang, G.; Wang, H. Characterization of Hotspot Exonuclease Domain Mutations in the DNA Polymerase ϵ Gene in Endometrial Cancer. *Front. Oncol.* 2022, *12*, 1018034.

(59) Park, J.; Ko, Y. S.; Yoon, J.; Kim, M. A.; Park, J.-W.; Kim, W. H.; Choi, Y.; Kim, J. H.; Cheon, Y.; Lee, B. L. The Forkhead Transcription Factor FOXO1 Mediates Cisplatin Resistance in Gastric Cancer Cells by Activating Phosphoinositide 3-Kinase/Akt Pathway. *Gastric Cancer* 2014, *17* (3), 423–430.

(60) Beretta, G. L.; Corno, C.; Zaffaroni, N.; Perego, P. Role of FoxO Proteins in Cellular Response to Antitumor Agents. *Cancers* 2019, *11* (1), 90.

(61) Achkar, I. W.; Abdulrahman, N.; Al-Sulaiti, H.; Joseph, J. M.; Uddin, S.; Mraiche, F. Cisplatin Based Therapy: The Role of the Mitogen Activated Protein Kinase Signaling Pathway. *J. Transl. Med.* 2018, *16* (1), 96.

(62) Wang, N.; Ma, T.; Yu, B. Targeting Epigenetic Regulators to Overcome Drug Resistance in Cancers. *Signal Transduct Target Ther* 2023, *8* (1), 69.

(63) Yang, C.; Zhang, J.; Ma, Y.; Wu, C.; Cui, W.; Wang, L. Histone Methyltransferase and Drug Resistance in Cancers. *J. Exp. Clin. Cancer Res.* 2020, *39* (1), 173.

(64) Sun, J.; Cai, X.; Yung, M. M.; Zhou, W.; Li, J.; Zhang, Y.; Li, Z.; Liu, S. S.; Cheung, A. N. Y.; Ngan, H. Y. S.; Li, Y.; Dai, Z.; Kai, Y.; Tzatsos, A.; Peng, W.; Chan, D. W.; Zhu, W. MiR-

137 Mediates the Functional Link between c-Myc and EZH2 That Regulates Cisplatin Resistance in Ovarian Cancer. *Oncogene* 2019, *38* (4), 564–580.

(65) Sun, S.; Zhao, S.; Yang, Q.; Wang, W.; Cai, E.; Wen, Y.; Yu, L.; Wang, Z.; Cai, J. Enhancer of Zeste Homolog 2 Promotes Cisplatin Resistance by Reducing Cellular Platinum Accumulation. *Cancer Sci.* 2018, *109* (6), 1853–1864.

(66) Qiu, Z.; Zhu, W.; Meng, H.; Tong, L.; Li, X.; Luo, P.; Yi, L.; Zhang, X.; Guo, L.; Wei, T.; Zhang, J. CDYL Promotes the Chemoresistance of Small Cell Lung Cancer by Regulating H3K27 Trimethylation at the CDKN1C Promoter. *Theranostics* 2019, *9* (16), 4717–4729.

(67) Hugo de Almeida, V.; Guimarães, I. D. S.; Almendra, L. R.; Rondon, A. M. R.; Tilli, T. M.; de Melo, A. C.; Sternberg, C.; Monteiro, R. Q. Positive Crosstalk between EGFR and the TF-PAR2 Pathway Mediates Resistance to Cisplatin and Poor Survival in Cervical Cancer. *Oncotarget* 2018, *9* (55), 30594–30609.

(68) Morgan, E. L.; Macdonald, A. JAK2 Inhibition Impairs Proliferation and Sensitises Cervical Cancer Cells to Cisplatin-Induced Cell Death. *Cancers* 2019, *11* (12), 1934.

(69) Gutiérrez-Hoya, A.; Soto-Cruz, I. Role of the JAK/STAT Pathway in Cervical Cancer: Its Relationship with HPV E6/E7 Oncoproteins. *Cells* 2020, *9* (10), 2297.

(70) Huang, L.-L.; Rao, W. SiRNA Interfering STAT3 Enhances DDP Sensitivity in Cervical Cancer Cells. *Eur. Rev. Med. Pharmacol. Sci.* 2018, *22* (13), 4098–4106.

(71) Lucas, L. M.; Dwivedi, V.; Senfeld, J. I.; Cullum, R. L.; Mill, C. P.; Piazza, J. T.; Bryant, I. N.; Cook, L. J.; Miller, S. T.; Lott, J. H., 4th; Kelley, C. M.; Knerr, E. L.; Markham, J. A.; Kaufmann, D. P.; Jacobi, M. A.; Shen, J.; Riese, D. J., 2nd. The Yin and Yang of ERBB4: Tumor Suppressor and Oncoprotein. *Pharmacol. Rev.* 2022, *74* (1), 18–47.

(72) Partin, A.; Brettin, T. S.; Zhu, Y.; Narykov, O.; Clyde, A.; Overbeek, J.; Stevens, R. L. Deep Learning Methods for Drug Response Prediction in Cancer: Predominant and Emerging Trends. *Front. Med.* 2023, *10*, 1086097.

(73) Jin, I.; Nam, H. HiDRA: Hierarchical Network for Drug Response Prediction with Attention. *J. Chem. Inf. Model.* 2021, *61* (8), 3858–3867.

(74) Mucaki, E. J.; Zhao, J. Z. L.; Lizotte, D. J.; Rogan, P. K. Predicting Responses to Platin Chemotherapy Agents with Biochemically-Inspired Machine Learning. *Signal Transduct Target Ther* 2019, *4*, 1.

(75) Gao, Y.; Lyu, Q.; Luo, P.; Li, M.; Zhou, R.; Zhang, J.; Lyu, Q. Applications of Machine Learning to Predict Cisplatin Resistance in Lung Cancer. *Int. J. Gen. Med.* 2021, *14*, 5911–5925.

(76) Scarborough, J. A.; Eschrich, S. A.; Torres-Roca, J.; Dhawan, A.; Scott, J. G. Exploiting Convergent Phenotypes to Derive a Pan-Cancer Cisplatin Response Gene Expression Signature. *NPJ Precis Oncol* 2023, *7* (1), 38.

(77) Sui, Q.; Chen, Z.; Hu, Z.; Huang, Y.; Liang, J.; Bi, G.; Bian, Y.; Zhao, M.; Zhan, C.; Lin, Z.; Wang, Q.; Tan, L. Cisplatin Resistance-Related Multi-Omics Differences and the

Establishment of Machine Learning Models. *J. Transl. Med.* 2022, *20* (1), 171.

(78) Berthelet, J.; Foroutan, M.; Bhuva, D. D.; Whitfield, H. J.; El-Saafin, F.; Cursons, J.; Serrano, A.; Merdas, M.; Lim, E.; Charafe-Jauffret, E.; Ginestier, C.; Ernst, M.; Hollande, F.; Anderson, R. L.; Pal, B.; Yeo, B.; Davis, M. J.; Merino, D. Computational Screening of Anti-Cancer Drugs Identifies a New BRCA Independent Gene Expression Signature to Predict Breast Cancer Sensitivity to Cisplatin. *Cancers* 2022, *14* (10).

(79) Ngoi, N. Y. L.; Pham, M. M.; Tan, D. S. P.; Yap, T. A. Targeting the Replication Stress Response through Synthetic Lethal Strategies in Cancer Medicine. *Trends Cancer Res.* 2021, *7* (10), 930–957.

(80) Lira, M. E.; Xie, T.; Deng, S.; Kinong, J.; Gao, J.; Zhu, Z.; Lee, N.; Rejto, P.; Bienkowska, J.; Hardwick, J.; Wang, K.; Huang, S. Abstract 2749: Liquid Biopsy Testing Allows Highly-Sensitive Detection of Plasma CfDNA Mutations in 87 Breast Cancer-Related Genes. *Cancer Research*. 2017, pp 2749–2749.

(81) Barretina, J.; Caponigro, G.; Stransky, N.; Venkatesan, K.; Margolin, A. A.; Kim, S.; Wilson, C. J.; Lehár, J.; Kryukov, G. V.; Sonkin, D.; Reddy, A.; Liu, M.; Murray, L.; Berger, M. F.; Monahan, J. E.; Morais, P.; Meltzer, J.; Korejwa, A.; Jané-Valbuena, J.; Mapa, F. A.; Thibault, J.; Bric-Furlong, E.; Raman, P.; Shipway, A.; Engels, I. H.; Cheng, J.; Yu, G. K.; Yu, J.; Aspesi, P.; de Silva, M.; Jagtap, K.; Jones, M. D.; Wang, L.; Hatton, C.; Palescandolo, E.; Gupta, S.; Mahan, S.; Sougnez, C.; Onofrio, R. C.; Liefeld, T.; MacConaill, L.; Winckler, W.; Reich, M.; Li, N.; Mesirov, J. P.; Gabriel, S. B.; Getz, G.; Ardlie, K.; Chan, V.; Myer, V. E.; Weber, B. L.; Porter, J.; Warmuth, M.; Finan, P.; Harris, J. L.; Meyerson, M.; Golub, T. R.; Morrissey, M. P.; Sellers, W. R.; Schlegel, R.; Garraway, L. A. The Cancer Cell Line Encyclopedia Enables Predictive Modelling of Anticancer Drug Sensitivity. *Nature*. 2012, pp 603–607.

(82) Ioffe, S.; Szegedy, C. Batch Normalization: Accelerating Deep Network Training by Reducing Internal Covariate Shift. In *Proceedings of the 32nd International Conference on Machine Learning*; Bach, F., Blei, D., Eds.; Proceedings of Machine Learning Research; PMLR: Lille, France, 07--09 Jul 2015; Vol. 37, pp 448–456.

(83) Srivastava, N.; Hinton, G.; Krizhevsky, A.; Sutskever, I.; Salakhutdinov, R. Dropout: A Simple Way to Prevent Neural Networks from Overfitting. *J. Mach. Learn. Res.* 2014, *15* (56), 1929–1958.

(84) Jolliffe, I. T. *Principal Component Analysis*; Springer New York, 2013.

(85) Akiba, T.; Sano, S.; Yanase, T.; Ohta, T.; Koyama, M. Optuna: A Next-Generation Hyperparameter Optimization Framework. In *Proceedings of the 25th ACM SIGKDD International Conference on Knowledge Discovery & Data Mining*; KDD '19; Association for Computing Machinery: New York, NY, USA, 2019; pp 2623–2631.

(86) Pedregosa, F.; Varoquaux, G.; Gramfort, A.; Michel, V.; Thirion, B.; Grisel, O.; Blondel, M.; Prettenhofer, P.; Weiss, R.; Dubourg, V.; Others. Scikit-Learn: Machine Learning in Python. *the Journal of machine Learning research* 2011, *12*, 2825–2830.

(87) Raudvere, U.; Kolberg, L.; Kuzmin, I.; Arak, T.; Adler, P.; Peterson, H.; Vilo, J. G:Profiler: A Web Server for Functional Enrichment Analysis and Conversions of Gene Lists (2019

Update). *Nucleic Acids Research*. 2019, pp W191–W198.

(88) Harrell, F. E., Jr; Califf, R. M.; Pryor, D. B.; Lee, K. L.; Rosati, R. A. Evaluating the Yield of Medical Tests. *JAMA* 1982, *247* (18), 2543–2546.

(89) Cox, D. R. Regression Models and Life-Tables. *J. R. Stat. Soc.* 1972, *34* (2), 187–202.

Chapter 5 Retrospective analysis of a deep learning model for prediction of palbociclib response in patients with ER+ HER2– advanced breast cancer

5.1 Abstract

Purpose. Cyclin-Dependent Kinases 4 and 6 inhibitors (CDK4/6i) have revolutionized treatment of ER+/HER2– advanced or metastatic breast cancer (BC). However, development of resistance is almost universal. There are presently no established biomarkers of CDK4/6i resistance in clinical practice, underscoring an unmet need. We previously released a visible and interpretable deep-learning model, Palbo-VNN, to identify multi-gene biomarkers of response to palbociclib (palbo), one of the CDK4/6i. Here we conduct a retrospective study to evaluate the utility of the model in patient identification for durable palbo response.

Methods. We investigated Palbo-VNN in patients with biopsy-proven ER+ HER2- advanced or metastatic BC and tissue-based genomic sequencing. Patient and disease characteristics, treatment course, and clinical outcomes were collected. Model prediction and interpretation were integrated to create a personalized report for each patient, yielding a predicted response score coupled to the primary genetic biomarkers and pathways supporting this score.

Results. 139 patients met inclusion criteria. In the first line setting, the patients with predicted sensitivity to palbo at diagnosis had progression free survival of 23.2 months vs 9 months for patients with predicted resistance (HR 0.38, 95% CI 0.18-0.82, p=0.01); median overall survival was not reached vs 36.9 months (HR 0.38, 95% CI 0.14-0.99, p=0.05). Biomarker interpretation revealed frequent resistance mechanisms in RTK signaling, DNA damage response, cell cycle regulation, and ubiquitination.

Conclusion. This study is among the first retrospective evaluations of a deep-learning model for prediction of CDK4/6i response in ER+ HER2- advanced or metastatic BC using tissue genomic sequencing as input. The model effectively predicted palbo sensitivity in our patient cohort and demonstrates the potential for machine learning to optimize patient selection for breast cancer therapy. Furthermore, Palbo-VNN could be harnessed to elucidate novel biological

mediators of palbo response. Future opportunities include prospective randomized trials to evaluate model-guided treatment selection and exploration of the resistance pathways.

5.2 Introduction

Estrogen receptor positive (ER+) human epidermal growth factor receptor 2 negative (HER2–) breast cancer, the most common breast cancer subtype, has seen marked advancements in recent years. The current standard of care in the first-line metastatic setting is the combination of cyclin-dependent kinase 4/6 inhibitors (CDK4/6i) with endocrine therapy (ET). Three CDK4/6i have been approved by the FDA for use in this setting – abemaciclib, palbo, and ribociclib. All three agents have been shown in multiple phase III trials to significantly increase progression-free survival (PFS), with overall survival (OS) benefit also seen with ribociclib[1]. Despite this advancement in care, overall response rates hover at around 50% for CDK4/6i therapy in the first-line setting and all patients ultimately develop resistant disease, suggesting that the remaining patients have primary resistance[2]. Even among those who respond, the eventual development of resistance is nearly universal.

To date, no biomarkers have entered clinical practice that predict response to CDK4/6i. Preclinical studies of CDK4/6i resistance have investigated loss of function alterations to antiproliferative pathway genes (TP53, RB1, BRCA1) or gain of function alterations to proliferation genes (PIK3CA, CCND1, ESR1); however, these markers are not yet established in clinical use[3]. Such absence underscores a critical unmet need to identify which patients are likely to derive benefit from CDK4/6i, versus which patients are resistant to therapy and warrant alternate treatment strategies. A clinical tool for patient selection would help ensure that patients receive effective treatments sooner and, ultimately, experience improved clinical outcomes and quality of life.

Deep learning is a powerful methodology that is beginning to impact many aspects of cancer care, including precision medicine and prediction of therapy response[4–6]. However, such

advanced models are difficult to interpret or generalize to real-world data. Meaningful interpretation of the relevant molecular mechanisms determining therapy response greatly enhances the model's ability to inform predictive biomarkers. Models trained on preclinical datasets should demonstrate accurate translation to patient data. Limited availability of gene alteration profiles with matched treatment outcomes makes generalizability especially challenging for therapy response models. We addressed these challenges in a recently published "visible" neural network (VNN) to understand how patterns of genetic alterations govern the tumor response to CDK4/6i[7]. This model, referred to as Palbo-VNN, integrated rare and common alterations across 718 genes with a knowledge map of multiprotein assemblies in cancer. Palbo-VNN was highly predictive of palbociclib outcomes in preclinical samples as well as in patients with metastatic breast cancer in the AACR GENIE database.

In this real-world study, we expand on our prior work to evaluate the efficacy of the Palbo-VNN model in patients with biopsy proven ER+, HER2– advanced breast cancer treated with palbo in combination with endocrine therapy (Figure 5.1). We further harness the known structure of the Palbo-VNN to assess molecular pathways of resistance, by evaluating altered genes among patients with tumors predicted to be sensitive versus those predicted to be resistant. Using the model, we construct a gene signature that can be applied to patients for future predictive studies.

5.3 Methods

5.3.1 Patient Selection

514 patients with biopsy proven ER+ HER2– advanced breast cancer and available tissue-based genomic sequencing data were treated with palbo between February 2016 and September 2023 at the University of California San Diego. Patients were excluded if they did not have biopsy proven breast cancer, did not have genomic sequencing from either a primary tumor site or metastatic site tissue biopsy, or did not receive palbo at any point during the specified

timeframe. Overall, 139 patients met the selection criteria. The authors obtained institutional review board approval for the present study.

5.3.2 Clinical Outcomes

The clinical data included patient demographics, disease characteristics (*de novo* vs recurrent metastatic breast cancer), therapy line in the metastatic setting, prior and subsequent therapies received. Clinical outcomes gathered included treatment duration, progression free survival (PFS) and overall survival (OS). OS and treatment duration were measured for all patients with tissue based genomic sequencing. PFS was calculated for all patients in the 1st line setting. PFS was defined by time passed between start of palbo and progression of disease as determined by clinician assessment or radiographic progression by RECIST 1.1 criteria or time to death, whichever occurred first. Overall survival is defined as the time from palbo start date to date of death.

5.3.3 Model Development

To train Palbo-VNN, we leveraged drug response data for 947 genomically characterized tumor cell lines, obtained from the Cancer Therapeutics Response Portal and Genomics of Drug Sensitivity in Cancer databases. A panel of 718 genes was assembled from the union of clinically relevant gene panels and studies, including FoundationOne CDx, Tempus xT, and Project GENIE. To compile genotypes for all cell lines, we extracted nonsynonymous coding mutations and copy number alterations for all 718 genes from the Cancer Cell Line Encyclopedia. Genes were marked as either mutated (1') or unmutated (0'), with mutations filtered missense/nonsense/nonstop mutations, frameshift insertions/deletions, splice site/region variations and in-frame insertions/deletions. Similarly, genes were marked as amplified (1') or unamplified ('0') and deleted ('1') or undeleted ('0'). Together, these three binary features (mutations, copy-number amplifications, and copy-number deletions) serve as the model input. The model structure was guided by a hierarchical map of multiprotein assemblies called NeST

(Nested Systems in Tumors). Training and optimization was conducted using nested five-fold cross-validation, resulting in five models.

5.3.4 Model Prediction

Palbo-VNN is an ensemble of five models. Tissue-based genomic sequencing data from commercially available vendors was used as input for each model. To assess Palbo-VNN in a prospective setting, a predetermined cut-off of 0.645 was used. In this blinded approach, a tumor with a predicted score of 0.645 or less in at least two models was categorized as sensitive to palbociclib (Palbo-VNNsen) or resistant otherwise (Palbo-VNNres).

5.3.5 SHAP Analysis

The Shapley additive explanations (SHAP) method was used to identify the most contributing input features for each prediction. Since Palbo-VNN predicts resistance, resistant features had positive SHAP scores and vice-versa. The predetermined cut-off of 0.645 was used as the base value.

5.3.6 Statistical Analyses

Patient baseline characteristics were summarized using descriptive statistics. Differences in treatment duration, PFS, and OS between Palbo-VNNsen vs Palbo-VNNres groups were reported using Kaplan Meier survival curves and analyzed using log-rank test and hazard ratio.

5.4 Results

5.4.1 Patient Selection

A total of 514 patients were identified in the UCSD electronic medical record with biopsy proven ER+ HER2- advanced and metastatic breast cancer and treated with palbo between February 2016 and November 2023. Of these patients, 204 had molecular testing via either blood based or tissue based NGS. 139 patients met inclusion criteria based on histological confirmation and the availability of tissue-based next generation sequencing (Figure 5.2). Key demographic

and clinical characteristics of the patients are summarized in table 1. The median age was 63 (range 33-91) with a median ECOG performance status of 1 (range 0-3). Among the 139 patients, 47 (34%) had *de novo* metastatic disease, 24 (17%) had prior localized disease with metastatic relapse within 2 years of adjuvant endocrine therapy (ET) initiation, and 57 (41%) had metastatic relapse after 2 years of adjuvant ET. Bone-only metastases were present in 34 (24%) of patients, visceral involvement in 92 (66%), and central nervous system involvement in 13 (9%). 75 (54%) of patients received palbo in the 1st line setting, 23 (17%) in the 2nd line setting, 14 (10%) in the 3rd line setting, and 27 (19%) in the 4th line and beyond setting. Among the patients with prior endocrine therapy, 41 (53%) received letrozole, 19 (24%) anastrozole, 29 (37%) exemestane, and 28 (36%) tamoxifen.

5.4.2 Model prediction

Among the overall population of 139 patients, 59 (42%) were predicted sensitive (Palbo-VNNsen) and 80 (58%) were predicted resistant (Palbo-VNNres). The median treatment duration among patients with Palbo-VNNsen vs Palbo-VNNres tumors were 27.0 months vs 12.0 months respectively, with HR of 0.50 (95% CI 0.32-0.78, p=2.2x10^{-3} by log-rank test). The OS for patients with Palbo-VNNsen vs Palbo-VNNres tumors were 59.8 months vs 31.9 months, respectively, with HR of 0.58 (95% CI 0.38-0.91, p=0.02 by log-rank test; Figure 5.3). Among the 75 patients treated in the 1st line setting (Table 5.1), 39 (52%) had tumor-derived NGS within 6 months before or up to 3 months after the start of palbo. Median treatment duration for Palbo-VNNsen group (n=19) within this subgroup was not reached, compared to 12.6 months in the Palbo-VNNres group (n=20), with HR of 0.35 (95% CI 0.13-0.93, p=0.04 by log-rank test). Median OS was not reached vs 36.9 months respectively, with HR of 0.38 (95% CI 0.14-0.99, p=0.05 by log-rank test). PFS was additionally analyzed by radiographic evaluation per RECIST 1.1 criteria, as well as by clinical evaluation by the treating clinician. Among evaluable patients (n=36), the PFS in the Palbo-VNNsen group (n=19) was 23.2 months vs 9.0 months in the Palbo-VNNres group (n=17),

HR of 0.38 (95% CI 0.18-0.82, p=0.01 by log-rank test; Figure 5.3). The statistically significant longer duration of treatment, PFS, and OS seen in patients with Palbo-VNNsen vs Palbo-VNNres tumors were also observed in the overall patient cohort treated with 1st line palbo, irrespective of timing of NGS testing.

5.4.3 Model interpretation

After the blinded analysis of model predictions, we unblinded the study to interpret which protein assemblies were contributing most to the model predictions. We ranked the predictive performance of the assemblies using the SHAP method (Methods). Most predictive assemblies included diverse mechanisms such as cell cycle arrest, transmembrane RTK signaling, and cytoskeleton, among others. Notably, the twenty most predictive assemblies included seven of the eight core assemblies identified in cell lines in the previous study[7] (Figure 5.4).

Next, we sought to develop a visualization schema for each patient based on palbo-VNN prediction and interpretation (Figure 5.5). For each patient, the schema included clinical outcomes, predictive score, and model explanation (figures 5.5A-C for patient #377 and figures 5.5D-F for patient #245). The clinical outcomes including PFS and OS were gathered in this study (Methods). The predicted score was calculated palbo-VNN predictions normalized by model predictions across the overall population. Predictive gene alterations and assemblies were identified using the SHAP method (Methods).

5.5 Discussion

CDK4/6i therapy has revolutionized the treatment landscape for advanced and metastatic ER+ HER2- breast cancer. Despite this, tools are lacking for prediction of resistance, either primary or acquired, to this class of therapy. While multiple biomarkers of interest have been studied in preclinical space, such as *CCND1* amplification or RB1 mutation, the clinical applicability of individual biomarkers for CDK4/6i response prediction has been limited. In part, individual genetic alterations may occur infrequently, and/or may occur in context of other

alterations that cumulatively contribute to response. Therefore, an approach that integrates networks of genetic signatures may offer a more comprehensive strategy for evaluating CDK4/6i sensitivity vs resistance.

The Palbo-VNN is a platform that synthesizes common and uncommon mutations organized hierarchically as assemblies into a quantitative assessment of drug response. This model incorporates knowledge of biological pathways in addition to individual genes, which gives it unique strength over most other drug prediction models. Our previous work published on the development and validation of this in cell lines, patient derived xenograft models, and in the AACR GENIE database of metastatic breast cancer patients. Furthermore, our prior work showed that the prediction was specific to CDK4/6i, rather than partner endocrine therapy, based on analysis of patients within the GENIE database treated with CDK4/6i with endocrine therapy vs those treated with endocrine therapy alone. The present study builds on this effort, and is among the first to our knowledge to demonstrate efficacy of a machine learning model in predicting CDK4/6i response in a real-world analysis of patients with advanced ER+ HER2- breast cancer treated with palbo. The model was effective in predicting patients with durable response in the overall population, as well as the patients treated with 1st line palbo, as assessed by duration of therapy and overall survival. Notably, the model most effectively stratified the durations of response, PFS, and OS among the patients treated with 1st line palbo that had NGS obtained before or near palbo start, as the input in this subgroup best reflects pre-treatment genetic contributors to response.

The efficacy of palbo-VNN in stratifying sensitive vs. resistant patients in the 1st line and overall patient cohort underscores its potential to bridge several important clinical gaps. While standard of care is to use CDK4/6i in the 1st line advanced or metastatic setting, recent prospective studies have supported the potential use of CDK4/6i in later line settings. The SONIA study is an investigator-initiated, randomized phase 3 study which investigated the efficacy, safety, and cost effectiveness of first vs second line CDK4/6i when added to endocrine therapy in

ER+ HER2- ABC or MBC. Patients in the study were randomized to first line CDK/6i with nonsteroidal aromatase inhibitor (NSAI) followed by fulvestrant at progression, or to first line NSAI followed by CDK4/6i plus fulvestrant upon progression. No significant difference was observed from time to randomization to progression on second line therapy and use of CDK4/6i in the second line was associated with a lower toxicity than its use in the first line[8]. Further studies have examined the efficacy of CDK4/6i beyond prior CDK4/6i. The MAINTAIN study is a phase 2 study that randomized patients to receive ribociclib or placebo in combination with endocrine therapy switch (exemestane or fulvestrant) in patients with ER+/HER2- ABC or MBC who had progressed on prior CDK4/6i. 86.5% of the patients had received prior palbo. The study demonstrated a PFS benefit with switch of endocrine therapy plus ribociclib vs switching endocrine therapy alone (mean PFS 5.29 vs 2.76 months, HR 0.57, p=0.06)[9]. More recently the phase 3 postMONARCH trial supported a benefit of sequential CDK4/6i use in patients randomized to abemaciclib plus fulvestrant compared to placebo plus fulvestrant after prior CDK4/6i (median PFS of 6.0 vs 5.3 months, HR=0.73, p=0.017)[10]. However, other studies such as the PACE trial examining 2nd line palbo plus fulvestrant vs placebo plus fulvestrant use did not demonstrate similar PFS benefit. While these studies challenged the first line, “one-size-fit-all” approach, the efficacy of second line CDK4/6i or sequential CDK4/6i remains uncertain. However the modest benefit, where seen, support that a tailored, biomarker driven approach harnessing machine learning technology like Palbo-VNN, could reshape patient selection for CDK4/6i in this later line setting, and improve outcomes.

To date, this study is the first to demonstrate the efficacy of the predictive power of a novel, pathway-driven deep learning tool for CDK4/6i response in a real-world, retrospective study. Currently, Palbo-VNN has been tested and validated in preclinical and retrospective clinical studies for palbo specifically. Given that clinical practice has shifted over recent years, favoring ribociclib use due to its OS benefit among the CDK4/6i, future directions include additionally validating the VNN model for abemaciclib and ribociclib. Furthermore, prospective study is

needed to confirm efficacy of the model, such as to optimize selection of sequential CDK4/6i use in the 2nd line and beyond setting, particularly for patients without an aberration in ESR1 or a mutation in the PIK3CA/AKT/PTEN pathway.

As precision oncology rapidly advances, models like Palbo-VNN have the potential to revolutionize treatment selection in cancer treatment. The Palbo-VNN model enables clinicians to move from single mutation-based to sophisticated machine learning approaches, providing insights into resistance pathways and novel therapeutic targets, and improving outcomes at an individual patient level.

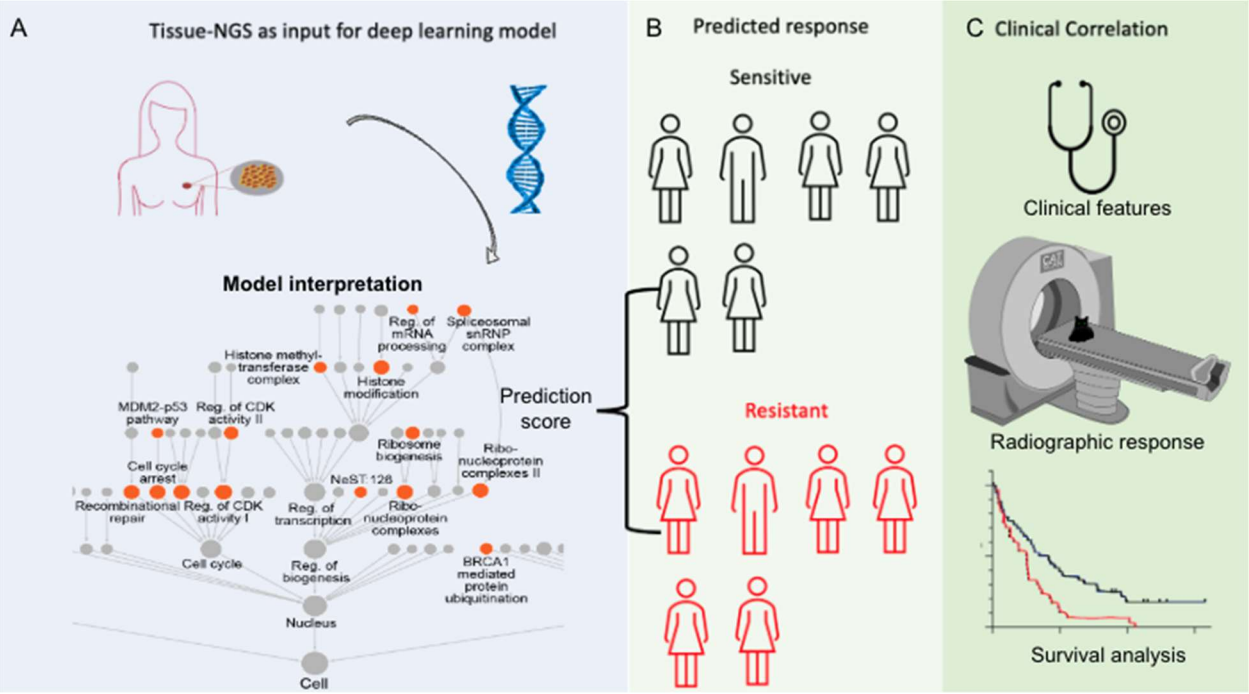

Figure 5.1: Study overview.

Visual representation study design. Patients with biopsy proven breast cancer (based on primary or metastatic tumor site) are included (panel A, top). Next generation sequencing performed on either a primary or metastatic tumor site is used as input for the visible neural network model (panel A, bottom). The genomic data is then processed through the visible, and interpretable hierarchical structure organized into biological assemblies of known protein-protein interactions and cellular function coded by genes tested in the next generation sequencing panel. A prediction score is generated by the model that allows patients to be sorted as sensitive or resistant. Finally, clinical correlation is made between predicted response and observed clinical features and outcomes.

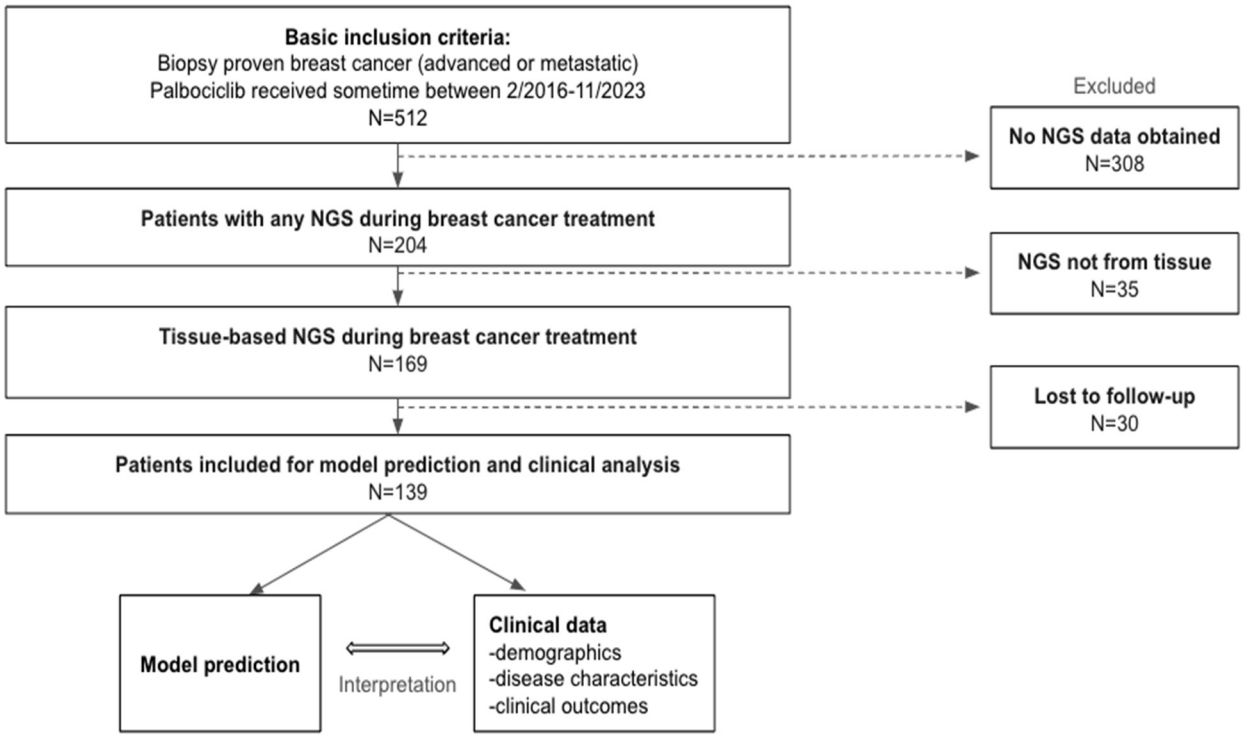

Figure 5.2: Patient selection flowchart.

Flow chart representation for patient selection for the study, including numbers included vs excluded based on key criteria.

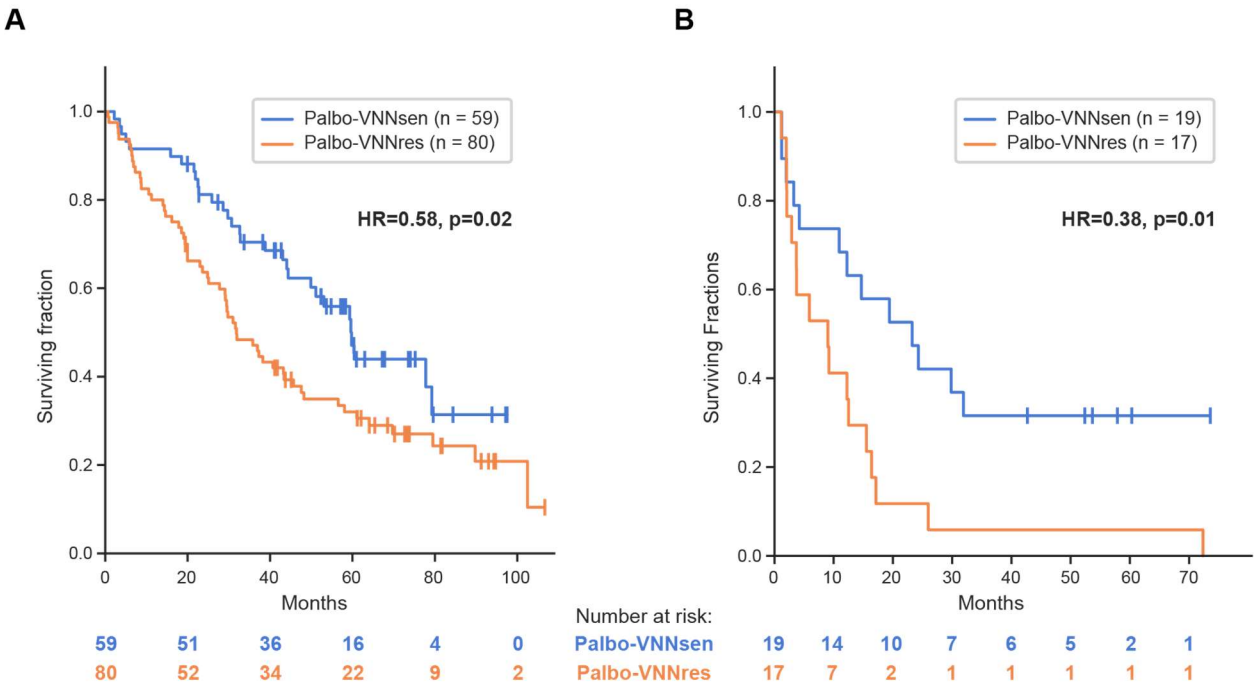

Figure 5.3: Clinical outcomes stratified by Palbo-VNN predictions.

A, Kaplan–Meier curve for OS of the overall patient population. Patients stratified by Palbo-VNN into predicted sensitive (Palbo-VNNsen, blue) and predicted resistant (Palbo-VNNres, orange). **B,** Kaplan–Meier curve for PFS of patients treated in the 1st line setting with tumor-derived NGS within 6 months before or up to 3 months after the start of palbo. Patients stratified by Palbo-VNN into predicted sensitive (Palbo-VNNsen, blue) and predicted resistant (Palbo-VNNres, orange). P-value by log-rank test.

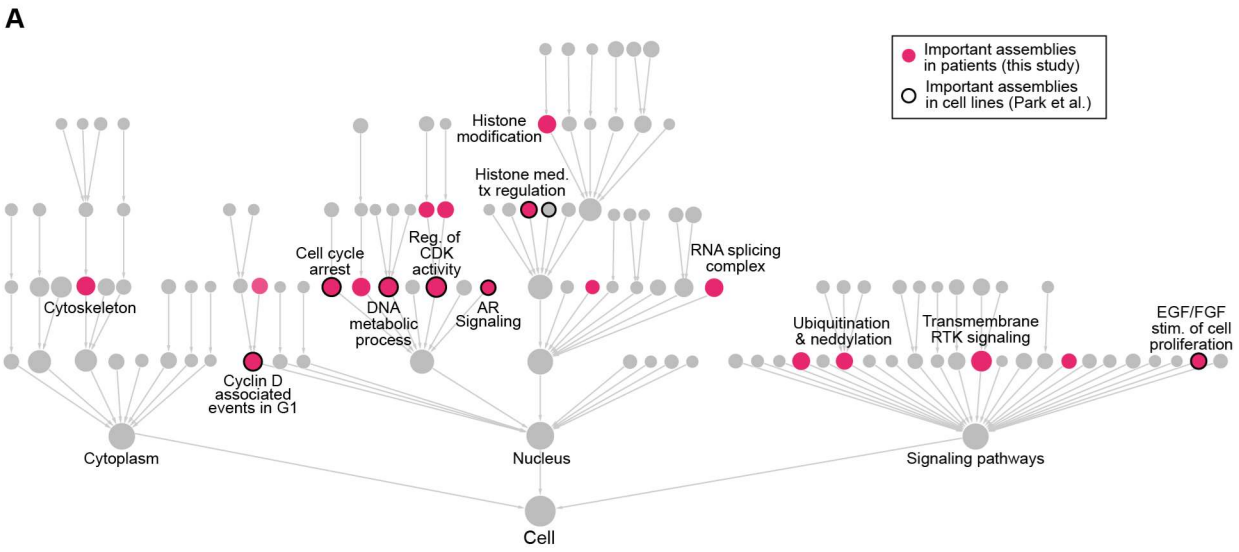

Figure 5.4: Palbo-VNN interpretation of the palbociclib response.

A, Nodes indicate protein assemblies; node sizes indicate assembly sizes in number of proteins; color marks twenty most predictive assemblies for the patient cohort in the current study. Assemblies important in cell lines are indicated by a black ring.

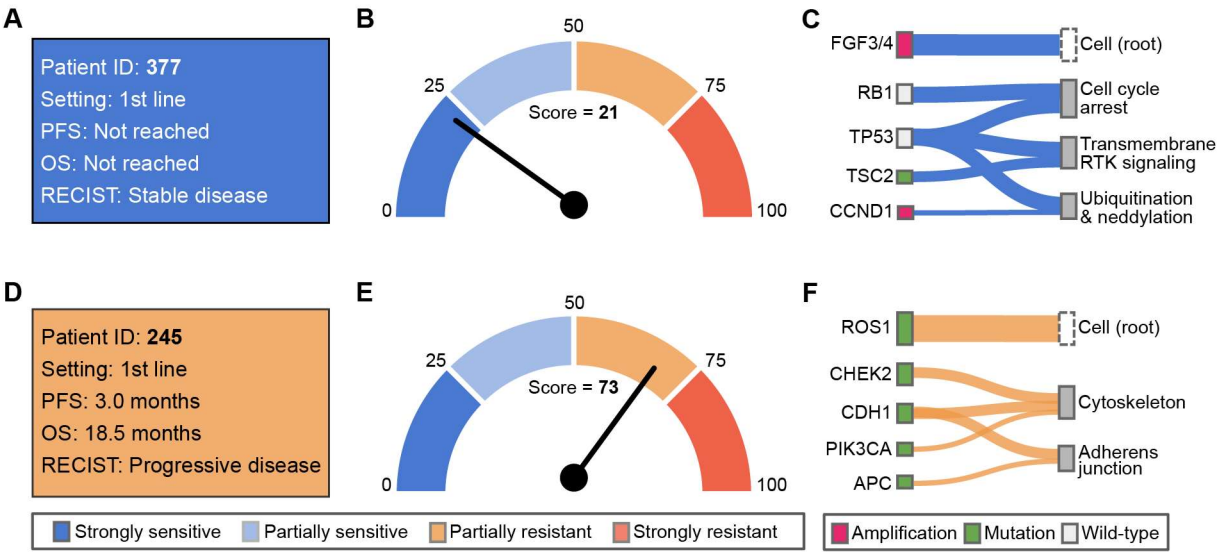

Figure 5.5: Examples of a patient prediction report.

A-C, Clinical outcomes, predicted score, and model explanation for patient #377. **A,** Treatment setting and clinical outcomes. **B,** Gauge plot indicating a strongly sensitive predicted score. **C,** Sankey diagram of five most-predictive gene alterations converging on the most predictive assemblies. **D-F,** Clinical outcomes, predicted score, and model explanation for patient #245. **D,** Treatment setting and clinical outcomes. **E,** Gauge plot indicating a moderately resistant predicted score. **F,** Sankey diagram of five most-predictive gene alterations converging on the most predictive assemblies.

5.7 Tables

Table 5.1: Patient demographic and clinical characteristics

Patient Characteristics Total patients=139	Median (range), Number (%)
Age	63 (33-91)
Race	
White	93 (67%)
Asian	19 (14%)
Other or mixed race	24 (17%)
Black or African American	2 (1%)
Unknown	1 (1%)
ECOG	
0	50 (36%)
1	67 (48%)
2	15 (11%)
3	2 (1%)
Unknown	5 (4%)
Sites of Metastases	
Visceral	92 (66%)
Bone	99 (71%)
Bone only	34 (24%)
Central nervous system	13 (9%)
Type of advanced breast cancer	
Relapse <2 years of adjuvant ET	24 (17%)
Relapse >2 years of adjuvant ET	57 (41%)
De novo metastatic disease	47 (34%)
Other	11 (8%)
Adjuvant Therapy Received (if prior localized)	
Letrozole	41 (53%)
Anastrozole	19 (24%)
Exemestane	29 (37%)
Tamoxifen	28 (36%)
Line of therapy for palbociclib	
1	75 (54%)
2	23 (17%)
3	14 (10%)
4+	27 (19%)

5.8 Acknowledgments

Chapter 5 contains unpublished material co-authored with Zhang, Xiaojie; Hassan, Saifa; Gu, Kelly; Yeung, Kay T.; Ideker, Trey. The dissertation author was a primary investigator and author of this chapter.

5.9 References

(1) Im, S.-A.; Lu, Y.-S.; Bardia, A.; Harbeck, N.; Colleoni, M.; Franke, F.; Chow, L.; Sohn, J.; Lee, K.-S.; Campos-Gomez, S.; Villanueva-Vazquez, R.; Jung, K.-H.; Chakravartty, A.; Hughes, G.; Gounaris, I.; Rodriguez-Lorenc, K.; Taran, T.; Hurvitz, S.; Tripathy, D. Overall Survival with Ribociclib plus Endocrine Therapy in Breast Cancer. *N. Engl. J. Med.* 2019, *381* (4), 307–316.

(2) Morrison, L.; Loibl, S.; Turner, N. C. The CDK4/6 Inhibitor Revolution - a Game-Changing Era for Breast Cancer Treatment. *Nat. Rev. Clin. Oncol.* 2024, *21* (2), 89–105.

(3) Watt, A. C.; Goel, S. Cellular Mechanisms Underlying Response and Resistance to CDK4/6 Inhibitors in the Treatment of Hormone Receptor-Positive Breast Cancer. *Breast Cancer Res.* 2022, *24* (1), 17.

(4) Ahn, J. S.; Shin, S.; Yang, S.-A.; Park, E. K.; Kim, K. H.; Cho, S. I.; Ock, C.-Y.; Kim, S. Artificial Intelligence in Breast Cancer Diagnosis and Personalized Medicine. *J. Breast Cancer* 2023, *26* (5), 405–435.

(5) Vachon, C. M.; Scott, C. G.; Norman, A. D.; Khanani, S. A.; Jensen, M. R.; Hruska, C. B.; Brandt, K. R.; Winham, S. J.; Kerlikowske, K. Impact of Artificial Intelligence System and Volumetric Density on Risk Prediction of Interval, Screen-Detected, and Advanced Breast Cancer. *J. Clin. Oncol.* 2023, *41* (17), 3172–3183.

(6) Shufang Yang, Zihui Wang, Changfu Wang, Changbo Li, Binjie Wang. Comparative Evaluation of Machine Learning Models for Subtyping Triple-Negative Breast Cancer: A Deep Learning-Based Multi-Omics Data Integration Approach. *J. Cancer* 2025, *15* (12), 3943–3957.

(7) Park, S.; Silva, E.; Singhal, A.; Kelly, M. R.; Licon, K.; Panagiotou, I.; Fogg, C.; Fong, S.; Lee, J. J. Y.; Zhao, X.; Bachelder, R.; Parker, B. A.; Yeung, K. T.; Ideker, T. A Deep Learning Model of Tumor Cell Architecture Elucidates Response and Resistance to CDK4/6 Inhibitors. *Nat. Cancer* 2024, *5* (7), 996–1009.

(8) van Ommen-Nijhof, A.; Konings, I. R.; van Zeijl, C. J. J.; Uyl-de Groot, C. A.; van der Noort, V.; Jager, A.; Sonke, G. S.; SONIA study steering committee. Selecting the Optimal Position of CDK4/6 Inhibitors in Hormone Receptor-Positive Advanced Breast Cancer - the SONIA Study: Study Protocol for a Randomized Controlled Trial. *BMC Cancer* 2018, *18* (1), 1146.

(9) Kalinsky, K.; Accordino, M. K.; Chiuzan, C.; Mundi, P. S.; Sakach, E.; Sathe, C.; Ahn, H.; Trivedi, M. S.; Novik, Y.; Tiersten, A.; Raptis, G.; Baer, L. N.; Oh, S. Y.; Zelnak, A. B.;

Wisinski, K. B.; Andreopoulou, E.; Gradishar, W. J.; Stringer-Reasor, E.; Reid, S. A.; O'Dea, A.; O'Regan, R.; Crew, K. D.; Hershman, D. L. Randomized Phase II Trial of Endocrine Therapy with or without Ribociclib after Progression on Cyclin-Dependent Kinase 4/6 Inhibition in Hormone Receptor-Positive, Human Epidermal Growth Factor Receptor 2-Negative Metastatic Breast Cancer: MAINTAIN Trial. *J. Clin. Oncol.* 2023, *41* (24), 4004–4013.

(10) Kalinsky, K.; Bianchini, G.; Hamilton, E.; Graff, S. L.; Park, K. H.; Jeselsohn, R.; Demirci, U.; Martin, M.; Layman, R. M.; Hurvitz, S. A.; Sammons, S.; Kaufman, P. A.; Muñoz, M.; Lai, J.-I.; Knoderer, H.; Sandoval, C.; Chawla, A. R.; Nguyen, B.; Zhou, Y.; Ravenberg, E.; Litchfield, L. M.; Smyth, L.; Wander, S. A. Abemaciclib plus Fulvestrant in Advanced Breast Cancer after Progression on CDK4/6 Inhibition: Results from the Phase III PostMONARCH Trial. *J. Clin. Oncol.* 2024, JCO2402086.